ON THE DEVELOPMENT OF A GHOST-CELL IMMERSED BOUNDARY METHOD AND ITS APPLICATION TO LARGE EDDY SIMULATION AND GEOPHYSICAL FLUID DYNAMICS

A DISSERTATION
SUBMITTED TO THE DEPARTMENT OF CIVIL AND ENVIRONMENTAL ENGINEERING
AND THE COMMITTEE ON GRADUATE STUDIES
OF STANFORD UNIVERSITY
IN PARTIAL FULFILLMENT OF THE REQUIREMENTS
FOR THE DEGREE OF
DOCTOR OF PHILOSOPHY

Yu-Heng Tseng
August 2003

I certify that I have read this dissertation and that, in my opinion, it is fully adequate in scope and quality as a dissertation for the degree of Doctor of Philosophy.

Joel H. Ferziger
(Principal Adviser)

I certify that I have read this dissertation and that, in my opinion, it is fully adequate in scope and quality as a dissertation for the degree of Doctor of Philosophy.

Robert L. Street

I certify that I have read this dissertation and that, in my opinion, it is fully adequate in scope and quality as a dissertation for the degree of Doctor of Philosophy.

Stephen G. Monismith

Approved for the University Committee on Graduate Studies.

Abstract

Ocean circulation off the west coast of the United States is driven by a variety of mechanisms, the most important of which are the seasonally varying wind stress and coastal irregularities. Although many studies have considered the flow near coastal irregularities, no study has explicitly focused on the interaction of a strong upwelling jet with a coastal prominence, e.g. a bay, canyon or cape. Coastal geometry and bathymetry are important in geophysical fluid dynamics (GFD) applications, but they are crudely approximated in most cases. Complex geometry is also found in a variety of engineering applications. The availability of accurate and efficient alternatives for dealing with arbitrary complex geometry would represent a significant advance.

The objectives of this study are to develop and verify an efficient ghost-cell immersed boundary method (GCIBM), to investigate the effects of coastal geometry on the eddy formation and turbulent mixing in coastal upwelling flow, and to apply the method to simulate the regional circulation in the vicinity of Monterey Bay. In the GCIBM, the boundary conditions are treated by prescribing body forces in a manner that yields a desired velocity on the surface. The surface need not to coincide with the coordinate lines and is free to move in time. The reconstruction procedure allows systematic development of numerical schemes for treating the immersed boundary while preserving the accuracy of the base solver.

In order to verify these claims, the GCIBM module is implemented in several existing numerical codes. The simulations are compared with experiments and/or boundary-fitted results. Three types of flows are studied. First, flow over a circular cylinder is simulated at two Reynolds numbers. The accuracy of the GCIBM is quantified, and the results suggest that the approach retains the overall second order

accuracy of the base solver i.e. the accuracy is not affected by the boundary treatment. The numerical results agree well with published experimental and boundary-fitted grid results. Second, three-dimensional turbulent flow over a wavy boundary is simulated using large-eddy simulation (LES). Both steady and unsteady cases are simulated and compared well with boundary-fitted results. Third, the method is implemented in an existing ocean model. Flow over a three-dimensional Gaussian bump is tested and the results are verified by a high resolution simulation.

We also investigate the eddy formation and the effects of coastal geometry in coastal upwelling, which is an important mechanism in coastal ocean dynamics. Cyclones/anti-cyclones and thin filaments observed in satellite infrared images of upwelling regions are rather well reproduced. The instabilities are confirmed to be of mixed baroclinic-barotropic and modified Rayleigh-Taylor types (Tadepalli, 1997). Nonlinear interactions limit the growth of the large scale structures and the latter generate 'fish-hook' structures. The Rayleigh-Taylor and mixed instabilities and fish-hook structures cause a sharp increase in mixing. Mixing and stirring are quantified using a mixedness parameter and energy budgets.

Finally, we extend the GCIBM to simulate the coastal circulation in the vicinity of Monterey Bay. Satellite images often show a cyclonic eddy in the bay and an anti-cyclonic eddy outside the bay during spring and summer. We compare the simulation results with observed mooring data and compare the simulated upwelling process with the satellite images. The mean currents follow the annual cycle of the seasonal circulation. The coastal geometry plays an important role on the generation and movement of coastal eddies. We also study the effects of Monterey Submarine Canyon on the large scale coastal circulation. Quantitative comparisons between hydrostatic and non-hydrostatic models are made to investigate the importance of the non-hydrostatic effects on the coastal ocean simulation. The non-hydrostatic model predicts the vertical structure more accurately than does the hydrostatic model. We also identify the deep Canyon contributes significantly to the non-hydrostatic effects and we conclude that the effects cannot be ignored in coastal ocean modeling with complex topography.

Acknowledgments

I will always be grateful to my advisors, Professor Joel Ferziger and Professor Robert Street, for giving me the opportunity to pursue a Ph.D. at Stanford University. I am indebted to my principal advisor, Professor Joel Ferziger, for his encouragement and support. I have learned a great deal from his good physical insights and quick thinking. Interacting with him has truly enriched my experience at Stanford. I thank Professor Robert Street, my co-principal advisor, for his continuous support to this work and useful suggestions. I would like to thank Stephen Monismith for serving my reading committee and for many helpful suggestions and discussions. I would also like to thank Professor Jeffrey Koseff and Professor Paul Durbin for several useful discussions and constant supports. In particular, I am grateful to Professor Paul Durbin and Gianluca Iaccarino for helping me to initialize the immersed boundary method research.

I would like to thank Dr. David Dietrich and Professor Robert Haney for providing me the ocean models and many helpful discussions. Without their help, I could not accomplish the work. Many thanks are due to Professor Leslie Rosenfeld for her useful discussion; Florence Wang and Steven Eittreim for providing me the Monterey Bay topography. I owe thanks to many of my colleagues in the EFML for their friendship and support. In particular, I would like to thank Professor Oliver Fringer for guiding me to get started with Zang's code; Dr. Derek Fong for giving me advices in physical oceanography; Dr. Emily Zedler for providing me the wavy boundary code and invaluable advices; Dr. Li Ding for his technical advice. Many thanks are due to Jeremy Bricker, Tina Katopodes, Gerard Ketefian, Lucinda Shih, Cary Troy for their discussions and great friendships. I would also like to thank all of the other

labmates for making my stay at the lab pleasant.

Finally, I want to thank my family especially my parents, to whom this thesis is dedicated. Over the years, they have always been standing behind me with constant encouragement and love. I also want to thank my sister, Yu-En, and brother in law, Jeff Hsieh, for their thoughtful consideration and support throughout my graduate study at Stanford. They give me wonderful experience living in California. I also thank my grandmother for her love and support for as long as I can remember. The completion of this work would not have been possible without the understanding and support from my family.

Financially support for this work was provided by NSF ITR/AP (GEO) grant number 0113111 (Ms. B. Fossum, Program Manager) and NASA AMES/Center for Turbulent Research, Stanford. These sponsors are gratefully acknowledged.

Dedication

Dedicated To My Parents

Nomenclature

Roman Symbols

A	ripple amplitude
a	coefficient in the interpolation function
B	coefficient matrix
C_D	drag coefficient
C_f	skin friction
C_p	pressure coefficient
C_L	lift coefficient
D	diameter of the upwelling flow domain
f	Coriolis parameter
f_i	immersed boundary forcing
f_s	vortex shedding frequency
G	ghost node
g	gravitational acceleration constant
g'	reduced gravity
H	nominal ocean depth

h	height of bump
h_{10}	initial upper layer depth
I	image node
L	length scale of bump
L_W	recirculation length
N_i	number of grid points in i direction
n	normal direction
O	the node at which boundary condition is satisfied
P	pressure boundary
p	dynamic pressure
p	power parameter
R_c	cape radius
R_0	tank outer radius
R_1	tank inner radius
Re	Reynolds number
St	Strouhal number
s	salinity
T	potential temperature
t	time
t_s	spin-up time
U_∞	upstream velocity

U_p disk edge velocity

u, v, w Cartesian velocities x, y and z directions

u_i Cartesian velocity

u_* disk friction velocity

u_i^* intermediate velocity

w_m interpolation weight

x_i Cartesian coordinate

x, y, z Cartesian coordinates

X_i fluid nodes

Greek Symbols

Δt time step

$\Delta x, \Delta y, \Delta z$ grid spacing

δ_{ij} Kronecker delta

ζ relative vorticity

θ circumferential coordinate

θ_* non-dimensional parameter for the upwelling flow

κ thermal diffusivity or molecular diffusivity

λ ripple wavelength

λ_s stationary width of the front

μ dynamic viscosity

ν kinematic viscosity

ρ density

ρ' perturbation relative density

ρ_0 reference density

ρ_b background relative density

ρ_* relative density

σ Rossby/Froude number

τ_{ij} subgrid-scale stress tensor

τ_w surface stress tensor

ϕ scalar variable

Ω rotation rate

Abbreviations

APE available potential energy

B-B baroclinic-barotropic

Bi-CGSTAB biconjugate gradient stabilized

CCS California current system

CFD computational fluid dynamics

CG conjugate gradient

CPU central processing unit

CU California undercurrent

DieCAST Dietrich/center for air-sea technology

EVP error vector propagation

EKE eddy kinetic energy

EFML Environmental Fluid Mechanics Laboratory

FEM finite element method

GCIBM ghost-cell immersed boundary method

GFM ghost fluid method

GFD geophysical fluid dynamics

IC inshore current

ILU incomplete lower-upper

LES large-eddy simulation

LST linear stability theory

MBARM Monterey Bay area regional model

MG multi-grid

MITGCM MIT global circulation model

NASA National Aeronautics and Space Administration

NHF non-hydrostatic factor

NM Narimousa and Maxworthy

N-S Navier-Stokes

OBCs Open boundary conditions

PDF Probability density function

POM Princeton ocean model

QUICK quadratic upstream interpolation for convective kinematics

RHS right-hand side

RPE reference potential energy

RT Rayleigh-Taylor

SGS subgrid scale

SIP strongly implicit procedure

SOMS Sandia ocean modeling system

TI turbulent intensity

TPE total potential energy

USGS U.S. Geological Survey

Contents

List of Tables

List of Figures

Chapter 1

Introduction

The purpose of this study is to develop a new ghost-cell immersed boundary method (GCIBM) and to verify the approach using several well-documented numerical examples. Furthermore, we extend the GCIBM to coastal ocean modeling, in which the realistic coastal geometry and bathymetry are well represented. Before proceeding to the real simulation, we investigate the effects of coastal geometry and eddy formation on the upwelling flow. This chapter discusses the background of this research, lays down the objectives, and outlines the current work.

1.1 Background

1.1.1 California current system and upwelling in Monterey Bay

Monterey Bay is located 100 km south of San Francisco and is one of several large bays on the West Coast of the United States. This area is important due to the abundance of marine life and many studies have examined the circulation in its vicinity (Collins *et al.*, 2000; Ramp *et al.*, 1997; Rosenfeld *et al.*, 1994). They found that the circulation is highly correlated to the California Current System (CCS). Generally speaking, the CCS is composed of two regions (Figure 1.1). In the offshore region, flow is dominated by a broad, weak ($10 - 30$ cm/s), shallow ($0 - 500$ m) equatorward flowing current,

the California Current (CC). The CC extends offshore to a distance of $900-1000\ km$ and flows year-round (Figure 1.1). Within about 100 km of the coast, two narrow poleward flowing boundary currents have been found, the Inshore Countercurrent (IC) and the California Undercurrent (CU). They are distinguished by the properties of the water they transport. The IC varies seasonally, appearing in fall and winter, and transports shallow, upper layer water. The IC is a weak current and has different names depending on location, e.g. the Davidson Current (north of Point Conception), and the Southern California Countercurrent (south of Point Conception). The CU is a narrow ($10-50\ km$) relatively weak subsurface flow and transports warm, saline equatorial waters (Batteen & Vance, 1998). The CU is strongest at around $100-300\ m$ depth with a mean speed of approximately 15 cm/s (Pierce *et al.*, 2000) at all latitudes on the west coast throughout the year.

The CCS contains three characteristic water masses (Marchesiello *et al.*, 2003): Pacific Subarctic Water (PSW), North Pacific Central Water (NPCW) and Southern Water (SW). The PSW is advected equatorward and has low salinity (s) and temperature (T), and high levels of oxygen and nutrients. The NPCW enters from the west and contains high s, T and nutrients, and low oxygen. The SW comes from the south with the CU (high s and T, low oxygen and nutrients).

Recent observations show that the currents along the west coast of the U.S. are quite energetic and have strong seasonal variability (Kelly *et al.*, 1998). They result from seasonal wind forcing and Rossby wave propagation (Marchesiello *et al.*, 2003). The seasonal pattern is generally described as the evolution of coastal jets which form during spring upwelling-favorable winds and later move off the shelf to become a deep-ocean CC flow out to approximately $127°W$, where its surface eddy kinetic energy (EKE) decreases between fall and spring. The offshore propagation of EKE is a robust feature of the annual cycle in this region. The maximum EKE occurs in summer and is associated with the seasonal coastal upwelling. Early studies suggested that the decay of the surface EKE results from dissipative vertical mixing (Kelly *et al.*, 1998; McCreary *et al.*, 1991). However, available evidence suggests that oceanic eddies in general are not highly dissipative; Gulf Stream rings and CC eddies maintain their identities for months (Garfield *et al.*, 1999). Haney *et al.* (2001)

examined the hypothesis that the surface EKE decreases westward beyond its maximum near $127°W$ because of a transformation of kinetic energy from shear to mean flows, i.e. barotropization. As a result, the surface EKE of the upper ocean decreases while the EKE of the rest of the ocean increases. The surface energy generated during the upwelling season propagates downward to the deep ocean via a transformation into barotropic currents (Marchesiello *et al.*, 2003). The process releases the available potential energy and converts it to kinetic energy. It is a known property of nonlinear geostrophic turbulence (Salmon, 1998; McWilliams *et al.*, 1994; Wiin-Nielson, 1962). With a quasi-geostrophic CCS model, Ikeda *et al.* (1984) showed that the growth of disturbances in the CC follows an inverse cascade due to nonlinear interactions. This interpretation was reconfirmed by Marchesiello *et al.* (2003). These recent studies pointed out an important requirement for modeling a coastal region: models must represent accurately the nonlinear terms in the momentum equations that are responsible for the energy transformation.

Upwelling occurs on the eastern boundaries of the oceans and is found off the coast of western North America. The upwelling is forced by the prevailing alongshore winds, which are enhanced by coastal mountain ranges and seasonal stratification to produce a strong low level atmospheric jet (Haney *et al.*, 2001). These winds force a surface Ekman transport 45 degrees to the right, i.e. in the offshore direction (Figure 1.2). This is a three-dimensional flow in which buoyancy, rotation, stratification and surface forcing are all significant, and plays an important role in the biology of the coastal environment. The 'upwelled' water occurs as a cool band along the coast, typically tens of kilometer wide, and is separated from the warmer offshore waters by a series of fronts, plumes and eddies extending more than 100 km offshore. Upwelled water is nutrient-rich and supports high levels of phytoplankton (organisms that form the base of the ocean bio-system). The coastal upwelling creates a mean cross-shelf flow and may grow to the point where it breaks the continuity of the along-shelf flow. This process transports large amounts of cold, nutrient-rich, upwelled water off the shelf (Barth, 1989).

Rosenfeld *et al.* (1994) studied the circulation in the vicinity of Monterey Bay during the upwelling season (i.e. spring and summer) when strong upwelling-favorable

(equatorward along-shore) winds result in strong near-surface horizontal temperature gradients and great biological productivity. The upwelling phenomenon is confined to a narrow region adjacent to the coast. Away from the coast, an Ekman layer develops in the upper ocean. The depth of this layer varies, but it has strong vertical shear. It features a net transport directed to the right of the wind.

On the west coast of the U.S., the effects of topography and instabilities play important roles in the along-shore coastal jets and the offshore Ekman transport. The topographic effect on the wind-driven coastal circulation has been shown by Narimousa and Maxworthy (1989) to form local upwelling centers and standing waves with offshore Ekman transport. However, the generation of instability in the coastal jets does not require topographic effects (McCreary *et al.*, 1991), but capes and ridges (Batteen, 1997; Tseng & Ferziger, 2001a) may promote locally enhanced cross-shore transport. In many places, bathymetry effects are so strong that they can cause major boundary current recirculation, separation and eddy shedding with environmentally important large cross-shelfbreak ventilation; prominent examples are: the Black Sea, where such effects dominate the circulation between the Rim Current and coast (Staneva *et al.*, 2001); and the climatologically important Gulf Stream separation problem (Dengg *et al.*, 1996; Townsend *et al.*, 2000).

The regional circulation in the Monterey Bay area is highly correlated to the coastal upwelling along the west coast of the U. S., and is tightly coupled to the CCS. An accurate numerical model in this region represents a significant progress to investigate the regional complex flow pattern. However, there are only a few numerical studies focusing on the regional circulation in the vicinity of Monterey Bay. The complicated coastal geometry and bathymetry (steep shelf, coastal bay and Monterey Canyon) in Monterey Bay area play important roles on the regional circulation. Most previous studies use simplified geometry, topography and forcing (Ly & Luong, 1999; Petruncio, 1996). These studies fail to accurately simulate the complex flow in this region with realistic topography and stratification unless an advanced data assimilation method is included (Shulman *et al.*, 2002). But before assimilating the data into any numerical model, the numerical model has to simulate the dynamics accurately.

In order to simulate the flow pattern with such complex geometry, a robust, higher-order numerical model is required to minimize the numerical errors, and we need to develop a new method to correctly represent the complex coastal topography.

1.1.2 Background of the immersed boundary method

In computational fluid dynamics, the primary issues are accuracy, computational efficiency, and, especially, the handling of complex geometry. All large scale geophysical flows involve complex three-dimensional geometry and turbulence. Accurate representation of multi-scale, time dependent physical phenomena is required. A grid that is not well-suited to the problem can lead to unsatisfactory results, instability, or lack of convergence.

There are many computational methods for solving incompressible flow in geometrically complex regions. Techniques that are often employed to handle geometry other than rectangular geometry are coordinate transformation and boundary-fitted grids (Zang *et al.*, 1994). These methods have the obvious advantage that the grid conforms to the irregular boundary. This is especially important when we model thin boundary layers. Another advantage is that the curvilinear meshes are topologically equivalent to Cartesian meshes in computational space. The equations of interest can be solved on the Cartesian mesh, taking into account geometrical terms, and the solution is transformed back to the curvilinear grid. The obvious disadvantage to these methods is that analytical transformations only exist for a limited range of geometries. To handle more complicated geometries, such as multiply-connected domains and irregular objects, one must resort to more complex transformations, a task that is quite challenging.

In some applications, finite element methods (FEM) on unstructured meshes are used almost exclusively. Since discrete spatial elements are aligned with the irregular boundary, important boundary effects can be well resolved. Moreover, an unstructured finite element mesh can be easily refined where details of the solution need to be resolved. The accuracy of the finite element method can be improved by using higher order interpolation schemes, and spectral accuracy can be achieved when spectrally

accurate polynomials fits are used as interpolating function. However, generating the meshes required by the FEM is as much art as science and higher order methods on an unstructured are expensive. Grid generation may also be difficult. Furthermore, to solve problems with a moving boundary, one must remesh every time the boundary moves. This can be very expensive.

The development of accurate and efficient methods that can deal with arbitrarily complex geometry would represent a significant advance. The immersed boundary method (IBM) has recently been demonstrated to be applicable to complex geometries while requiring significantly less computation than competing methods without sacrificing accuracy (Fadlun *et al.*, 2000; Verzicco *et al.*, 2000). The method specifies a body force in such a way as to simulate the presence of a surface without altering the computational grid. The main advantages of the IBM are memory and CPU savings and ease of grid generation compared to unstructured grid methods (Verzicco *et al.*, 2000). Bodies of almost arbitrary shape can be dealt with. Furthermore, flows with multiple bodies or islands may be computed at reasonable computational cost.

The IBM was first introduced by Peskin (1972). More recently, Goldstein *et al.* (1993) and Saiki and Biringen (1996) published extensions. They employed feedback forcing to represent the effect of solid body. The feedback force is added to the momentum equation to bring the fluid velocity to zero at the desired points. However, this technique may induce spurious oscillations and restricts the computational time step (Goldstein *et al.*, 1993), effectively limiting the technique to two-dimensions. Mohd-Yusof (1997) suggested an approach that introduces a body-force f so that the desired velocity distribution V is obtained at the boundary Ω. In principle, there are no restrictions on the velocity distribution V or the motion of Ω. He implemented the method for complex geometry in a pseudo-spectral code while avoiding the need for a small computational time step. The method costs no more than the base computational scheme. Fadlun *et al.* (2000) applied this approach to a three-dimensional finite-difference method on a staggered grid and showed that the approach was more efficient than feedback forcing.

A number of other immersed boundary methods have been applied to problems of

irregular geometry. Calhoun and LeVeque (2002; 2000) proposed a streamfunction-vorticity method to model irregular shapes in a Cartesian grid. The irregular boundary is represented by discontinuity conditions. They extended the method developed by McKenney *et al.* (1995) to solve a Poisson equation on an irregular region using a Cartesian grid. Pember *et al.* (1995) presented an adaptive Cartesian mesh solver for the Euler equations. Their method treats the boundary cells as regular cells, thus avoiding instability problems. Almgren *et al.* (1997) developed a Cartesian grid projection method for the incompressible Euler equations in complex geometry. The same group also proposed a second-order accurate method for solving the Poisson equation on two-dimensional Cartesian grids with embedded boundaries (Johansen & Colella, 1998). McCorquodale *et al.* (2001) extended this approach to the solution of the time dependent heat equation. On the other hand, Udaykumar *et al.* (2001) and Ye *et al.* (1999) have presented a finite-volume Cartesian method without momentum forcing. They reshaped the immersed boundary cells to fit the local geometry and used quadratic interpolation to calculate the fluxes across the cell faces while preserving second-order accuracy. They showed that the method is applicable to moving geometry problems. However, the above studies mainly focus on two-dimensional applications. Particularly, the streamfunction-vorticity method is hard to extend to three dimensions. Kirkpatrick *et al.* (2003) presented a second-order accurate IBM on a non-uniform, staggered three-dimensional Cartesian grid. The approach requires truncating the Cartesian cells at the boundary to create new three-dimensional cells which conform to the shape of the surface. The reshaped-cell method developed by Kirkpatrick *et al.* (2003), Udaykumar *et al.* (2001), and Ye *et al.* (1999) is very similar to the shaved cell approach in MIT General Ocean Model (MITGCM) (Adcroft *et al.*, 1997). The shaved cell idea is not entirely new; a simple variant of it was introduced more than thirty years ago (Chan & Street, 1970). However, the implementation for the reshaped cell approach is complicated and only no-slip boundary conditions can be applied. Developing an efficient IBM will be very useful in GFD.

1.2 Motivations and objectives

As shown above, many studies have considered flow near coastal irregularities off the west coast of the United States. However, no study has explicitly focused on the interaction of a strong upwelling jet with a coastal prominence, e.g. a bay or a cape. A realistic regional ocean model should completely resolve the eddies in steep bathymetry without geometrical smoothing and simulate and/or parameterize shallow coastal zone processes which have a short length scale. Data assimilation should not be used if the numerical model cannot simulate the general circulation. One of our major purposes is to accurately represent the coastal dynamics of Monterey Bay area without data assimilation.

In coastal ocean modeling, we desire to capture the evolution and interaction of various scales, from dissipative scales to mesoscale eddies. Stair-step boundaries, which follow the grid coordinate, are often used but are not accurate and create numerical problems. An appropriate representation of the boundary is key. In addition, moving and deforming geophysical flow domains (e.g. a wavy surface at the top and sediment transport at the bottom) further complicate numerical flow simulations. When boundary-fitted meshes are employed, the grid must be either regenerated or deformed as the geometry changes, adding considerably to the computational complexity.

It is clear that the availability of high-accuracy, high-efficiency alternatives to deal with arbitrary complex geometry would represent a significant advance in GFD. Methods that retain the computational efficiency and accuracy of the optimized numerical codes appear to be particularly compelling. We will formulate and demonstrate a new ghost cell immersed boundary method in which the boundary conditions treatment is dependent of the grid. The boundary is prescribed in a manner that yields the desired boundary condition on the surface; the surface need not coincide with the coordinate lines and is free to move in time. There are only few studies based on this technique for turbulent flow and no extensive application to GFD as yet.

The main objective of the current work is to develop and verify the immersed boundary method. Besides, we apply the method to a high-resolution coastal ocean

model and study regional circulation in the vicinity of Monterey Bay subject to the effects of complex geometry and bathymetry. We also present a combination of theory and simulation on coastal upwelling with the aim of understanding the origin and nature of the structures found in the real ocean. For the coastal ocean simulation, we use both hydrostatic and non-hydrostatic models to evaluate non-hydrostatic effects on the coastal region. To the best of our knowledge, this is the first high resolution, non-hydrostatic, simulation of the regional circulation in the vicinity of the Monterey Bay. The aims of the current work are in the following:

1. Develop the GCIBM for coastal ocean modeling to handle different boundary conditions and complex coastal geometry efficiently and accurately.

2. Validate the GCIBM for laminar and turbulent flows using established experimental and numerical results.

3. Study the formation of cyclonic and anti-cyclonic eddies in a laboratory upwelling simulation.

4. Examine turbulent mixing and energy budget in upwelling regions and the effects of coastal geometry on it.

5. Apply a high-resolution coastal ocean model to simulate the Monterey Bay area.

6. Evaluate non-hydrostatic effects on the regional flow in the vicinity of a coastal region.

7. Investigate the effects of realistic, steep bathymetry on coastal circulation.

1.3 Outline

The structure of this dissertation is illustrated in Figure 1.3. We develop the new ghost-cell immersed boundary method, which can deal with different types of boundary conditions accurately in a Cartesian grid. Either staggered or non-staggered grids can be treated. We then validate the approach in several flows with complex geometry. The validation includes uniform flow over a circular cylinder, turbulent flow over

a wavy boundary, and geophysical flow over a three-dimensional bump. These numerical examples show the ability of the current GCIBM to handle complex geometry. Finally, we apply the GCIBM to the Monterey Bay Area Regional Model (MBARM) and study regional circulation in the vicinity of the Monterey Bay area. Since the seasonal variation of the circulation is highly correlated to the coastal upwelling, we also investigate the upwelling flow using numerical simulation of a laboratory upwelling flow. The MBARM is one-way coupled to a larger scale California current system model. The effects of topography are investigated. This region is chosen because detailed observational results are available. We also study the effects of Monterey Canyon on the general recirculation.

The remainder of this dissertation is organized as follows. Chapter 2 introduces the governing equations and the numerical formulation of each model. Chapter 3 discusses the numerical implementation of the GCIBM. The generalized ghost-cell method and the polynomial reconstruction schemes are laid out. Different boundary conditions and the implementation to both non-staggered and staggered grids are discussed. Chapter 4 validates the approach for flow over a cylinder and evaluates the model's accuracy. We also extend the new method to LES of three-dimensional turbulent flow over a wavy boundary and compare the results with a well-resolved boundary-fitted grid simulation. Chapter 5 illustrates the implementation on the MIT global circulation model (MITGCM) and compares the GCIBM results with previous methods for simulating geophysical flow. Chapter 6 investigates the eddy formation in the coastal upwelling flow and the effects of coastal geometry on it. Turbulent mixing is also quantified. Chapter 7 extends the GCIBM to a regional ocean model and studies the regional circulation in the Monterey Bay area. Finally, conclusions and recommendations are drawn in Chapter 8.

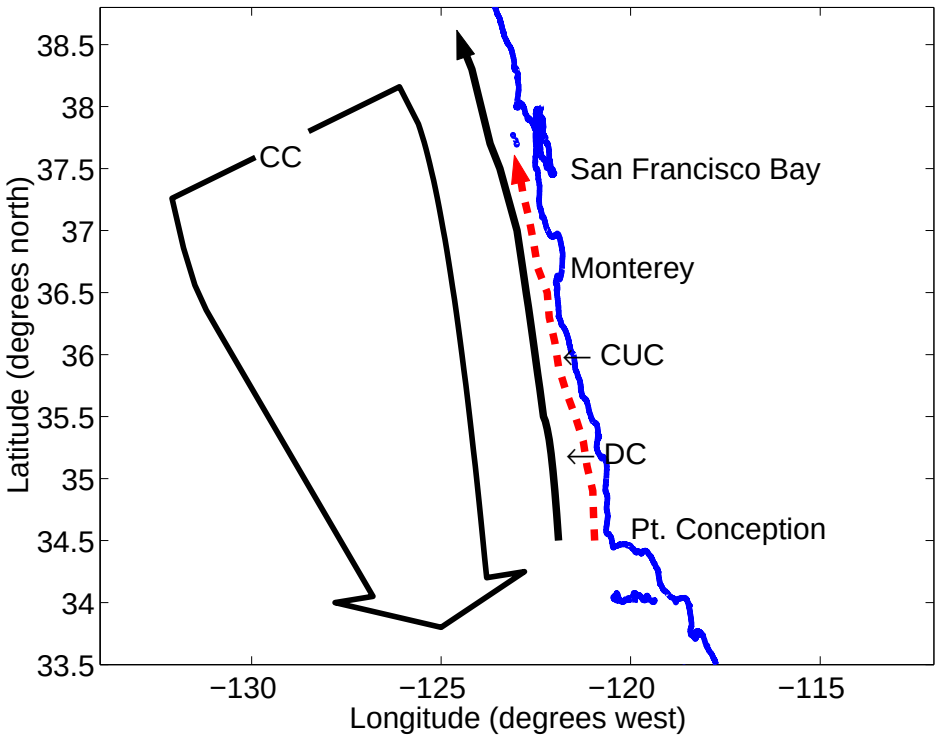

Figure 1.1: Schematic diagram of the California Current System (CCS).

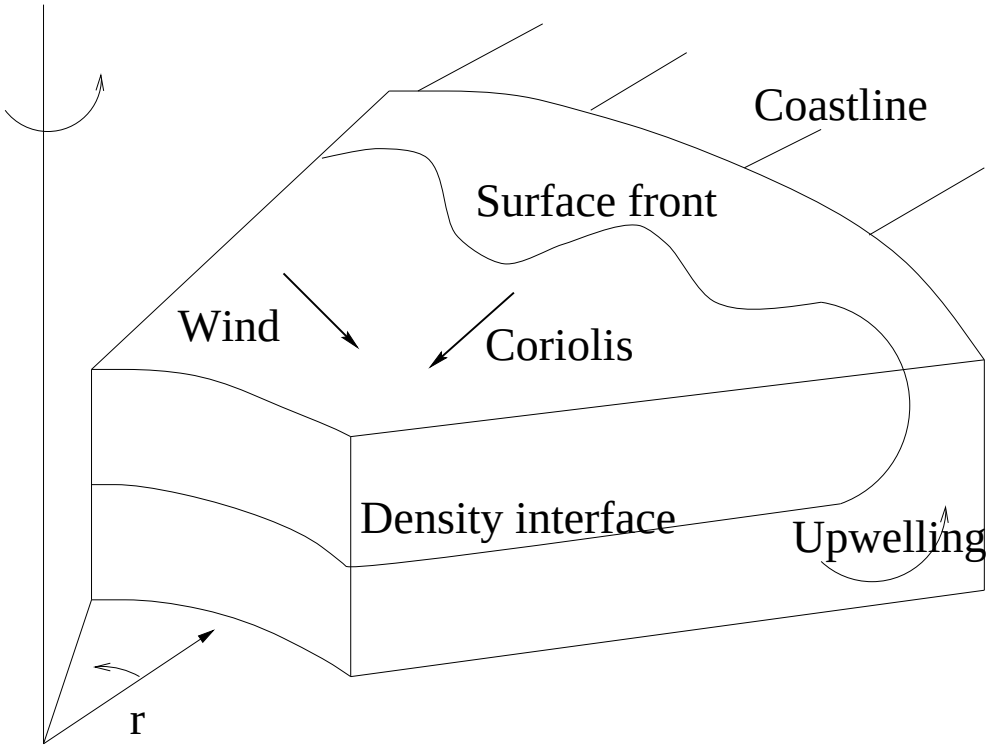

Figure 1.2: Schematic diagram of the upwelling process.

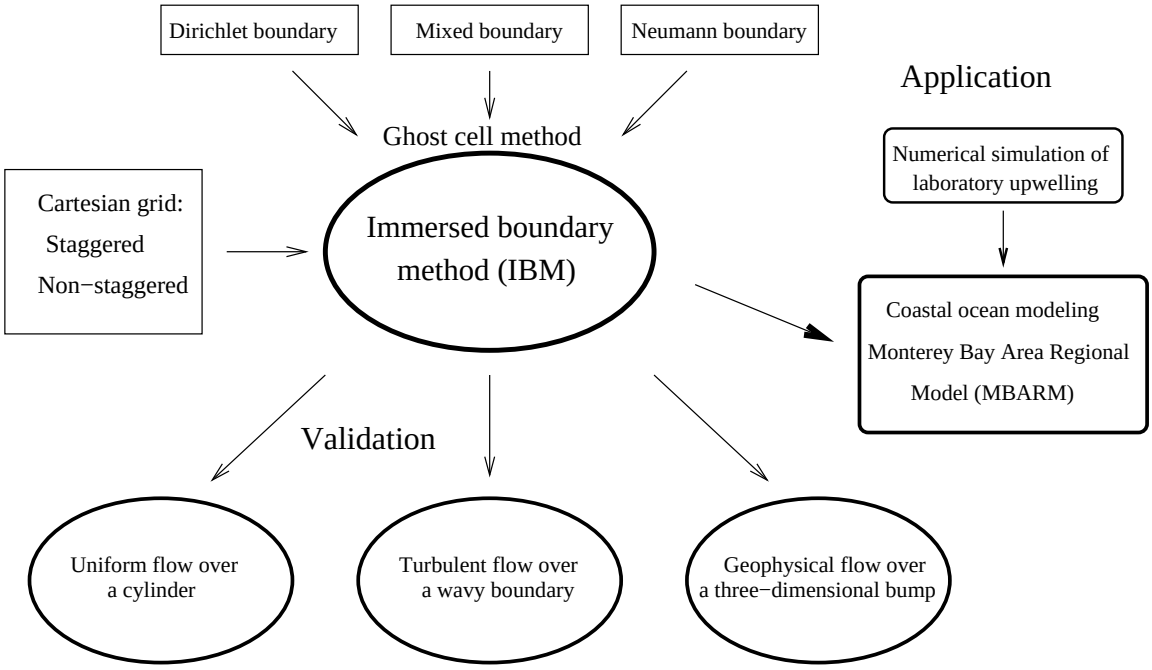

Figure 1.3: The structure of this dissertation.

Chapter 2

Mathematical and Numerical Formulation

2.1 Introduction

The governing equations for unsteady, three-dimensional, non-hydrostatic, rotating flows are the continuity, Navier-Stokes, and scalar transport equations. The implementation of immersed boundary method requires the generation of a Cartesian grid covering the domain of interest without the physical boundaries being taken into account. The governing equations are solved on the underlying Cartesian mesh and a forcing term is introduced to model the effect of the presence of the body. We implement the immersed boundary method on several examples, ranging from laboratory flows to large scale geophysical flows, using three different numerical codes. These are the EFML code, MIT global circulation model (MITGCM), and DieCAST (Dietrich Center for Air Sea Technology) ocean model. The mathematical formulation will be introduced here.

This chapter is organized as follows. The governing equations are introduced in Section 2.2. The numerical algorithms of the three codes are briefly introduced and compared in Section 2.3. A short summary is in Section 2.4.

2.2 Governing Equations

In most stratified flows, density varies by only a few percent, so we may employ the Boussinesq approximation. In order to model the flows of interest, we consider the continuity equation and the three-dimensional, unsteady, incompressible Navier-Stokes (N-S) equations in Boussinesq form with the Coriolis force included. A boundary forcing term f_i is added to the N-S equation. Writing these governing equations in conservative form, we have

$$\frac{\partial u_j}{\partial x_j} = 0 \tag{2.1}$$

$$\frac{\partial u_i}{\partial t} + \frac{\partial}{\partial x_j}(u_i u_j + p\delta_{ij} - \nu\frac{\partial u_i}{\partial x_j}) = -g\rho'\delta_{i3} + 2\Omega(-u_1\delta_{i2} + u_2\delta_{i1}) + f_i \tag{2.2}$$

where $\rho' = (\rho_* - \rho_b)$ is a perturbation relative density, $\rho_* << 1$ is the relative density, ρ_b is the background relative density, p is the dynamic pressure defined in Zang (1993) and $\nu = \mu/\rho_0$ is the kinematic viscosity. f_i is the additional forcing and is zero everywhere except at the immersed boundary. Ω is the effect of rotation. The Einstein convention is used to imply summation over repeated indices and the direction of gravity is defined in the negative x_3 direction for convenience. Furthermore, the scalar transport equation for salinity (s) is

$$\frac{\partial s}{\partial t} + u_j\frac{\partial s}{\partial x_j} = \frac{\partial}{\partial x_j}(\kappa\frac{\partial s}{\partial x_j}) \tag{2.3}$$

where κ is the molecular diffusivity.

In ocean modeling, the governing equations are very similar to the above equations set, except for the addition of heat transport equation for potential temperature (T) which is defined as the temperature of a parcel of water at the sea surface after it has been raised adiabatically from some depth in the ocean,

$$\frac{\partial T}{\partial t} + u_j\frac{\partial T}{\partial x_j} = \frac{\partial}{\partial x_j}(\kappa\frac{\partial T}{\partial x_j}) \tag{2.4}$$

and an equation of state to relate density to the potential temperature and salinity:

$$\rho = \rho(T, s, p) \tag{2.5}$$

We will introduce and compare each model's numerical algorithms briefly in the following section.

2.3 Numerical formulation

2.3.1 EFML code

The governing equations (2.1)-(2.3) are solved using a finite-volume technique. The method of fractional steps (a variant of the projection method), which splits the numerical operators and enforces continuity (Kim & Moin, 1985) by solving a pressure Poisson equation, is adopted. The diagonal viscous terms in Equation (2.2) are discretized with a Crank-Nicholson scheme and all other terms are treated explicitly with the second-order Adams-Bashforth scheme. All spatial derivatives are discretized using second-order central differences with the exception of convective term. That term is discretized using QUICK (Leonard, 1979) in which the velocity components on the cell faces are computed from the nodal values using a quadratic interpolation scheme. Further details of the method and discussion regarding to the cell-center velocity (u_i) and face-averaged velocities (U_i) can be found in Zang *et al.* (1994) and Zang (1993). The original three-dimensional pressure Poisson equation is solved by a multi-grid (MG) method. In the current study, a preconditioned Bi-CGSTAB iterative method is used to solve the pressure Poisson equation. The performance of several iterative solvers will be discussed in Section 4.2.

For three-dimensional turbulent flows at high Reynolds number, it is not possible to resolve all of the spatial and temporal scales, so large eddy simulation (LES) will be used. We solve for the large scale motions while fluctuations at scales smaller than the filter width are modeled using a subfilter-scale model. The equations for the resolved field are obtained by filtering Equations (2.1)-(2.3). The filtered equations of LES are given in Appendix A. The subgrid scale (SGS) term τ_{ij} is modeled with

Zang's dynamic mixed model (Zang *et al.*, 1993). The scale-similarity term allows backscatter and the Smagorinsky component provides dissipation.

2.3.2 MIT global circulation model (MITGCM)

The state of the ocean is characterized by the three-dimensional velocity field (u_j, $j = 1-3$), potential temperature (T), salinity (s), pressure (p), and density (ρ). The complete set of governing equations (2.1)-(2.5) is solved using a finite-volume technique and an Arakawa 'c' staggered grid in the MIT global circulation model. The numerical procedure of MITGCM is very similar to that of the EFML code, but all terms (including the viscous terms) are treated explicitly with the second-order Adams-Bashforth scheme. All spatial derivatives are discretized using second-order central differences. Various higher-order monotonic schemes can be chosen for the convective term.

The MITGCM use a height (z)-coordinate system to avoid many problems caused by the σ or bathymetry following coordinate. In order to accurately represent the bathymetry, the model has been designed so that cells which abut the bottom may be shaved to accommodate irregular topography and coastlines (Adcroft *et al.*, 1997). A major difference between the MITGCM and EFML codes is the pressure Poisson solver in the 'pressure correction' step. The pressure field is separated into surface, hydrostatic, and non-hydrostatic components. As in a hydrostatic model, the two-dimensional surface pressure is first solved for. The hydrostatic pressure field is then used to solve for the non-hydrostatic pressure component. A preconditioned conjugate-gradient method is used to solve the Poisson equation in both two and three dimensions. The method exploits the fact that as the horizontal scale of the motion becomes much larger than the vertical scale, the motion becomes more hydrostatic and the three-dimensional Poisson equation becomes increasingly anisotropic and its solution is dominated by the vertical variation. More details and discussion of the model can be found in Marshall *et al.* (1997a; 1997b).

2.3.3 Dietrich Center for Air Sea Technology model (DieCAST)

The hydrostatic DieCAST model, originally derived from the Sandia Ocean Modeling System (SOMS), has been improved significantly in the past ten years (Dietrich *et al.*, 1987; Dietrich & Ko, 1994; Dietrich, 1997). The non-hydrostatic version of DieCAST model solves the equations (2.1)-(2.5) and has been developed recently (Dietrich & Lin, 2002). Many other versions of the model exist. Options include free-surface, shaved-cells, sophisticated advection schemes, and turbulence closures (Lu *et al.*, 2001; Sheng *et al.*, 1998; Sanderson & Brassington, 1998b).

The DieCAST model uses a blend of Arakawa 'a' collocated and Arakawa 'c' staggered grids to avoid the inaccuracy of the pressure adjustment on the 'a' grid and the Coriolis term on the 'c' grid. The model adopts a filtered leap-frog scheme to advance in time. All spatial derivatives are discretized using fourth-order central differences on a control volume. The spatial accuracy of the DieCAST Model has been validated using resolution sensitivity studies for several applications (Roache, 1998; Sanderson, 1998; Sanderson & Brassington, 1998a). The fourth-order accuracy is achieved except for the vertical pressure gradient, and the lateral boundary zone, where second-order accuracy is obtained.

The numerical procedure of solving the non-hydrostatic equations is prescribed in Appendix E. The current iterative procedure is very cost-effective in three dimensions because it only requires a two-dimensional pressure Poisson solver. The Poisson equation is solved by an efficient error vector propagation (EVP) solver (Roache, 1995).

2.4 Summary

The general governing equations for unsteady, three-dimensional, non-hydrostatic, rotating flows are the continuity, Navier-Stokes, and scalar transport equations. In the ocean, an equation of state is also required. Three different numerical models are used in the current study, ranging from LES to existing ocean models. Each has its own characteristics. The immersed boundary module, which will be discussed in

Chapter 3, is added to each of the above models. Some modifications are made to optimize the performance of each code.

Chapter 3

The Generalized Ghost Cell Immersed Boundary Method

3.1 Introduction

Most large scale geophysical flows involve complex three-dimensional geometry, moving boundaries, high Reynolds numbers, and turbulence. Accurate representation of multi-scale, time dependent physical phenomena in numerical models is thus a principal concern. In particular, a grid that is not well suited to the problem domain can lead to unsatisfactory results, instability, or lack of convergence. In coastal ocean modeling, we desire to capture the evolution and interaction of various scales, from dissipative scales to mesoscale eddies. The immersed boundary method (IBM) is an appropriate means of treating the complex boundary efficiently and accurately using Cartesian grids. In this chapter, we extend the idea of Fadlun *et al.* (2000) via a ghost cell approach. In Fadlun *et al.* (2000), the velocity at the first grid point outside the body (u_i in Figure 3.1) is obtained by linearly interpolating the velocity at the second grid point (u_{i+1}) and the velocity at the body surface (V), see Figure 3.1. This approach applies momentum forcing within the flow field. The interpolation direction (the direction to the second grid point) used by Fadlun *et al.* (2000) is either the streamwise (x) or the transverse (y) direction. They also successfully implemented the immersed boundary algorithm in large-eddy simulation (LES) of the

turbulent flow in a motored axisymmetric piston-cylinder assembly (Verzicco *et al.*, 2000). This approach does not reduce the stability of the underlying time-integration scheme, and a very good quantitative agreement with experimental measurements was obtained. For comparable accuracy, the computational requirements for the IBM approach are much lower than simulations on unstructured, boundary-fitted meshes given in published papers (Verzicco *et al.*, 2000; Haworth & Jansen, 2000).

The current approach attempts to achieve higher-order representation of the boundary using a ghost zone inside the body. The ghost cell method is very popular for treating two-phase flows, thus obtaining accurate discretization across the interface (Fedkiw, 2002; Fedkiw *et al.*, 1999; Xu *et al.*, 1997). The particular method proposed by Fedkiw *et al.* (2002; 1999) is known as the Ghost Fluid Method (GFM) and was developed to capture discontinuities such as shocks, detonations, and deflagrations. They also used the technique to solve a variable coefficient Poisson equation on an irregular domain using a Cartesian grid (Gibou *et al.*, 2002; Liu *et al.*, 2000). Forrer and Jeltsch (1998) provided a higher-order wall treatment based on Cartesian grids using the ghost-cell idea. However, the method has been implemented only for two-dimensional compressible inviscid flows with symmetry boundary conditions. In geophysical fluid dynamics (GFD), the ghost cell method promises not only to represent realistic complex geometry but also to provide the flexibility needed to impose various boundary conditions including a log-law boundary condition.

We describe the systematic treatment of various boundary conditions in this chapter. The approach imposes the specified boundary condition by extrapolating the variable to a ghost node inside the body. High order extrapolation is used to preserve the overall accuracy. The present approach is more flexible with respect to the incorporation of boundary conditions. In order to verify the accuracy of the GCIBM, flow over a circular cylinder and a three-dimensional turbulent flow over wavy boundary are simulated using LES in the next chapter. We will also extend the current approach to an existing ocean model and compare the GCIBM results with previous stair-step and partial-cell ones in chapter 5. The main advantage of the current approach is the ease of programming, which only requires that an immersed boundary module be added to an existing code. The current method can readily be implemented in any

existing Cartesian grid code. This chapter is organized as follows. The generalized ghost cell method and the numerical implementation of the GCIBM are provided in Section 3.2. Different boundary conditions and the reconstruction schemes are laid out in Section 3.3-3.5. The implementation of GCIBM on staggered grids is discussed in Section 3.6. Finally, a short summary is given in Section 3.7.

3.2 Ghost cell method for an immersed boundary

The objective of our study is to develop an efficient flow solver using the GCIBM. The treatment of the momentum equation is now defined at each time step so as to enforce the boundary condition, thus the approach is similar to the forcing used by Mohd-Yusof (1997) and Fadlun *et al.* (2000). The force depends on the location and the fluid velocity and thus is a function of time. Its location, x_i is not generally coincident with the grid but the forcing must be extrapolated to these nodes. The forcing f_i is zero inside the fluid and is non-zero in the ghost cell zone which is used to represent the presence of complex boundary. If the Navier-Stokes (N-S) equation (2.2) is discretized as

$$\frac{u_i^{n+1} - u_i^n}{\Delta t} = RHS_i + f_i \tag{3.1}$$

where RHS_i contains convective and viscous terms and the pressure gradient. The boundary conditions can be either Dirichlet or Neumann types.

The current ghost cell method extrapolates the velocity (V_i^{n+1}) and pressure fields to the ghost cells using nearby fluid points and associated boundary information (see Section 3.3). As an example, if the forcing f_i must yield $u_i^{n+1} = V_i^{n+1}$ in accord with the immersed boundary condition, we obtain

$$f_i = -RHS_i + \frac{V^{n+1} - u^n}{\Delta t} \tag{3.2}$$

This forcing causes the desired boundary condition to be satisfied at every time step. There are no free constants and the boundary conditions are enforced to within the numerical precision. Evaluating the force f requires essentially no additional CPU

time since there are no new terms to compute. Nor does it influence the stability of the time advancement scheme.

The force in Equation (3.2) is correct for the case in which the position of the unknowns on the grid coincides with the immersed boundary; this requires the boundary to lay on coordinate lines or surfaces, which is not possible for complex geometries. Many different techniques have been adopted and they can be classified into two groups: (a) schemes that spread the forcing function over the vicinity of the immersed surface and (b) schemes that produce a local reconstruction of the solution based on the boundary values (Iaccarino & Verzicco, 2003). In fact, the two approaches are equivalent. The original Peskin (1977) method, which substitutes a discrete Dirac δ function in Equation (3.2), belongs to the first category. The local reconstruction scheme (b) has been proven to be more flexible (Fadlun *et al.*, 2000; Verzicco *et al.*, 2000) and can be designed so that it has high degree of accuracy. The current ghost cell method belongs to the second category. The numerical procedure we use is the following.

1. Detect the boundary and determine the adjacent ghost cells (preliminary step).

2. Extrapolate to find the ghost cell value required to impose the boundary condition implicitly. The interpolation scheme is discussed in Sections 3.3 and 3.4.

3. Obtain the predicted field (intermediate velocity u_i^*) of the fractional step procedure (Kim & Moin, 1985; Ferziger & Perić, 2001).

4. Solve the pressure Poisson equation to satisfy the continuity equation. Some discussion of the pressure solver is provided in Section 4.2.

5. Update the velocity field (u_i^{n+1}) to the next time step.

The immersed boundary is represented by piecewise linear segments. We identify the cells that are cut by the boundary and determine the intersections of the immersed boundary with the sides of these cells. The computational domain is divided into two regions: the *physical* domain and the *ghost cell* domain. They are illustrated in Figure 3.2(a). The physical domain is the flow region (x). The ghost cells lie just

inside the body adjacent to computational nodes in the flow domain. The values of flow variables at the ghost cells are computed using a local reconstruction scheme involving the ghost node and neighboring flow nodes.

The ghost cells can be detected automatically if a structured grid is used. All of the possibilities for the boundary line intersecting an arbitrary cell are shown in Figure 3.3. Each node is the center of a rectangular cell and x is the cell center. A cell belongs to the physical flow domain if the immersed boundary does not cover the cell center as in Figures. 3.3(a) and (c). The shaded areas are inside the boundary. If the immersed boundary covers the cell center, the cell is the ghost cell (Figures 3.3(b) and (d)). Local refinement is needed if the curvature is large.

3.3 Dirichlet boundary conditions

We express the local flow variables (ϕ) in terms of a polynomial and use it to evaluate the ghost point values. The accuracy depends on the degree of the polynomial. Although polynomials of higher degree are expected to be more accurate, they often lead to boundedness problems and numerical instability. The value of ϕ at the internal node closest to the surface is obtained by extrapolation from the nearby values. We use linear and quadratic approaches which preserve the second-order accuracy of the overall numerical scheme. The scheme is equally applicable to both steady and moving boundaries. In the case of moving bodies, the points at which the boundary condition is enforced must be recomputed at every time step but this does not affect the reconstruction scheme.

3.3.1 Linear reconstruction

The simplest approach in 2-D is to construct a triangle with the ghost node and the two nearest fluid nodes as the vertices. This choice minimizes the probability of numerical instability. In Figure 3.2, G is the ghost node, X_1 and X_2 are the two nearest fluid nodes and O is the node at which the boundary condition is to be satisfied. O can be chosen as the midpoint of the boundary segment within the cell

or the point on the boundary at which $\overrightarrow{GO}$ is normal to the boundary. We choose the former for simplicity. A linear interpolation in 2D is:

$$\phi = a_0 + a_1 x + a_2 y \tag{3.3}$$

The ghost cell value is then a weighted combination of the values at the neighboring nodes (X_1, X_2 and O) obtaining by evaluation of the Equation (3.3) at the ghost point. The coefficients can be expressed in terms of the nodal values:

$$a = B^{-1}\phi \tag{3.4}$$

where, for linear interpolation, B is a 3×3 matrix whose elements can be computed from the coordinates of the three points. When the velocity at the boundary is specified:

$$B = \begin{bmatrix} 1 & x_0 & y_0 \\ 1 & x_1 & y_1 \\ 1 & x_2 & y_2 \end{bmatrix} \tag{3.5}$$

It is convenient to evaluate the matrices B at each point initially and store them for use during the solution procedure. The major drawback with this extrapolation is that large negative weighting coefficients are encountered when the boundary point is close to one of the fluid nodes used in the extrapolation. Although algebraically correct, this can lead to numerical instability, i.e. the absolute value at the ghost point may be greater than the nearby fluid point values and the solution may not converge.

Two approaches are used to remedy the difficulty. The first is to use the image of the ghost node inside the flow domain (Majumdar *et al.*, 2001) to ensure positive weighting coefficients. The point I is the image of the ghost node G through the boundary as shown in Figure 3.4(a). The flow variable is evaluated at the image point using the interpolation scheme. The value at the ghost node is then $\phi_G = 2\phi_O - \phi_I$.

The other approach is to alter the piecewise linear boundary. When the boundary is close to a fluid node (normal distance of fluid point G' to the boundary $\overline{OG'} <$

$0.1\Delta x$, Δx is the cell size) and far from the ghost point as in Figure 3.4(b), we simply move the boundary point to the fluid node closest to the boundary (Gibou *et al.*, 2002). Since the boundary is approximated as piecewise linear, the accuracy is hardly affected when the boundary segment is divided into two pieces, see Figure 3.4(b). Gibou *et al.* (2002) demonstrated that this approach could be used to obtain the second order accuracy in solving the Poisson equation on the irregular domain. The original piecewise linear boundary is shown as the dash-dot $(-\cdot)$ line connecting boundary intercepts. This ensures that large negative weighting coefficients will not occur. The following numerical example adopts the first approach since additional image point is involved.

3.3.2 Quadratic reconstruction

Most second-order accurate finite volume flow solvers assume quadratic variation of flow variables near the wall. Use of higher order interpolation retains the formal second order accuracy of the scheme. In two dimensions, if the flow variables are assumed to vary in a quadratic manner in both the x and y directions, the value of ϕ is expressed as

$$\phi = a_0 + a_1 x + a_2 y + a_3 x^2 + a_4 xy + a_5 y^2 \tag{3.6}$$

The six constants of the assumed polynomial are evaluated from five neighboring fluid nodes and the wall point (Figure 3.2(b)). The matrix B in Equation (3.4) is replaced by a 6×6 matrix:

$$B = \begin{bmatrix} 1 & x_0 & y_0 & x_0^2 & x_0 y_0 & y_0^2 \\ 1 & x_1 & y_1 & x_1^2 & x_1 y_1 & y_1^2 \\ \cdots & \cdots & \cdots & \cdots & \cdots & \cdots \\ 1 & x_5 & y_5 & x_5^2 & x_5 y_5 & y_5^2 \end{bmatrix} \tag{3.7}$$

The ghost node values are either extrapolated or evaluated using an image point. The reconstruction procedure is similar to that for the linear polynomial. The influence of the schemes on the overall accuracy is compared in the numerical examples. Majumdar *et al.* (2001) tested the ghost-cell immersed boundary using second-order

bilinear and quadratic interpolation schemes for a RANS solver and they found that the solutions do not have any significant difference.

For three dimensional domains, we need to modify the interpolation scheme in Equations (3.3) and (3.6). More neighbor nodes are involved, e.g. for linear reconstruction, the variable in the cell center is interpolated using four points (three nearest neighbor nodes and one boundary point). A three dimensional illustration is shown in Figure 3.5. The black dots (•) represent the three closest neighboring cells with respect to the boundary point O, see Figure 3.5. These points can be located initially and stored. For quadratic reconstruction, ten points (nine neighbors) are needed. The remainder of the solution procedure remains the same as that described above. A 4×4 linear system will be solved for linear construction and a 10×10 system will be solved for quadratic one.

Furthermore, more elaborate, high order schemes may be used in three dimensions. It is well known that high order polynomial interpolations may introduce wiggles and spurious extrema. The inverse distance weighting proposed by Franke (1982) has the property of preserving local maxima and producing smooth reconstruction. This scheme is suitable for reconstructing variables that are smoothly varying without exhibiting large maxima. The interpolation at the ghost cell is:

$$\phi_G = \sum_{m=1}^{n} w_m \phi_m / q \tag{3.8}$$

$$w_m = (\frac{R - h_m}{R h_m})^p \tag{3.9}$$

$$q = \sum_{l=1}^{n} (\frac{R - h_l}{R h_l})^p \tag{3.10}$$

where ϕ_m (ϕ_G) represents the solution at a certain location (ghost cell), w_m represents the weight, and h_m is the distance between the ghost cell (ϕ_G) and the location of ϕ_m. p is an arbitrary positive real number called the power parameter (typically $p = 2$). R is the distance from the ghost point to the most distant point used in the construction, and n is the total number of the construction points.

It is important to note that for the forcing of Saiki and Biringen (1996) and

Goldstein *et al.* (1993), the velocity at the immersed boundaries was imposed by a fictitious force. In the current approach, the boundary condition is imposed directly. This implies that, in contrast to the feedback forcing method, the stability limit of the current integration scheme is the same as that without the immersed boundaries, thus making simulation of complex three-dimensional flows practical. Higher order extrapolation/interpolation schemes to evaluate the variables at the ghost cells can preserve at least second-order spatial accuracy (Udaykumar *et al.*, 2001; Ye *et al.*, 1999).

3.4 Neumann boundary conditons

The method computes the velocity up to the boundary using the neighboring points. With the polynomial reconstruction scheme, we do not solve any equations on the ghost cells. The treatment of Dirichlet boundary conditions has been described in the non-staggered Cartesian grid approach. A similar scheme can be used for Neumann boundary conditions. The only difference is in the construction of matrix B in Equation (3.4). This makes the current approach applicable to a variety of boundary conditions.

For example, the pressure boundary condition requires the wall normal derivative to be zero at the boundary:

$$\frac{\partial P}{\partial n}|_{\Omega} = 0 \tag{3.11}$$

The normal derivative on the boundary can be decomposed as

$$\frac{\partial P}{\partial n} = \frac{\partial P}{\partial x}\hat{n}_x + \frac{\partial P}{\partial y}\hat{n}_y \tag{3.12}$$

where $\hat{n}_x$ and $\hat{n}_y$ are the components of the unit vector normal to the boundary. Since $\hat{n}_x$ and $\hat{n}_y$ are known, the computation of the normal gradient at any point is straightforward. Linear reconstruction requires two fluid nodes and one boundary node. The Neumann condition at the boundary node is stored in the first element of ϕ in Equation (3.4) and the known flow variables on the two fluid nodes are stored in the second and third elements of ϕ. Quadratic reconstruction requires five fluid

nodes and one boundary node. See Figure 3.2(b) for the notation. Index O locates at the boundary, $tan(\theta_0)$ is the slope along the normal direction at surface O.

(a) Linear reconstruction

$$B = \begin{bmatrix} 0 & -sin(\theta_0) & cos(\theta_0) \\ 1 & x_1 & y_1 \\ 1 & x_2 & y_2 \end{bmatrix}.$$

θ_0 is the local slope at the boundary node.

(b) Quadratic reconstruction

$$B = \begin{bmatrix} 0 & -sin(\theta_0) & cos(\theta_0) & -2sin(\theta_0)x_0 & cos(\theta_0)x_0 - sin(\theta_0)y_0 & 2cos(\theta_0)y_0 \\ 1 & x_1 & y_1 & x_1^2 & x_1y_1 & y_1^2 \\ \cdots & \cdots & \cdots & \cdots & \cdots & \cdots \\ 1 & x_5 & y_5 & x_5^2 & x_5y_5 & y_5^2 \end{bmatrix}.$$

Finally, the coefficients can be obtained systematically for both reconstructions:

$$\begin{bmatrix} a_0 \\ a_1 \\ \cdots \\ a_m \end{bmatrix} = B^{-1} \begin{bmatrix} \frac{\partial P_0}{\partial n} \\ P_1 \\ \cdots \\ P_m \end{bmatrix} \tag{3.13}$$

where index m is 2 for linear reconstruction (three unknowns) and is 5 for quadratic reconstruction (six unknowns). $\frac{\partial P_0}{\partial n}$ is the Neumann boundary condition for pressure and P_m is the neighboring pressure field. The flexibility of current approach is demonstrated by the examples presented in Chapter 4.

3.5 Mixed Dirichlet and Neumann (Robin) condition

Sometimes, one has a mixed or Robin boundary condition in a physical/engineering problem. A linear combination of the variable (ϕ) and its wall normal derivative is prescribed.

$$\alpha\phi + \beta\frac{\partial\phi}{\partial n} = f \tag{3.14}$$

where f is the known function and α and β are the coefficients. Since our ghost cell method solves a linear system (Equation (3.4)) at each boundary grid point, the ghost cell variables for the mixed Robin boundary can be expressed by solving the following system,

$$a_R = B_R^{-1}\phi \tag{3.15}$$

where $B_R = \alpha B_D + \beta B_N$ is a linear combination of the matrices B_D and B_N, the matrices for Dirichlet and Neumann conditions. α and β are the coefficients from the Robin boundary condition.

3.6 Non-staggered and staggered grid arrangements

The above immersed boundary treatment focused on the non-staggered (collocated) grid arrangement. Whether a cell is a ghost cell or not is determined by the relation between the cell center and the physical boundary. The use of staggered grids for the solution of the N-S equations has a number of advantages. Fadlun *et al.* (2000) applied the IBM approach to a three-dimensional finite-difference method on a staggered grid. However, they did not use ghost cells and their interpolation scheme is applied only in the x or y directions.

The current ghost-cell approach can be easily extended to staggered grid arrangement. The three velocity components and the pressure are computed on different grids. For each velocity component and pressure we find different weighted coefficients at the boundary, i.e. we need to solve a different linear system for each

variable. A numerical example of a staggered grid treatment is given in Chapter 5. A two-dimensional schematic of the velocity allocation is shown in Figure 3.6. The U and V components are located on different faces for each cell. The staggered grid arrangement increases the required storage. However, the increase is not significant since the boundary has a lower dimension than the domain.

3.7 Summary

The aim of this study is to develop an immersed boundary method using second-order ghost cell reconstruction and demonstrate its applicability. The computation is done on a structured orthogonal mesh. The forcing is imposed by introducing ghost-cells outside the boundary and does not reduce the stability limit of the time-advance scheme. The main advantages of the current approach are the ease of implementation in existing codes and ease of grid generation. This is demonstrated by application to three existing codes in the following chapters. The method also allows the use of various types of boundary conditions and grid arrangements.

It is worth pointing out how our methodology differs from the immersed boundary method of Ye *et al.* (1999) and Fadlun *et al.* (2000). First, the interpolation scheme differs from theirs. Second, the reshaped cell method in Ye *et al.* (1999) complicates the numerical algorithm and extension to other boundary conditions and moving boundaries is difficult. Third, the current approach uses ghost cells rather than reshaped cells to enforce the boundary condition.

This method does not require any internal treatment of the body except the ghost cells since a fractional step method is used and the forcing is only on the boundary. Internal treatment was required by Goldstein *et al.* (1993) and Mohd-Yusof (1997) in their spectral simulations to alleviate the problem of spurious oscillations near the boundary.

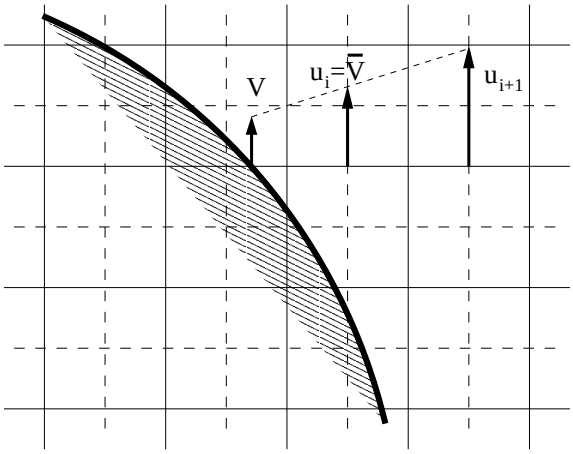

Figure 3.1: Sketch of the velocity interpolation procedure in Fadlun *et al.* (2000) on a staggered grid.

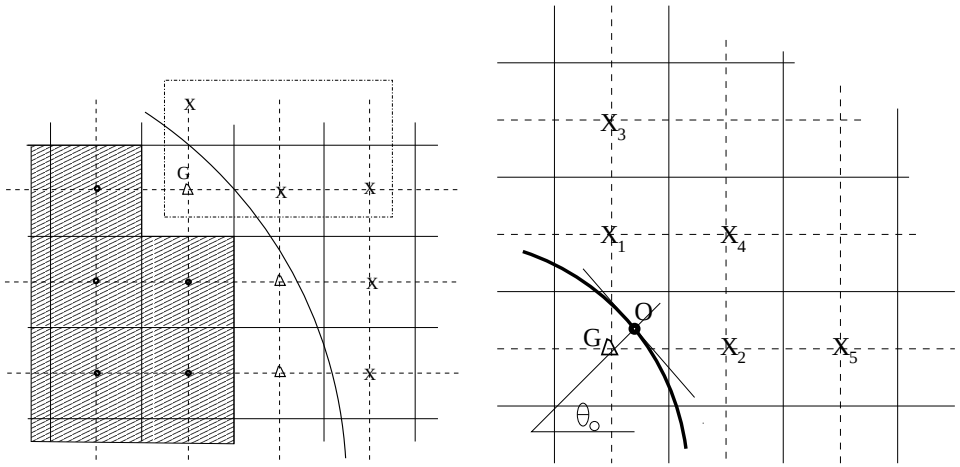

(a) (b)

Figure 3.2: (a) Schematic of computational domain with an immersed boundary. x: point in the physical domain, Δ: the ghost cell domain. (b) Schematic of the points used to evaluate the variable located at a ghost cell G point.

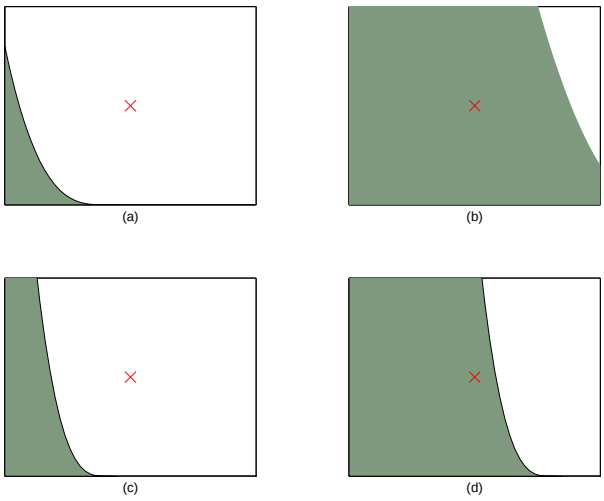

Figure 3.3: Possibilities for a boundary line intersecting an arbitrary Cartesian cell. The shaded areas are inside the boundary. If the shaded region covers the cell center, this cell is identified as a ghost cell.

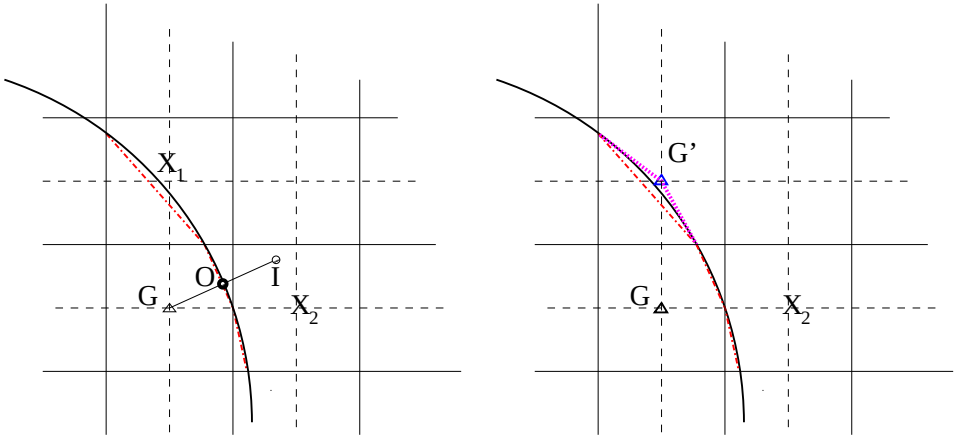

Figure 3.4: Special treatment to minimize numerical instability. (a) Schematic of a ghost cell using the image method (**I** is the image point). (b) Schematic of adding an additional ghost cell G' if the boundary is close to the fluid points. -· is the linear piecewise approximation to the boundary. $\cdots$ is the boundary approximated by two piecewise segments.

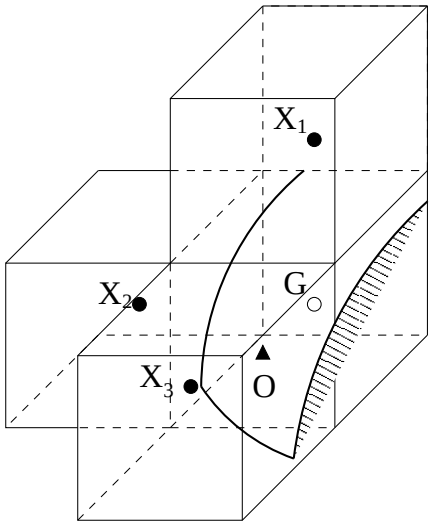

Figure 3.5: Schematic of the points used to evaluate the variable located at a ghost cell point G in three dimension. Linear construction relies on three nearest neighbor nodes and a boundary surface point (point O).

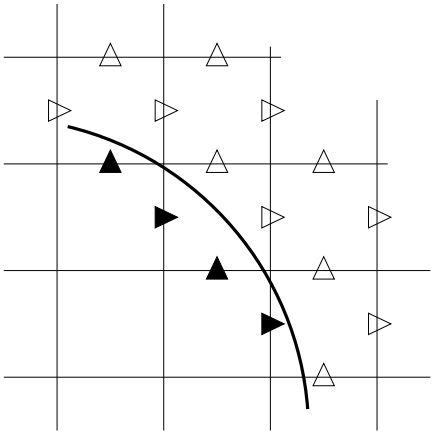

Figure 3.6: Schematic of computational domain with an immersed boundary for two-dimensional staggered grid (U, V components are located on the cell face). ▷: the location of U component in fluid domain; ▶: the ghost cell location of U component; Δ: the location of V component in fluid domain; ▲: the ghost cell location of V component.

Chapter 4

Examples of Laboratory Scale Flows

4.1 Introduction

In order to validate the proposed GCIBM, we simulate a uniform flow over a cylinder and evaluate the accuracy. The method is then applied to three-dimensional turbulent flow over a wavy boundary. The results are compared with boundary-fitted grid simulations. In this chapter, the GCIBM is implemented in the EFML code developed in our laboratory (Zang *et al.*, 1994). The numerical method has been introduced in Section 2.3. Section 4.2 discusses the performance of the pressure Poisson solver. Section 4.3 provides the uniform flow over a cylinder example. Finally, an example of three dimensional turbulent flow over a wavy boundary is given in Section 4.4.

4.2 Convergence of the Poisson solver

The flow solver uses a pressure correction method to satisfy the continuity equation. For high Reynolds numbers and highly stretched grids, it is difficult to converge the Poisson equation to machine accuracy. When we simulate complex geometry using immersed boundary method, the slow convergence is further exacerbated because the immersed boundaries modify the linear system. Therefore, use of schemes like the

multigrid (MG) or conjugate gradient (CG) method is very desirable. However, the MG procedure converges slowly on anisotropic grids. The presence of the immersed boundaries also complicates implementation of the multigrid procedure since prolongation and restriction are difficult to perform near the boundary. Krylov subspace methods (Golub & van Loan, 1996) are an attractive alternative since they are designed for general sparse matrices and do not assume anything about the structure of the matrix. The presence of the immersed boundary poses no additional complication for these methods.

The convergence rate of these procedures depends critically on the choice of the preconditioner. Jacobi and Gauss-Seidel preconditioners are easy to implement and are used often but the improvement is not very significant (Ferziger & Perić, 2001; Saad, 1996). Incomplete factorization preconditioned conjugate gradient methods are robust general-purpose techniques for solving linear systems. The biconjugate gradient stabilized (Bi-CGSTAB) iteration method is chosen for the current solver as it has been shown to be efficient (Saad, 1996; Golub & van Loan, 1996). It is applicable to non-symmetric matrices and provides relatively uniform convergence. We have adopted Stone's Strongly Implicit Procedure (SIP) preconditioner to accelerate the convergence, as it is more efficient than incomplete lower-upper decomposition (ILU) (Stone, 1968). The detailed numerical procedure of Bi-CGSTAB iterative method with SIP preconditioning is provided in Appendix B. Interested readers may refer to Ferziger and Perić (2001) for further discussion of the SIP method. The convergence of point Gauss-Seidel, Bi-CGSTAB, Bi-CGSTAB with an ILU preconditioner and Bi-CGSTAB with the SIP preconditioner is shown in Figure 4.1. Incomplete factorization preconditioning (both ILU and SIP) for Bi-CGSTAB accelerates the convergence significantly. The SIP preconditioner provides a dramatic reduction in iteration number.

4.3 Uniform flow past a cylinder

Here we simulate steady and unsteady flow past a circular cylinder immersed in an unbounded uniform flow. This flow is attractive because the flow behavior depends on

Reynolds number and is not easy to simulate accurately using Cartesian grids. The Reynolds number is defined as $Re_D = U_\infty D/v$, where D is the cylinder diameter. At very low Reynolds number, it is a creeping flow. At somewhat higher Reynolds numbers (up to $Re = 50$), two symmetrical standing vortices are formed but remain attached to the cylinder. At still higher Re, these vortices are stretched and wavy behavior of the tail is observed. At even higher Re, alternating vortex shedding called the Kármán vortex street is found. This flow has been studied quite extensively and a number of numerical and experimental data sets exist for it.

Simulations have been performed at $Re_D = 40$ and 100 and results are compared with established experimental and numerical results. The simulations have been performed in a domain ($l \times w = 32D \times 16D$) large enough to minimize the effect of the outer boundary on the development of the wake. Resolution from 24 to 96 ghost cells around the cylinder is used. Figure 4.2 shows the streamlines for $Re = 40$. The flow is symmetric about the streamwise axis. The drag coefficient ($C_D = F_d/(1/2)\rho U_\infty^2 D$) and the length of the recirculation zone L_W are compared with established results in Table 4.1. The comparison is quite good.

Figures 4.3 and 4.4 show the pressure coefficient (C_p) and skin-friction (C_f) along the cylinder surface at $Re = 40$ using linear extrapolation (a) and quadratic extrapolation (b). Numerical results obtained with a boundary-fitted grid are also shown (Majumdar *et al.*, 2001). An accurate interpolation scheme is required. In the present study, both the pressure and velocity at the surface are linearly interpolated from the nearest cells. The results are very close to those obtained from the boundary-fitted grid solution. The pressure coefficient (C_p) and skin-friction (C_f) converge to the boundary-fitted grid results as the resolution is increased. The pressure at the surface is obtained from the nearest cell center pressure outside the cylinder and the ghost cell by assuming that the wall-normal derivative of the pressure is zero at the surface. On a boundary-fitted grid, the normal distance to the wall can be controlled and varied continuously along the body surface. With very coarse resolution (24 ghost cells around the cylinder), quadratic reconstruction yields more oscillation than linear reconstruction.

A grid resolution study was performed to analyze the accuracy of the ghost cell

approach. A domain size of $6D \times 5D$ with the cylinder center located at the domain center is chosen for this purpose. The L_∞ norm of the error in the streamwise and spanwise velocity components is shown in Figure 4.5. The dash-dot $(-\cdot)$ line indicates slope 2 in log-log coordinates. The results suggest that the overall accuracy is second-order for both the linear and quadratic extrapolation, i.e., the order is not affected by the boundary treatment. However, the accuracy is slightly better when the higher-order polynomial boundary treatment is used. These results are consistent with the well known result that the use of an approximation of one order lower accuracy at the boundary does not reduce the overall accuracy of a scheme (LeVeque & Oliger, 1983). The difference in overall accuracy is simply due to the difference in accuracy of the methods at the points near the boundary and is thus small. Figure 4.6 shows the L_∞ norm of the error in the streamwise and spanwise velocity components at the cylinder boundary. The upper dash-dot $(-\cdot)$ lines have slopes 2 and 1. The convergence of the second order treatment is faster than the linear treatment at the boundary points. The overall performance of the solver is not affected greatly by the boundary treatment. The results are consistent with expectation. However, the higher order boundary approximation will be necessary if the IBM is implemented with a higher order or spectral code.

At higher Reynolds number, the wake becomes unstable to perturbations. Instantaneous vorticity contours at two time steps are shown for $Re = 100$ in Figure 4.7. We see the Kármán vortex street, indicating that the vorticity field is well captured by the present method. Figure 4.8 shows the time evolution of the lift coefficient measured for $Re = 100$. The time-averaged drag coefficient C_D and rms-averaged lift coefficient C_l are provided in Table 4.1. Both agree well with the computational results obtained from a body-fitted mesh (Dias & Majumdar, 2001) and previous studies. The Strouhal number ($St = f_s D/U_\infty$) is a key quantity that characterizes the vortex shedding process where f_s is the vortex shedding frequency. St is tabulated in Table 4.1 and matches well with the experiments of Williamson as reported in Lai and Peskin (2000). Figure 4.9 shows the variation of streamwise and spanwise velocity components at a particular point $1.4D$ right behind the cylinder center. It is

interesting to note that the oscillation frequency of the streamwise velocity component is twice that of the spanwise component which is the shedding frequency. This is because vortices shed from the two sides of cylinder alternately.

4.4 LES of turbulent flow over a wavy boundary

Next, large eddy simulation is employed to simulate flow over a wavy boundary. The GCIBM described in Section 3.2 is compared with the results of Zedler and Street (2001) who used a non-orthogonal, boundary-fitted grid to compute turbulent flow over a wavy boundary and study sediment transport in the flow. Their results have been compared with laboratory experiments for the same geometry (Calhoun & Street, 2001). The purpose of this study is to illustrate the applicability of the GCIBM to LES and to assess the method by comparing with boundary-fitted grid results. The computational requirements (both CPU and memory) are significantly lower for a Cartesian grid. The calculations are three dimensional and both steady and unsteady flows are treated.

The bottom boundary configurations mimic straight crested transverse ripples $A\sin(2\pi x/\lambda)$, where $A = 0.254\ cm$ is the ripple amplitude; and $\lambda = 5.08\ cm$ is the ripple wavelength. The domains are identical with dimensions of $20.3\ cm \times 4.8\ cm \times 2.1\ cm$ ($L \times W \times H$) as shown in Figure 4.10. The steady flow is driven by a uniform pressure gradient that yields a Reynolds number of about 2400, based on the channel height of 2.1 cm and the mean streamwise velocity. The unsteady flow is driven by an oscillatory pressure gradient that yields the same Reynolds number based on the maximum velocity. The boundary conditions are periodic on all lateral boundaries, free-slip (zero stress) at the top and no-slip at the wavy bottom.

4.4.1 Steady flow simulations

For purposes of comparing with boundary-fitted grid results, vertical profiles at five locations in one wavelength of the topography are shown. The mean streamwise

velocities and Reynolds shear stress are compared in Figures. 4.11(a) and (b) respectively. The differences between the GCIBM and boundary-fitted profiles for the mean streamwise velocities are very small. In particular, the profiles in the outer regions (beyond $(y - y_0) = 0.3h$, y_0 being the height of bottom topography) identified by Calhoun and Street (2001) are almost identical. A detailed comparison of the mean streamwise velocities in the vicinity of the crest is shown in Figure 4.12. The differences between the average velocity profiles over the crest are small. The Reynolds stress ($-\overline{u'v'}$) at each location in the simulation using GCIBM compares well with the boundary-fitted grid profile (Figure 4.11(b)).

The contours of mean vertical velocity from the GCIBM and boundary-fitted grid results are compared in Figure 4.13. The agreement is very good. Positive velocity is denoted by the solid contours and negative velocity by the dashed ones. The vertical velocity is more sensitive to the method than the streamwise velocity since its magnitude is much smaller. The recirculation is apparent in the mean vertical velocity contour as positive vertical velocities on the downward sloping portion of the surface. The vertical velocity contours obtained with the GCIBM are very similar to the contours produced by the boundary-fitted grid.

In order to illustrate the structure of the instantaneous vortex cores we have plotted contours of the second invariant of the velocity gradient tensor (Jeong & Hussain, 1995) in Figure 4.14. This approach is a variant of the pressure minimum method. The vortex cores resemble those in channel flow, but they are longer, taller and have a greater angle of inclination (Calhoun & Street, 2001). These vortices result from the Görtler instability associated with boundary curvature. A detailed description of these vortices can be found in previous studies (Calhoun & Street, 2001; Zedler & Street, 2001). The current study identifies the same structures, indicating that the GCIBM adequately resolves turbulent boundary layer.

Contours of the components of the turbulence intensity (TI) are shown in Figure 4.15. The maximum streamwise $\overline{u'^2}$ is found above the center of the trough and is associated with the shear layer that detaches from the surface at the separation point. Contours of the vertical TI show that the maximum is located slightly downstream of the location of the maximum of the streamwise TI. The maximum value is about one

third of the streamwise value. Henn and Sykes (1999) noted an increase in spanwise velocity fluctuations on the upstream slopes of their wavy boundary and suggested that the precise mechanism responsible is not yet known. Calhoun and Street (2001) concluded that Görtler instability appears to be important in the formation of the vortices and associated with the increase in spanwise velocity fluctuation. As shown in Figure 4.15(b), the spanwise TI shows a marked increase on the upslope close to the wavy surface. The magnitude and location suggest a localized production mechanism associated with the waviness of the boundary. These features confirm the link between the streamwise vortices and the increase of spanwise TI found by Calhoun and Street (2001).

4.4.2 Unsteady flow simulations

We also simulated the unsteady flow over a wavy boundary produced by an oscillatory pressure gradient. A small recirculation zone forms just before the pressure gradient has attained its maximum negative value. As the flow slows down due to the adverse pressure gradient, spanwise vortices form and are lifted off the bottom to roughly the height of the wave crests. Quantitative comparisons between the GCIBM approach and boundary-fitted grid results of the spanwise-averaged streamwise velocity at four time steps are given in Figure 4.16. These velocity profiles are phase averaged over ten cycles to obtain stable statistics. Sample taking starts after the flow reaches an oscillatory steady state. The mean profiles show good agreement with boundary-fitted simulations.

Figure 4.17 provides the instantaneous, spanwise-averaged velocity vector field at $t = 0.25T$. The time $t = 0$ corresponds to the maximum pressure gradient. Recirculation zones appear behind the ripple crests in the instantaneous velocity vector plot but are confined to the bottom few grid points. These are similar to vortices obtained with boundary-fitted grids (Zedler & Street, 2001). The flow behavior in both the steady and unsteady cases in the current study is nearly the same as that in studies that used boundary-fitted grids (Calhoun & Street, 2001; Zedler & Street, 2001), indicating that the present method accurately captures the three-dimensional

turbulent flow field.

Fig 4.18 presents the vortex formation/transport process by showing the vortex cores at different time steps. The formation cycle occurs twice per period, once on either side of a wave trough. It starts as the flow accelerates ($t/T = 0.25$) and forms the recirculation zone. The vortex structures are generated by boundary layer separation and the growth of three-dimensional disturbances (Scandura *et al.*, 2000). These structures are advected downstream as the flow slows down. The boundary layer on the lee side thickens and the recirculation zone is lifted from the bottom. Some of the vortices are centered over the trough. This structure breaks up into a more complex, three-dimensional structure as the flow slows further. After the flow switches direction ($t/T = 0.5$), these complex structures are lifted off the bottom and advected over the crest (Figure 4.18(c)). They are stretched in the streamwise direction and lose some of their strength as the flow accelerates in the other direction ($t/T = 0.75$). Then the process repeats in the other direction. The current results are very similar to those simulated in Scandura *et al.* (2000) and the nonlinear effects appear important for the growth of three dimensional instability.

4.5 Summary

We use the existing EFML code to demonstrate the ghost-cell immersed boundary method. A laminar flow simulation over a cylinder was carried out to verify the accuracy. Simulations were performed at $Re_D = 40$ and 100. Two symmetrical standing vortices were formed at low Reynolds number and a Kármán vortex street was observed at high Reynolds number. The simulation results were in good agreement with established experimental and numerical data. A grid resolution study was conducted to verify the solution convergence. Both linear and quadratic reconstructions of the GCIBM did not affect the overall second-order accuracy of the underlying solver even though the quadratic one had slightly better convergence. The numerical example showed that the GCIBM could represent complex geometry accurately.

Further, large-eddy simulation was used to investigate three-dimensional turbulent flow over a wavy boundary, which was represented by the GCIBM approach. The

accuracy of the current method was validated by comparing with previous boundary-fitted grid results (Zedler & Street, 2001). Both steady and unsteady flows were simulated. A steady flow simulation provided not only the mean and turbulence statistics but also visualization of the Görtler vortices. The unsteady oscillatory flow displayed the three-dimensional vortex formation/transport cycle, which was shown to be important for sediment transport. The simulation results of this study compared well with the boundary-fitted grid results. The numerical test illustrates that the GCIBM can be successfully extended to three-dimensional turbulent flow in complex geometry.

Table 4.1: Comparison of recirculation length, drag coefficient and Strouhal number with previous studies

	Re=40		Re=100		
	L_W/D	C_D	$St = f_s D/U_\infty$	C_D(avg)	C_L(rms)
Current Study (72 ghost cells around the cylinder)	2.21	1.53	0.164	1.42	0.29
Ye *et al.* (1999)	2.27	1.52	-	-	-
Lai and Peskin (2000)	-	-	0.165	1.4473	0.3299
Kim *et al.* (2001)	-	1.51	0.165	1.33	-
Dias and Majumdar (2001)	2.69	1.54	0.171	1.395	0.283
Williamson (Exp. as reported in Lai and Peskin (2000))	-	-	0.166	-	-

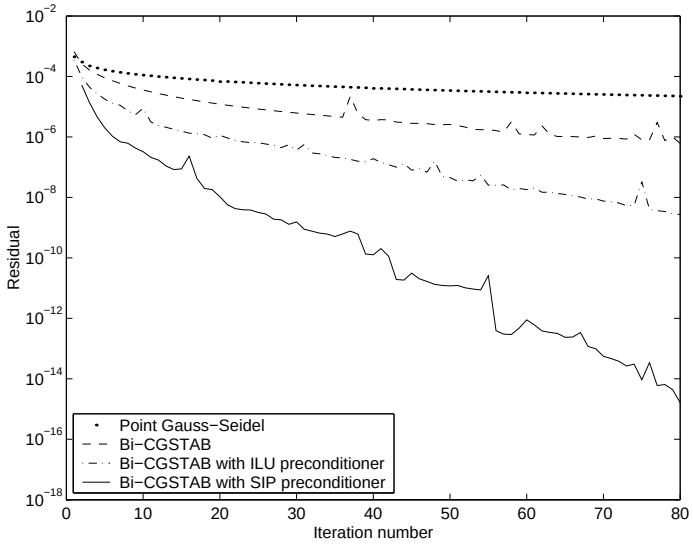

Figure 4.1: The convergence rate of point Gauss-Seidel, Bi-CGSTAB, Bi-CGSTAB with ILU preconditioner and Bi-CGSTAB with SIP preconditioner applied to the pressure equation for the simulation of 3-D turbulent flow over wavy boundary.

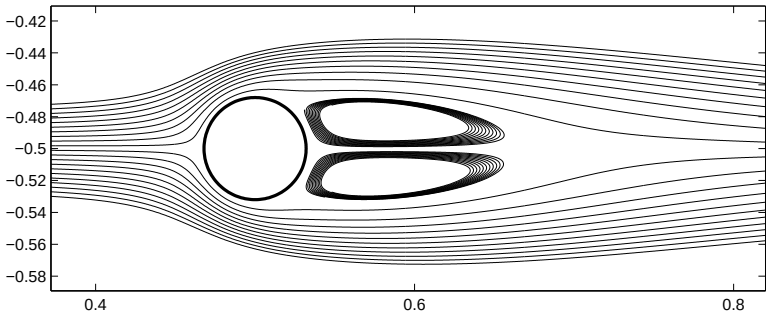

Figure 4.2: Streamline of the flow around a cylinder at $Re = 40$.

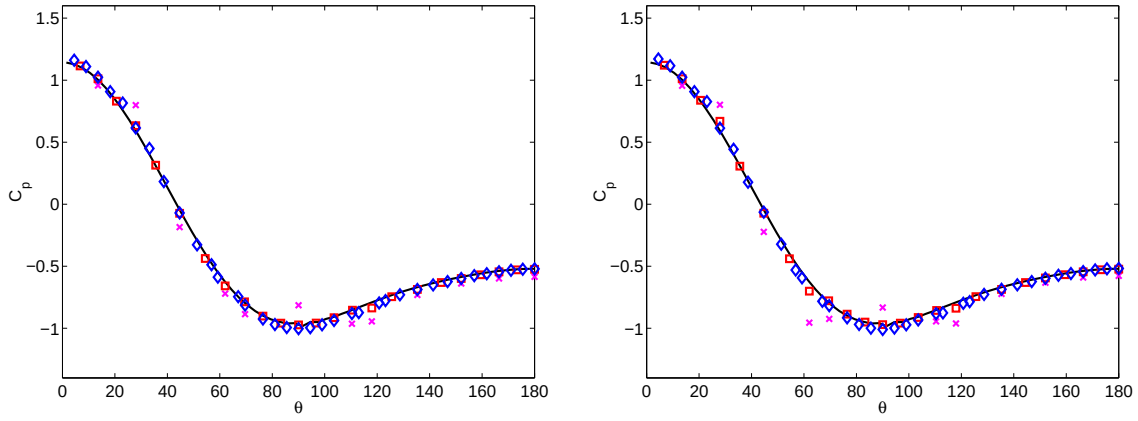

(a) (b)

Figure 4.3: The pressure coefficient (C_p) for flow around a cylinder ($Re = 40$). (a) Linear polynomial reconstruction (1^{st} order). (b) Quadratic polynomial reconstruction (2^{nd} order). −: boundary-fitted grid; x: 24 ghost cells; □: 48 ghost cells; ◇: 72 ghost cells.

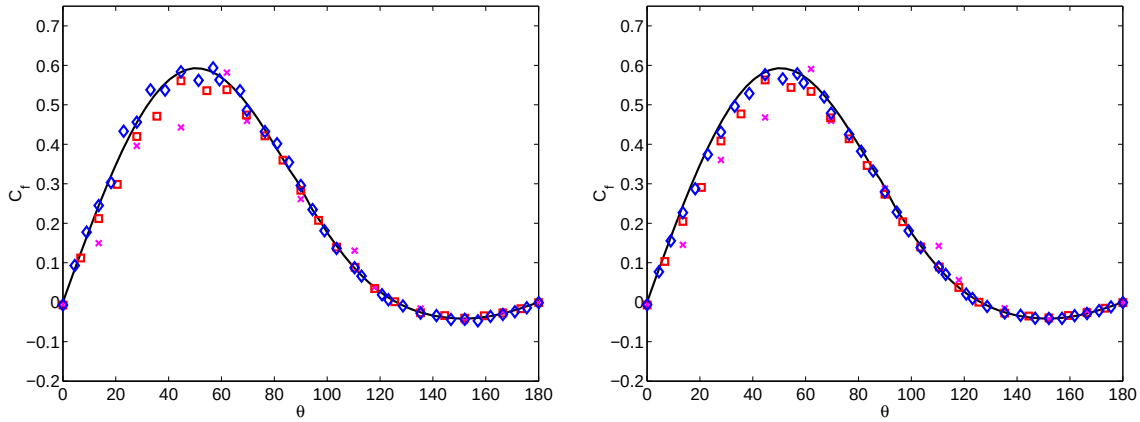

(a) (b)

Figure 4.4: The skin-friction (C_f) for flow around a cylinder ($Re = 40$). (a) Linear polynomial reconstruction (1^{st} order). (b) Quadratic polynomial reconstruction (2^{nd} order). −: boundary-fitted grid; x: 24 ghost cells; □: 48 ghost cells; ◇: 72 ghost cells.

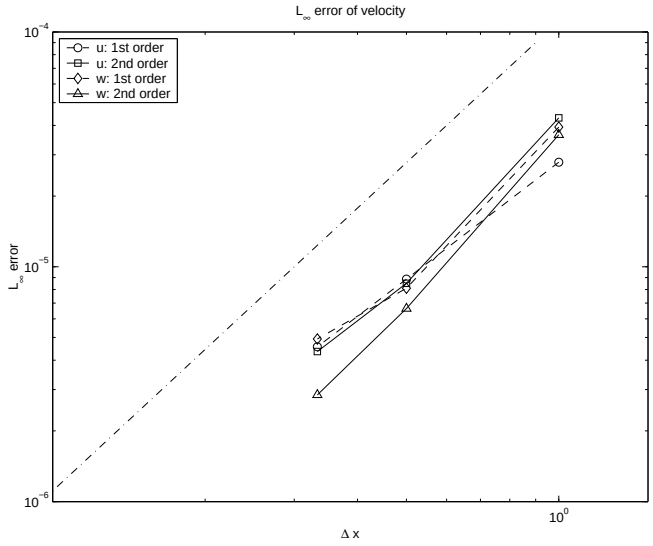

Figure 4.5: L_∞ norm error of the streamwise (u) and spanwise (v) velocity components vs. the computational grid size. $\circ$, $\diamond$: linear polynomial reconstruction, $\square$, Δ: quadratic polynomial reconstruction.

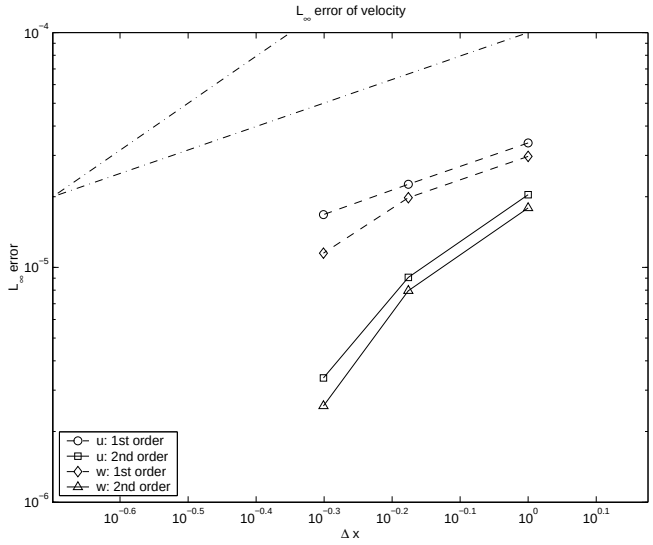

Figure 4.6: L_∞ norm error of the streamwise (u) and spanwise (v) velocity components along the cylinder boundary vs. the computational grid size. $\circ$, $\diamond$: linear polynomial reconstruction, $\square$, Δ: quadratic polynomial reconstruction. The upper $-\cdot$ lines have slope 2 and 1.

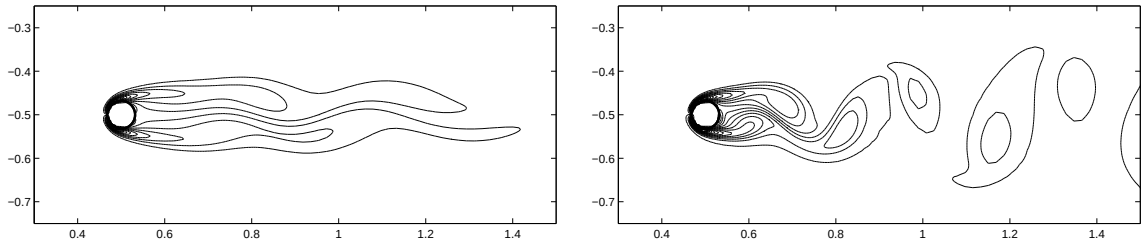

(a) (b)

Figure 4.7: The instantaneous vorticity contours plot in the near wake of the circular cylinder for $Re = 100$ at (a) $t = 30.52T$ ($T = U_\infty/D$) (b) $t = 61.04T$.

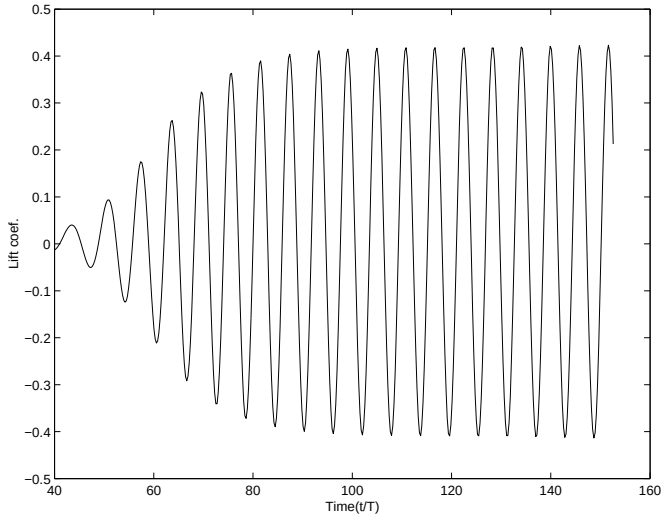

Figure 4.8: The lift coefficient at $Re = 100$ as a function of time.

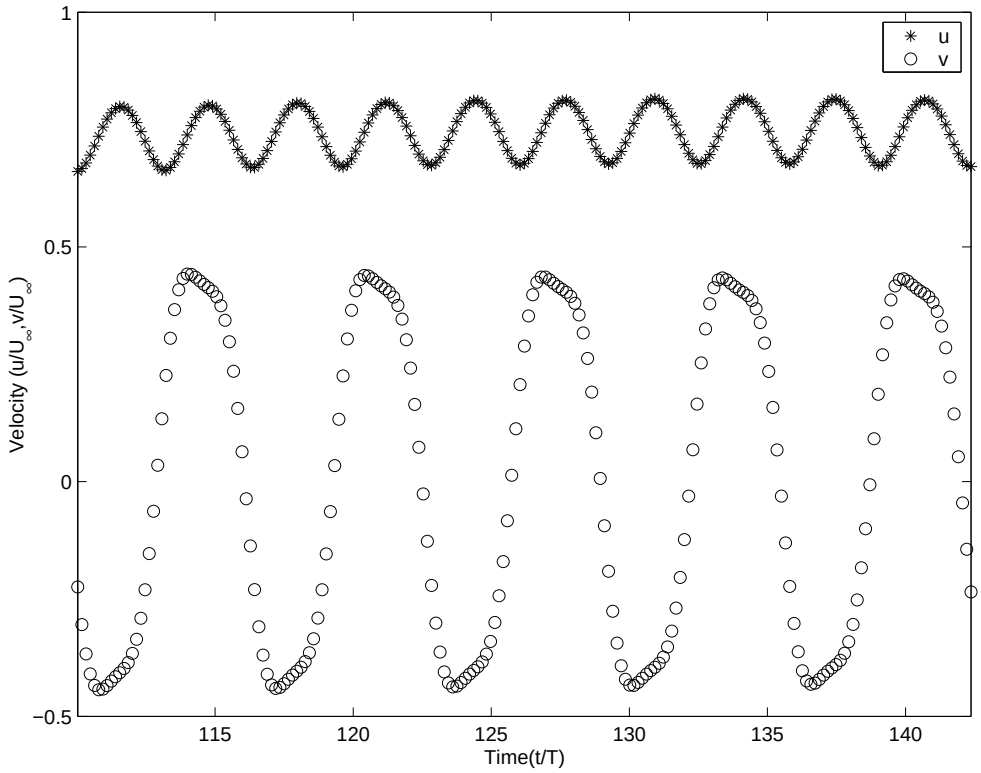

Figure 4.9: The velocity at the point $1.4D$ right behind the cylinder center in the flow over a cylinder at $Re = 100$.

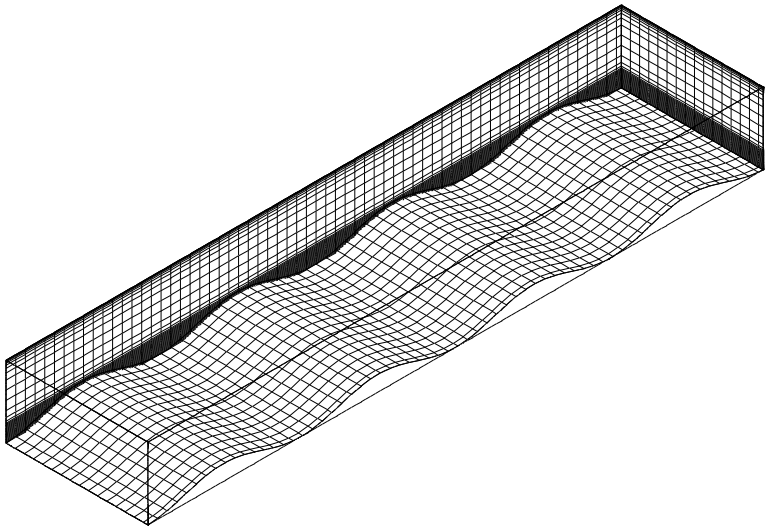

Figure 4.10: The computational domain for the wavy channel flow; the domain size is 20.3 $cm \times 2.1\ cm \times 4.8\ cm$. The bottom wavy boundary is derived from the boundary-fitted grid (every second grid point in each direction is shown).

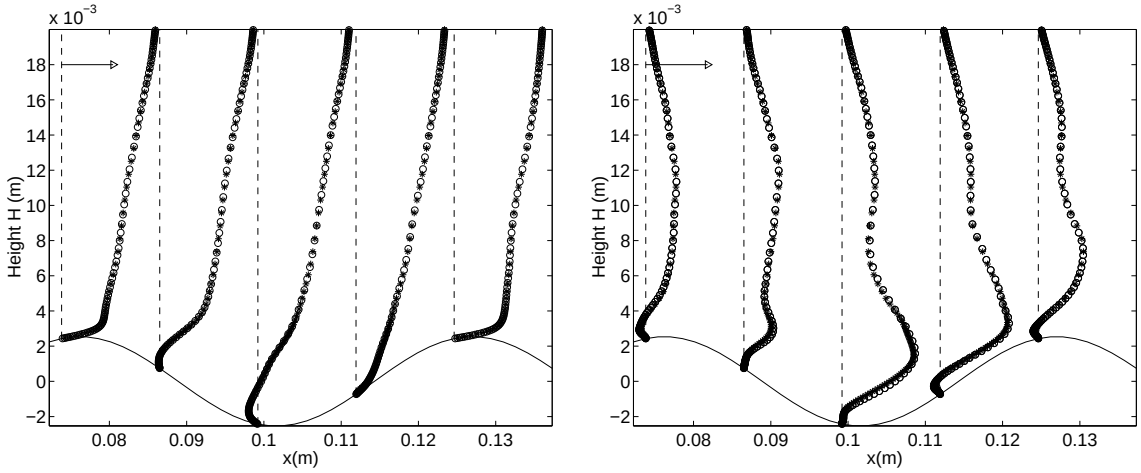

(a) (b)

Figure 4.11: (a) Comparisons of streamwise velocity profile from the GCIBM and boundary-fitted grid results for steady flow. The arrow at the top denotes 0.1 m/s ($0.56U_{max}$). (b) Comparisons of turbulent Reynolds stress between the GCIBM and boundary-fitted grid results for steady flow. The arrow at the top denotes 0.0002 m^2/s^2. $\circ$: boundary-fitted grid results and $*$: GCIBM results.

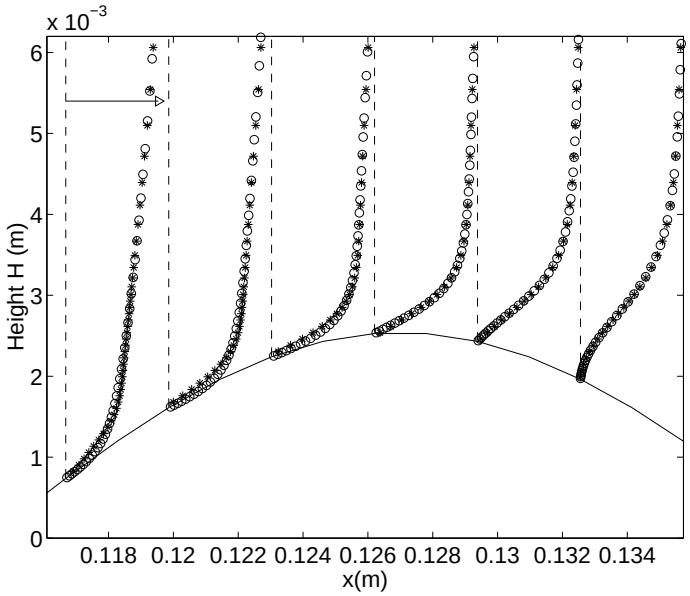

Figure 4.12: Comparisons of streamwise velocity profile between the GCIBM and boundary-fitted grid results for steady flow in the vicinity of the crest. ∘: boundary-fitted grid results and ∗: GCIBM results.

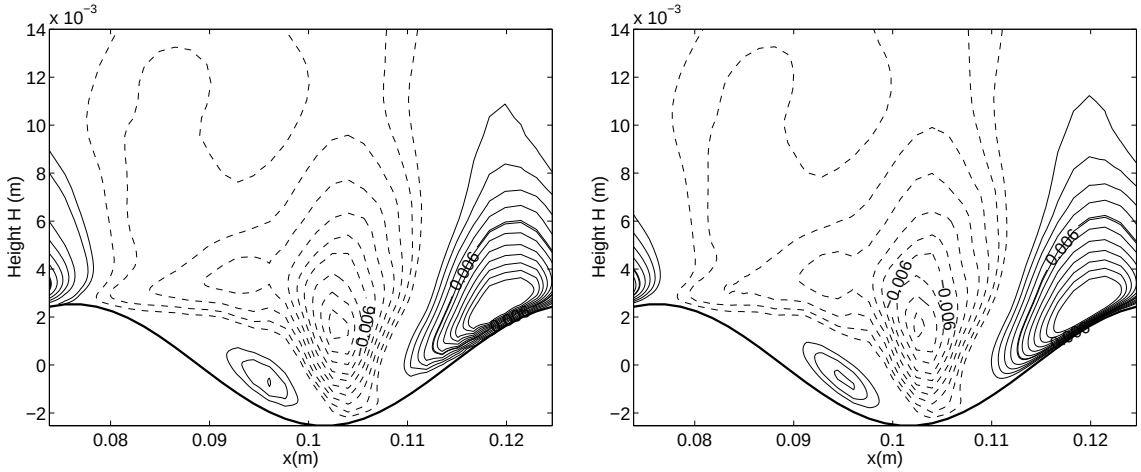

(a) (b)

Figure 4.13: Comparisons of mean vertical velocity contours between the GCIBM and boundary-fitted grid results for steady flow over one wavelength of the topography. (a) GCIBM (b) boundary-fitted grid. −−: negative velocity, −: positive velocity. The boundary-fitted grid result is much smoother in the up-slope region since more grid points are used.

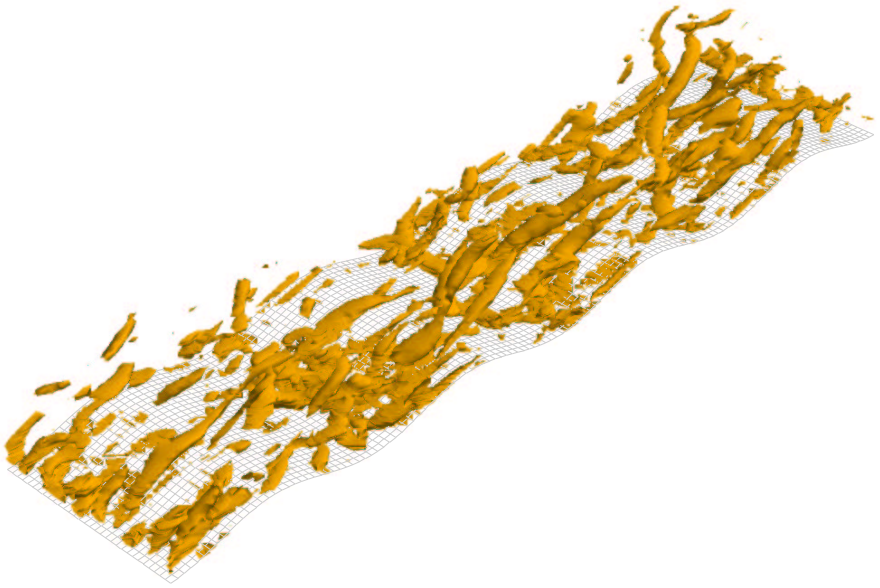

Figure 4.14: Instantaneous snapshot of vortex cores plotted as isocontours of $\lambda_2 = -50$ in fully developed steady wavy flow with the GCIBM approach.

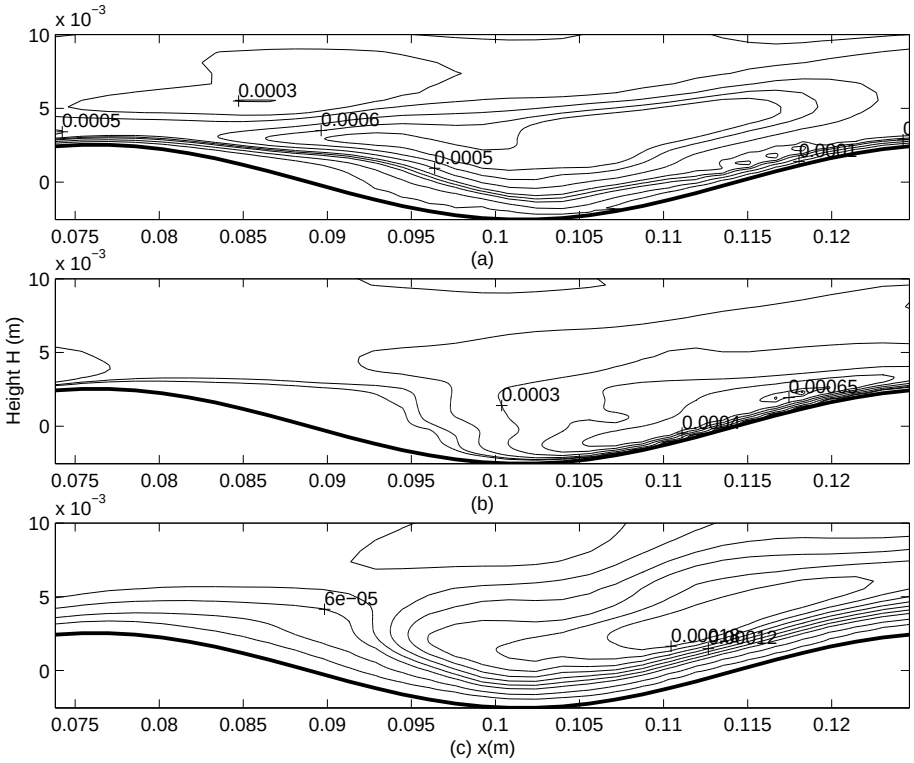

Figure 4.15: Contours of mean flow turbulence intensity. (a) Streamwise turbulence intensity $\overline{u'^2}$ (b) Spanwise turbulence intensity $\overline{v'^2}$ (c) Vertical turbulence intensity $\overline{w'^2}$.

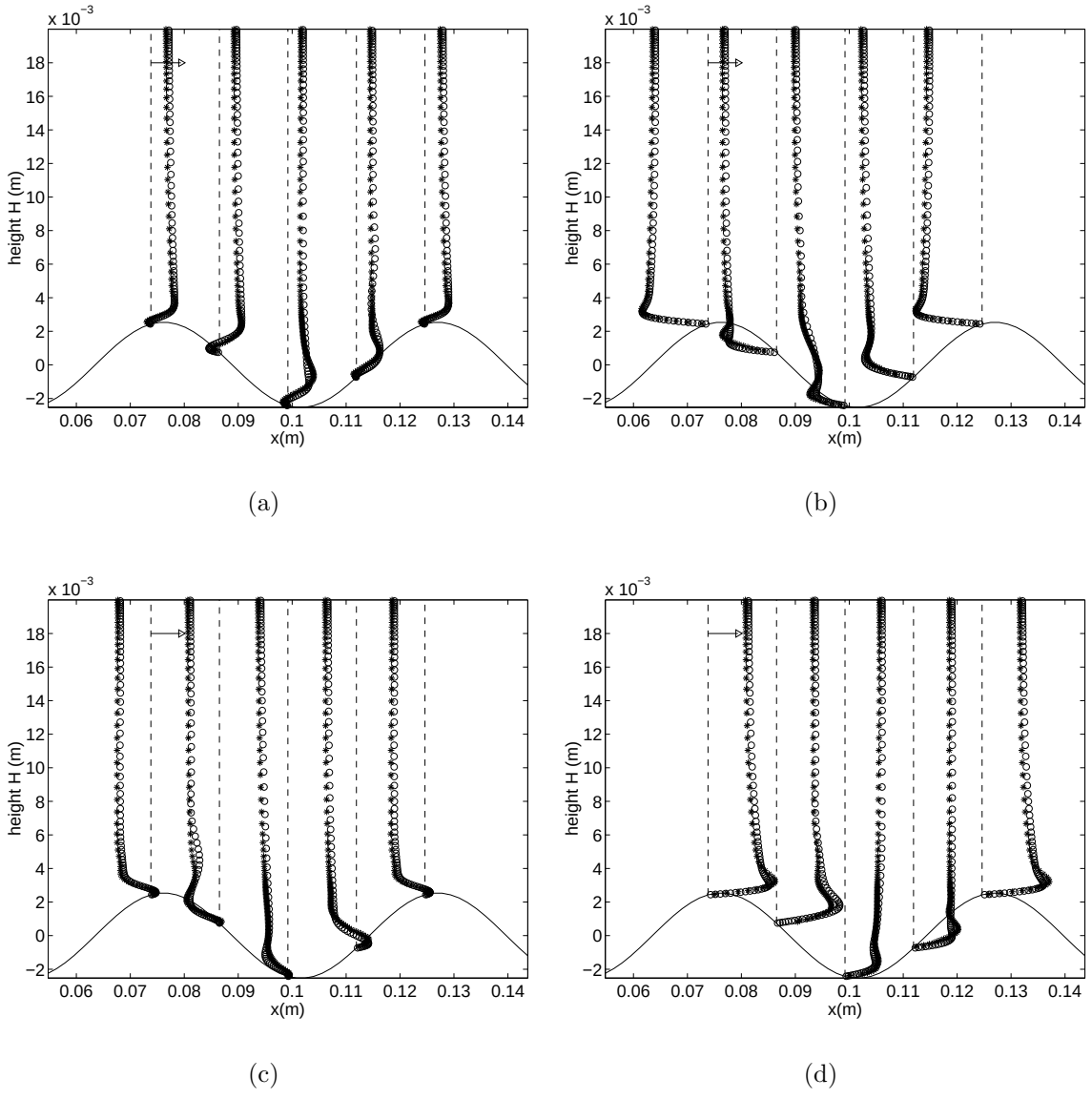

Figure 4.16: Comparison of streamwise velocity at different time steps. (a) t=0.25T (b) t=0.5T (c) t=0.75T (d) t=T. T is the time period imposed by the oscillatory pressure gradient. $\circ$ denotes the boundary-fitted grid result and $*$ denotes the GCIBM result.

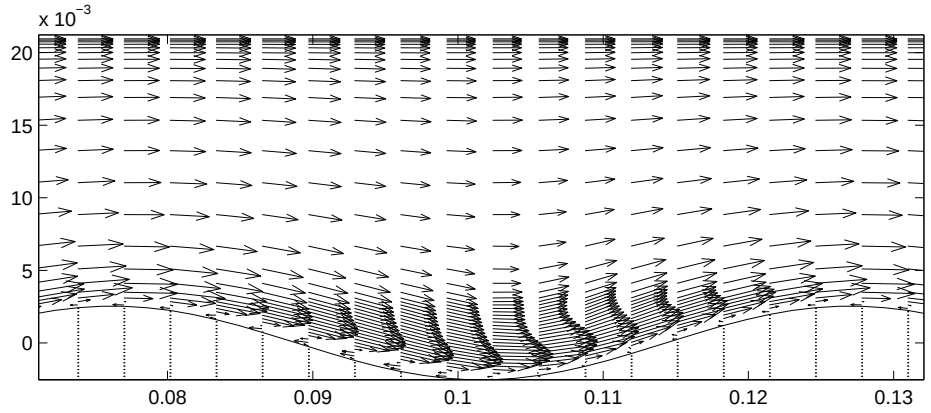

Figure 4.17: Instantaneous, spanwise-averaged velocity vector plot at $t = 0.25T$ using GCIBM. (every second grid point in each direction is shown).

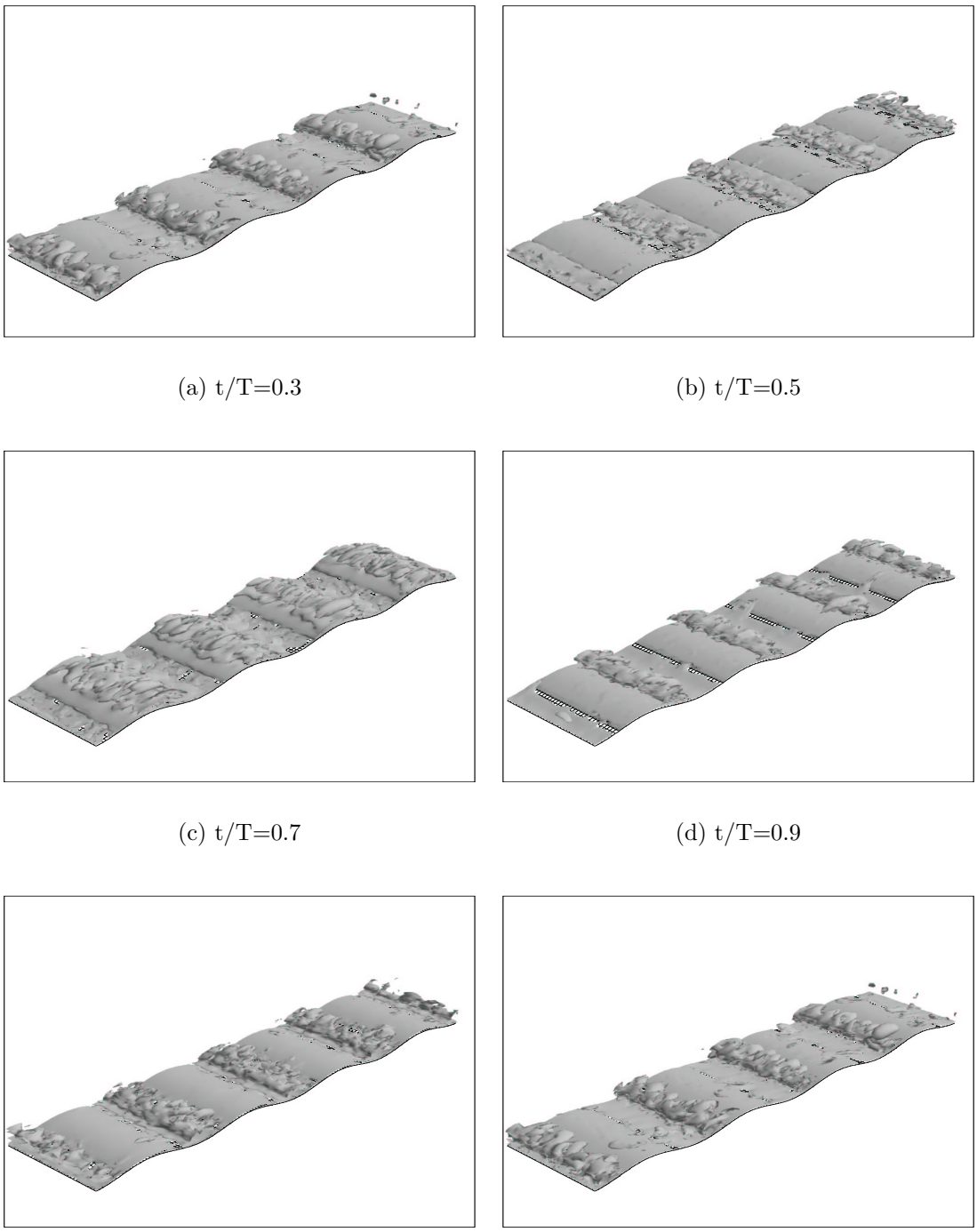

(a) t/T=0.3

(b) t/T=0.5

(c) t/T=0.7

(d) t/T=0.9

(e) t/T=1.1

(f) t/T=1.3

Figure 4.18: Vortex structures plotted with the λ_2 method for different flow phases during a time period $T(t/T = 0.3$ to $t/T = 1.3)$. $t/T = 0, 1$ corresponds to the phase of maximum oscillatory pressure gradient. The vortices are localized between two contiguous wave crests.

Chapter 5

Geophysical Flow over a Three-Dimensional Gaussian Bump

5.1 Introduction

In the previous chapter, we validated the ghost cell approach using uniform flow over a cylinder and turbulent flow over a wavy boundary. In this chapter, we extend the current approach to a realistic geophysical application. The numerical experiment tests the approach in the presence of three-dimensional topography and validates the GCIBM module in an existing general ocean model. The model is described in Section 5.2. The model setup is provided in Section 5.3. Finally, the simulation results and comparisons are provided in Section 5.4.

5.2 Model description

To test the flexibility of GCIBM, we use the existing MIT Global Circulation Model (MITGCM) to simulate a geophysical flow over a three-dimensional Gaussian bump. The MITGCM is an incompressible, finite volume, second order accurate, $z-$coordinate ocean model (Marshall *et al.*, 1997b). The equations are written out in full in Marshall *et al.* (1997b). Adcroft *et al.* (1997) presented two alternatives to the stair-step representation of topography in MITGCM, shaved-cell and partial-cell methods. Both

alternatives treat the boundary by modifying the shape of the cells intersected by the boundary. The shaved-cell method allows the topography to take a piecewise linear representation and the partial-cell method uses a simpler piecewise constant representation. Both methods show dramatic improvement compared to the traditional stair-step representation. The shaved-cell approach performs slightly better than partial-cell approach. However, the storage requirements for the former are excessive and the implementation is much more complicated so the simpler partial-cell method is provided in the MITGCM code. The shaved-cell method is essentially the same as that proposed in Ye *et al.* (1999) for engineering applications. In the current validation, we compare the GCIBM with both stair-step and partial-cell methods.

5.3 Model setup

The model configuration is the same as the three-dimensional test case provided in Adcroft *et al.* (1997). A three dimensional Gaussian bump is placed in a periodic channel of length 400 km and width 300 km. The ocean depth is 4.5 km. The bump has a characteristic horizontal length scale of 25 km and is centered in the channel. It rises to a height of 90% the depth of the ocean. The setup is essentially a typical seamount problem. For example, Fieberling seamount is a topographic feature in the Pacific Ocean that looks very much like a Gaussian bump.

The model is initialized with a barotropic inflow of 25 cm/s. A periodic boundary condition is used in the streamwise direction. Some of the parameters are shown in Table 5.1. Eight equally spaced levels are used in the vertical and the stratification is initially linear. A high resolution simulation run with 24 vertical levels ($N_x \times N_y \times N_z = 240 \times 180 \times 24$) is used to verify the simulation results. The high resolution case uses the partial-cell approach to represent the bottom topography.

5.4 Simulation results

The flow is deflected to the left as it passes over the bump due to the effect of the Coriolis force and a cyclonic eddy forms behind the seamount. In time, an anti-cyclone

is formed and the first eddy is shed and advected downstream. The stratification is strong so the wake structure is similar to that of a two-dimensional wake in each layer. Figure 5.1 illustrates the isotherms along the streamwise cross-section through the center of the Gaussian bump. The three-dimensional structure of the cyclonic eddy at $t = 10$ days in terms of the iso-contour of relative vorticity with $\zeta = 0.2\zeta_{max}$ from the high resolution simulation is shown in Figure 5.2. Only positive vorticity (cyclone) is shown. Figure 5.3 shows the nondimensional depth integrated relative vorticity (ζ/f) at $t = 10$ days. We use this high resolution result as the standard.

Figure 5.4 shows the comparison of the results between the stair-step grid and the GCIBM implementation for 5 km resolution ($N_x \times N_y \times N_z = 80 \times 60 \times 8$). The effect of the topography in steering the flow is very similar in the two results. The distortion of the cyclonic tail, upstream of the bump, is an effect of the periodic boundary conditions and should be ignored. The orientation of the elliptic cyclonic eddy is slightly different but the processes of eddy formation, shedding and advection seen in the GCIBM version (Figure 5.4(b)) are quite close to those observed in the high resolution simulation but the latter is smoother. Very few differences are observed between the GCIBM and high resolution simulations in Figure 5.3. These include the larger maximum in the tail and the smoother solution in the high resolution case. On the whole, the solutions are qualitatively similar. Despite the differences, it is clear that the GCIBM method does a credible job in representing the flow over this large topographic feature. The difference between the solutions using GCIBM and the stair-step grid are more significant. There is a stronger local maximum within the tail in the GCIBM solution. The stair-step grid result has a much wider shed cyclonic vortex. In addition, we observe much more small-scale noise near the bump in the stair-step solution.

We also conducted two additional simulations for each topography representation in order to test the convergence. Figures 5.5 and 5.6 show the solutions for two finer resolutions, $\Delta x = 2.5$ km and $\Delta x = 1.67$ km, respectively. We keep the vertical resolution unchanged. The solutions differ from the original ones (Figure 5.4) only in fine detail, the overall structure being the same. The amplitude of the cyclonic eddy

increases as the resolution is made finer, suggesting that coarse resolution underestimates the eddy strength. As we increase the horizontal resolution (i.e. reduce Δx, Δy only), the GCIBM solutions converge to the correct results. In the case of the stair-step grid, as the resolution is increased, the noise near the bump increases and the cyclonic eddy is distorted. The 'rings' of grid-scale noise become more pronounced with increased resolution.

We can assess the degree of convergence by comparing the maximum strength of the cyclonic eddy, the values of which are shown in Table 5.2. As the grid spacing is reduced, the strength of the cyclone increases. The high resolution study has a maximum strength of 871. Based on the strength for the three representations, it appears that the GCIBM and partial-cell results are converging to the high resolution solution but the stair-step grid solution appears to be asymptoting to a lower value. This series of experiments clearly indicates that the GCIBM representation converges to the high resolution solution with increased horizontal resolution.

Table 5.1: Parameters for the numerical simulation of flow over three-dimensional Gaussian bump.

	MITGCM
Channel length (km)	400
Channel width (km)	300
Nominal ocean depth H (m)	4500
Height of bump h (m)	4050
Length scale of bump L (m)	25
Stratification NH/fL	1.5
Barotropic inflow u_i (cm/s)	25
Horizontal biharmonic viscosity (m^4/s)	5×10^9
Vertical Laplacian viscosity (m^2/s)	1×10^{-3}
Horizontal biharmonic diffusion (m^4/s)	1×10^9
Vertical diffusion (m^2/s)	1×10^{-5}

Table 5.2: Comparison of the high resolution case shows the maximum vorticity strength of 871.

Resolution (size)	Stair-step	GCIBM	Partial-cell
5 km ($60 \times 80 \times 8$)	714.8	798.4	796.5
2.5 km ($120 \times 160 \times 8$)	766.0	828.3	825.5
1.67 km ($180 \times 240 \times 8$)	774.4	847.8	844.3

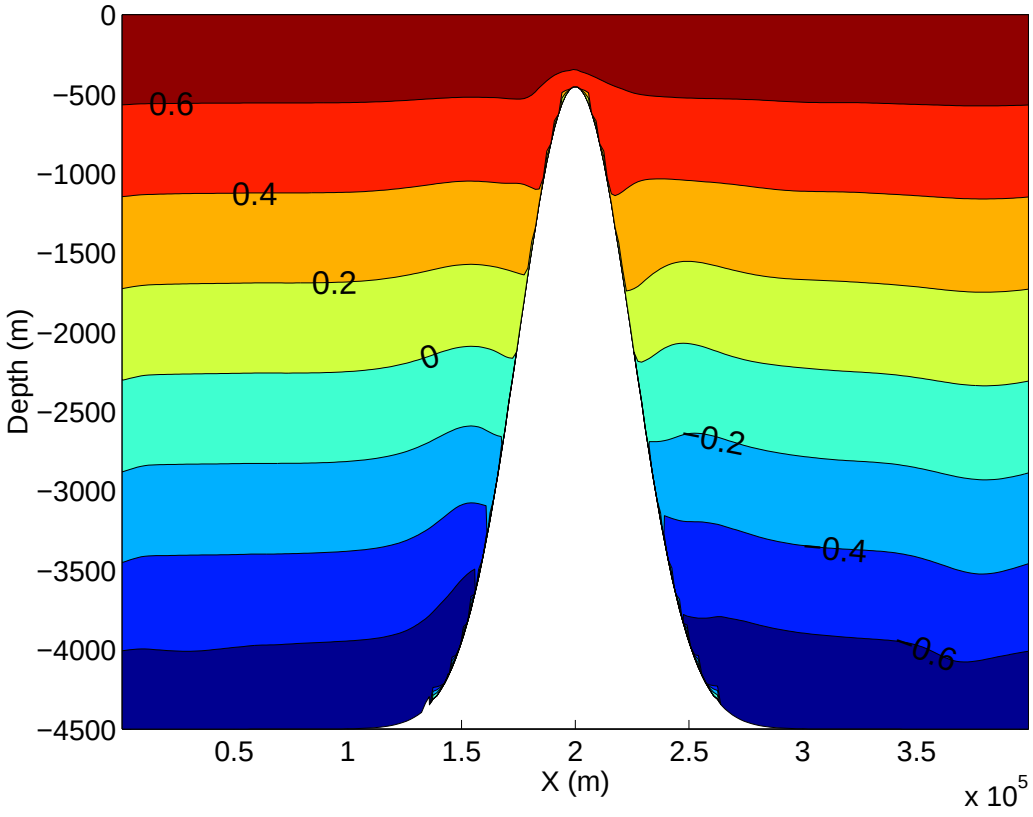

Figure 5.1: A cross-section of the potential temperature deviation ($^{\circ}C$) along the streamwise centerline through the bump at $t = 10$ days.

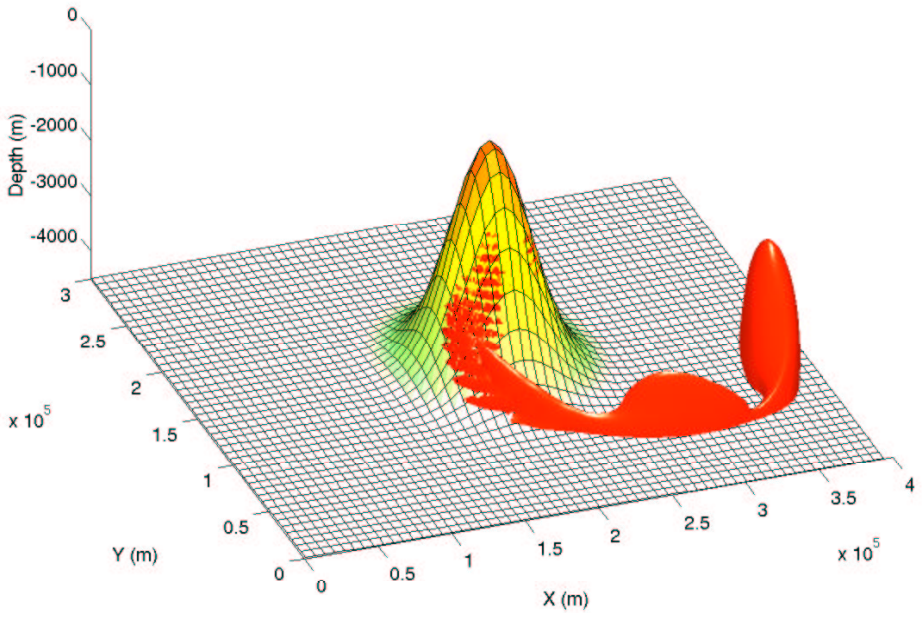

Figure 5.2: The three-dimensional structure of iso-contour of relative vorticity $\zeta = 0.2\zeta_{max}$ at $t = 10$ days.

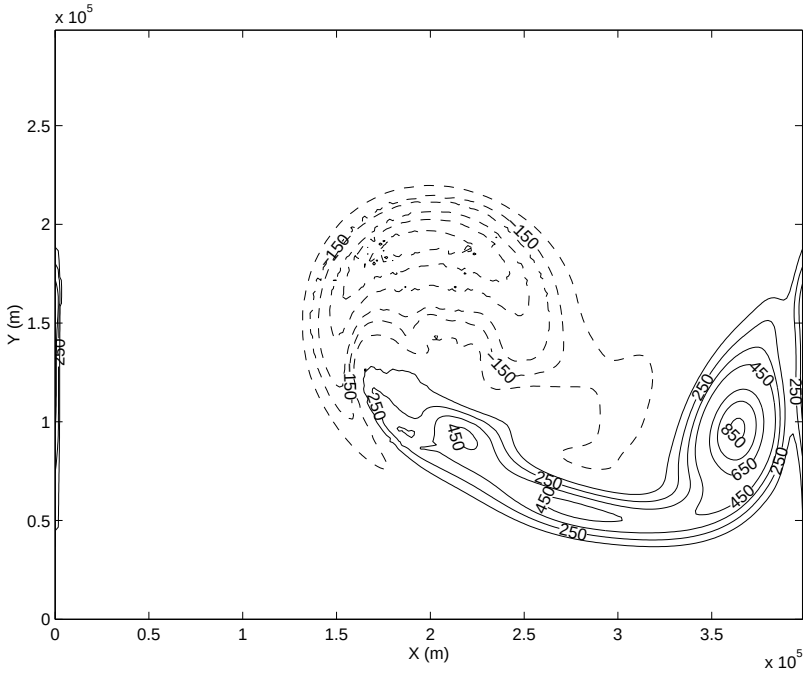

Figure 5.3: Nondimensional depth integrated relative vorticity ζ/f at $t = 10$ days at fine grid resolution ($N_x \times N_y \times N_z = 240 \times 180 \times 24$).

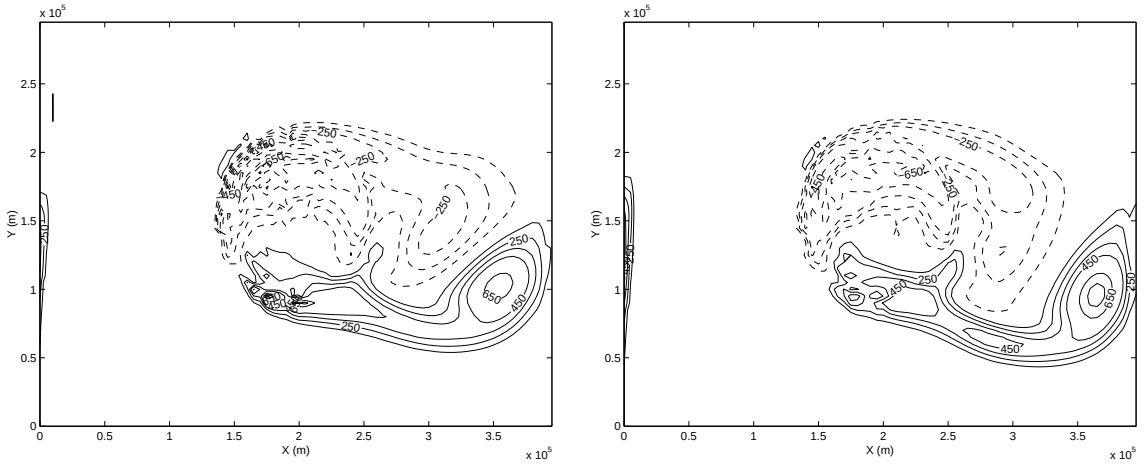

(a) (b)

Figure 5.4: Contours of nondimensional depth integrated relative vorticity ζ/f at $t = 10$ days at horizontal resolution $\Delta x = 5\ km$. (a) stair-step representation of topography. (b) GCIBM representation of topography. ($N_x \times N_y \times N_z = 80 \times 60 \times 8$).

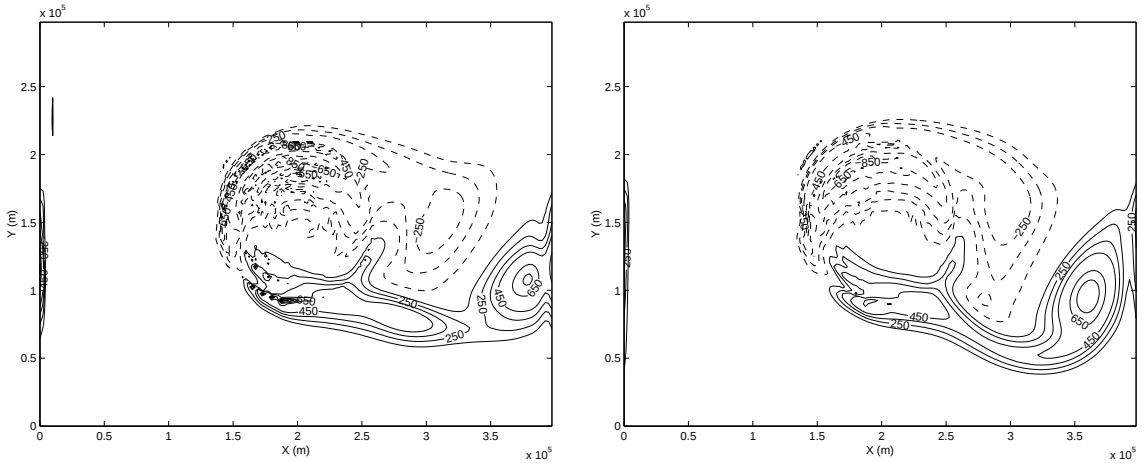

(a) (b)

Figure 5.5: Contours of nondimensional depth integrated relative vorticity ζ/f at $t = 10$ days at horizontal resolution $\Delta x = 2.5\ km$. (a) stair-step representation of topography. (b) GCIBM representation of topography. ($N_x \times N_y \times N_z = 160 \times 120 \times 8$).

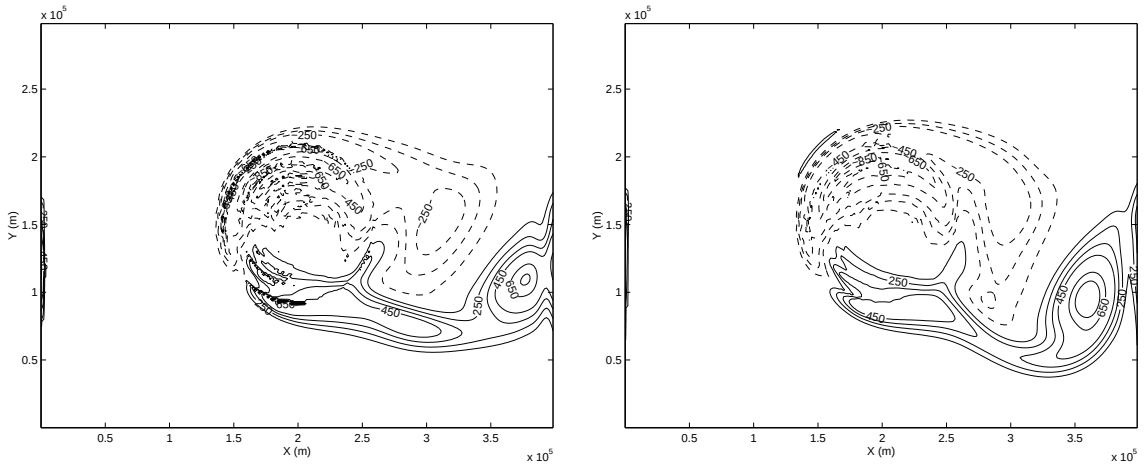

(a) (b)

Figure 5.6: Contours of nondimensional depth integrated relative vorticity ζ/f at $t = 10$ days at horizontal resolution $\Delta x = 1.67\ km$. (a) stair-step representation of topography. (b) GCIBM representation of topography. ($N_x \times N_y \times N_z = 240 \times 180 \times 8$).

Chapter 6

Effects of Coastal Geometry and the Formation of Cyclonic/ Anti-Cyclonic Eddies in Coastal Upwelling

6.1 Introduction

Before proceeding to the realistic ocean model with realistic geometry and topography, we simulate a simplified laboratory upwelling flow to study the effects of coastal geometry on eddy formation. Coastal perturbations modify the coherent structures which travel in the windward direction, changing their structure. The mechanisms of generation of these structures have been studied with simplified models but are not completely understood. We present animations derived from the simulations to investigate the process of formation of cyclonic/anti-cyclonic eddies. The physical geometry is a circular tank with a sloping bottom and a cape at the outer boundary.

The cape produces strong vortex stretching due to the acceleration of the flow around it. The continued vortex stretching results in vortex tearing in the cape vicinity which causes greater stirring than in the no-cape flow. These processes explain

observed features of laboratory experiments and field observations. The coastal perturbation inhibits the development of these structures and produces thin filaments extending offshore and downstream of the perturbation. These are important features of coastal upwelling.

Laboratory experiments designed to study coastal upwelling flow have been conducted (Narimousa & Maxworthy, 1987a; Narimousa & Maxworthy, 1987b; Monismith, 1986; Narimousa & Maxworthy, 1985). Narimousa and Maxworthy (1985) created a two-layer stratified fluid in a rotating cone-cylinder tank; hereafter, we abbreviate Narimousa and Maxworthy as NM. The top disk was rotated differentially with respect to the system rotation to simulate a surface wind stress. As a result, the density interface elevated near the outer wall and, when the surface stress was strong enough, the interface intersected the surface and formed a front that migrated offshore. The front was unstable under certain conditions and azimuthal waves appeared and grew to large amplitude. Using flow visualization, NM observed plumes, jets, and pinched-off cyclones near the front. They also studied the effects of bottom topography (Narimousa & Maxworthy, 1985) and coastline perturbation (Narimousa & Maxworthy, 1987b) and observed several important features. When a cape was present, the first sign of upwelling always occurred adjacent to its upstream side and standing waves were found downstream. The relative importance of coastal topographic features such as capes, bathymetry and wind stress in generating instabilities in upwelling regions remains unclear (Allen *et al.*, 1995; Lentz, 1995).

Numerical simulation can be used together with analytical modeling and laboratory experiments in the study of the coastal ocean. Zang and Street (1995; 1993) used large eddy simulations (LES) to study a configuration similar to that of the laboratory experiments of NM (1987b). Here, we use an extended version of this model to study the influence of coastal perturbations on upwelling. We focus on the formation of the cyclonic/anti-cyclonic eddies generated by the instability. As upwelling is a three dimensional process, interactions among the vortices are complex and irregular. The vortex structures are quite complicated. The formation of the filaments or strong offshore jets provides an efficient mechanism for exchange between the shelf and the deep ocean. The fish-hook structures observed in the laboratory probably have the

same origin as the off-shore filaments. It is found that Rayleigh-Taylor and mixed instabilities and fish-hook structures cause a sharp increase in mixing. A mixedness parameter and energy budgets are used to quantify mixing in the current study. An efficient method for calculating available potential energy using probability density function (pdf) is applied in the energy budget analysis (Tseng & Ferziger, 2001b).

This chapter is organized as follows. Section 6.2 briefly describes the numerical simulation. Section 6.3 investigates the formation of the eddies. Section 6.4 presents the influence of a coastal perturbation on the instabilities and features such as fish-hook structures due to them. Section 6.5 quantifies turbulent mixing in the upwelling flow and investigates the effects of the presence of a cape on it. Finally, a summary is given in Section 6.6.

6.2 Description of the simulations

The numerical method is essentially the same as that used in Chapter 4 for the laboratory scale flows. Rather than the ocean, we shall simulate the laboratory experiments of NM (1987a; 1987b; 1985) in which the wind stress is simulated by rotating the top lid relative to the tank at angular velocity $\Delta\Omega = 2\pi/\Delta T$, where ΔT is the rotation period of the lid. Hence, at the top of the domain, the azimuthal velocity is $u_h = -\triangle\Omega \times r$. A no-slip condition is used for the tangential velocity while the normal velocity is zero on the top, side, and bottom walls. Periodic boundary conditions are used for the flow in the azimuthal (long-shore) direction. In the initial condition the fluid is 'two-layer' stratified and the density field is horizontally uniform.

We conducted two sets of simulations, one with and the other without coastline perturbations. We give the parameters for both simulations here. One quadrant of the tank is simulated using periodic boundary conditions in the azimuthal direction. The domain is an annular region with a sloping bottom (see Figure 6.1 for a typical grid). The grid resolution is $82 \times 82 \times 82$ ($N_r \times N_\theta \times N_z$), which has been shown to be adequate to fully resolve this flow (Tadepalli, 1997). Cui and Street (2003) studied the whole tank rather than a quadrant. The simulation was performed on a distributed memory massively parallel computer. The filtered Navier-Stokes equations are solved

in the rotating frame. The initial vertical density distribution has a hyperbolic tangent profile approximating the two-layer structure in the experiments. There is no initial azimuthal or horizontal density variation. No data is available on the initial interface thickness or density distribution.

The geometry for the simulations with a cape is obtained from the function defined as 'Witch of Agnesi' (Beyer, 1981) which relates the radial excursion distance to the azimuthal angle:

$$d(\theta) = \frac{D_c}{\beta}\left(\frac{1}{(\theta-\theta_0)^2 R_1^2 + \alpha^2} - \frac{1}{\theta_0^2 R_1^2 + \alpha^2}\right) \tag{6.1}$$

$$\beta = \frac{1}{\alpha^2} - \frac{1}{\theta_0^2 R_1^2 + \alpha^2} \tag{6.2}$$

where $d(\theta)$ is the radial excursion distance and has a maximum at $\theta = 45^\circ$ (Figure 6.1 (b)). The parameters of the simulation are given in Tables 6.1 and 6.2. The cape geometry defined above is slightly different from the cylinder of radius R_c used in the laboratory experiments of NM (1987b) and is larger than that used in Zang (1993). However, the maximum width of the cape is chosen as the cape radius (R_c) in their experiments (case: cape M) which was designed to be representative of the coastline perturbations. Since we employ periodic boundary conditions in the azimuthal direction (Zang & Street, 1995), these simulations are representative of an upwelling flow with four capes, one in each quadrant. The boundary conditions were described above.

Algebraic stretching is employed to control the grid spacing to allow resolution of the boundary layers on the inner and outer boundaries of the tank. An exponentially damped stretching function ($e^{-9(i-N)^2/N^2}$, N = number of grid points in the radial direction) is used to avoid large deformations of the grid cells in the interior of the domain, which can deteriorate solution accuracy (Figure 6.1).

The parameters of the simulations are matched to those in the experiments of NM (1991; 1987b) and are given in Table 6.1. The Reynolds number ($Re = \rho U_p R_0/\mu$ where U_p the disk edge velocity, R_0 the outer radius of the annulus, ρ the density and μ the viscosity of water) of the simulations must be lower than that of the experiments

for computational efficiency. This is permitted because the flow behavior becomes independent of Re when the latter is large enough and because the dominant instability mechanisms are inviscid. Other non-dimensional parameters include the Rossby number and the layer Froude numbers. The Rossby number is $Ro = U_p/f(R_0 - R_1)$, where U_p is the maximum lid velocity and is of the order of $O(10^{-2})$. The layer Froude numbers are defined as $f^2\lambda_s^2/g'h_{10}$ where λ_s is the theoretical stationary width of the density front, $g' = g\Delta\rho/\rho_1$ is the reduced gravity and h_{10} is the initial upper layer depth. The spin-up time (Linden & Heijst, 1984), used as the reference time scale, is $t_s = (h_{10}/\Delta\Omega)((\Omega + \Delta\Omega)/\nu)^{\frac{1}{2}}$ where $\Delta\Omega$ is the differential lid angular velocity and Ω is the tank rotation angular velocity.

6.3 The formation of coherent structures

Tadepalli (1997) applied linear stability theory (LST) to the upwelled surface front and compared the results with the experiments of NM (1987b). He found the instability to be of mixed type but predominantly baroclinic. An early weak Rayleigh-Taylor (R-T) instability modifies the surface front. Although the instability mechanisms were identified, the structures are nonlinear and more complicated than those predicted by LST.

When the top lid rotates anti-cyclonically relative to the cyclonically rotating fluid, fluid near the top surface is driven radially inward by the Coriolis force, creating the top Ekman boundary layer. Heavy fluid moves toward the outer wall and upward to replace it. When heavy fluid finally overlies light fluid, a weak modified R-T instability occurs both near the outer wall and closer to the center. This process, together with Ekman pumping causes a cross-shore circulation in the radial-vertical plane that has azimuthal vorticity associated with it. This vorticity can be seen in an isosurface plot (ω_θ) in Figure 6.2(a); the isosurface shown corresponds to $\omega_\theta = 0.8U_p/D$ where D is the diameter of the domain. Initially, the azimuthal vorticity appears near the outer boundary. It then moves away from the wall as the flow adjusts toward geostrophic balance. The wave-bands found near the center are much less energetic than the baroclinic-barotropic (B-B) instability mode that occurs later (Tadepalli, 1997). An

intensive mixing zone then develops between the surface front and the coast. The mixing and friction reduce the azimuthal vorticity near the wall (Figure 6.2(b)).

At this stage, the vertical vorticity (ω_z) in the vicinity of surface front is essentially a vortex sheet (Figure 6.3(a)). The folding that follows is very sensitive to small perturbations. As the disturbance grows, it quickly takes on a more B-B character. Small amplitude azimuthal waves first appear at the primary front. They develop into a series of cyclones and anti-cyclones. Cyclonic eddies are usually found at the front while anti-cyclonic eddies are found closer to the wall. The cyclonic eddies often pinch off from the front to form isolated vortices. In the current simulation, six isolated vortices form as predicted by LST and seen in the laboratory experiments (Tadepalli, 1997; Narimousa & Maxworthy, 1987b); see Figure 6.3 (c) and (d). We trace the cyclonic eddies via an isosurface with $\omega_z = 1.1U_p/D$. The isolated vortices move off-shore slowly and then decay (Figure 6.3 (e) and (f)).

The B-B instability produces quasi-horizontal convection that is best visualized in two dimensions. These azimuthal frontal waves are observed often in satellite infrared (IR) images during the upwelling season. The formation of these large scale structures could also be associated with coastal geometry or bottom topography (Lentz, 1995; Narimousa & Maxworthy, 1989). Also, a few thin filaments of heavy fluid are observed to move offshore after $t = 1.5t_s$ in the density animation. The details of these events depend strongly on the initial perturbations and no coastal perturbation effects are present. Coastal geometry effects will be discussed in the next section.

The 3-D isosurface of vertical vorticity shown in Figure 6.3 demonstrates the formation of eddies ($t = 0.94t_s$ to $t = 1.68t_s$). The mechanism is three-dimensional and involves vortex stretching. The stretching is seen in the later parts of Figure 6.3 in which the azimuthal vorticity is growing and elongated due to the susceptibility of the quasi-two dimensional vortices to secondary instability. If a vortex develops a slight kink due to a small perturbation, the velocity field it induces lifts or lowers the kink. This process is very effective in stretching vortices. A great deal of turbulence production takes place by vortex stretching. In the current simulation with a well-defined coastline, the filaments may develop into the fish-hook structures seen in the laboratory. A still wider variety of processes can take place in this complicated tangle

of vortices, and the three-dimensional flow is more sensitive to small disturbances than the earlier stages of the flow.

6.4 The effects of coastal perturbations on the large scale structure

Coastline perturbations and topography (Brink, 1988; Breaker & Mooers, 1986; Flament *et al.*, 1985) play a significant role in the dynamics of coastal currents and fronts and produce some of the features observed in the satellite infrared images. Topographic features such as capes and ridges (Luther & Bane, 1985) have a profound influence on the large-scale features. However, the mechanisms are not understood in detail. In this section, we explore the large-scale structures and quantify the influence of a coastal perturbation using the simulations with and without a cape.

6.4.1 Modification of instabilities with coastal perturbations

Figure 6.4 compares snapshots taken from the animations of the scalar field with and without the coastline perturbation at $z = 0.93h$ at $t = 1.12t_s$. During the initial upwelling, the primary front is drawn closer to the 'coastline' on the downstream side of the cape. The front downstream of the cape is wider than the no-cape front (Figure 6.4(b)). This has been observed in Zang (1993). The presence of the cape forces the fluid to turn seaward in the upstream of the cape and the upwelled water is advected downstream. Contour plots of the vertical vorticity at the same horizontal sections are shown in Figure 6.5. In the simulation with a cape, the vorticity field is more irregular and the strongest vorticity is located near the cape rather than being spread over the whole boundary. A strong perturbation in the azimuthal velocity is observed just downstream of the cape as shown by the enlarged velocity vector plot in Figure 6.6. Very strong recirculation occurs adjacent to the back of the cape and coincides with the separation zone. In Zang (1993), no significant difference is observed between the cases with and without a cape. This is attributed to the coarse resolution ($N_r \times N_\theta \times N_z = 64 \times 64 \times 64$) and the smaller cape in Zang (1993).

NM (1987b) indicated that baroclinic waves interact with standing waves on the downstream side of the cape. Their observations were based on visual examination of the features observed in the experiments but no quantitative measurements were made to confirm the existence of the standing waves. The current simulations (similar to case:M of their experiments) suggest that the waves on the surface front are the result of mixed baroclinic-barotropic instability and move in the direction of the surface forcing (clockwise) in the rotating frame (Tadepalli, 1997). The major difference between our simulations and NM's experiments is the value of disk friction velocity ($u_* = \sqrt{\tau_w/\rho}$) so that there is a significant difference in the nondimensional parameter $\theta_* = g'h_{10}/u_* f\lambda_s$ shown by NM to be an important parameter for determining stability and the size and drift velocity of the baroclinic waves in coastal upwelling. We obtain u_* from the surface shear stress at the disk which has been verified by the grid resolution studies (Cui & Street, 2003). However, NM inferred u_* from an analysis of previous experiments. θ_* is the combination of Rossby radius normalized by λ_s and the Richardson number ($\theta_* = \sigma Ri^{1/2}$) from (Narimousa & Maxworthy, 1985). $\sigma = \sqrt{g'h_{10}}/f\lambda_s$ is the 'Rossby/Froude' number defined by Lesieur *et al.* (2000) normalized by λ_s for two-layer stratified flow, which is used commonly in the baroclinic instability criterion. $Ri = g'h_{10}/u_*^2$ represents the strength of the stratification forcing governing the size and drift velocity of the baroclinic waves.

The flow becomes unstable as θ_* decreases. θ_* in our simulation is $\theta_* = 1.12$ which is smaller than the lowest value of θ_* ($\theta_* \approx 2$) in NM. They mainly focused on the cases in which a stable standing wave existed. The standing wave usually became unstable later and propagated offshore for small θ_*. Eventually, a cyclone pinched off. These observations are reproduced in our simulations. Cui and Street (2003) showed that the critical value of θ_* is roughly 5.4. For $\theta_* > 5.4$, the frontal instabilities are less intense and no pinched-off eddies are observed. The animation shows the formation of the first baroclinic wave, which is the largest and most significant one (Tadepalli, 1997). It forms downstream of the cape (Narimousa & Maxworthy, 1987b). The baroclinic waves are modified by the cape, mainly in the troughs (which are closer to the 'coastline'). The front excursions are more irregular (Figure 6.7) than those without the cape. In the latter case, they are nearly periodic.

The mechanism of formation can be explained in terms of vortex stretching. The front excursions are caused by the presence of the large-scale vortices. The vortices are elongated by the strain caused by the cape (Figure 6.8). Let us trace the vortex 'A' in Figures 6.7 and 6.8. As it moves clockwise, it is stretched by the strain produced by the acceleration of the fluid passing the cape. Figure 6.8 shows the absolute vertical vorticity at the same time as in Figure 6.7. As the flow evolves, the surface front (Figure 6.7) meanderings increase, causing distortion of the density front. All the vortices are elongated as they have already moved past a cape. (Recall that the periodicity implies that there are four capes.) The increased stretching of the front results in increased mixing and increases the strength of azimuthal vorticity, particularly in the vicinity of the cape. Strong azimuthal vorticity is always found just downstream of the cape. The dynamics can be described in terms of the vertical vorticity. Continued stretching results in tearing of the vortex (Figure 6.8). This simulation provides a quantitative explanation for the results observed by NM (1987b) with a coastal perturbation. Figure 6.7 also shows the creation of a diverging flow just downstream of the cape, which provides a mechanism for the production of long, thin offshore filaments of upwelled water observed in the ocean. The flow divergence causes the upwelled water to advect in the offshore direction.

6.4.2 Fish-hook structures

A great deal of alongshore variability of the large meanders is observed in satellite measurements. Strong winds can break these meanders, forming detached eddies that have been observed off the West Coast of the United States (Kosro, 1987). The laboratory experiments of NM (1991; 1987b) reproduced many of these features. Upwelling filaments are the most prominent feature; however, the generation mechanism is still unclear. They are related to the fish-hook structures observed in the laboratory and in the current simulation (Cui & Street, 2003; Tadepalli, 1997).

Nonlinear interactions that moderate the growth of the large-scale structures become important when the density front becomes highly non-axisymmetric (when $t > 3t_s$). Fish-hook structures are a by-product of these nonlinear interactions and

originate from the modulation of the large-scale structures (Tadepalli, 1997). Some vortices grow in size at the cost of others. As a result, eddies of different sizes are observed. Figures 6.9 (a)-(f) show a pair of counter-rotating vortices that pump upwelled high density fluid from the outer edge of the tank toward the center. The corresponding contours of relative vertical vorticity are shown in Figure 6.10 and confirm the presence of an elongated vortical structures created by the pumping action. As the fluid has different velocity than the local fluid, it moves relative to it, producing the fish hook. The angle of the fish-hook is governed by a second, relatively weak, pair of counter-rotating vortices that draws the fluid ejected by the first pair of vortices back toward the coast. In Figures 6.9(e) and (f), we see another fish-hook structure that was formed upstream with different strength. The strength of the fish-hook structure grows as time evolves.

A schematic of the process is given in Figure 6.11 (Tadepalli, 1997). The fish-hook structures are advected in the lid rotation direction (clockwise) as is evident in the sequence in Figure 6.9. Figure 6.12 shows the scalar field at four different heights, indicating that these structures are not two-dimensional; their intensity decreases with depth. The front excursion due to the fish-hook grows, trapping a pocket of low density fluid. This suggests a possible mechanism for production of isolated pockets seen in the ocean. This process causes considerable horizontal and vertical mixing. In the presence of a cape, the fish-hook structure is less pronounced. In its place, there are more thin filaments of a kind frequently observed in coastal regions.

6.5 Mixing in upwelling flows

As noted above, it is widely believed that coastline perturbations and topography have a significant effect on coastal currents, fronts, and upwelling and are responsible for the major features observed in satellite infrared (IR) images (Breaker & Mooers, 1986) and enhanced mixing. In this section, we will concentrate on the mixing events occurring in the simulation.

It is important to distinguish between the processes of stirring and mixing. The former involves the bringing of fluids of different density into contact through the

action of strain, which may result from turbulence. After the fluid has been stirred, it may re-stratify through gravitational action, returning the fluid to its original height. Mixing requires that the fluids combine at the molecular level and is an irreversible process. It is difficult to quantify mixing in either field measurements or laboratory experiments because very detailed data are required. In this study, we quantify mixing by using a mixedness parameter (M) and by computing the reference potential energy (RPE).

6.5.1 Mixedness parameter

The mixedness parameter defined below measures the fraction of the fluid that has been mixed (Tadepalli, 1997). This mixedness parameter M is essentially the one proposed by Roshko (1976) for the mixing fluid of different velocities and is defined by:

$$M(t) = \frac{1}{V}\int_V c(1-c)dV = \overline{c} - \overline{c^2} \tag{6.3}$$

where V is the total volume of the domain, $\overline{c} = \frac{1}{V}\int_V c dV$, $\overline{c^2} = \frac{1}{V}\int_V c^2 dV$ and $c = (\rho - \rho_0)/\Delta\rho$, ρ_m is the density of the fluid in the upper layer (the minimum density found in the flow), and $\Delta\rho = \rho_M - \rho_m$ is the density difference between the lower and upper layers. Since $0 \leq c \leq 1$, $M = 0$ and $M = 0.25$ for the completely unmixed and fully mixed situations, respectively. Figure 6.13 shows the evolution of the mixedness parameter in the upwelling flow with and without the cape. The observed mixedness is much smaller than 0.25, since mixing occurs only in a small portion of the flow. The amount of mixed fluid increases monotonically with time, as it must. Greater mixing is observed in the case of cape flow due to the larger front excursions and vortex stretching described above. The sharp increase of mixing in event E_1 is due to the initial Rayleigh-Taylor instability. Event E_2 is due to the onset of the mixed-instability of the front and the event E_3 is due to the formation of the fish-hook structures.

The definition of the mixedness parameter in (6.3) is appropriate since its rate of

change is positive definite and is proportional to the scalar dissipation χ:

$$\frac{k}{2}dM/dt = \frac{k}{2}\int \bigtriangledown c \cdot \bigtriangledown c \; dV \propto \chi > 0 \tag{6.4}$$

where k is the diffusivity for density. This indicates that M is a monotonic function of time. It can also be related to the entropy.

6.5.2 Energy budgets

The reference potential energy is a direct measure of potential energy change due to irreversible diapycnal mixing (Tseng & Ferziger, 2001b; Winters *et al.*, 1995). Energy budgets thus provide another index for quantifying mixing. The reference potential energy state has the minimum potential energy that can be obtained through adiabatic redistribution of the density (Winters *et al.*, 1995). Tseng and Ferziger (2001b) developed an efficient approach for calculating the RPE through the probability density function (pdf). The approach requires significantly less computation than the standard approach, especially in three dimensions. We extend the pdf approach to the investigation of mixing in upwelling flow.

The evaluation of available potential energy (APE), which is the difference between the actual total potential energy (TPE) and the potential energy of a reference state (RPE), is important to characterize the energy budgets in the ocean. The reference state is the one with minimum potential energy that can be obtained through the adiabatic redistribution of the density (Winters *et al.*, 1995):

$$APE = TPE - RPE \tag{6.5}$$

APE represents the part of the potential energy that is available for conversion into kinetic energy during adiabatic readjustment. The total potential energy in a cylindrical domain of volume V is

$$TPE = \int_V \rho g z dV \tag{6.6}$$

where ρ is the density of the fluid and z is the vertical spatial coordinate. Note that $\rho = \rho(\mathbf{x}, t)$.

We next relate APE to the pdf. Let $\tilde{\rho}$ be the independent density variable in probability sample space, $\rho \in [\rho_m, \rho_M]$, where ρ_m and ρ_M are the minimum and maximum values of the density. The probability of density ρ in the range between $\tilde{\rho}$ and $\tilde{\rho} + d\tilde{\rho}$ is $P(\tilde{\rho})d\tilde{\rho}$. $P(\tilde{\rho})$ may be defined in terms of the volume integral of a delta function

$$P(\tilde{\rho}) \equiv \frac{1}{V}\int_V \delta(\tilde{\rho} - \rho)dV \tag{6.7}$$

Let us define $Z_r(\rho)$ to be the height of fluid of density ρ in the minimum potential energy state and let dZ_r be the thickness of the layer containing fluid of density between $\tilde{\rho}$ and $\tilde{\rho} + d\tilde{\rho}$. We use the notation $Z_r(\rho)$ in order to distinguish the pdf reference state from the spatial reference state, $Z_*(\mathbf{x})$. If we assume that all fluid layers have the same horizontal surface area A, the volume occupied by this fluid is

$$AdZ_r\Big|_\rho = VP(\tilde{\rho})d\tilde{\rho}\Big|_\rho \tag{6.8}$$

If the domain is not cylindrical, the horizontal section A is function of the vertical coordinate. Note that $\tilde{\rho}$ is a dummy (independent) variable in probability space. The reference state profile $Z_r(\rho)$ can be obtained by integrating (6.8) over $\tilde{\rho}$:

$$Z_r(\rho) = H\int_\rho^{\rho_M} P(\tilde{\rho})d\tilde{\rho} \tag{6.9}$$

where $H = V/A$ is the height of the domain. The RPE can be written as

$$RPE = gA\int_0^H \rho Z_r(\rho)dZ_r \tag{6.10}$$

We can express the reference density profile as a function of the reference coordinate Z_r, *i.e.* $\rho(Z_r)$. The reference potential energy then becomes

$$RPE = gA\int_0^H \rho(Z_r)Z_r dZ_r \tag{6.11}$$

The calculation of the APE thus consists of the following steps. The density field is scanned and the fluid in each control volume is put into a bin. At the end of the scan, the normalized number of control volumes in each bin gives the pdf. Equation (6.9) is then used to compute $Z_r(\rho)$. Finally, Equation (6.10) gives the RPE. As the TPE can be computed during the scan, we have enough information to compute the APE. This process is much more efficient than the sorting process used by (Winters *et al.*, 1995), especially in two and three dimensions. It is easily applied to field or laboratory data.

The extension of the pdf approach to an arbitrary domain with complex geometry is straightforward. $Z_r(\rho)$ can be obtained directly from

$$\int_0^{Z_r(\rho)} A(z)dz = V \int_\rho^{\rho_M} P(\tilde{\rho})d\tilde{\rho} \tag{6.12}$$

where $A(z)$ is the horizontal section area instead of constant section area A.

In order to ensure accuracy in calculating the RPE, we employed an adaptive mesh in probability sample space, which allows for the possibility of delta functions in the initial density pdf *i.e.* large amounts of fluid near the maximum and minimum densities (Figure 6.14(a)). Specifically, we use a Chebyshev transformation for discretizing the sample space instead of a uniform grid when the program detects a steep density gradient near the upper or lower bound of the probability space. When the probability is highly concentrated near ρ_M, the mesh near the boundary is chosen such that $x_j = dx\ cos(\theta_j),\ \theta_j = 0, ..., \frac{\pi}{2}$, and dx is the uniform mesh used in the other regions. Since it gives a finer grid near the boundaries, the Chebyshev transformation is a good choice for discretizing the pdf. More detailed discussions and numerical examples can be found in Tseng and Ferziger (2001b).

The evolution of the energy budgets in the cases with and without the cape is shown in Figure 6.15. Both RPE and TPE are slightly larger in the simulation with coastal perturbation. The evolution of the RPE and TPE in the two cases are quite similar. Figure 6.16 shows the instantaneous rate of change of RPE and TPE. There are three peaks, corresponding to the three mixing events in Figure 6.13. The peak of the TPE growth rate at event E_3 is less than that at events E_1 and E_2 because the fish-hook generation process is more localized than the others. The increased

irreversible mixing at the later stages of evolution mainly results from the increased interfacial area between the fluids of different density.

APE is the portion of potential energy available for conversion to kinetic energy. The cape case generates significant potential energy and thus greater global stirring due to the instability (Figure 6.15). This is as expected. The APE is primarily located at the upwelling front and increases as the front migrates. Figure 6.17 shows the instantaneous rate of the increase of the APE. The transfer between kinetic energy and available potential energy is significant when the instability occurs, implying that most of the energy involved in the upwelling process is stored as APE. Slightly greater stirring occurs in the simulation with the cape.

6.6 Summary

The aim of this chapter was to understand the formation of the cyclonic/anti-cyclonic eddies and the effects of coastal perturbation on the features of coastal upwelling. To accomplish this, we performed large eddy simulations of laboratory experiments with and without a small cape on the boundary. The upwelled front modification is explained in detail. The three-dimensional visualizations help one understand the dynamics of coherent structures. The animation shows the generation of large-scale eddies by B-B instability. The existence of such structures explains the three-dimensional evolution of the B-B instability. The vertical vorticity is quasi-two dimensional. The azimuthal vorticity is more complicated and is fully three dimensional. The other animation concerns a flow past a cape. Use of various views helped to track the creation of secondary vortices.

The simulation suggests the waves on surface front resulting from mixed B-B instability are modified by the cape and the front excursions become more irregular. The results identify several important features observed in the laboratory and the ocean. The large fish-hook structures observed in the upwelling experiments are predicted by the numerical model. They are generated by the pumping action of two pairs of counter-rotating vortices. They are responsible for both horizontal and vertical mixing.

The coastal perturbation inhibits the development of these structures and instead produces many thin filaments extending offshore and downstream of the cape. The primary front is the most energetic region of the flow. The front is more irregular and mixing is enhanced by the presence of a cape. Strong vortex stretching is observed as a result of the acceleration around the cape. Continued vortex stretching results in vortex tearing. The large scales propagate in the downwind direction and are not phase-locked by the cape. A steep increase in the amount of mixed fluid is caused by the Rayleigh-Taylor instability, mixed baroclinic-barotropic instability and the fish-hook structures. This is shown by the mixedness parameter and energy budgets. The potential energy evolution indicates increased stirring as these instabilities occur. The simulation shows more available potential energy in mixed instability. The result agrees well with the energy spectrum analysis (Tadepalli, 1997). Interestingly, a small cape in the simulation increases the APE significantly, which implies more stirring, but does not change the RPE greatly. This is not surprising and results from the global property of reference potential energy. We believe that locally stronger stirring near the frontal modification enhances irreversible mixing near the coastal boundary.

Table 6.1: Parameters of the simulations (Narimousa & Maxworthy, 1991)

Tank Rotation $\Omega(s^{-1})$	2.27
Lid Rotation $\Delta\Omega(s^{-1})$	0.185
Total Depth H (m)	0.20
Density Diff. $\Delta\rho(kg/m^3)$	18
Tank Radius $R_0(m)$	0.45
Slope	0.27
Reynolds number Re	2995
Schmidt number Sc	723

Table 6.2: Parameters of the cape geometry

α	$D_c(m)$	θ_0	$R_c(m)$	$R_1(m)$
0.08	2.8E-04	45°	4.5E-2	4.5E-1

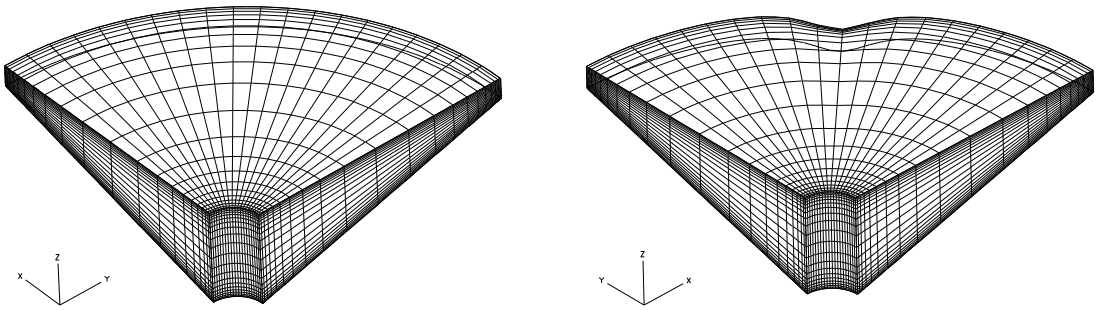

(a) (b)

Figure 6.1: (a) Grid for numerical simulation of upwelling flow. (b) The grid for numerical simulation with a cape (Every fourth grid is shown).

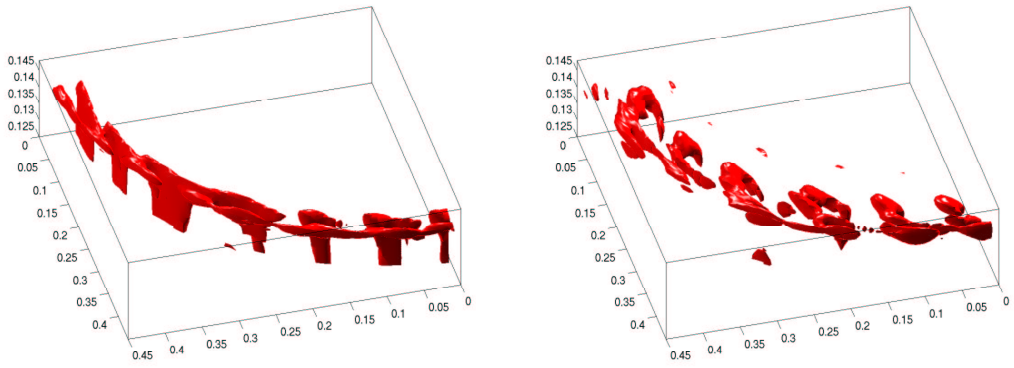

(a) (b)

Figure 6.2: Azimuthal vorticity in the neighborhood of the primary front. The $\omega_\theta = 0.8U_p/D$ isosurface is shown at (a) $t = 1.12t_s$ (b) $t = 1.34t_s$.

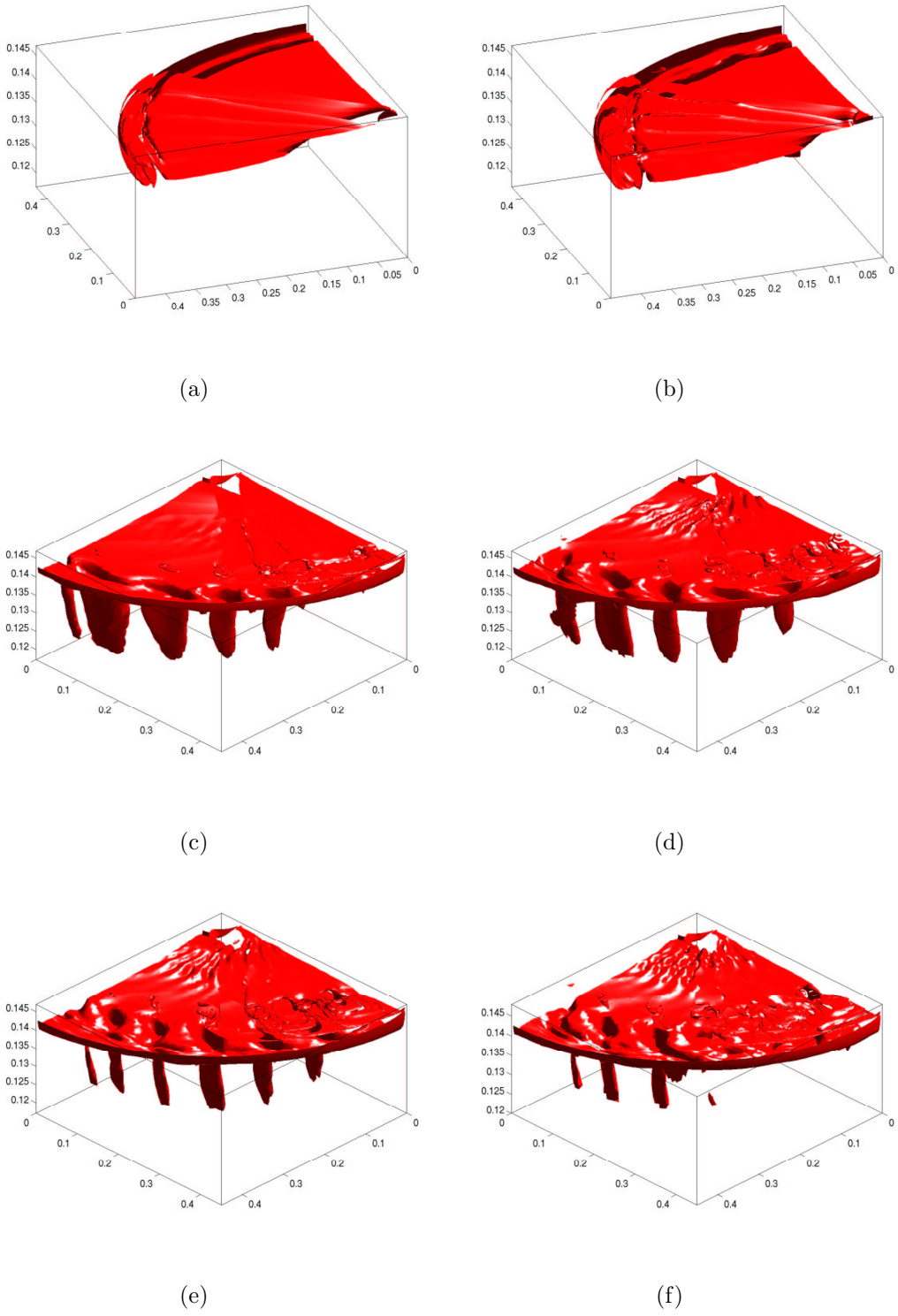

Figure 6.3: Vertical vorticity in the neighborhood of the primary front. The $\omega_z = 1$ isosurface is shown at (a) $t = 0.94t_s$ (b) $t = 1.02t_s$ (c) $t = 1.14t_s$ (d) $t = 1.32t_s$ (e) $t = 1.50t_s$ (f) $t = 1.68t_s$.

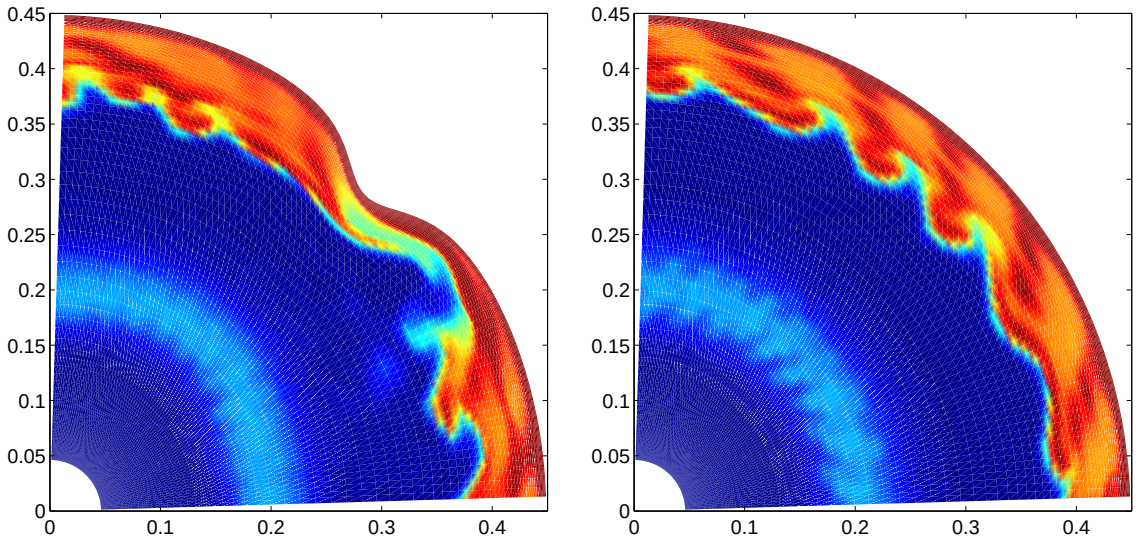

Figure 6.4: Density field in the neighborhood of the primary front with (a) and without (b) the coastline perturbation at $t = 1.12t_s$ and $z = 0.93h$.

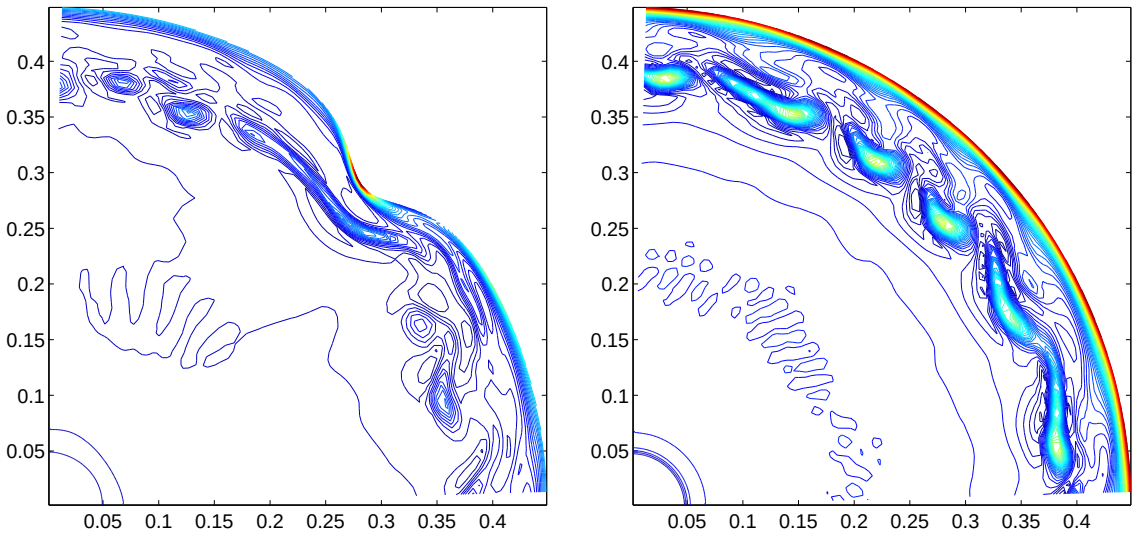

(a) (b)

Figure 6.5: Vertical vorticity in the neighborhood of the primary front with (a) and without (b) the coastline perturbation at $t = 1.12t_s$ and $z = 0.93h$.

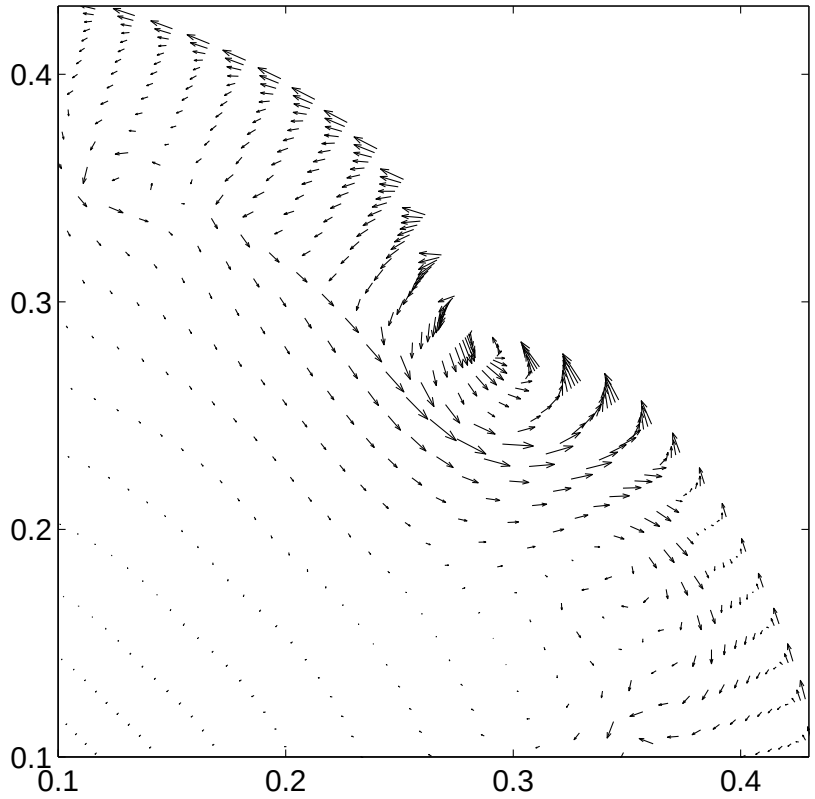

Figure 6.6: Horizontal velocity vectors near the perturbated coastline at $t = t_s$ and $z = 0.93h$ (Every second grid is shown and the reference frame is traveling with the frontal waves).

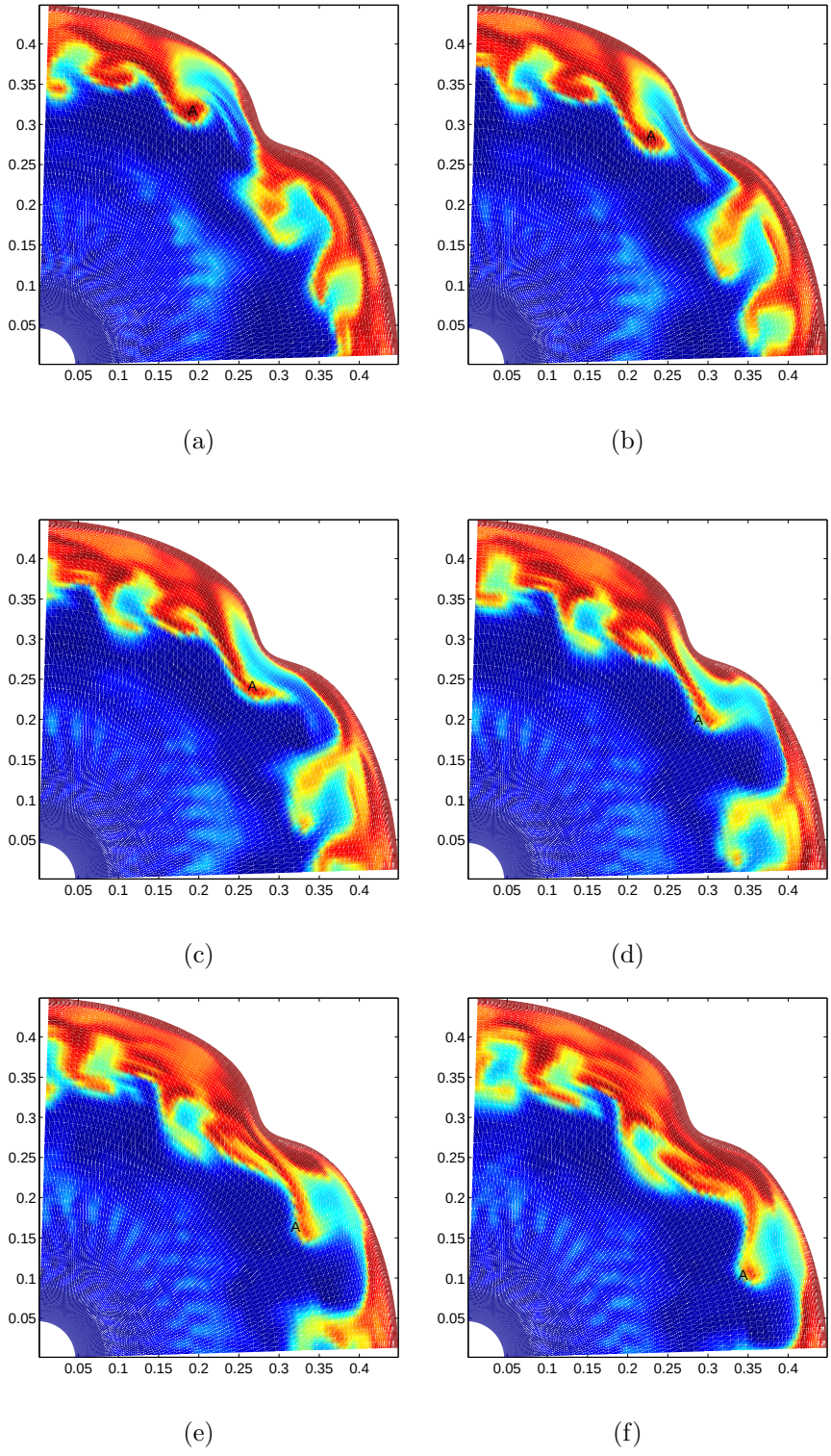

Figure 6.7: Density field with coastal perturbation in the neighborhood of the primary front at (a) $t = 1.38t_s$, (b) $t = 1.41t_s$, (c) $t = 1.44t_s$, (d) $t = 1.47t_s$, (e) $t = 1.51t_s$, (f) $t = 1.54t_s$ at $z = 0.93h$.

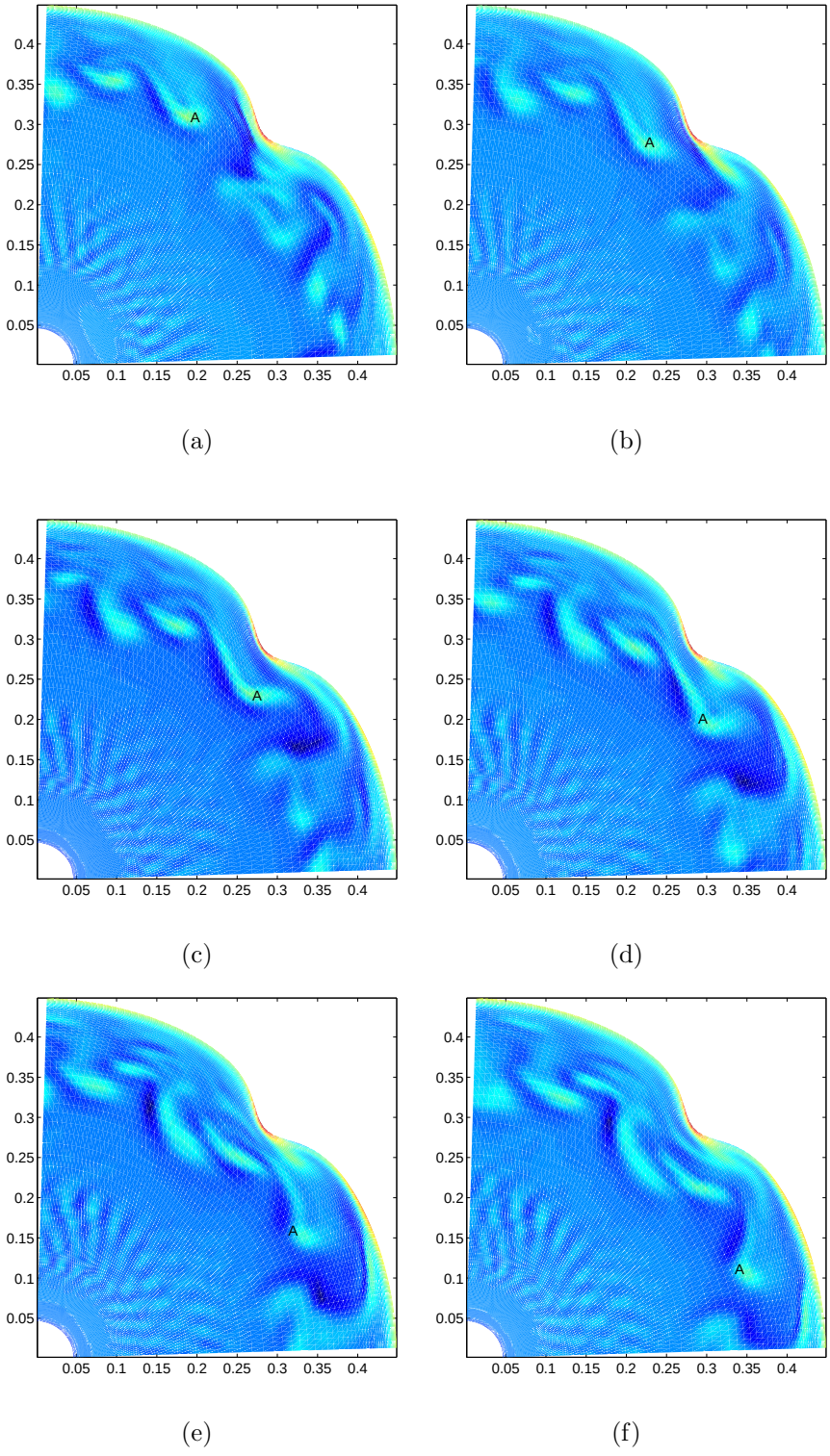

Figure 6.8: Vertical vorticity with coastal perturbation in the neighborhood of the primary front. (a) $t = 1.38t_s$, (b) $t = 1.41t_s$, (c) $t = 1.44t_s$, (d) $t = 1.47t_s$, (e) $t = 1.51t_s$, (f) $t = 1.54t_s$ at $z = 0.93h$.

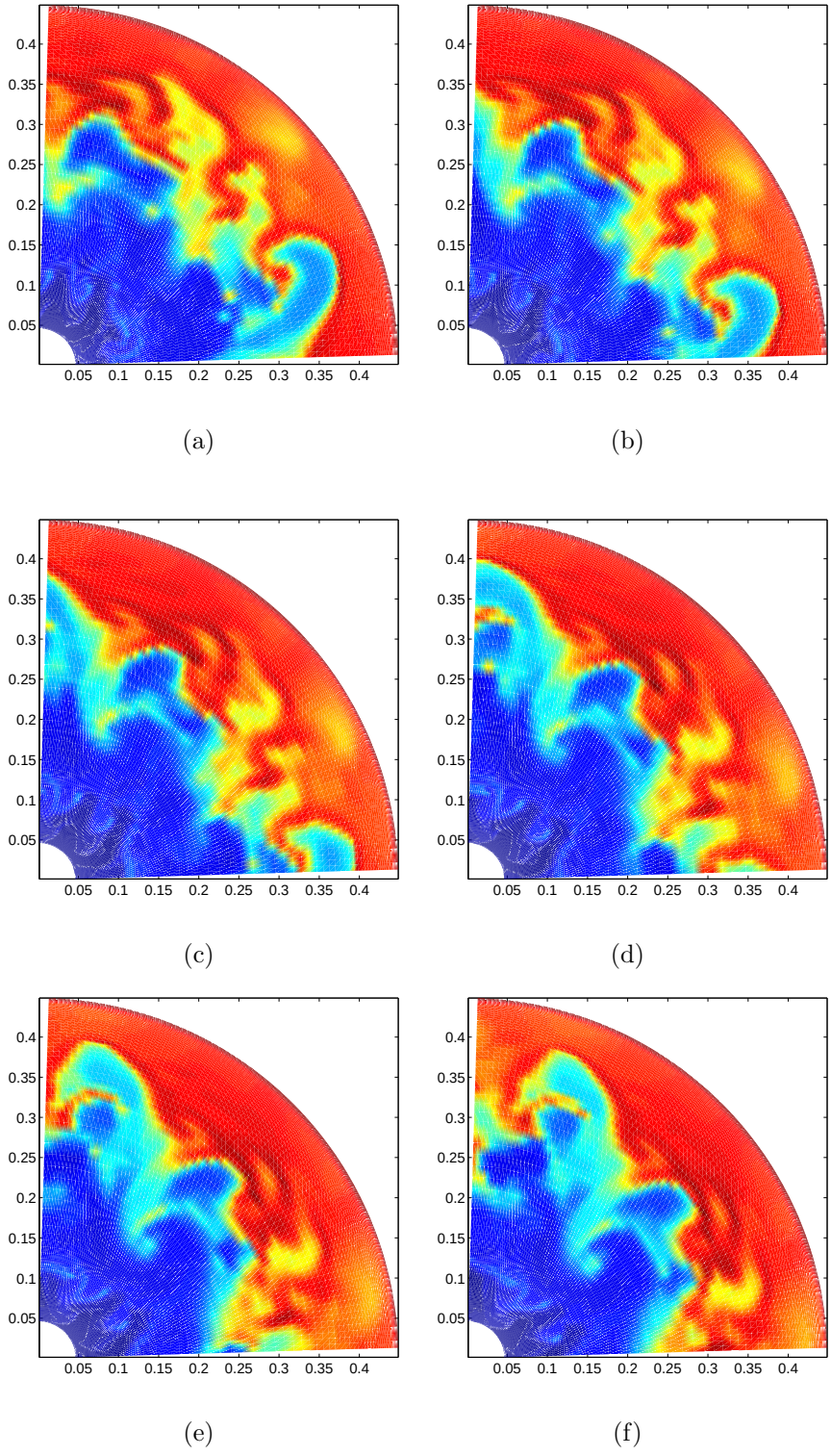

Figure 6.9: Density field at $z = 0.93h$, $t = 3.67t_s$ (a), $3.70t_s$ (b), $3.73t_s$ (c), $3.77t_s$ (d), $3.80t_s$ (e), $3.83t_s$ (f).

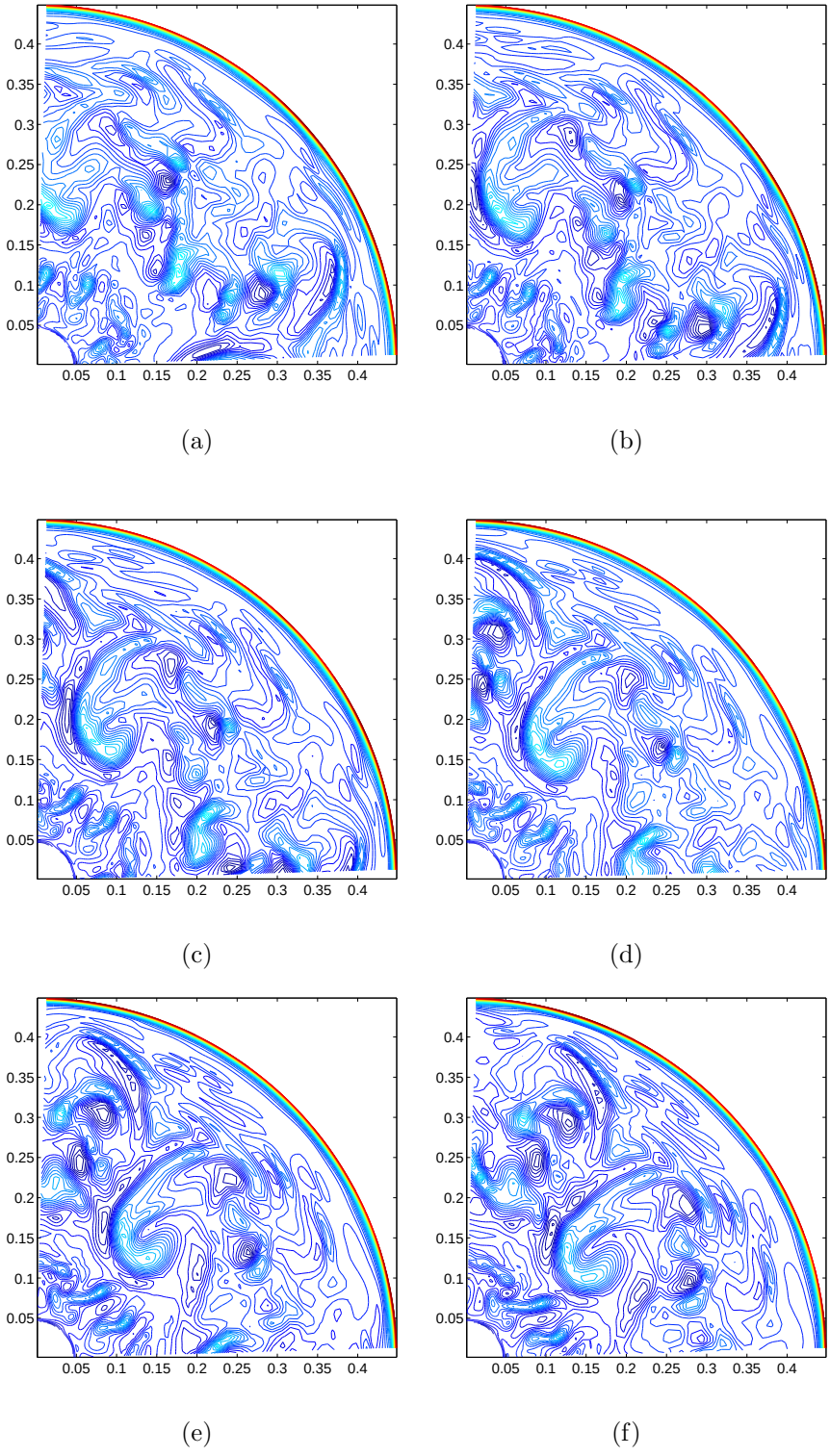

Figure 6.10: Relative vorticity field at $z = 0.93h$, $t = 3.67t_s$ (a), $3.70t_s$ (b), $3.73t_s$ (c), $3.77t_s$ (d), $3.80t_s$ (e), $3.83t_s$ (f). Dark lines indicate negative relative vertical vorticity (clockwise).

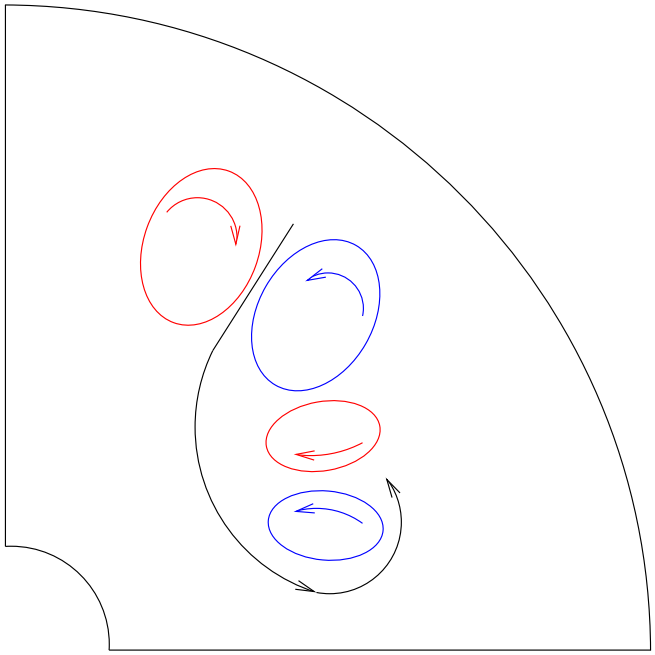

Figure 6.11: The figure shows the possible mechanism of formation of the fish-hook structures.

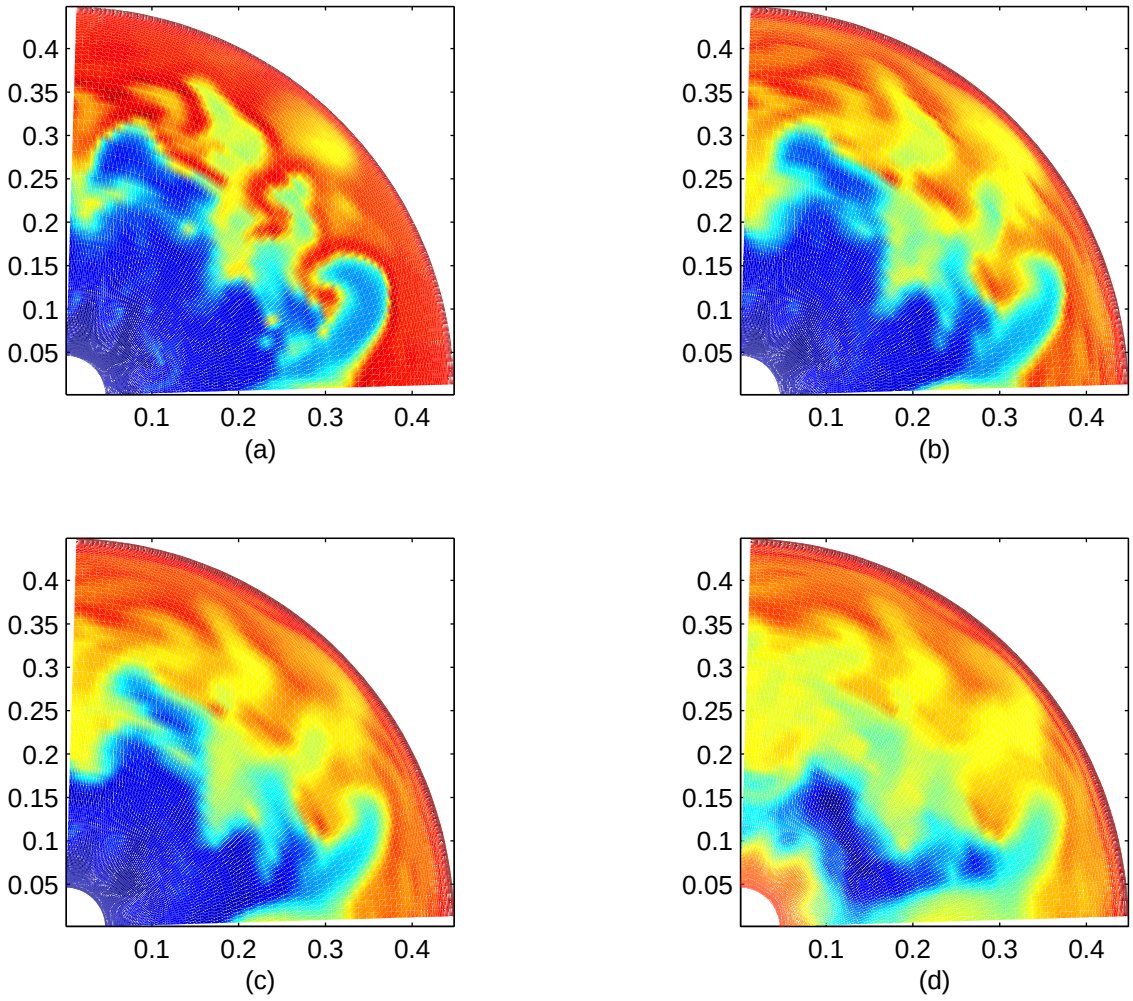

Figure 6.12: Horizontal sections of the scalar field at $t = 3.9t_s$ indicating the fish-hooks for $z = (a)0.93h$, (b)$0.86h$, (c)$0.72h$, (d)$0.50h$ respectively.

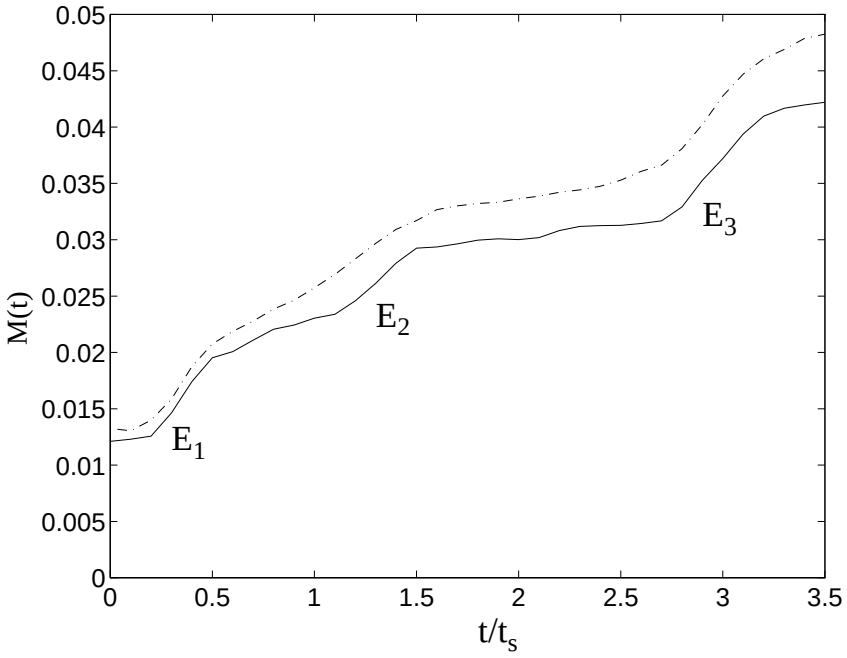

Figure 6.13: Mixedness parameter for upwelling flow with $(-\cdot)$ and without coastline $(--)$ perturbation.

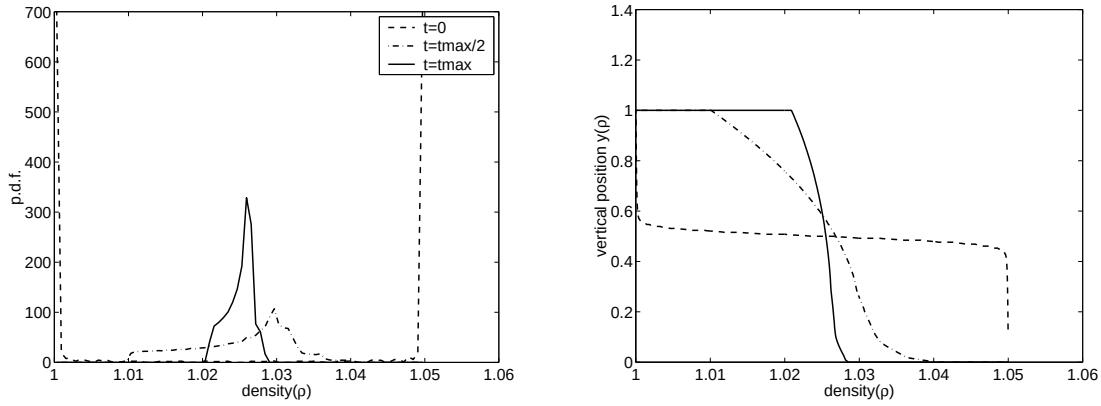

(a) (b)

Figure 6.14: (a) Typical pdf of density at the initial, intermediate, and final states of lid-driven cavity flow. (b) The reference state $y(\rho)$ at the initial $(--)$, intermediate $(-\cdot)$, and final states $(-)$.

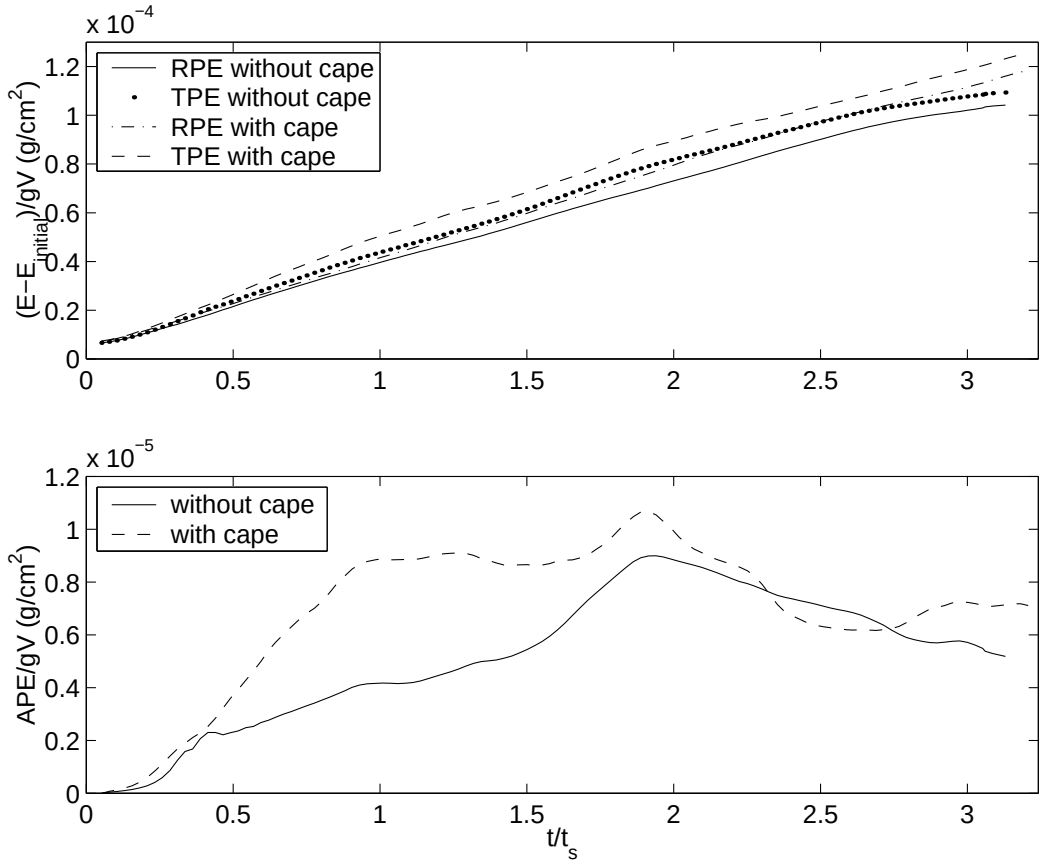

Figure 6.15: (a) The evolution of RPE and TPE. The initial RPE has been subtracted. (b) The evolution of APE.

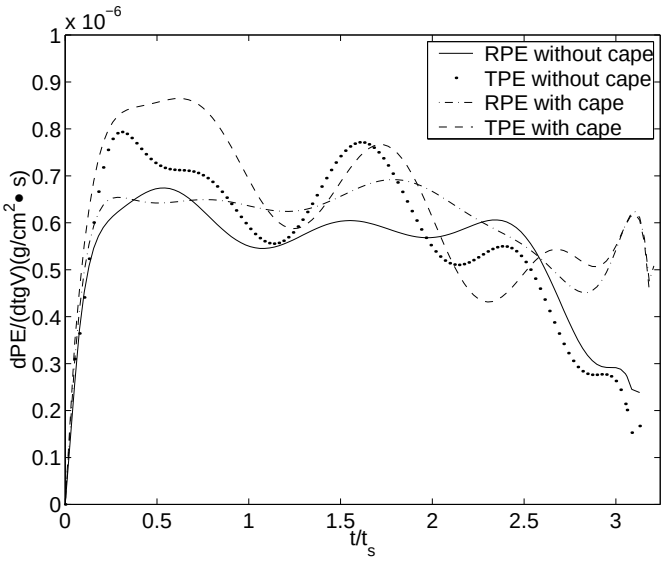

Figure 6.16: The instantaneous creation rate of RPE and TPE (with $(-\cdot)$ and without coastline $(-)$ perturbation).

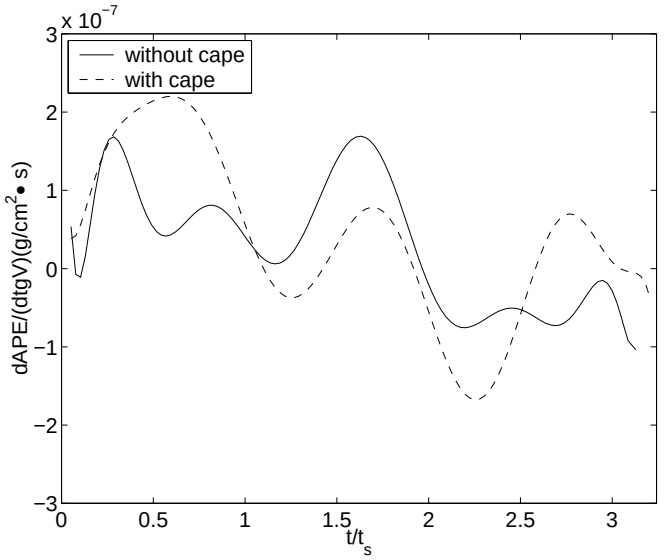

Figure 6.17: The instantaneous rate of APE without $(-)$ and with coastline $(--)$ perturbation).

Chapter 7

High Resolution Numerical Simulation of the Monterey Bay Region

7.1 Introduction

Ocean circulation off the west coast of the United States is driven by a variety of forces. One of the most important of these is the seasonally varying wind stress. The response of the coastal ocean to the strong equatorward winds during the summer produces a net offshore transport in the surface Ekman layer. Winds become predominantly upwelling favorable after the spring transition, and the upwelling regime persists through summer and early fall before returning to winter conditions after a fall transition (Paduan & Rosenfeld, 1996). In the previous chapter, we investigated the formation of the eddies subject to the surface wind forcing in a laboratory upwelling flow and the effects of simplified coastal geometry. In this chapter, we study the regional flow in the vicinity of Monterey Bay using realistic surface forcing and coastal topography. This region is important due to the abundance of marine life and interesting due to the complex geometry. The regional circulation is part of the California Current System.

While many experimental studies have examined the flow in the vicinity of Monterey Bay (see Chapter 1), there are only a few numerical studies focusing on the regional circulation. The Princeton Ocean Model (POM) developed by Blumberg and Mellor (1987) is widely used for studying the coastal ocean, and, to the best of our knowledge, is the only model that has been used to simulate this region until now (Shulman *et al.*, 2002; Ly & Luong, 1999; Lewis *et al.*, 1998; Petruncio, 1996; Daily, 1995). POM is a three-dimensional model that computes the time evolution of sea surface elevation, currents, salinity and temperature. The model uses curvilinear orthogonal coordinates in the horizontal direction and a σ-coordinate in the vertical direction. Unfortunately, there are problems with the σ-coordinate system over relatively steep bathymetry with realistic temperature and salinity fields (Allen *et al.*, 2003; Lewis *et al.*, 1998; Haney, 1991).

The modeling studies have mostly used simplified dynamics, domains, and forcing, with coarse spatial resolution or/and short integration times. Shulman *et al.* (2002) developed a high resolution, data assimilating POM of Monterey Bay used in the Innovative Coastal-Ocean Observing Network (ICON). Their simulation was used to hindcast the regional circulation of Monterey Bay and employed realistic wind forcing and surface conditions. The model adopted a data assimilation scheme to improve both the correlation between the ICON model and the observed currents and the predicted location and intensity of upwelling events. However, recent studies show that hydrostatic, σ-coordinate models give very poor results when baroclinic modes dominate the flow over a steep slope in the nearshore area, in other words, a coastal region with a submarine canyon or shelf (Allen *et al.*, 2003). Allen *et al.* (2003) studied upwelling flow over a simplified submarine canyon by running laboratory experiments and comparing the results with a numerical model. The results do not compare well due to non-hydrostatic effects in the homogeneous cases and an error in vertical advection in the stratified cases. The vertical advection error had not been identified before and mainly results from the use of terrain-following coordinates in the model. The hydrostatic, σ-coordinate type model could make the simulation worse in the simulation of coastal flow subject to realistic bathymetry.

7.1.1 Objectives

In this chapter, we produce a high-resolution numerical model of a coastal area in which the dynamics are determined by the complex geometry of a coastline, steep bathymetry, and the influence of the water masses that constitute the CCS. Our goal is to simulate the regional-scale ocean response with realistic dynamics (annual cycle), forcing, and domain. In particular, we focus on non-hydrostatic effects (by comparing the results of hydrostatic and non-hydrostatic models) and the role of complex geometry, i.e. the bay and submarine canyon, on the nearshore circulation. To the best of our knowledge, the current study is the first to simulate the regional circulation in the vicinity of Monterey Bay using a non-hydrostatic model.

7.2 Monterey Bay area regional model (MBARM)

In order to study the regional circulation in the vicinity of Monterey Bay while avoiding numerical errors introduced by the σ-coordinate and non-hydrostatic effects, we used the non-hydrostatic, z-level, mixed Arakawa A and C grid, fourth-order accurate Dietrich/Center for Air-Sea Technology (DieCAST) ocean model, which provides high computational accuracy and low numerical dissipation and dispersion. The Monterey Bay area regional model (MBARM) is one-way coupled to a larger scale California current system DieCAST model and uses the immersed boundary method to represent the coastal geometry and bathymetry.

7.2.1 Model description

The model uses a blend of collocated and staggered grids structures (Arakawa A and C grids). The Coriolis terms are evaluated on the 'a' grid and thus have no spatial interpolation error, which is a significant advantage for a dominant term (Dietrich, 1997). The governing equations and the numerical procedures are given in Appendix C. Fourth-order central differencing is used in the control volume approximation to compute all advection and horizontal pressure gradient terms, except

adjacent to boundaries where second-order accuracy is used. Sanderson and Brassington (1998a) presented a detailed analysis of the accuracy of the DieCAST model and studied the underlying numerical scheme. Sanderson (1998) further discussed the rationale for using higher resolution and higher-order numerics to achieve numerical accuracy. He used a scaling analysis and numerical examples to explore the gains in accuracy achieved by grid refinement and increased order of differencing operators. The most computationally efficient strategy for achieving accuracy required fourth-order accurate differencing schemes in a three-dimensional unsteady flow. His analysis demonstrated that there was no advantage in going beyond fifth-order.

All control volumes are collocated (e.g. momentum, energy, salinity and the incompressibility approximation to mass conservation are all applied on the same control volume grid). Note that most ocean models are only second order accurate, even though they may use higher order interpolation schemes to evaluate the control volume flux. DieCAST, instead of using the mid-point rule, uses volume integration to evaluate the mass flux to achieve fourth-order accuracy overall. The approach can be derived by integrating the conservative form of the continuum equation over specified control volumes (Appendix D).

The control volume equations for momentum, energy and salinity involve fluxes across the control volume boundaries. The equations for all quantities to which conservation laws are applied are solved on the same grid and gives smaller numerical dispersion (Dietrich, 1997), and has other advantages compared to staggered grid approaches. Accurate, low dissipation numerics are required in order to simulate the coastal eddies that dominate the circulation in Monterey Bay. Appendix E details the numerical procedure of the non-hydrostatic modification of the DieCAST model (Dietrich & Lin, 2002; Dietrich, 1997). The non-hydrostatic model has been used to investigate the convective adjustment problem in the ocean which is commonly parameterized through vertical mixing (Dietrich & Lin, 2002).

The model uses a rigid-lid approximation. At the regional ocean scale, the 'slow modes' (low frequency, long time scale motion) dominate the ocean circulation. Use of a rigid lid excludes the 'fast mode' associated with barotropic free surface waves. Free-surface 'fast modes' lead to very little net material displacement over time scales

long compared to their period; indeed, even on a short time scale, the material displacement is quite small. For the slow modes that dominate the ocean circulation, the surface elevation field may be derived from the model-determined sea-surface pressure at the rigid lid. The surface height signal of the slow modes is almost identical to that inferred from the pressure against the rigid lid. The rigid-lid approximation does not affect internal gravity wave speeds. Thus, it does not affect geostrophic adjustment of the baroclinic mode that dominates the general circulation. The rigid-lid approximation also simplifies the treatment of open boundaries because it greatly reduces the range of frequencies that must be addressed.

The Poisson equation is solved by an efficient error vector propagation (EVP) elliptic solver (Roache, 1995). Density is determined from a nonlinear equation of state relating density to potential temperature, salinity and pressure. We present the MBARM results with realistic coastal bathymetry. The bathymetry filters used in some models would result in underprediction of the intensity of the coastal current and eddies. This in turn would result in weakened coastal eddies as the CCS interacts with the filtered bathymetry and smoothed coastal abutments.

7.2.2 Model setup

The domain of MBARM extends from 36.1° to 37.4°N and from the California coast out to 122.9°W (Figure 7.1); the horizontal grid size is uniformly 1/72° ($\approx 1.5\ km$) for the medium grid (Figure 7.1), and 1/108° ($\approx 1\ km$) for the fine grid. The vertical grid has 28 levels. The surface buoyancy flux is computed by nudging both the temperature and the salinity toward Levitus' monthly climatology (Levitus, 1982). This is equivalent to adding heat and/or freshwater to the top layer. The wind stress is from Hellerman and Rosenstein's monthly climatology (Hellerman & Rosenstein, 1983). The wind stress is shown in Figure 7.2. The southeast wind field intensifies during spring and summer and weakens during fall and winter. Vertical viscosity and diffusivity are the sum of the terms which parameterize laminar diffusivity and vertical Reynolds stresses as proposed by Pacanowski and Philander (1981). The horizontal eddy viscosity and diffusivity are 20 m^2/s. This gives a damping time of

nearly a month for disturbances of size 10 km.

Bathymetry is unfiltered USGS 250 m resolution topography (Wong & Eittreim, 2001). The bottom topography and the coastal geometry are adequately represented by the immersed boundary module. The sea floor is insulated and partial-slip as parameterized by a bottom drag coefficient of 0.002. Significant momentum exchange with the California current occurs through the open boundary; this will be discussed in the next section.

7.2.3 Open boundary treatment

At present, one of the greatest limitations in regional modeling is the open boundary conditions (OBCs). The currents in the vicinity of Monterey Bay and the offshore CC have distinctive spatial scales, $O(1-10)$ km vs. $O(100-1000)$ km. In order to focus on the regional circulation without requiring extremely intense computational resources, we have to couple the region to the larger scale through an open boundary. The open boundary should allow perturbations generated inside the computational domain to leave it without deterioration of the inner model solution and allow physically important external information to advect inward.

The rigid-lid approximation simplifies the treatment of open boundaries by greatly reducing the range of frequencies that must be addressed. The Orlanski-like radiative approximation is excellent when dealing with a single dominant phase speed (Orlanski, 1976). The Orlanski radiation condition solves an one-dimensional wave equation at the boundary, thus allowing waves to propagate out of the domain, but it is not accurate when a wide range of phase speeds must be addressed. A simple upwind open boundary treatment works nicely in some models, including DieCAST (Haney *et al.*, 2001; Dietrich, 1997).

The model is one-way coupled from a larger scale CCS model (Haney *et al.*, 2001). The CCS model domain is shown in Figure 7.3 and has resolution $1/12^{\circ}$. The same climatological forcing is used in the CCS model. The dotted line shows the uniform grid (every sixth grid is shown). The MBARM is initialized by interpolation of the coarse CCS model results after two years of simulation. A schematic diagram of the

grid arrangement for the one-way nesting is shown in Figure 7.4. All open boundary conditions are based on boundary fluxes. A pure upwind advective scheme is used at the three lateral open boundaries (north, south, and west) for all variables:

$$\frac{\partial \phi}{\partial t} + U_n \frac{\partial \phi}{\partial n} = 0 \tag{7.1}$$

where

$$\frac{\partial \phi}{\partial n} = \begin{cases} (\phi - \phi_o)/\Delta x_n & U_n \geq 0 \\ (\phi_i - \phi)/\Delta x_n & U_n < 0 \end{cases} \tag{7.2}$$

and U_n is the normal velocity on the open boundary. ϕ represents any of the three velocity components, temperature or salinity at the boundary. ϕ_o is the variable on the open boundary obtained from the CCS model and ϕ_i is the variable at one grid point inside the open boundary, Δx_n is the grid spacing in the direction normal to the boundary. Thus, large scale data are advected inward at an inflow boundary and the interior data is advected outward at an outflow boundary. A boundary flow adjustment is made at every time step to insure that there is no net inflow into the modeled region.

It is argued that the primitive equations are ill-posed when an inappropriate open boundary condition is used. If the number of boundary conditions is not appropriately specified, the solution of the primitive equation will lead to the exponential growth of energy and numerical instability (Oliger & Sundstrom, 1978). According to Oliger and Sundstrom (1978) and Mahadevan *et al.* (1996), the numerical problem is well-posed if the velocity vector, salinity, and temperature are specified at the inflow boundary condition and the normal velocity is specified at the outflow boundary. The above open boundary treatment satisfies these requirements and is well-posed. Palma and Matano (2000) investigated the performance of combinations of OBCs using POM. They found that the best overall performance of OBCs was a flow relaxation scheme for barotropic modes, radiation condition for baroclinic modes, and combined advection and relaxation for the scalar field. In fact, the current scheme corresponds to a simplified version of the scheme suggested by Palma and Matano (2000).

7.3 Simulation Results

7.3.1 Grid sensitivity study

We performed a grid sensitivity study to assess the effects of grid resolution on the simulation results. A finer grid $1/108^\circ$ ($1km$) resolution result was used for the first ten days. The number of vertical layers was not changed in order to match the lateral open boundary data from the larger scale simulation. Changing the number of vertical layers requires vertical interpolation at the boundary and this may affect the performance of our open boundary treatment. Vertical refinement has to ensure that the variables in the model are at exactly the same physical locations as those in the larger scale model. The surface velocity fields, temperature and salinity for both grids of day 10 are shown in Figure 7.5.

The medium and finer resolution simulations exhibit very similar patterns offshore, including the region close to where the lateral OBCs are applied, but the small-scale coastal eddies and jets differ nearshore. There are more of them in the higher resolution case. These facts show that the OBCs are adequately imposed and that offshore eddies can be fully resolved using the medium $1/72^\circ$ resolution. All of the small-scale features in the finer resolution simulation occur near the coastline and appear to have short time scales. They appear to be result of a rapidly growing, surface-trapped, short-wavelength frontal mode, similar to the ageostrophic, unstable mode described in previous studies (Marchesiello *et al.*, 2003; Barth, 1994; McCreary *et al.*, 1991). The occurrence of similar weak absolute vorticity is also seen just upstream of the separation point of the Black Sea Rim Current (Staneva *et al.*, 2001) where fine scale negative vorticity elements peel off and merge into the very strong Sevastopol wake recirculation eddy. The weak vorticity means that there is little local vortex stretching, resulting in extremely rapid release of available potential energy associated with the steep shelfbreak Rim Current front (Staneva *et al.*, 2001).

The eddy variability in these simulations is apparently due to instabilities of the coastal currents through shear and baroclinic instabilities close to the coast. These eddies and jets may move further offshore and influence the rest of the domain. Marchesiello *et al.* (2003) observed this small-scale variability in their simulation,

and they attributed these characteristics to upwelling fronts and filament structures where the anticyclonic shear is comparable to Coriolis parameter f. They suggested the possibility of a transition regime where frontal instabilities start to impact coastal currents and offshore mesoscale eddies.

The present results suggest further refinement of the grid in the coastal region is necessary in order to fully resolve the complex coastal geometry where the non-linear effects play important roles. However, refining the grid with realistic coastal geometry may introduce more small-scale variability unless the rough boundary layer is fully resolved (Baggett *et al.*, 1997). This is impractical at present.

7.3.2 General description

Using Levitus' surface climatological forcing (temperature and salinity), the simulation reproduces many important features of the observed annual cycle of the CCS including the strengthening of the equatorward jet in spring and the weakening of the jet in autumn and winter. Coastal eddies occur primarily near some major headlands, especially Point Ano Nuevo, Pacific Grove and Point Sur. To examine the general circulation in the vicinity of Monterey Bay, we focus on the annual mean flow and seasonal variability.

Annual mean flow

The mean velocity fields for a simulation year at different depths (10.1, 50, 100, 300, 400, 700 m) are shown in Figure 7.6. As mentioned in the introduction, the major features in the Monterey Bay area are the shallow, equatorward, broad California Current and two narrow poleward boundary currents (California Undercurrent and Inshore Current) along the coast. These flows are seen in Figure 7.6. The surface flow is affected by surface wind forcing. Vertical shear layers appear at moderate depth ($50 - 200$ m). The mean velocity pattern clearly delineates the extent of poleward flow associated with the inshore currents.

Collins *et al.* (2000) estimated the upper 1000 m depth-averaged mean velocity

based on 19 cruises conducted from April 1988 to April 1991. They reported a west-northwestward ($290°T - 310°T$) flow with a mean speed of $3.7 - 5.3$ cm/s at four inshore stations C1-C4 (at latitude $36.3°N$, $33 - 65$ km away from the shore). We estimate the one-year depth-averaged annual mean flow along the line connecting the four inshore stations C1-C4 (Collins *et al.*, 2000). The comparison is shown in Table 7.1. The mean magnitude (4.7 cm/s) is slightly higher than that predicted in Shulman et al. (2002) using a hydrostatic model with data assimilation. The annual mean flow in the current study is in good agreement with observation without data assimilation. The result shows that the current one-way coupling at lateral boundary and the surface forcing are appropriate and data assimilation is not required. More detailed comparison with observation is provided in the following section.

Seasonal variability

Seasonal mean velocity fields at several depths (10.1, 50, 100, 300, 400, 700 m) are shown in Figures 7.7 to 7.10 for a simulation year. The along-shore component of the wind stress has been shown to be a key ingredient for generating realistic vertical and horizontal structures and the surface equatorward and subsurface poleward currents. These currents are baroclinically and barotropically unstable, resulting in the generation of meanders, filaments and eddies.

In the spring, defined as February to April (Figure 7.7), the equatorward flow strengthens and dominates the flow from a depth of 100 m to the surface. This equatorward flow is upwelling-favorable. A weak cyclonic eddy is observed within Monterey Bay, and is associated with the equatorward flow past a coastal bay. There is also a large-scale, anti-cyclonic eddy around 50 km from the coast that extends down to depth 100 m where the eddy is stretched significantly by the coastal bathymetry (Figure 7.7(c)). The subsurface northward flow exists below depth 300 m during spring which is consistent with the year round northward flow associated with the CU. The transition from CC to CU occurs around depth $200-500$ m and the strongest CU occurs at depth 300 m, which is consistent with previous observations.

In summer (Figure 7.8), the southward flow in the upper ocean strengthens and tends to move offshore, forming the filaments observed in the satellite images. Point

Sur is the location where the offshore flow is most significant and satellite images also show that filaments occur there frequently. The current simulation shows this to be an effect of local topography on the enhancement of flow toward steep bathymetry and the steering effect of the Pacific Grove headland. The same conclusion was suggested by observations (Ramp *et al.*, 1997). We can still see the CU at depth, and the undercurrent follows the contour of coastal bathymetry closely.

Autumn is the season in which the dominant flow changes from equatorward to poleward in the upper ocean (Figure 7.9). By October upwelling favorable circulation occurs much less frequently, and near-surface flow along the central coast is under the influence of the northward flowing Davidson Current, which generally reaches its maximum speed at the surface in December (Paduan & Rosenfeld, 1996). Tisch *et al.* (1992) found poleward geostrophic flow throughout the water column in a narrow band inshore of the anticyclonic eddy in November 1988 off Point Sur. The seasonal-averaged velocity fields show that the northward flow intensifies and occurs at all depths. This northward intensified flow represents the IC and CU currents. The large-scale anti-cyclonic eddy moves far offshore. The model intensification of the CU and IC during autumn is in good agreement with observations (Collins *et al.*, 2000). A weak mean equatorward flow can be observed along the coastline near the surface (Figures 7.9 (a), (b)). It is mainly associated with the anti-cyclonic eddies generated along the coast through baroclinic instabilities and upwelling fronts.

Figure 7.10 shows the mean flow in wintertime (November to January) at several depths. The velocity fields at all levels show very similar spatial structure. The CCS is dominated by the poleward flow. A narrow banded equatorward flow can still be observed in the shallow region. The poleward currents off Point Sur usually flow toward the northwest (along-shore), while the summer equatorward currents flow toward the southwest rather than southeastward along the large-scale bathymetry. This feature of the flow is reproduced by the simulation (Figures 7.7-7.10) and can likely be attributed to the local topography, which tends to steer currents from the north offshore (Ramp *et al.*, 1997).

Surface temperature fields for different seasons (days 115-385) are shown in Figures 7.11(a)-(d). In spring, when upwelling-favorable winds are strongest, elongated

squirts of cold water form narrow filaments that extend several hundred kilometers from the coast. In Figure 7.11(b), one such filament is pulling cold upwelled seawater south and then west in the southwest corner of the domain. The coastal eddy field continues to intensify slightly for another month, but by late summer it begins to relax and propagate westward as the upwelling favorable winds diminish along the coast. The cold filaments propagate further offshore and the sea surface temperature field starts to warm up during autumn (Figure 7.11(c)). Note that the color scales are different in Figure 7.11 to accommodate each season's maximum and minimum. The instability mechanisms and vortex formation processes are investigated in Chapter 6 using numerical simulation of the laboratory experiment. Fall is a time of transition from the upwelling regime to the winter storm-dominated situation. The transition is marked by the warmest surface temperatures and marked stratification (Figure 7.11(d)).

In the annual cycle of sea surface temperature (SST), spring is the coolest time of the year. Spring and early summer are periods of upwelling. The upwelling signal is evident in the currents and the temperature in our simulation. During the late summer and early autumn there are increases in temperature, and intensification of the poleward undercurrent.

There is little correlation between the local wind variability (within a day) and the observed currents. The established currents during upwelling-favorable winds are dominated primarily by much longer period wind forcing (Ramp *et al.*, 1997). Long period wind forcing is also responsible for the generation of currents as well as for the intense and complex meander, eddy, and filament structures both in the field and our simulation.

In summary, the seasonal cycle is characterized by the formation of surface baroclinic jets in the spring of each year shortly after the onset of upwelling-favorable winds. A variety of instabilities subsequently occurs along the jet, and the entire field (jets and eddies) propagates offshore during summer and autumn. Most filaments occur in summer, forming cold and warm mushroom-like patterns at multiple scales, especially south of Monterey Bay. In fall, meanders and eddies are the dominant patterns, both inshore and offshore of CC.

7.3.3 Comparison with mooring data

We compare the model temperatures with those measured by Sea-Bird MicroCAT CTDs mounted on MBARI's M1 ($122.03°W$, $36.75°N$) and M2 ($122.39°W$, $36.70°N$) surface moorings (for location, see Figure 7.1). Since the model is forced by the average climatology at the sea surface, we do not expect the model to match the observations exactly. The observed time series of temperatures at the M1 and M2 mooring stations for various depths are presented in Figures 7.12 and 7.13, respectively. These data display an annual cycle with cold temperatures during upwelling seasons and warmer temperatures during the rest of the year, except for the anomalous 1997-1998 El Niño year.

We focus on two years of temperature data without anomalies which have extensive continuous data (Figures 7.14 and 7.15). The seasonal variation is more significant near the surface rather than at depth. The model results are shown in Figure 7.16 for the M1 and M2 mooring locations, respectively. The results repeat annually, thus showing that the annual cycle is captured in our model. The model results reproduce many of the observed trends. These include the annual variation in temperature, cooling of surface and subsurface temperatures during spring upwelling, warming water masses during summer and early autumn, and slight cooling during late autumn. The near surface temperature ($10\ m$) at M2 varies between $10 - 15°$ which is in the same range as the observations. The temperature at M1 is $1 - 2°$ lower than that at M2, which is again consistent with the measurements. The model-predicted annual variation in the upper ocean agrees with the observation well. At depth $300\ m$, the temperature varies from $7 - 9°$ at both the M1 and M2 stations. The results are consistent with the observational data, and the temperature fields at depth are not sensitive to location.

Overall, the model predictions are in reasonable agreement with observations without data assimilation. A more quantitative model-data comparison is made difficult by the existence of interannual variability in both the simulated and observed fields. The most important result of the simulation is the fact that, as in the observation, the annual cycle is evident and well reproduced in the simulation.

7.3.4 Comparison with observation results

During periods of upwelling-favorable winds (spring and summer), there is a band of cold water which flows equatorward across the mouth of Monterey Bay with typical near-surface speeds of $20-30cm/s$. Figures 7.17(a)-(d) show the surface temperature from day 109 to day 115 and show a typical spring upwelling event. The upwelling centers are found north and south of Monterey Bay near Point Ano Nuevo and Point Sur (Figure 7.17(d)). Point Ano Nuevo has been identified to be the source of cold, salty near-surface water frequently seen in the bay (Rosenfeld *et al.*, 1994). The upwelled (cold) water is advected southward across the bay and then breaks into two streams: one water mass moves offshore and the other equatorward. A warm anticyclonic feature is often found off the mouth of Monterey Bay, or just south of it (Ramp *et al.*, 1997; Paduan & Rosenfeld, 1996). This feature was also seen in advanced very high resolution radiometer (AVHRR) imagery (Figures 7.18 and 7.19). The simulation produces patterns very similar to those observed in the satellite images. A warm anticyclone is also apparent in the simulation. Meanders of the California current with anticyclonic circulation have often been reported (Breaker & Broenkow, 1994; Ramp *et al.*, 1997; Paduan & Rosenfeld, 1996).

Within the bay, a cyclonic circulation is often observed (Breaker & Broenkow, 1994). This circulation is mainly caused by the coastal geometry and is shown in the simulation (Figure 7.20(a)). The cyclonic circulation within Monterey Bay is consistent with the observed circulation (Figure 7.20(b)). HF radar-derived velocity fields during late summer 1992 and 1994 reveal a band of equatorward flow across the mouth of Monterey Bay with cyclonic circulation inside the bay and anticyclonic circulation offshore (Figure 7.21). This late summer flow pattern is similar to April-July flow patterns observed in the Monterey Bay area using AVHRR imagery and drifter measurements, and CTD data and Acoustic Doppler Current Profiler (ADCP) observations (Paduan & Rosenfeld, 1996; Rosenfeld *et al.*, 1994; Rosenfeld *et al.*, 1995). The equatorward flow across the mouth of Monterey Bay and the cyclonic circulation are seen in our simulation during springtime and are associated with the advection of upwelled water from the Ano Nuevo upwelling center (Figure 7.17).

7.3.5 Hydrostatic versus Non-Hydrostatic modeling

The growth of meanders and filaments of upwelled water has been demonstrated in many previous studies using hydrostatic models. However, it is still not clear how the non-hydrostatic mode affects the regional circulation in a coastal region with complex bathymetry and upwelling. Casulli and Stelling (1998) assessed the effects of the hydrostatic approximation in various applications. In general, the hydrostatic model is not accurate if the vertical velocity is important. The vertical momentum and the non-hydrostatic pressure component cannot be neglected when the bottom topography changes abruptly (e.g. near continental shelf edges and in deep canyons). Chao and Shaw (2002) studied coastal upwelling meanders and filaments using a non-hydrostatic model. Their idealized model does not include complex bathymetry, coastal irregularity or unsteady wind forcing. Their results show that the growth rates of meanders and filaments are enhanced by non-hydrostatic effects. Vertical acceleration due to non-hydrostatic effects enhances downwelling motion for seaward (westward) surface currents and upwelling motion for landward surface currents (Chao & Shaw, 2002). Unstable stratification could further enhance strong vertical acceleration. In order to investigate non-hydrostatic effects on Monterey Bay, we compare the results of hydrostatic and non-hydrostatic models. In the hydrostatic model, the vertical velocity is derived from the incompressibility condition.

The monthly-averaged (May, days 120-150) velocity fields at various depths are presented in Figures 7.22-7.27 for hydrostatic and non-hydrostatic models, respectively. Significant differences can be observed along the coast and inside the deep Monterey Canyon. The velocity field is averaged monthly in order to filter out shorter time scale variation. Shorter scale results are likely to show larger non-hydrostatic effects. The horizontal velocity field in non-hydrostatic model shows a significant departure from hydrostatic prediction in both upper and deep ocean. At depth 10.1 m, a net mean flow crosses the mouth of Monterey Bay and a cyclonic eddy is observed inside the bay in the non-hydrostatic model. The near surface flow patterns resemble those observed from the satellite images (Figures 7.18 and 7.19) and are more realistic since vertical acceleration is included. The mean flow directions near the southern boundary center are opposite in the hydrostatic and non-hydrostatic models. The

regional circulation is energetic and the complex nearshore topography enhances the inaccuracy of the hydrostatic approximation. In particular, significant differences are found in the water column near Monterey Canyon between latitudes $36.3°N$ and $36.9°N$ at all depths (Figures 7.22-7.29).

The instantaneous surface current and pressure fields from days 130 to 160 are shown in Figures 7.30 and 7.31 for the hydrostatic and non-hydrostatic models, respectively. We mainly focus on the surface circulation in the strong upwelling season. On day 130, only minor differences are found between the hydrostatic and non-hydrostatic models. As the upwelling favorable wind intensifies, more eddies and meanders are generated in the non-hydrostatic model and the differences between the models become significant. The enhanced instability in the non-hydrostatic model confirms the results of Chao and Shaw (2002). The strong non-hydrostatic effects result from the realistic coastal topography. Positive pressure fields are associated with anti-cyclonic eddies and the negative ones with cyclonic eddies. It is clear that vigorous mesoscale eddies exist in the simulation domain (Figures 7.31).

The comparisons of the averaged velocity fields in June (days 150-180) are shown in Figures 7.32-7.39. A cyclonic eddy is found in the non-hydrostatic model but disappears in the hydrostatic model. On the shelf, the variability on the small scales ($\approx 10\ km$) is also found. These sub-mesoscale patterns are fast growing and are concentrated in the upper water column ($< 100\ m$), as opposed to the deeper mesoscale eddies (Figures 7.36-7.37). The eddy fields at depth in the hydrostatic and non-hydrostatic models are also very different. In the hydrostatic model, a strong anti-cyclonic eddy is formed in the domain center just above the bottom topography (Figure 7.36(a) and Figure 7.37(a)). In the much deeper ocean (Figure 7.38 and Figure 7.39), significant differences are observed very close to the shore. These results show that non-hydrostatic effects are important where there are strong inclines in the topography even at depth.

The vertical velocity differences between the hydrostatic and non-hydrostatic models at various depths are shown in Figure 7.40. The difference in the vertical velocity is large along the canyon wall at all depths. These results show that sudden steep

changes in slope cause vertical accelerations which violate the hydrostatic approximation. The vertical acceleration across complex topography is not surprising. It has also been found that the bores produced by internal wave reflection at topography are poorly represented by the hydrostatic model (Rosenfeld *et al.*, 1999; Legg & Adcroft, 2003). In realistic topography, alongslope tides produce internal hydraulic jumps and solitary wave packets as they flow over corrugations. This is not well represented by hydrostatic models.

Note that the treatment of OBCs may also enhance the difference when the perturbation moves toward the open boundary. Only the normal velocity at the open boundary is specified. The shear along the open boundary may enhance the growth of the perturbation. The detailed velocity fields at depths 10.1 m and 50 m in the southwest corner of the domain are shown in Figures 7.41 and 7.42. Small scale eddies are formed and interact with the open boundaries. Note that the domains extend further west and south to includes the intermediate regions where the depth is smoothed out to match the different depths between the coupling coarse and fine grids (Figure 7.4). The western and southern boundaries are directly coupled to the CCS simulation. The intermediate regions are involved in the calculation.

To quantify the non-hydrostatic effects, we compare the non-hydrostatic and hydrostatic diagnostic terms in the momentum equation of the non-hydrostatic model. The vertical acceleration can be used as a measure to indicate the non-hydrostatic contribution to the solution. The non-hydrostatic term (NHT) includes the local vertical acceleration ($\partial w/\partial t$) and the horizontal and vertical advections. We normalize the NHT by the root mean square value of the buoyancy term $\rho' g$, so that the non-hydrostatic factor (NHF) is

$$NHF = \frac{NHT}{\rho' g} = \frac{\frac{\partial w}{\partial t} + u\frac{\partial w}{\partial x} + v\frac{\partial w}{\partial y} + w\frac{\partial w}{\partial z}}{\rho' g} \tag{7.3}$$

where $\rho' = (\rho - \overline{\rho})/\rho_0$; $\overline{\rho}$ is the horizontal mean density and ρ_0 is the background density. The normalization factor measures the size of the hydrostatic terms. Removing the horizontal mean density has no effect on the hydrostatic flow so this is a good normalization.

The monthly averaged, normalized NHF at various depths is shown in Figure 7.43 in shallow region (170 m, 250 m, 360 m, 500 m) and in Figure 7.44 in the deep canyon (1500 m, 1900 m). It is interesting to see that the NHF is nearly zero in a large portion of the simulation domain except close to the steep bathymetry (most nearshore area), which is consistent with the comparison given above. Non-hydrostatic effects are important close to the coast (nearshore region) and in the deep Monterey Canyon. Hydrostatic approximation is appropriate except the steep topography area. The maximum normalized non-hydrostatic factor is $O(10)$ but the red shading indicates the region in which the NHF is in excess of 1×10^{-2}. The ratio of the non-hydrostatic term to the hydrostatic term is on the order of $O(0.01 - 10)$ in the red region of the figures. This suggests that non-hydrostatic effects are very important in coastal ocean modeling. We suggest that the onshore difference between hydrostatic and non-hydrostatic may occur through nonlinear feedback to a larger quasi-hydrostatic scale. The steep bathymetry plays an important role on forcing the vertical acceleration beyond hydrostatic expectation. It has also been shown by Chao and Shaw (2002) that the growth rate of instability could be enhanced by the non-hydrostatic modes.

The complex geometry increases the nonlinearity and alters the meso-scale coastal circulation. There are significant differences in the regional circulation patterns between hydrostatic and non-hydrostatic models. However, this seems not to be the case with two-dimensional pure convective adjustment as shown in Dietrich and Lin (2002), where only the small-scale modes involved in convective adjustment are significantly non-hydrostatic. The large-scale modes remain unchanged, and this may be due to the two dimensionality, which may prohibit some instability mechanisms. In fact, as shown in the current non-hydrostatic simulation, the vertical velocity is very important nearshore and cannot be neglected. The increase in horizontal and vertical transport may greatly enhance the small-scale turbulent mixing near the coast. These complex and enhanced coastal transport processes cannot be interpreted using previous hydrostatic models since these effects were underestimated in hydrostatic models.

From the current results, we conclude that the hydrostatic approximation is not appropriate for dealing with nearshore regions. Complex bathymetry contributes significantly to the variability of the nearshore eddies. The comparison illustrates

that non-hydrostatic effects play important roles at the head of Monterey Canyon and influence the regional circulation in the vicinity of Monterey Bay. An idealized coastal model with a simplified canyon should be helpful to further quantify non-hydrostatic effects on coastal flows and turbulent mixing since the lateral open boundary and seasonally varying flow complicates the analysis.

7.3.6 Effect of Monterey Canyon on large scale motion

Irregularities in the coastline geometry also have been shown to be important for 'anchoring' upwelling and filaments and enhancing the growth of meanders and eddies. Historically, many people believed that the Monterey Submarine Canyon is responsible for strong upwelling of nutrient-rich water in the Monterey Bay (Gore, 1990). Until recent years, many studies showed that the source of cold, salty, near-surface upwelled water is associated with convection from north of the bay (near Point Ano Nuevo) rather than Monterey Canyon (Rosenfeld *et al.*, 1994). They found that stratification isolates the upper water column from topographic influence. However, Narimousa and Maxworthy (1985) found that the bottom topography had a large effect on the meandering upwelling jet in their laboratory experiments. In this section, we try to gain a clear understanding of how the complex topography of the Monterey submarine canyon influences the overlying water circulation and properties.

The near-surface currents respond to wind forcing with maximum equatorward flow during spring. Our study focuses mainly on the spring upwelling. Figures 7.45 and 7.46 show the latitudinal (along-shore) velocity in a cross-shore section at latitudes 36.52° and 36.76° respectively (the horizontal lines in Figure 7.1). The velocity on four days (day 115, 125, 135, and 145) is shown. Monterey Canyon should have a small effect at latitude 36.52° but a significant effect at latitude 36.76°, which roughly cuts through the canyon. The strongest equatorward flow is restricted to the upper $100 - 200\ m$ but sometimes propagates down to depth. The poleward undercurrent, an ubiquitous feature of eastern boundary currents, is deep and weak during the early part of the year, and intensifies to a maximum in the fall and winter as the Davidson current (Figure 7.10). The nearshore, equatorward jet has a maximum speed of

$50cm/s$ and the undercurrent has a maximum speed of 20 cm/s at depth $200-400$ m. These values are in a good agreement with estimates from observations (Collins *et al.*, 2000; Ramp *et al.*, 1997). The near surface equatorward currents have very similar vertical structure at both latitudes 36.52° and 36.76°. In Figures 7.45(a)-(c), we find that the CU is poleward. Two poleward currents flows are observed across the Monterey canyon (Figures 7.46(b)-(d)). They are roughly divided by the near surface equatorward flow; one flows poleward at longitude $122.5W$ and the other flows along the shore ($122.2W$) respectively. Breaker and Broenkow (1994) concluded that the waters from the CU would enter Monterey Bay at intermediate depths (roughly 25 m − 150 m depth) and follow the topography within the interior of the canyon until certain levels. From their analysis and early observation results, they found that flow separation may occur, producing cyclonic circulation and upwelling in deeper regions (below 300 m). Our simulation also shows that the CU could enter the canyon following the canyon topography and as in Figures 7.45 and 7.46 (positive alongshore velocity).

The vertical velocity at the same cross-sections is shown in Figures 7.47 and 7.48. We see positive vertical velocity along the canyon slope most of time (Figure 7.47). Interestingly, there is occasionally local overturning circulation. The overturning implies complicated flow patterns and enhanced mixing in this region. In addition, the vertical velocity is stronger inside the canyon ($36.76°N$) than at latitude $36.52°N$. The major change of vertical velocity occurs close to the shore, which is consistent with our previous discussion of non-hydrostatic effects. The vertical velocity offshore is quite small, and the hydrostatic approximation is appropriate far from the coast. These results suggest that the local topography may have a significant effect on the regional circulation, particularly along the shore.

Figures 7.49 and 7.50 show the longitudinal velocity located at longitude $122.4°W$ and $122.1°W$, respectively, on the same days. Several features are noteworthy. First, the small scale eddies occur frequently in the upper 200 m of the ocean near the coast (positive and negative velocities side by side). The $122.4°W$ cross-shore section is near Point Ano Nuevo, which is one of the upwelling centers in the vicinity of Monterey Bay (Figure 7.1). Second, the CU is evident along the coast at both latitudes. At

longitude $122.1°W$, we see a westward offshore current at all depths around latitude $36.2°N$ Figures 7.50. This feature has been found in observations and is mainly due to the effect of local bathymetry (Ramp *et al.*, 1997). We also observe small and weak eddies at depth. The eddy sizes in the canyon are much smaller than those observed elsewhere.

The latitudinal velocity also shows larger temporal variability close to the shore (longitude $122.1°W$) than that off shore (longitude $122.4°W$) in Figures 7.50 and 7.49. The effects of stratification are clearly seen offshore in Figure 7.49. However, the stratification at longitude $122.4°W$ is not trivial and Monterey Canyon is responsible for the complicated recirculation.

Figures 7.53 and 7.54 show the vertical velocity at the same longitudes and time. At longitude $122.4°W$, the vertical velocity is small between latitudes $36.3°N$ and $36.5°N$ which is roughly the region of the deep canyon ($> 2000\ m$). Some local vertical overturns are found in the mouth of Monterey Bay (Figures 7.54). Note that downwelling flow is observed near the upstream rim of the canyon (at longitude $122.4°W$ in Figure 7.53). Downwelling flow in this region is frequently observed in the field (Hickey, 1997) during upwelling season and is counter to that predicted by a $\sigma-$coordinate numerical model (Allen *et al.*, 2003). The current study shows that the topography of Monterey Canyon may have a significant influence on the local circulation, including vertical transport, and thus an enhancing turbulent mixing in that region. In the next section, we further compare the numerical simulation of Monterey Bay area with and without the Monterey Canyon.

7.3.7 Comparison of the circulation with and without the Monterey Canyon

In the coastal ocean, the circulation is strongly affected by the topography. With the numerical model, we can assess the importance of such effects. The influence of the Monterey Canyon is particularly important due to its steep topography.

In order to emphasize the importance of the canyon in establishing the current in the vicinity of Monterey Bay, we performed a non-hydrostatic simulation for the

same year, with everything exactly the same except for the bottom bathymetry. We eliminate Monterey Canyon by replacing it with a flat bottom at depth 880 m. The bathymetry in the absence of the canyon is shown in Figure 7.55. The effects of the canyon are evident from the comparison between the results with and without the canyon. Figures 7.56-7.58 show the monthly-averaged velocity field at various depths during June using the non-hydrostatic, MBARM model in the absence of the Monterey Canyon. We compare them with the simulations with actual topography in Figures 7.32-7.37. Interestingly, the simulation results in the absence of the canyon resemble the results of the hydrostatic model more than the non-hydrostatic simulation results. In the upper ocean (Figure 7.56), a cyclonic eddy is found near the southwest corner, which is also observed in the hydrostatic model (Figures 7.32(a) and 7.33(a)). At depth 700 m, a pair of cyclonic and anti-cyclonic eddies is formed (Figure 7.58 (b)). A very similar pair of eddies is found in the hydrostatic model with realistic bathymetry (Figure 7.37(a)) but not in the non-hydrostatic model (Figure 7.37(b)). The similarity between the non-hydrostatic simulation in the absence of the canyon and the hydrostatic model in the presence of the canyon is not surprising. When the deep canyon is removed, the vertical scale in the simulation domain becomes very thin (small) relative to the horizontal scale. Non-hydrostatic effects are suppressed and vertical acceleration does not play an important role in the flow. In this case, the hydrostatic approximation is appropriate.

This numerical experiment demonstrates the influence of topography on the coastal circulation. We conclude that the Monterey Canyon contributes significantly to the regional circulation in the Monterey Bay area and reconfirm the conclusion drawn in Section 7.3.5 that non-hydrostatic effects are dominant in this region. In coastal ocean modeling, the non-hydrostatic effects have to be taken into account in the presence of complex coastal topography.

7.4 Summary

The high resolution MBARM was used to investigate the regional ocean circulation in the Monterey Bay area. The model is non-hydrostatic and has the immersed boundary

module built into it. The model is also coupled to a larger scale CCS model. The Monterey Bay area circulation is highly correlated to the CCS. The surface flow pattern in spring/summer is different from that in autumn/winter. Within the bay a cyclonic circulation is often observed. This feature is a result of coastal geometry. A warm anticyclone is often seen near the mouth of Monterey Bay.

The model reveals several features of the general circulation in the vicinity of Monterey Bay. These features have been reported in the past. The simulated results are also consistent with mooring measurements and observations seen in AVHRR images and radar-derived surface currents. Some filaments and coastal meanders are observed in the simulation. In the upwelling season, we find that Point Ano Nuevo and Point Sur are the upwelling centers, and many cyclonic eddies are caused by topographic effects. We investigated the effect of the Monterey submarine canyon on flow during the spring upwelling season, during which the surface equatorward current dominates. We showed that Monterey Canyon contributes significantly to the non-hydrostatic modes by comparing the results with and without the canyon. Most previous studies used idealized geometry and filtered bathymetry, which is too smooth to realistically represent the geometry of Monterey Canyon. In particularly, non-hydrostatic effects seem to play an important role in determining the non-linear dynamics of the nearshore circulation. The non-linear dynamics are also enhanced by the complex coastal geometry, e.g. a coastal bay and a submarine canyon. These non-hydrostatic effects cannot be ignored in coastal ocean modeling.

In the current study, the surface cyclonic eddy frequently observed inside Monterey Bay is attributed to the effect of coastal geometry and bathymetry. The location and size of the eddy closely resemble the atmospheric Santa Cruz eddy (Lozej, personal communication, 2003). Is there any correlation between them? Are they coupled or enhanced by each other? The influence of this interaction must be investigated with a coupled atmospheric-ocean model in the future.

Table 7.1: Comparison of annual mean flow

	Depth-averaged annual velocity magnitude (cm/s)	Depth-averaged annual velocity direction ($^{\circ}T$)
MBARM results	4.7	301
Numerical results with data assimilation (Shulman *et al.*, 2002)	3.13	308
Observation (Collins *et al.*, 2000)	3.7-5.3	290-310

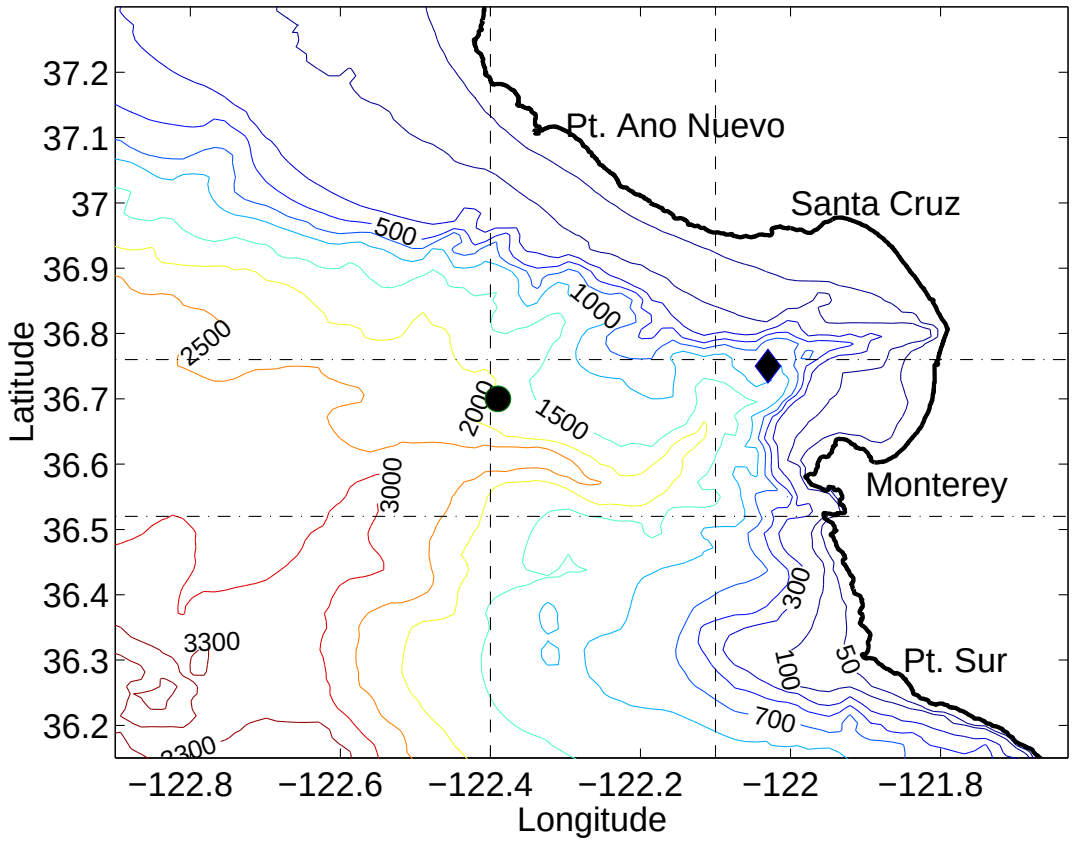

Figure 7.1: The model domain of Monterey Bay area and bathymetry. Locations of moorings M1, M2 are marked by a circle and a diamond, respectively. '−.': lines at latitude $36.52°N$ and $36.76°N$, '−−': lines at longitude $122.4W$ and $121.1°W$. The horizontal uniform grid is shown by the dotted lines (Every sixth grid is shown).

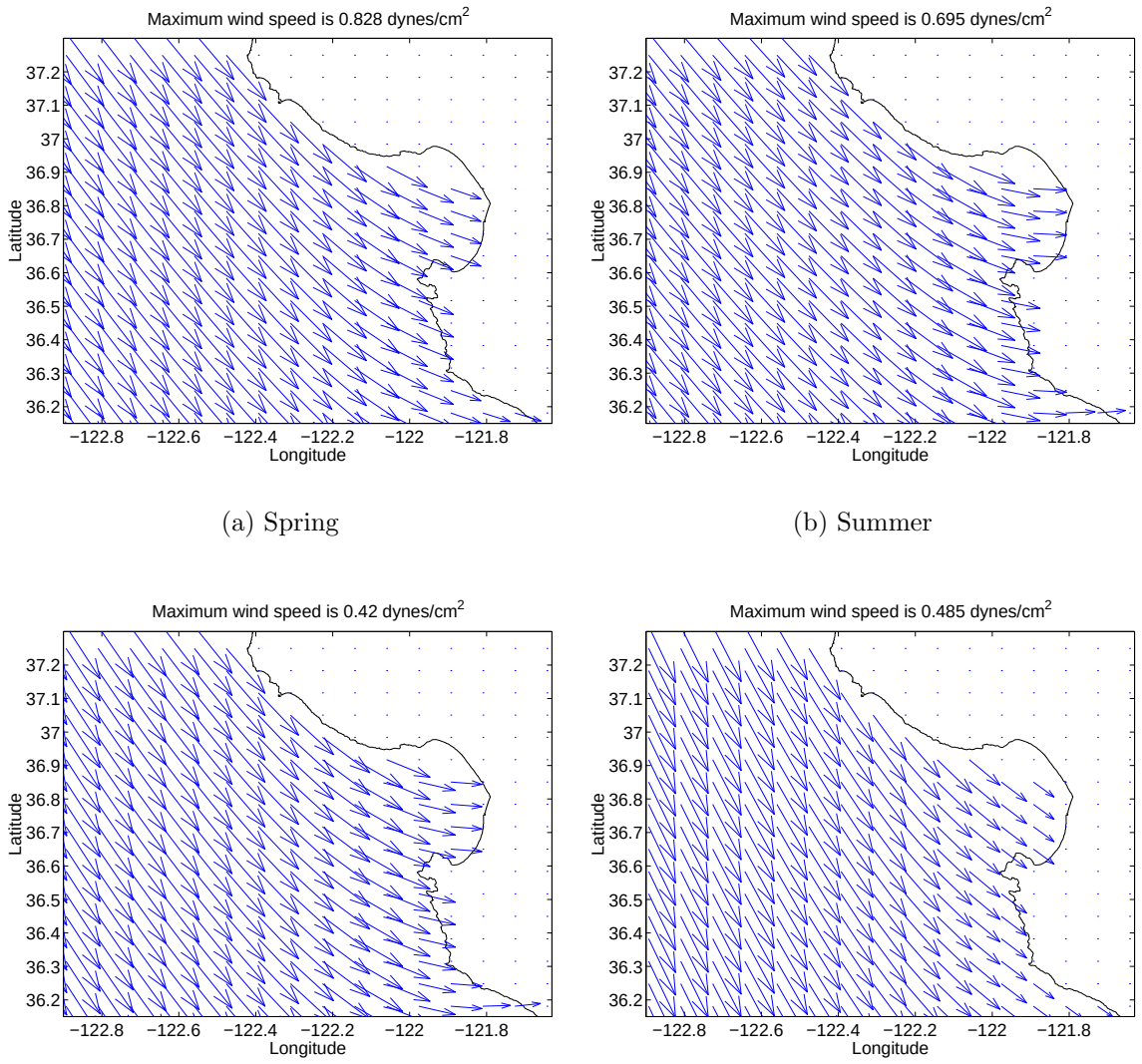

(a) Spring

(b) Summer

(c) Autumn

(d) Winter

Figure 7.2: The monthly wind stress in different seasons. (a) Spring; (b) Summer; (c) Autumn; (d) Winter.

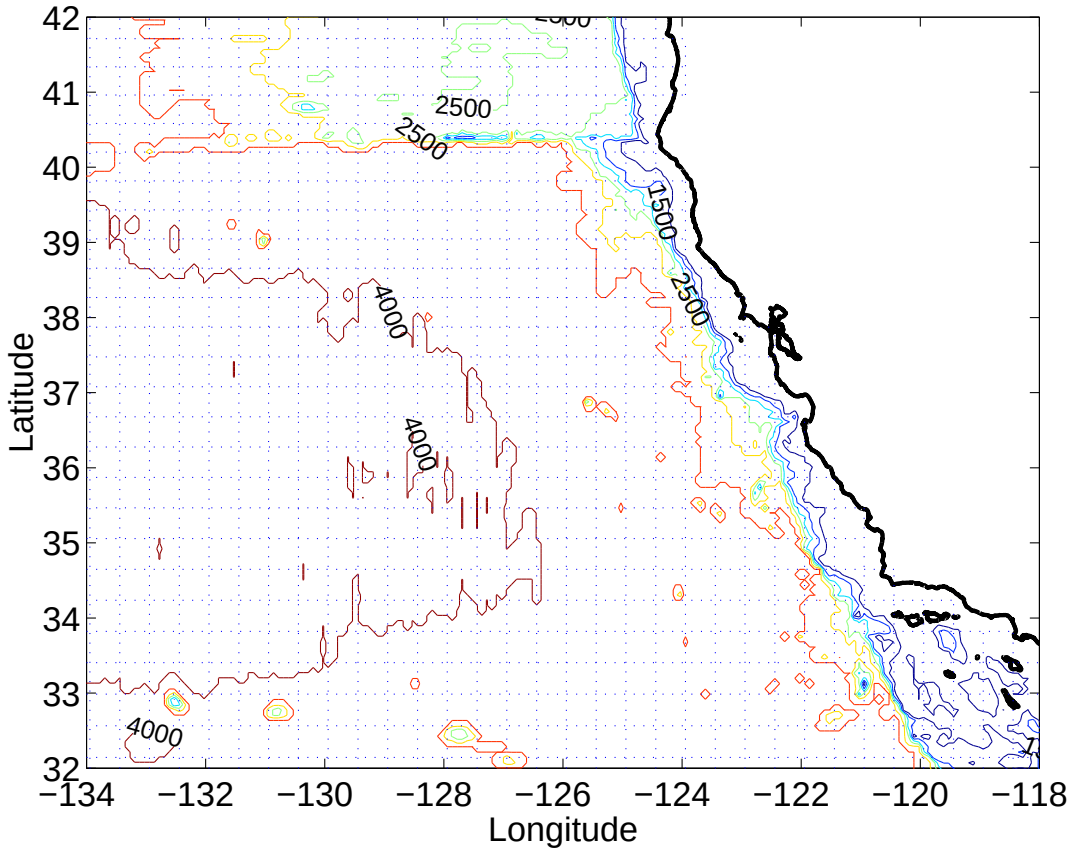

Figure 7.3: The domain and bathymetry of the California current system model used for nesting. The grid is shown by the dotted lines (Every sixth grid is shown).

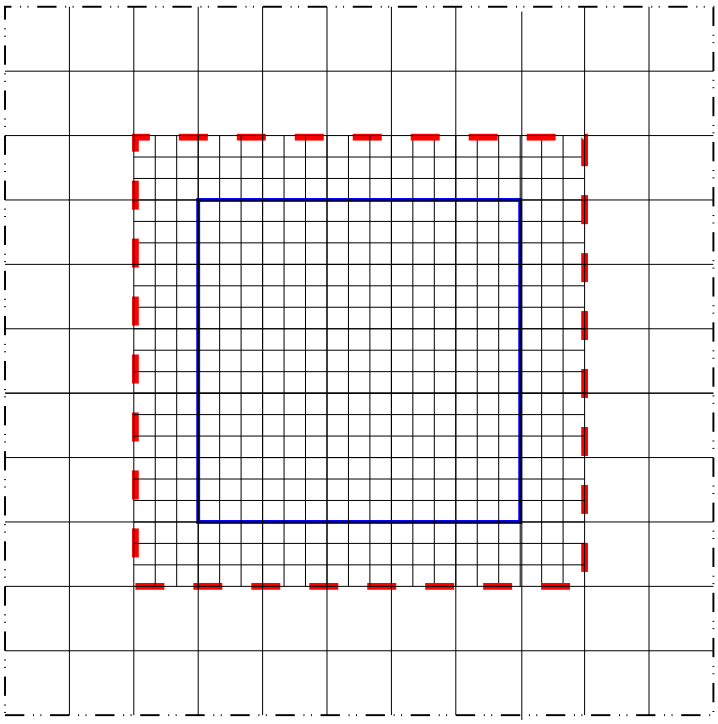

Figure 7.4: Schematic diagram of grid arrangement for the nesting. Both coarse (larger domain) and fine (smaller domain) grids are shown. The simulation domain is bounded by the dashed line. There is an intermediate region where the depth is smoothed out to match the different depths between these two grids (bounded by the solid and dashed lines).

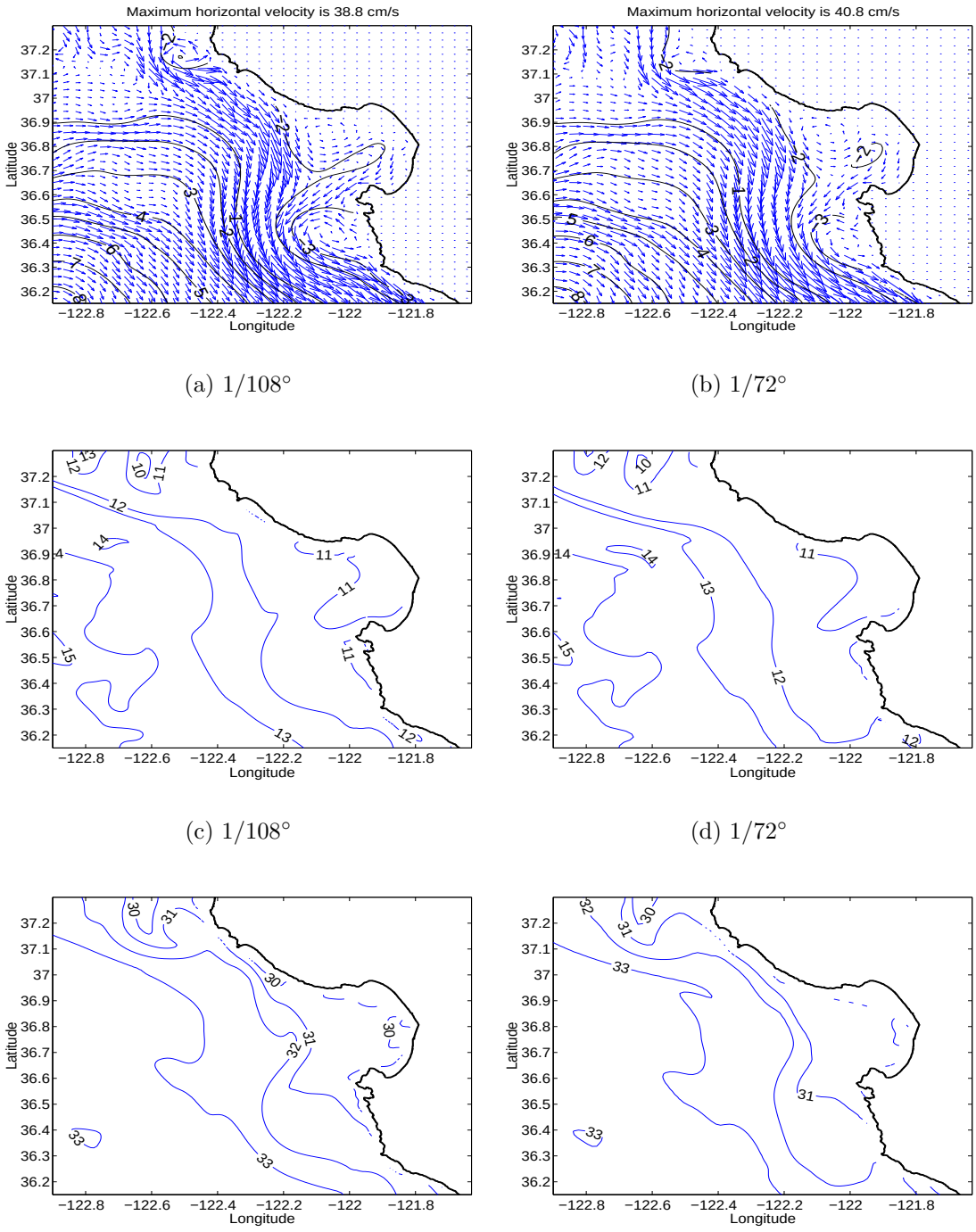

(a) 1/108° (b) 1/72°

(c) 1/108° (d) 1/72°

(e) 1/108° (f) 1/72°

Figure 7.5: The grid sensitivity study using a high resolution grid 1/108° ($\approx 1\ km$) and a medium grid 1/72° at day 10. Surface velocity and pressure fields (a), (b); surface temperature contours (c), (d); surface salinity contours (e), (f).

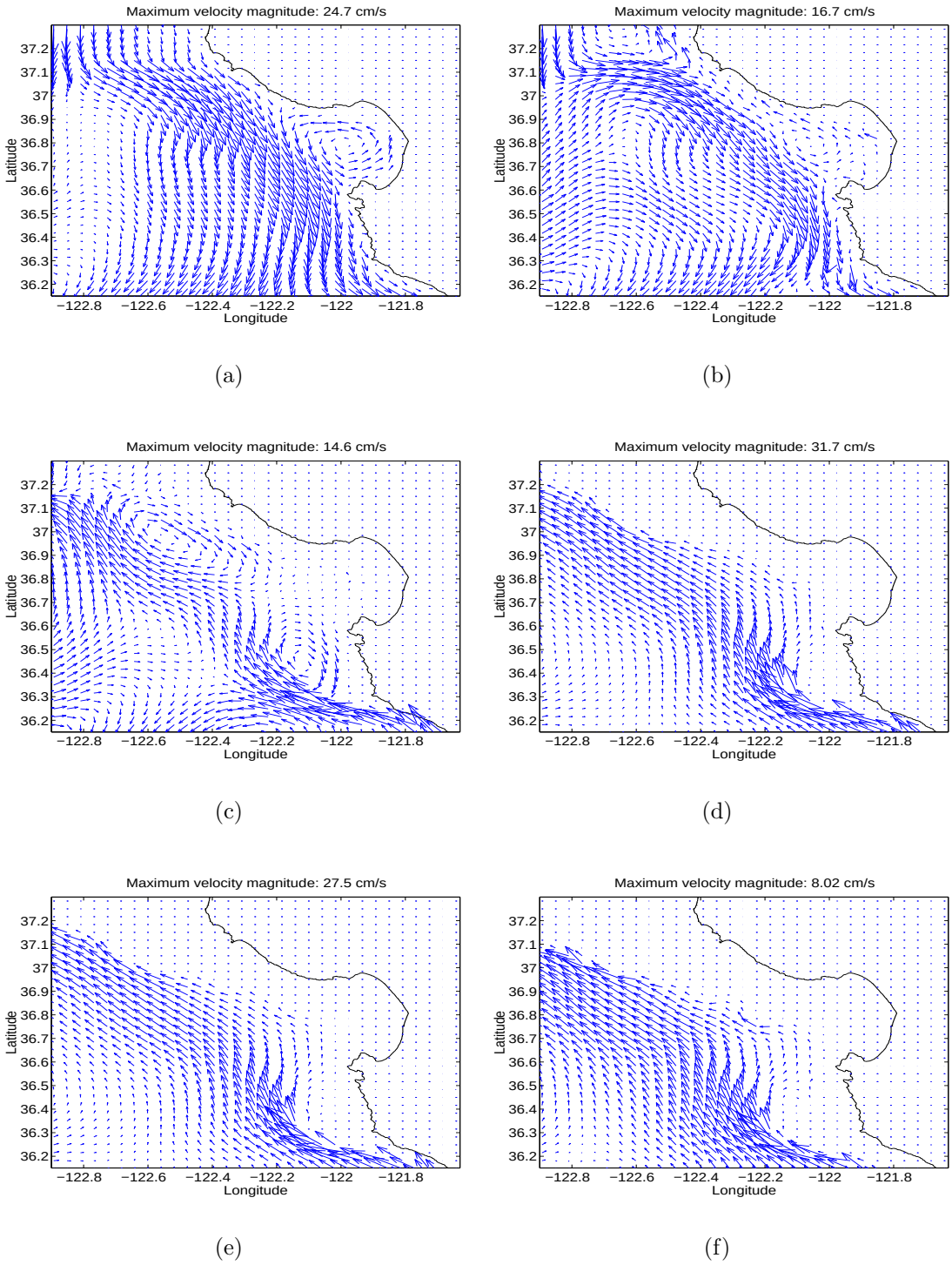

(a) (b)

(c) (d)

(e) (f)

Figure 7.6: The annual mean velocity field at various depths for a year. At depth (a) 10.1 m, (b) 50 m, (c) 100 m, (d) 300 m, (e) 400 m,(f) 700 m.

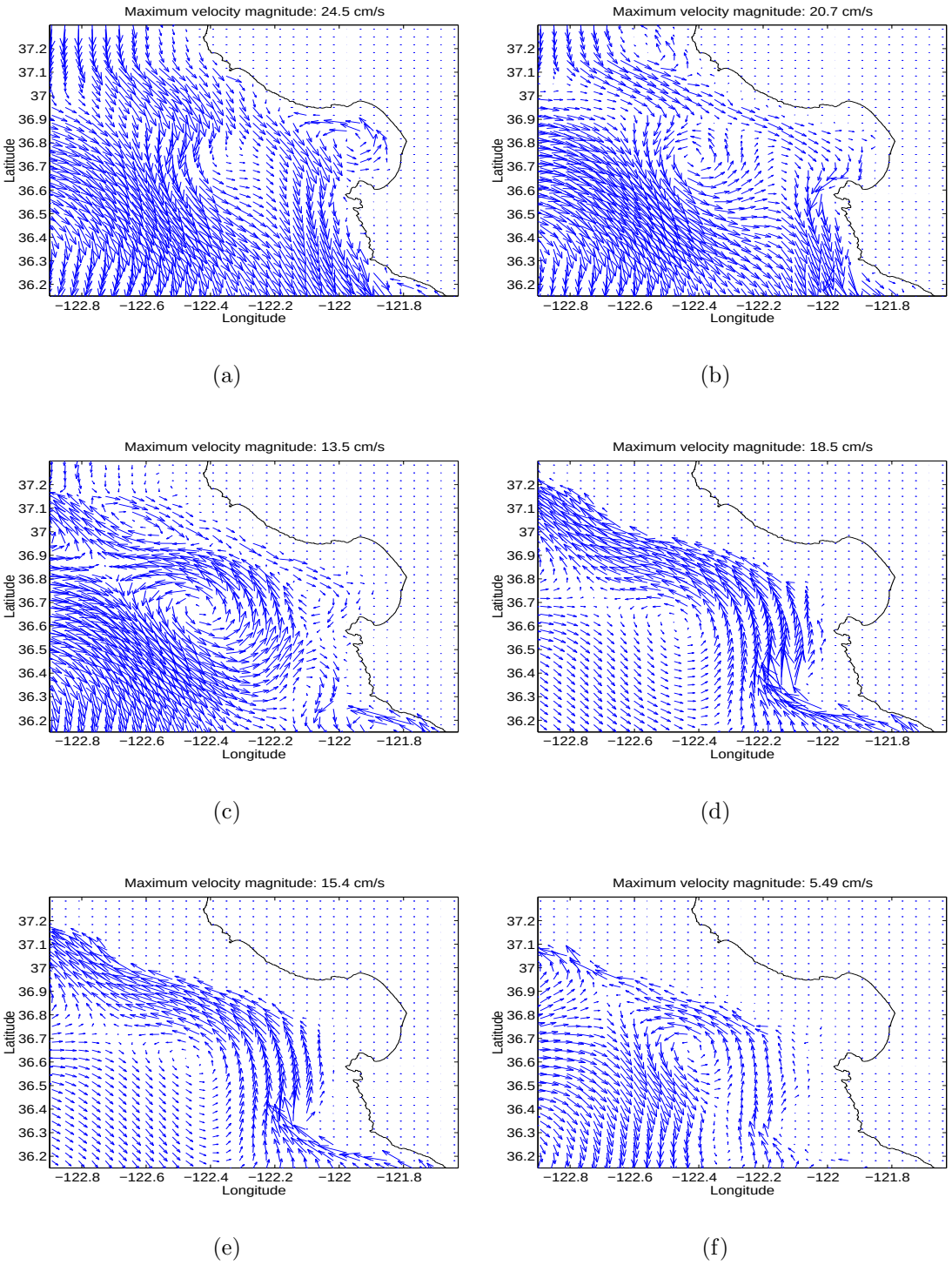

(a) (b)

(c) (d)

(e) (f)

Figure 7.7: The mean velocity field at various depths during spring. At depth (a) 10.1 m, (b) 50 m, (c) 100 m, (d) 300 m, (e) 400 m,(f) 700 m.

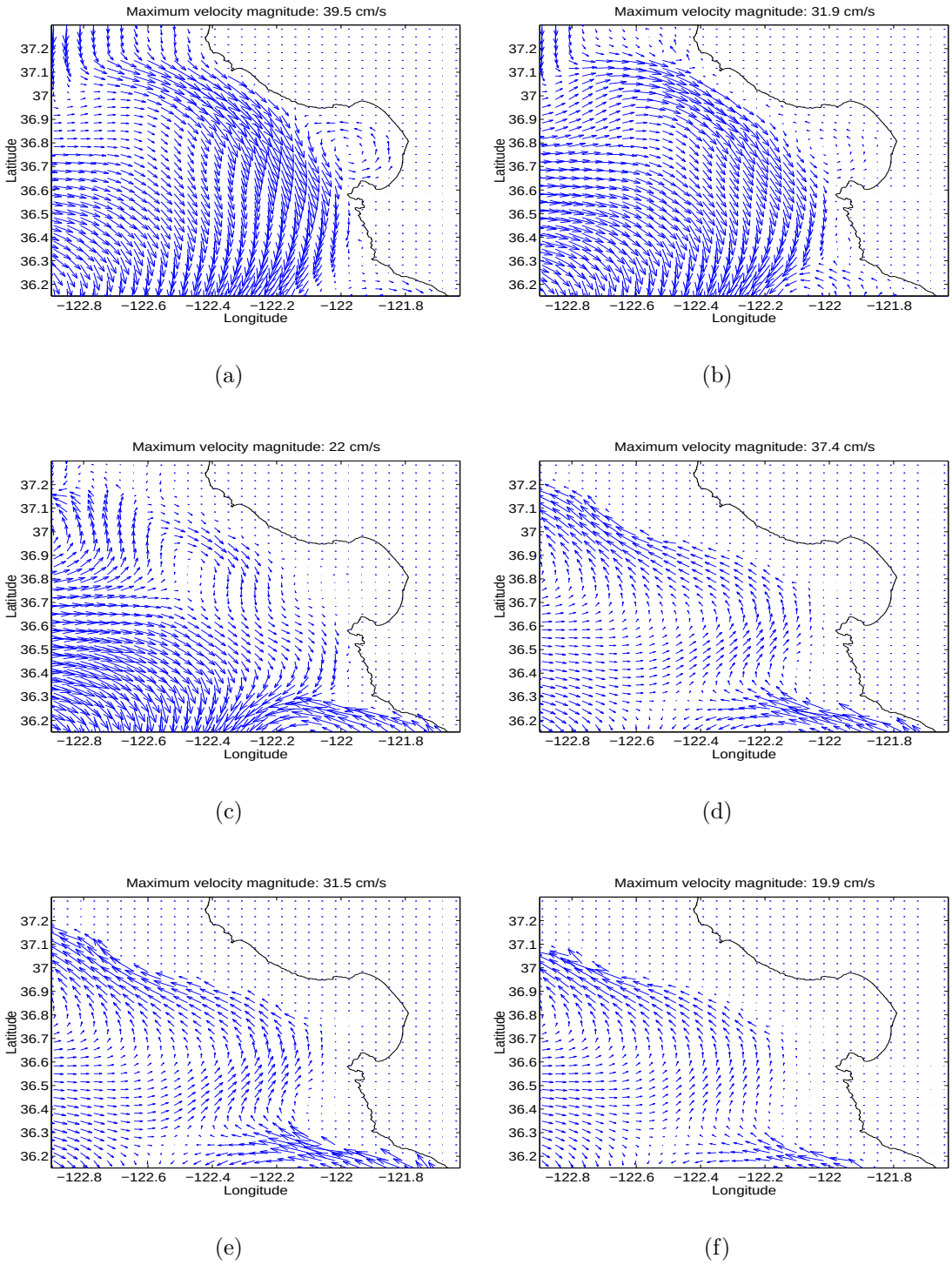

(a) (b) (c) (d) (e) (f)

Figure 7.8: The mean velocity field at various depths during summer. At depth (a) 10.1 m, (b) 50 m, (c) 100 m, (d) 300 m, (e) 400 m, (f) 700 m.

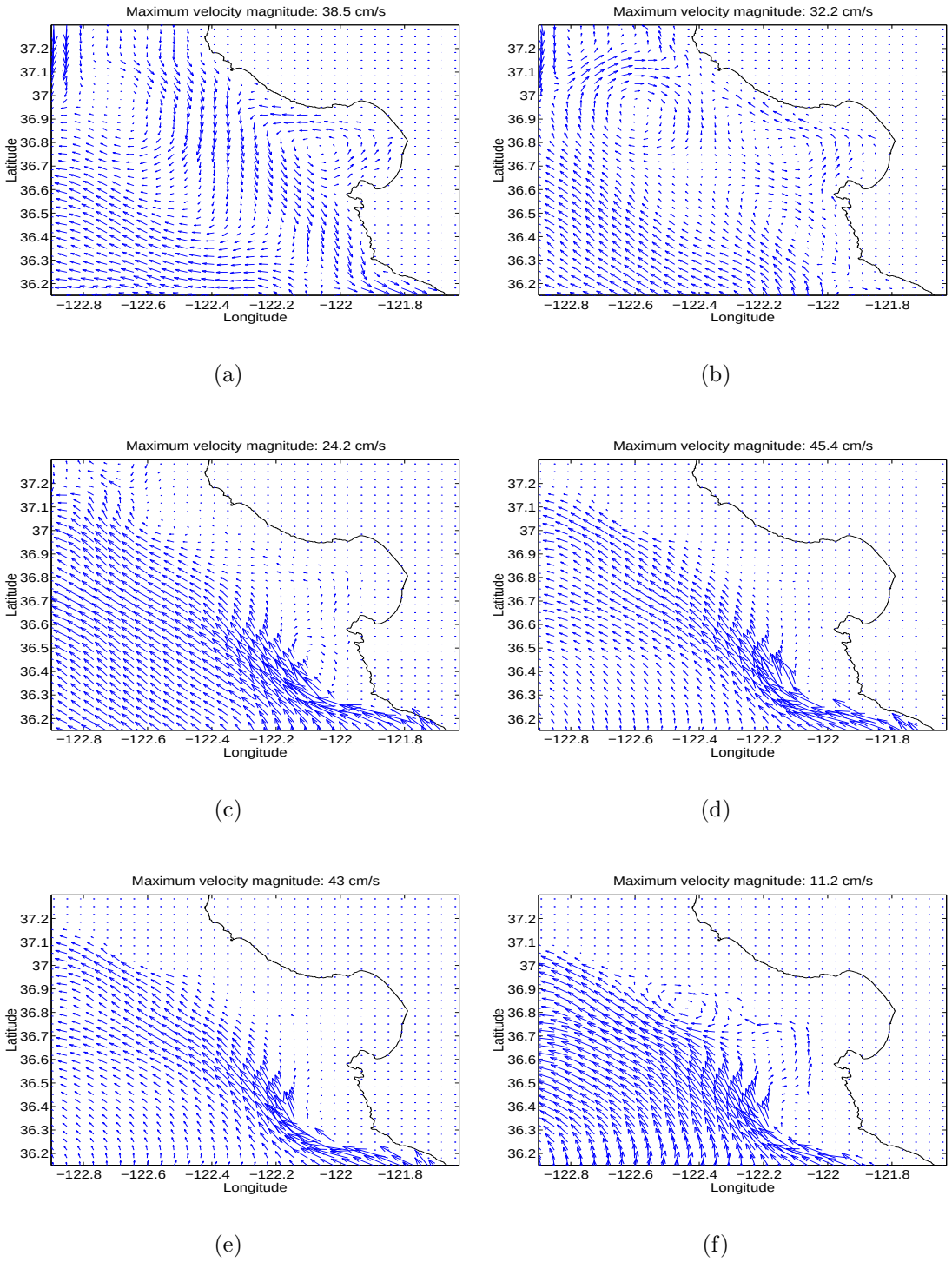

(a) (b)

(c) (d)

(e) (f)

Figure 7.9: The mean velocity field at various depths in Autumn. At depth (a) 10.1 m, (b) 50 m, (c) 100 m, (d) 300 m, (e) 400 m, (f) 700 m.

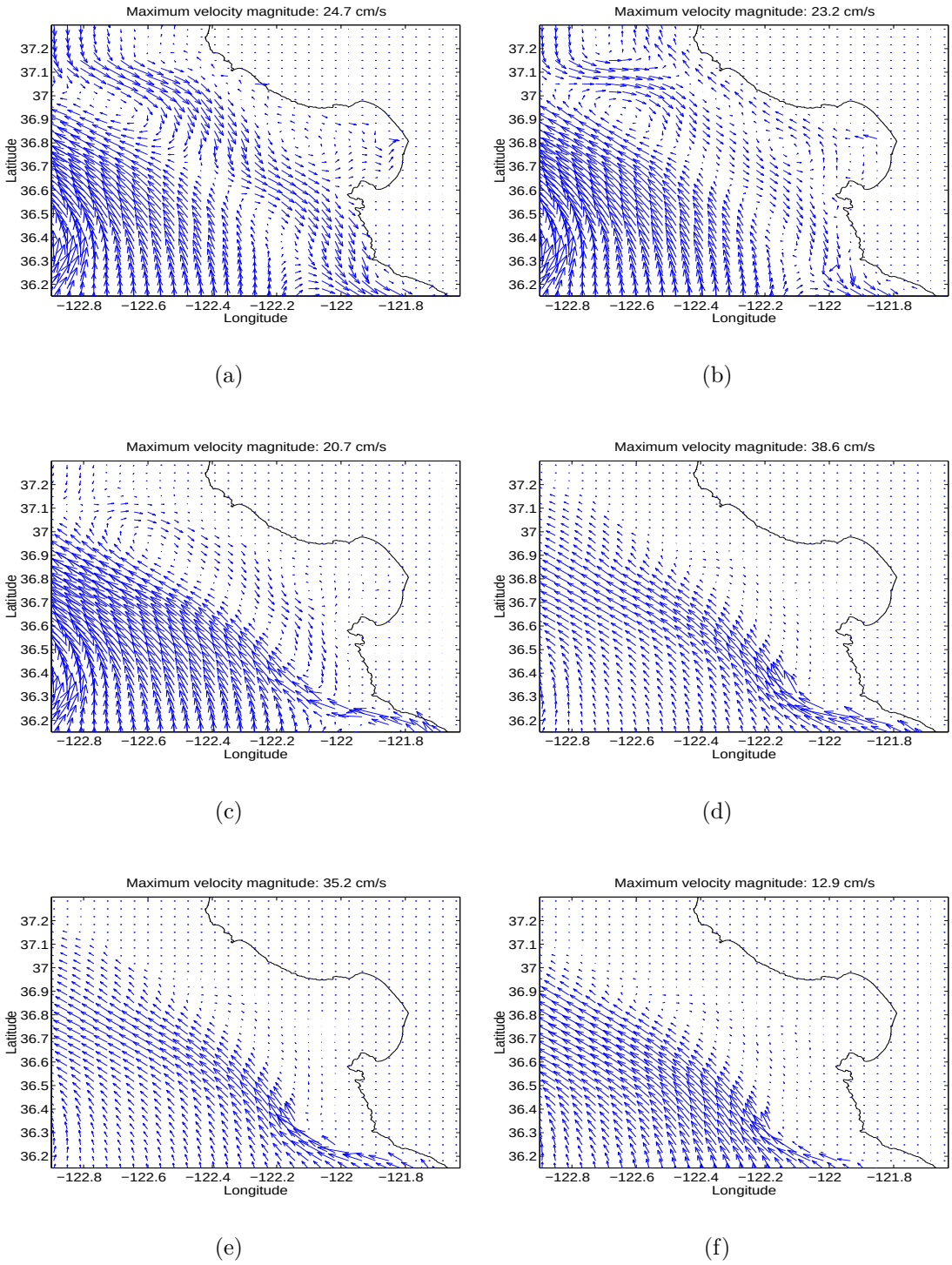

(a) (b) (c) (d) (e) (f)

Figure 7.10: The mean velocity field at various depths during winter. At depth (a) 10.1 m, (b) 50 m, (c) 100 m, (d) 300 m, (e) 400 m, (f) 700 m.

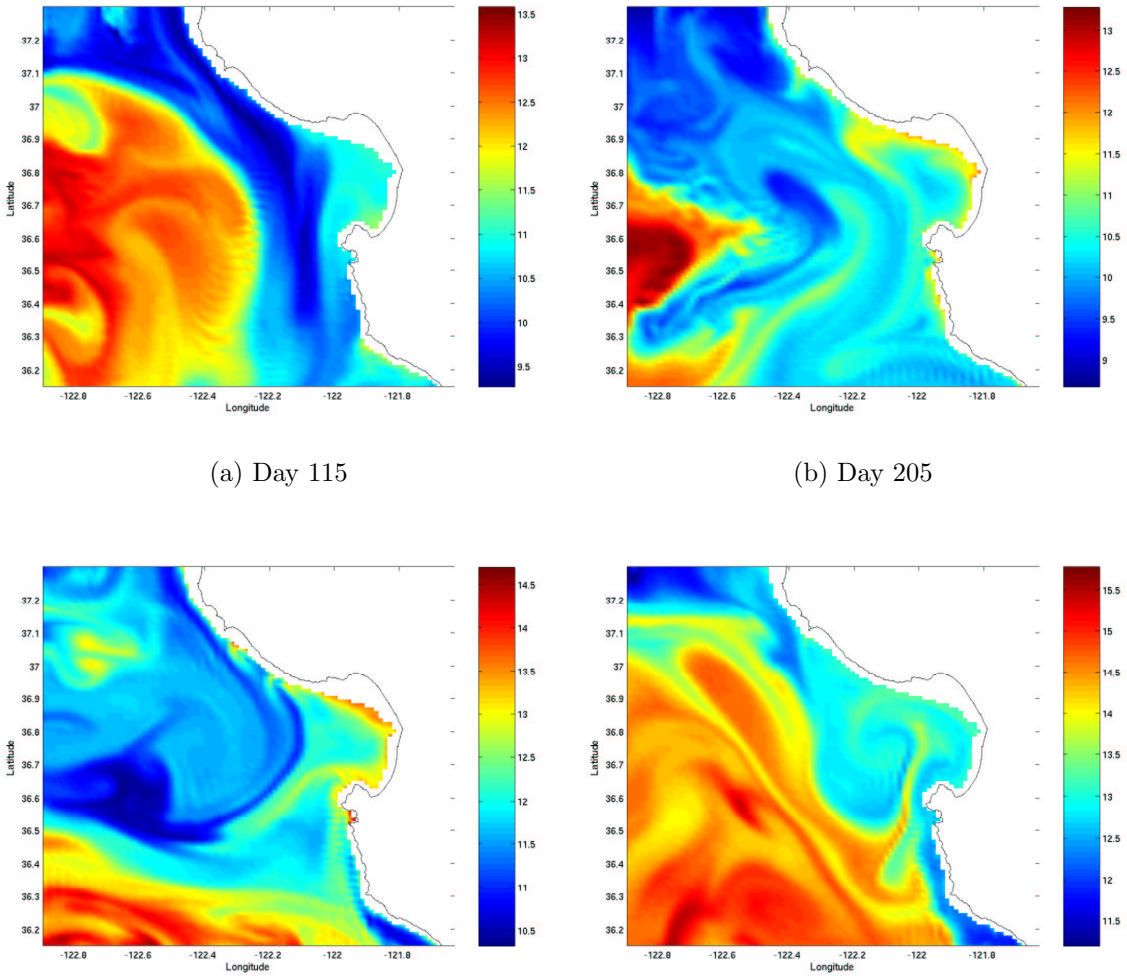

(a) Day 115

(b) Day 205

(c) Day 295

(d) Day 385

Figure 7.11: The sea surface temperature in different seasons. (a) Spring (day 115); (b) Summer (day 205); (c) Autumn (day 295); (d) Winter (day 385).

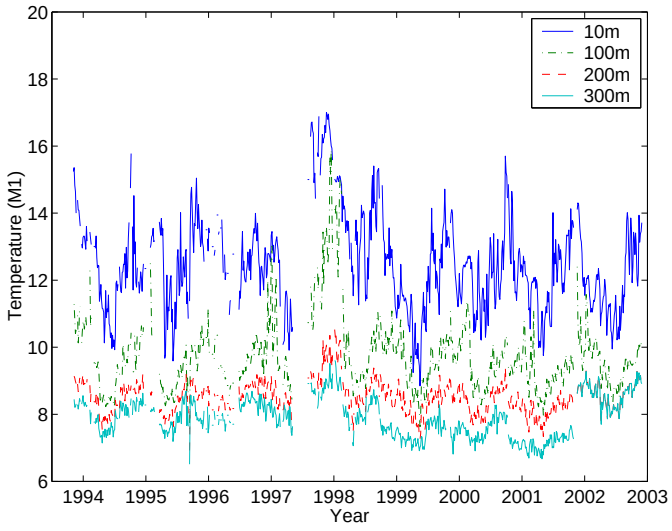

Figure 7.12: Observed time series of temperature at mooring station M1 (year 1993-2002).

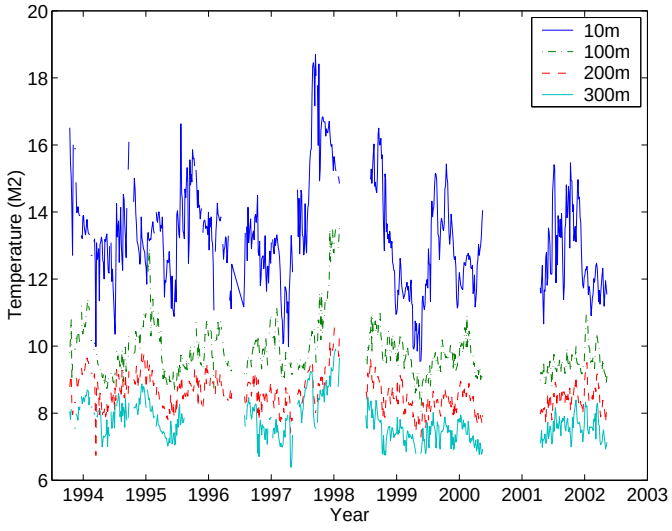

Figure 7.13: Observed time series of temperature at mooring station M2 (year 1993-2002).

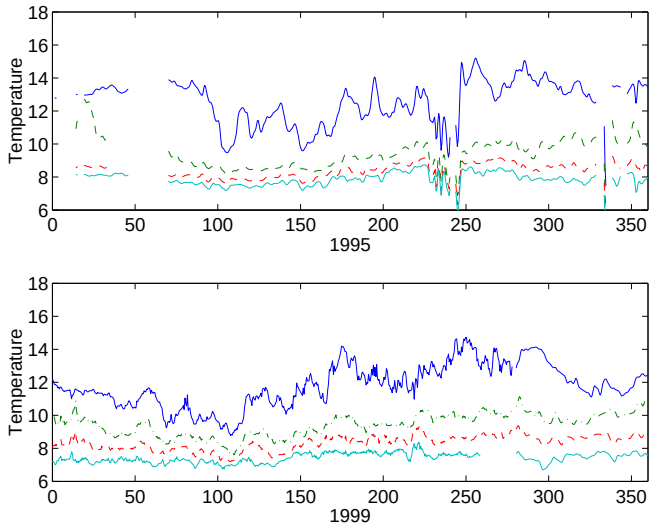

Figure 7.14: Observed time series of temperature at station M1 for years 1995 (top) and 1999 (bottom). The legend is the same as Figure 7.12.

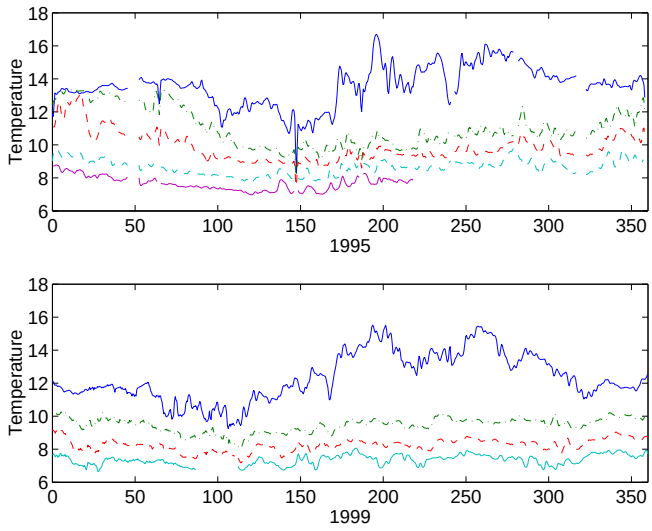

Figure 7.15: Observed time series of temperature at station M2 for years 1995 (top) and 1999 (bottom). The legend is the same as Figure 7.13.

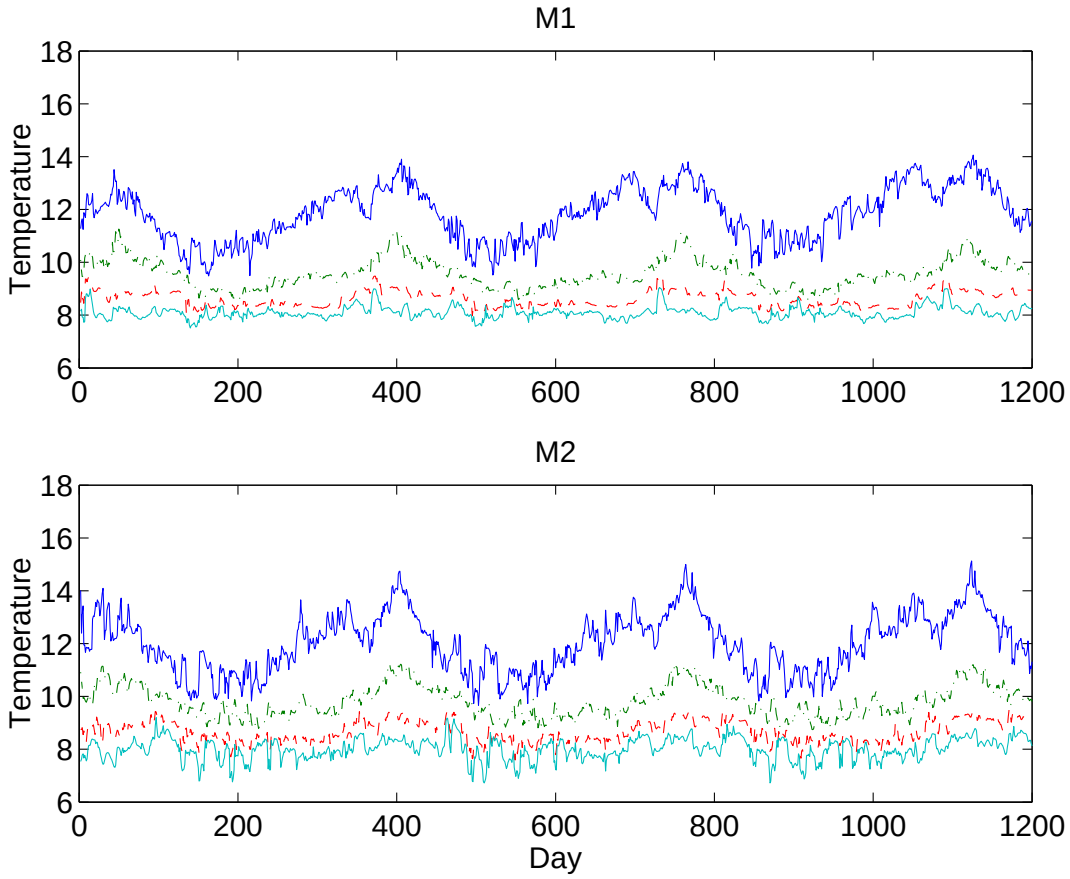

Figure 7.16: Model time series of temperature at stations M1 (top) and M2 (bottom) for three simulation years. The model repeats smoothly after 40 days, thus showing that the annual cycle is accurately responded. The legend is the same as Figure 7.12.

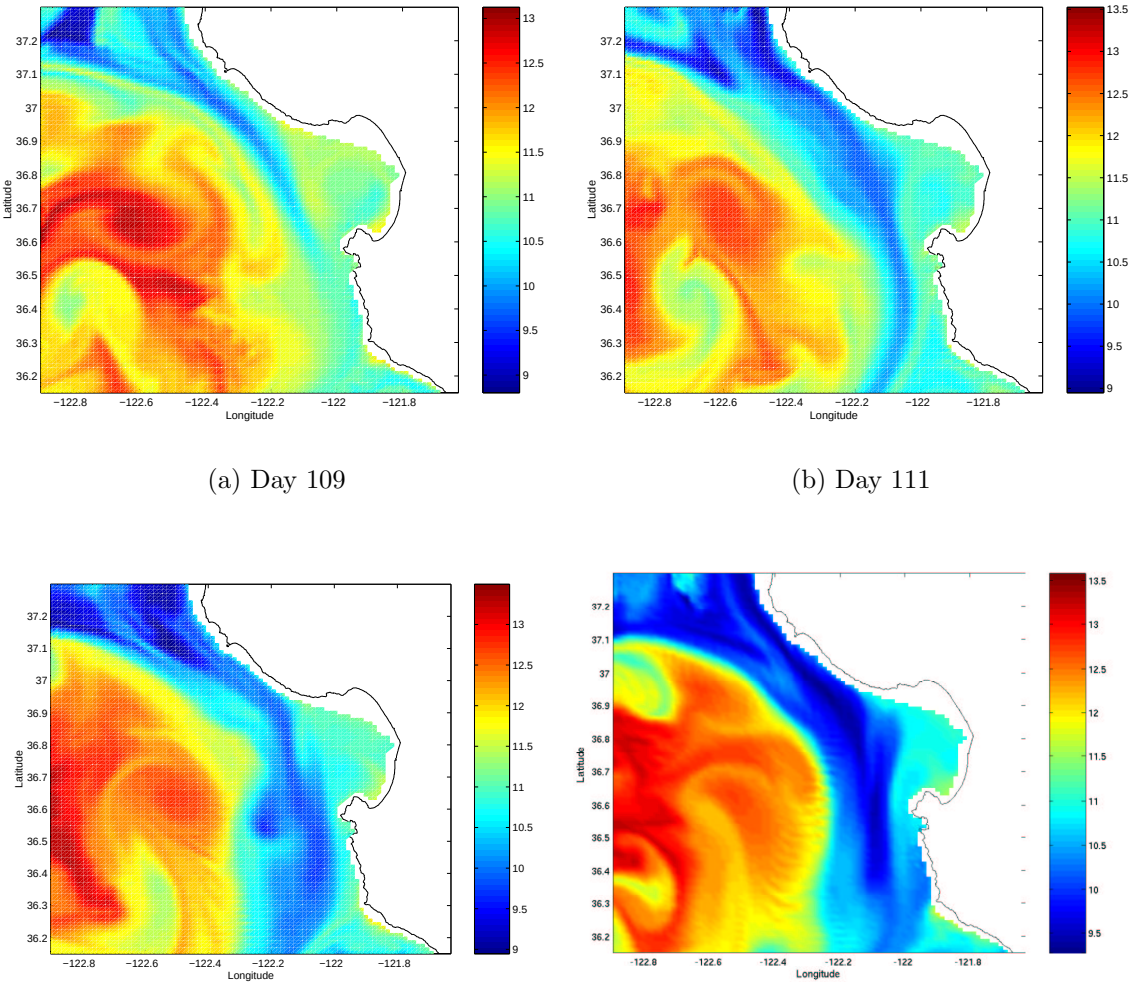

(a) Day 109

(b) Day 111

(c) Day 113

(d) Day 115

Figure 7.17: The surface temperature field from day 109 to day 115.

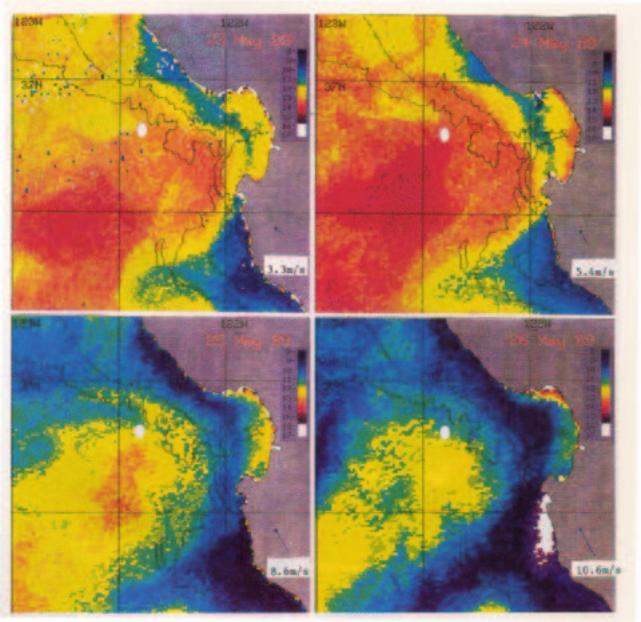

Figure 7.18: Sea surface temperature (SST) from AVHRR images for May 23-26, 1989 (Rosenfeld *et al.*, 1994).

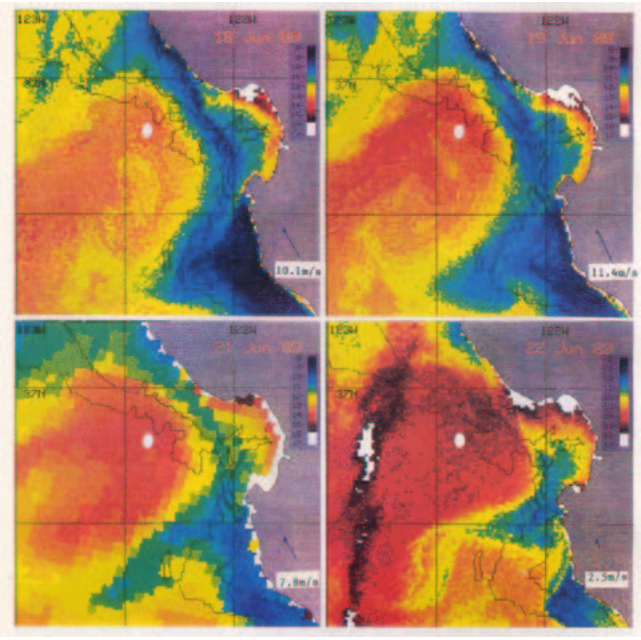

Figure 7.19: SST from AVHRR images for June 18, 19, 21 and 22, 1989 (Rosenfeld *et al.*, 1994).

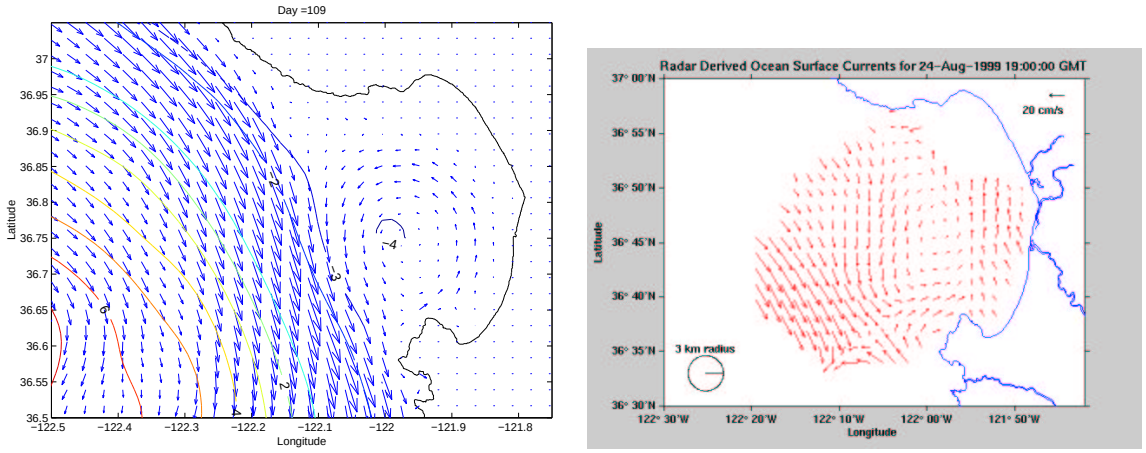

(a) (b)

Figure 7.20: (a) The simulated surface current and pressure on day 109. (b) The daily averaged (33hr low-pass filtered) radar-derived current vectors on August 24, 1999 from the Radar and Drifter (RAD) Lab at the Naval Postgraduate School. Source: http://www.oc.nps.navy.mil/∼radlab

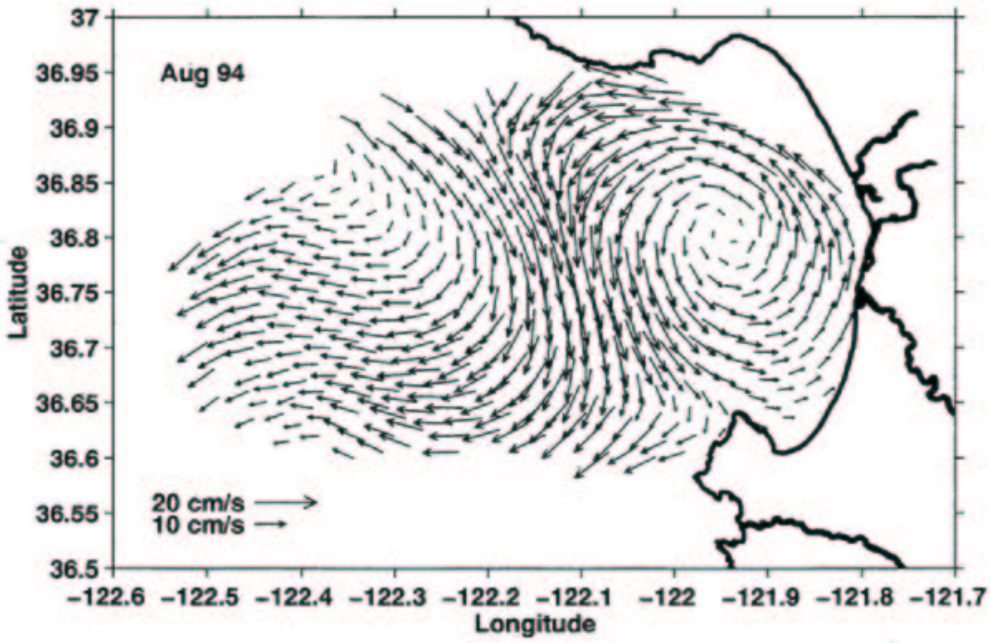

Figure 7.21: Averaged radar-derived current vectors for August 1994. [Figure 12 in Paduan and Rosenfeld (1996)]

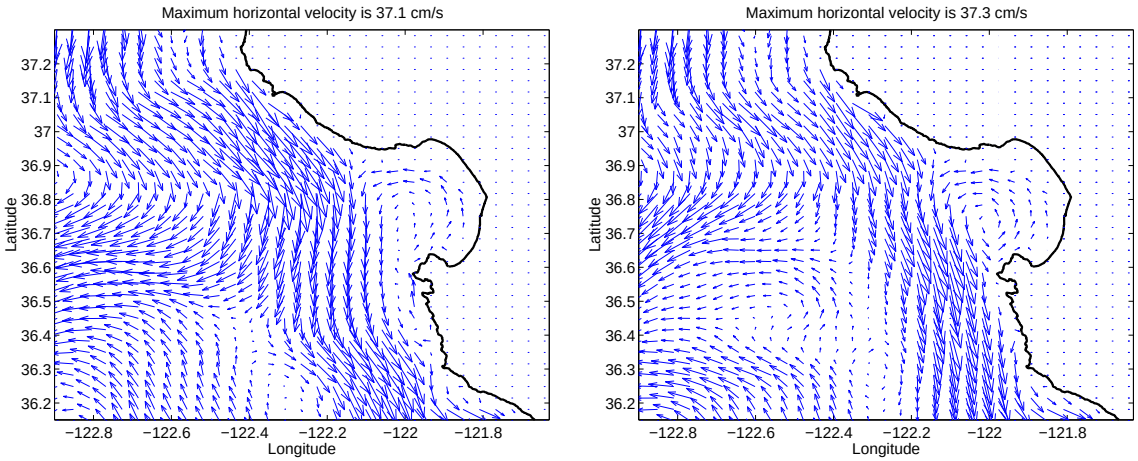

(a) (b)

Figure 7.22: The velocity field at depth 10.1 m using the high-resolution MBARM models. The velocity field is monthly averaged during May (day 120-150). (a) hydrostatic and (b) non-hydrostatic.

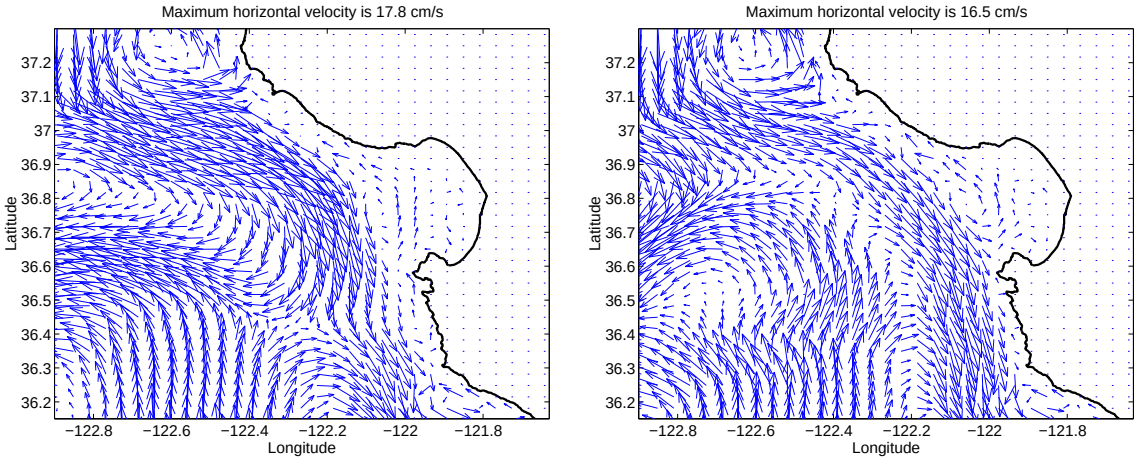

(a) (b)

Figure 7.23: The velocity field at depth 50 m using the high-resolution MBARM models. The velocity field is monthly averaged during May (day 120-150). (a) hydrostatic and (b) non-hydrostatic.

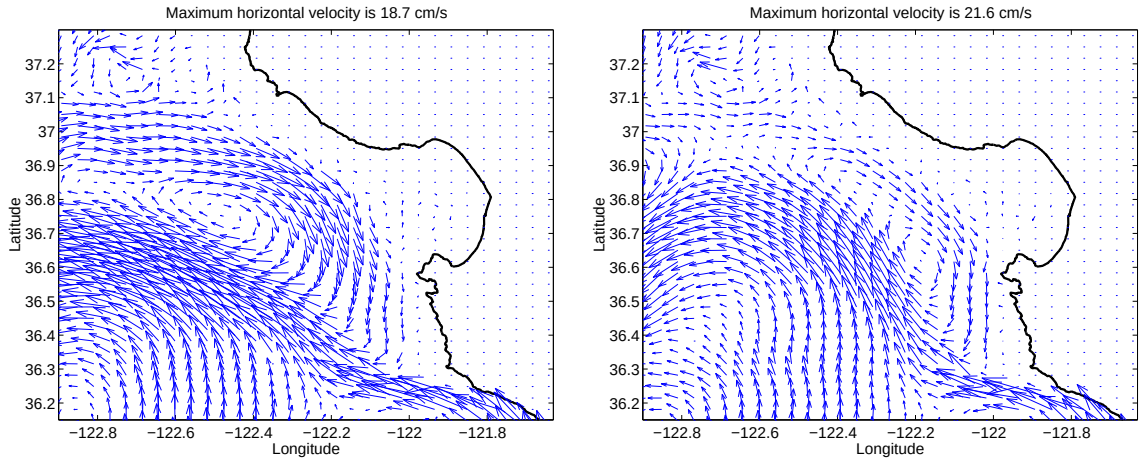

(a) (b)

Figure 7.24: The velocity field at depth 100 m using the high-resolution MBARM models. The velocity field is monthly averaged during May (day 120-150). (a) hydrostatic and (b) non-hydrostatic.

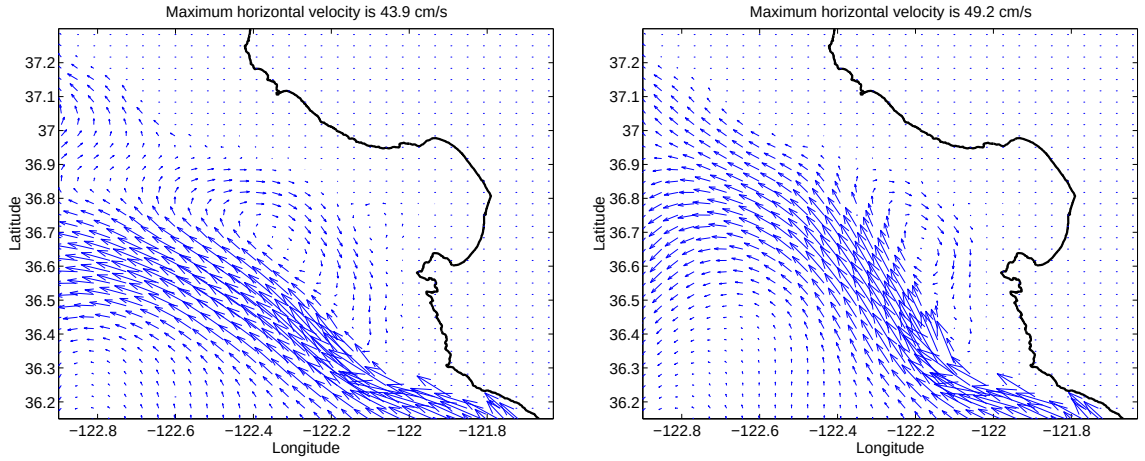

(a) (b)

Figure 7.25: The velocity field at depth 300 m using the high-resolution MBARM models. The velocity field is monthly averaged during May (day 120-150). (a) hydrostatic and (b) non-hydrostatic.

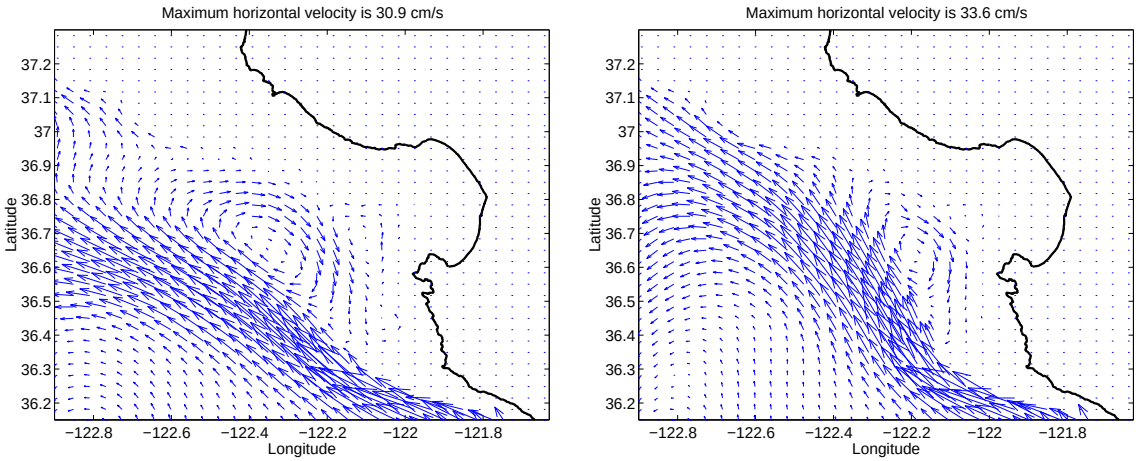

(a) (b)

Figure 7.26: The velocity field at depth 500 m using the high-resolution MBARM models. The velocity field is monthly averaged during May (day 120-150). (a) hydrostatic and (b) non-hydrostatic.

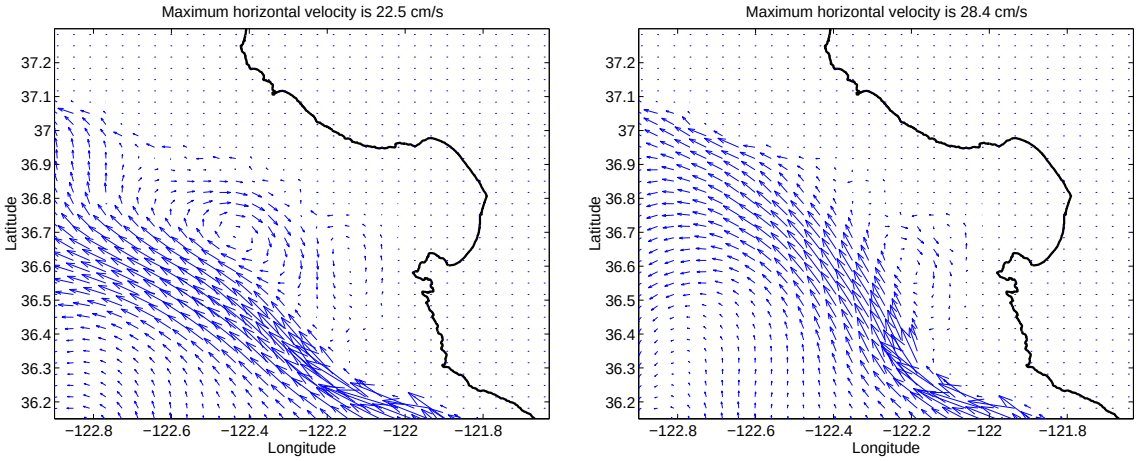

(a) (b)

Figure 7.27: The velocity field at depth 700 m using the high-resolution MBARM models. The velocity field is monthly averaged during May (day 120-150). (a) hydrostatic and (b) non-hydrostatic.

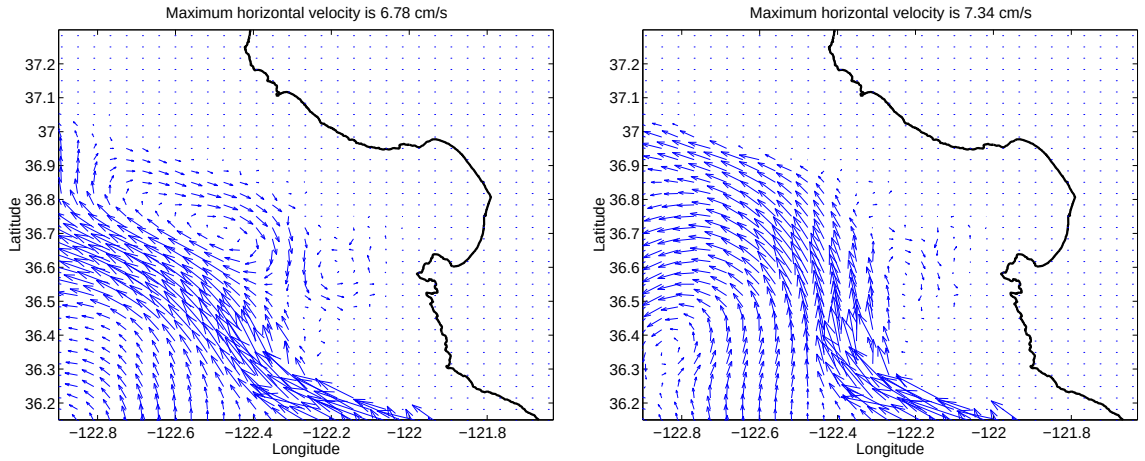

(a) (b)

Figure 7.28: The velocity field at depth 1000 m using the high-resolution MBARM models. The velocity field is monthly averaged during May (day 120-150). (a) hydrostatic and (b) non-hydrostatic.

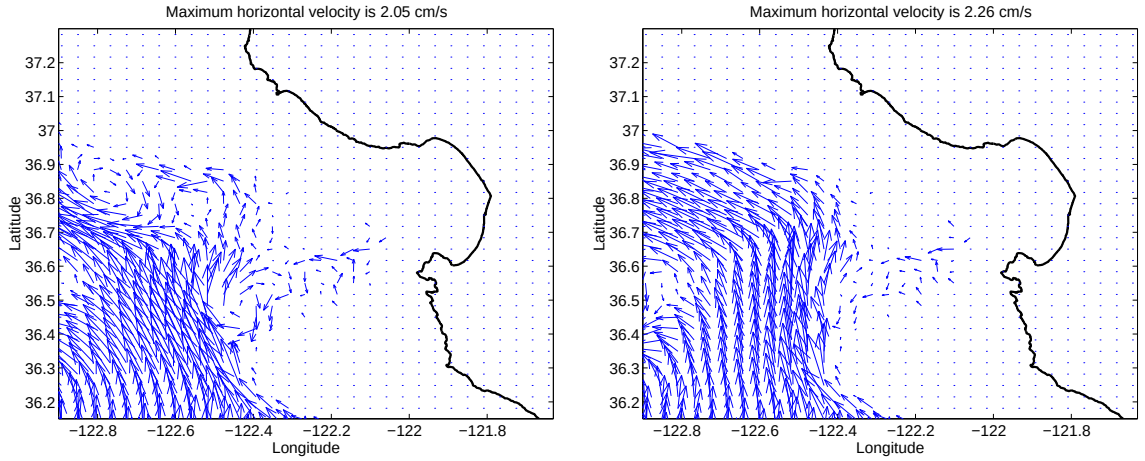

(a) (b)

Figure 7.29: The velocity field at depth 1500 m using the high-resolution MBARM models. The velocity field is monthly averaged during May (day 120-150). (a) hydrostatic and (b) non-hydrostatic.

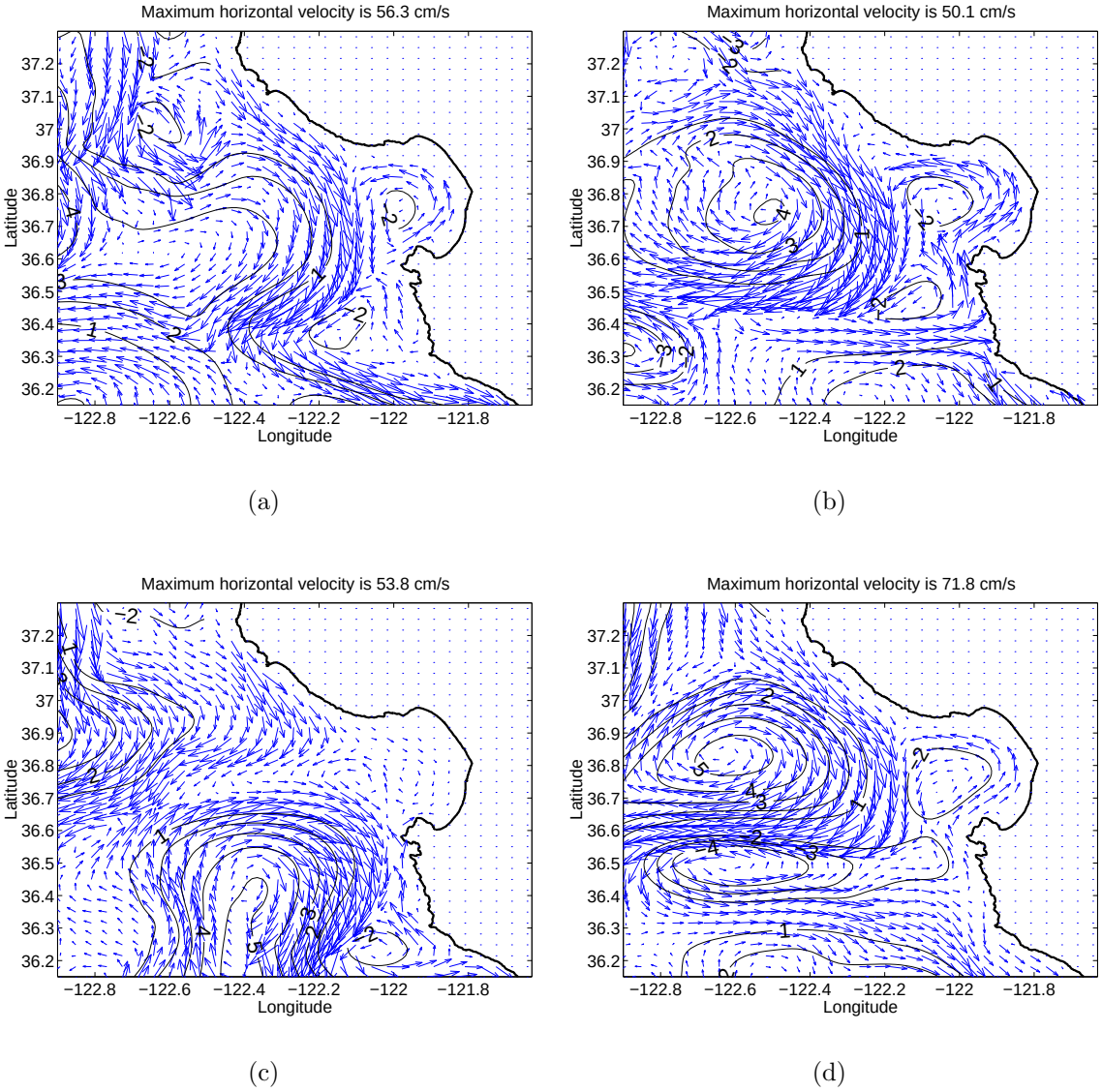

(a) (b)

(c) (d)

Figure 7.30: The simulated surface current and pressure using the high-resolution, hydrostatic MBARM model on day (a) 130, (b) 140, (c) 150, and (d) 160.

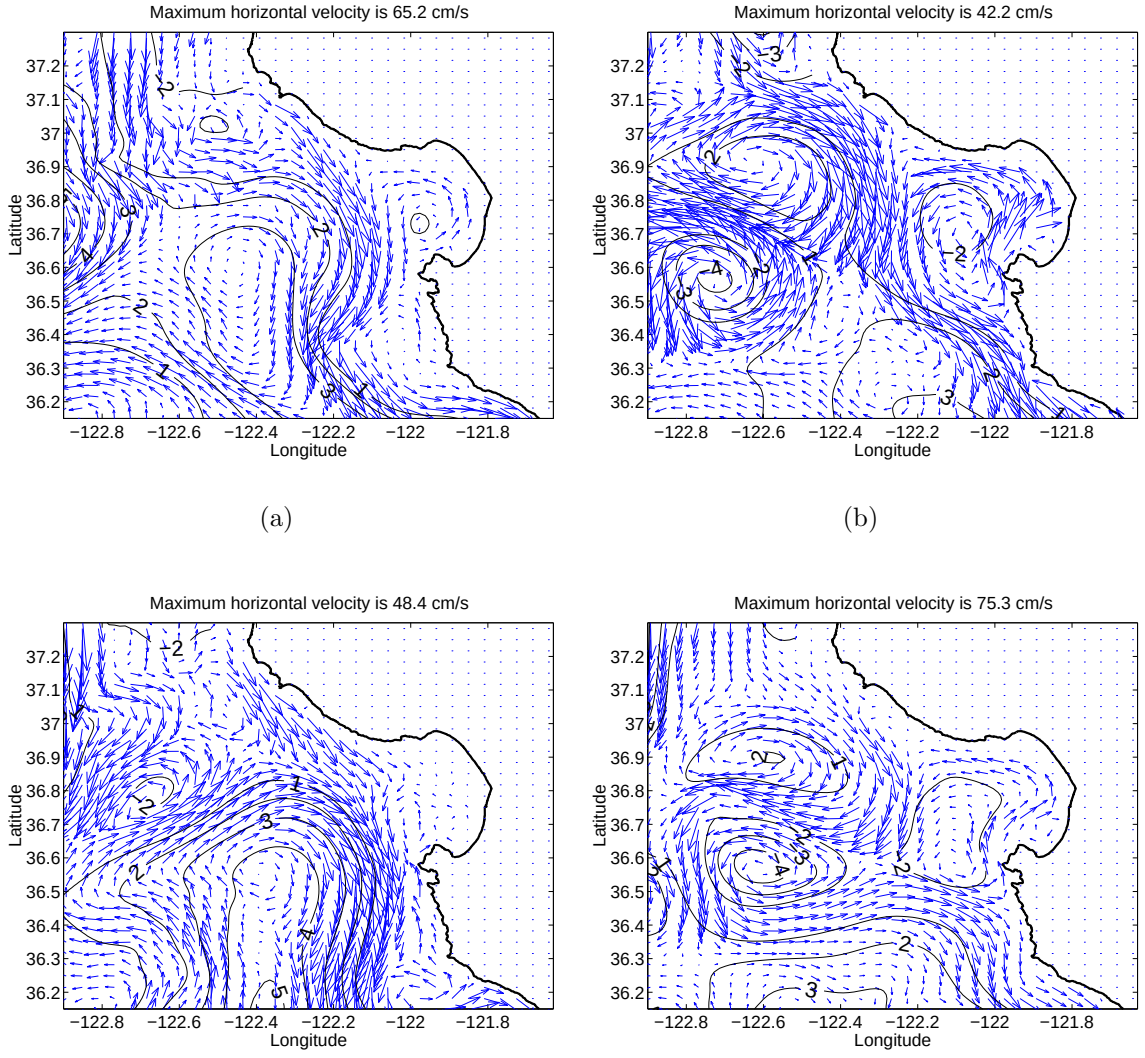

(a) (b)

(c) (d)

Figure 7.31: The simulated surface current and pressure using the high-resolution, non-hydrostatic MBARM model on day (a) 130, (b) 140, (c) 150, and (d) 160.

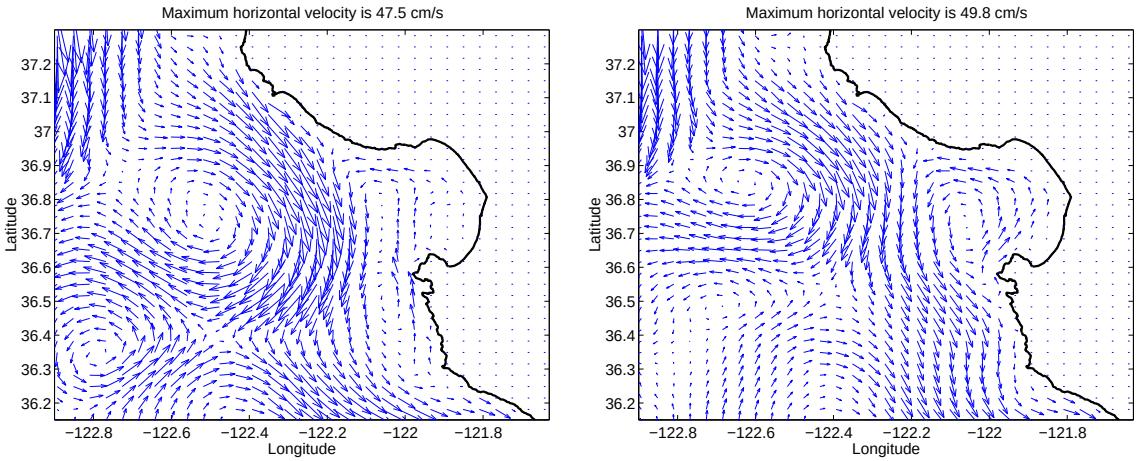

(a) (b)

Figure 7.32: The velocity field at depth 10.1 m using the high-resolution MBARM models. The velocity field is monthly averaged during June (day 150-180). (a) hydrostatic and (b) non-hydrostatic.

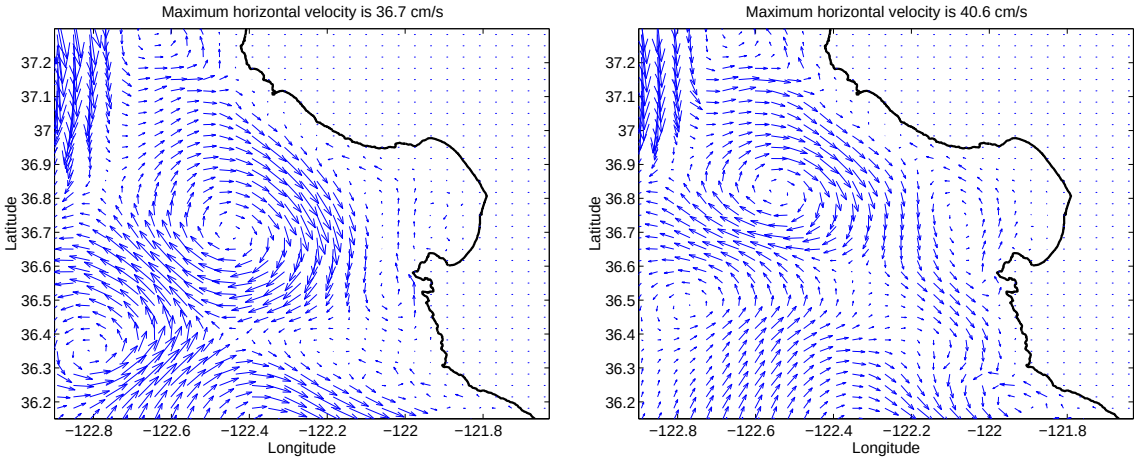

(a) (b)

Figure 7.33: The velocity field at depth 50 m using the high-resolution MBARM models. The velocity field is monthly averaged during June (day 150-180). (a) hydrostatic and (b) non-hydrostatic.

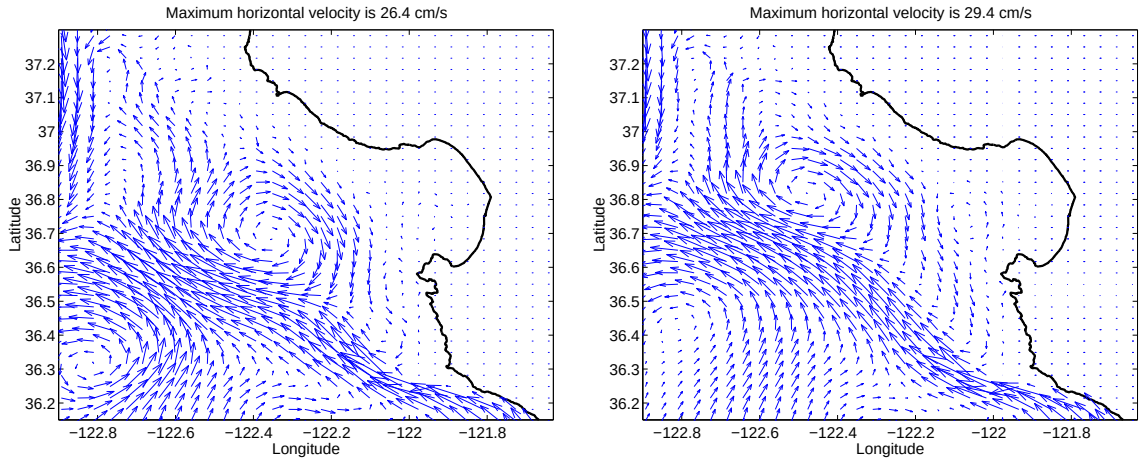

(a) (b)

Figure 7.34: The velocity field at depth 100 m using the high-resolution MBARM models. The velocity field is monthly averaged during June (day 150-180). (a) hydrostatic and (b) non-hydrostatic.

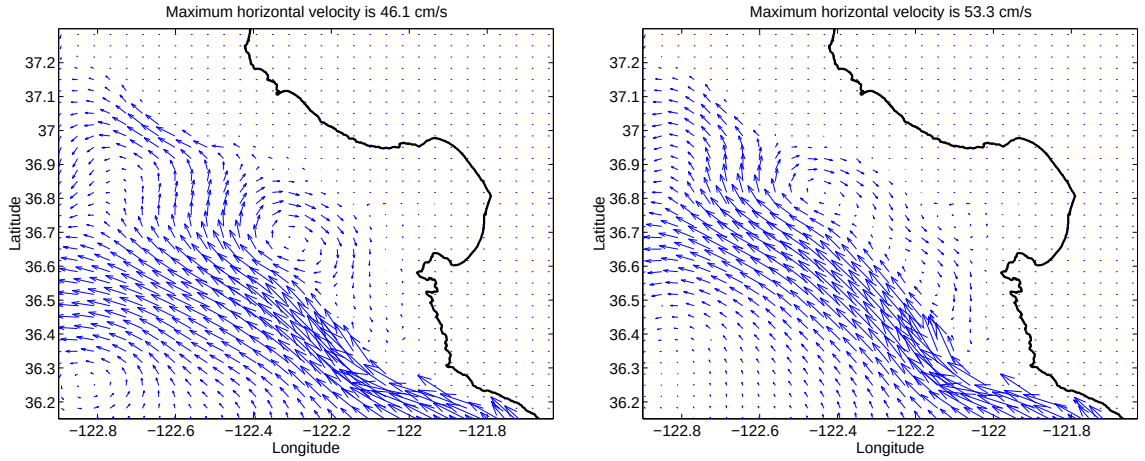

(a) (b)

Figure 7.35: The velocity field at depth 300 m using the high-resolution MBARM models. The velocity field is monthly averaged during June (day 150-180). (a) hydrostatic and (b) non-hydrostatic.

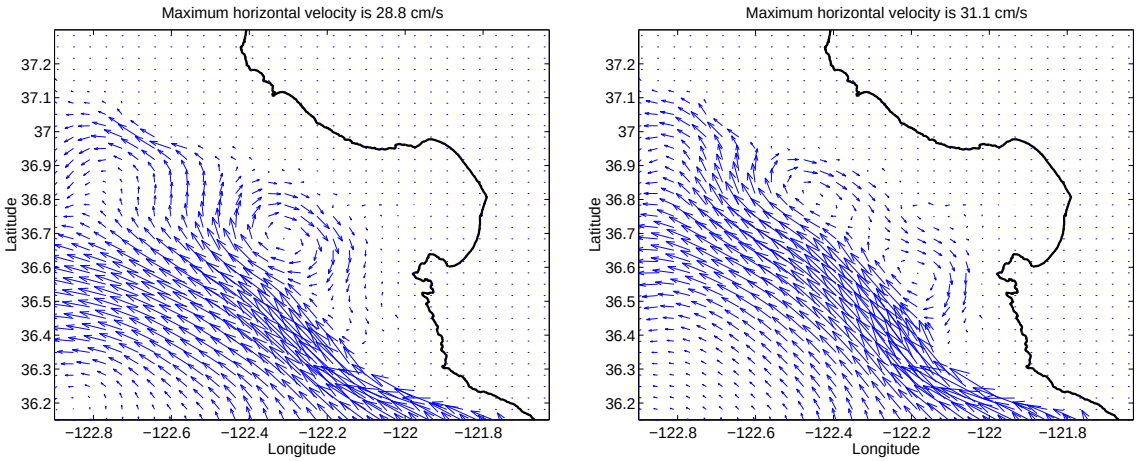

(a) (b)

Figure 7.36: The velocity field at depth 500 m using the high-resolution MBARM models. The velocity field is monthly averaged during June (day 150-180). (a) hydrostatic and (b) non-hydrostatic.

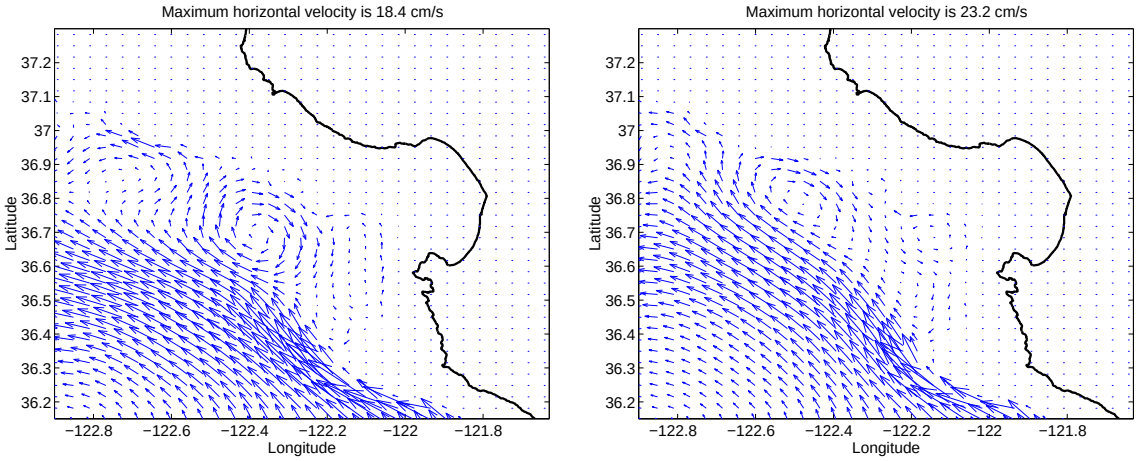

(a) (b)

Figure 7.37: The velocity field at depth 700 m using the high-resolution MBARM models. The velocity field is monthly averaged during June (day 150-180). (a) hydrostatic and (b) non-hydrostatic.

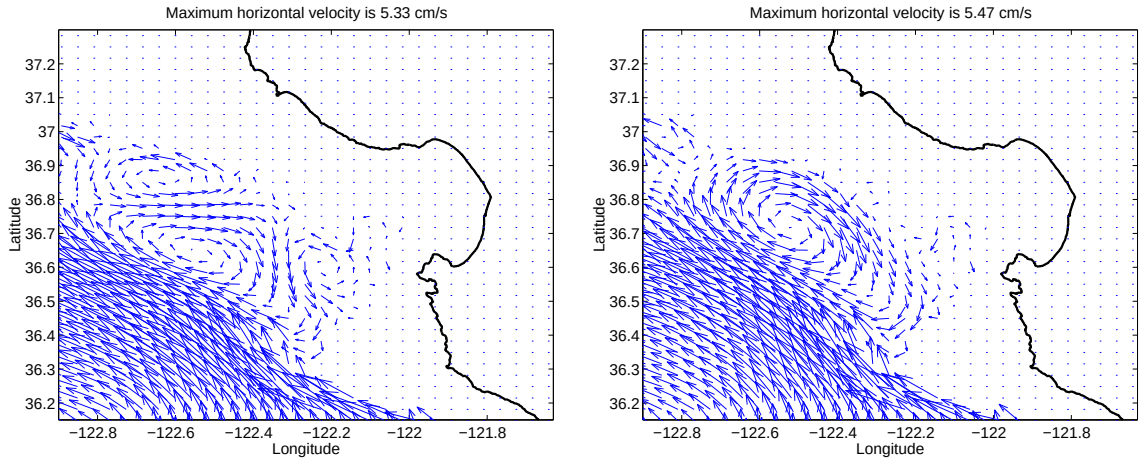

(a) (b)

Figure 7.38: The velocity field at depth 1000 m using the high-resolution MBARM models. The velocity field is monthly averaged during June (day 150-180). (a) hydrostatic and (b) non-hydrostatic.

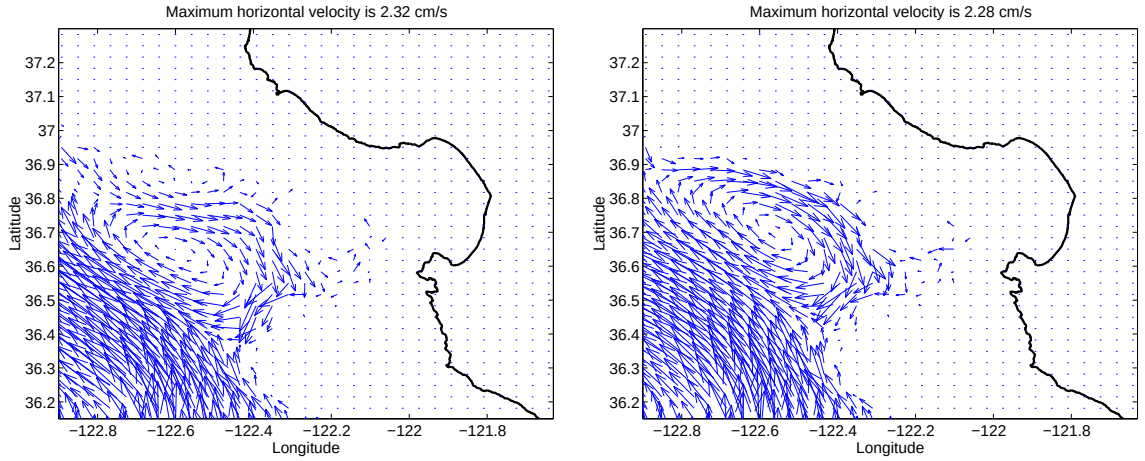

(a) (b)

Figure 7.39: The velocity field at depth 1500 m using the high-resolution MBARM models. The velocity field is monthly averaged during June (day 150-180). (a) hydrostatic and (b) non-hydrostatic.

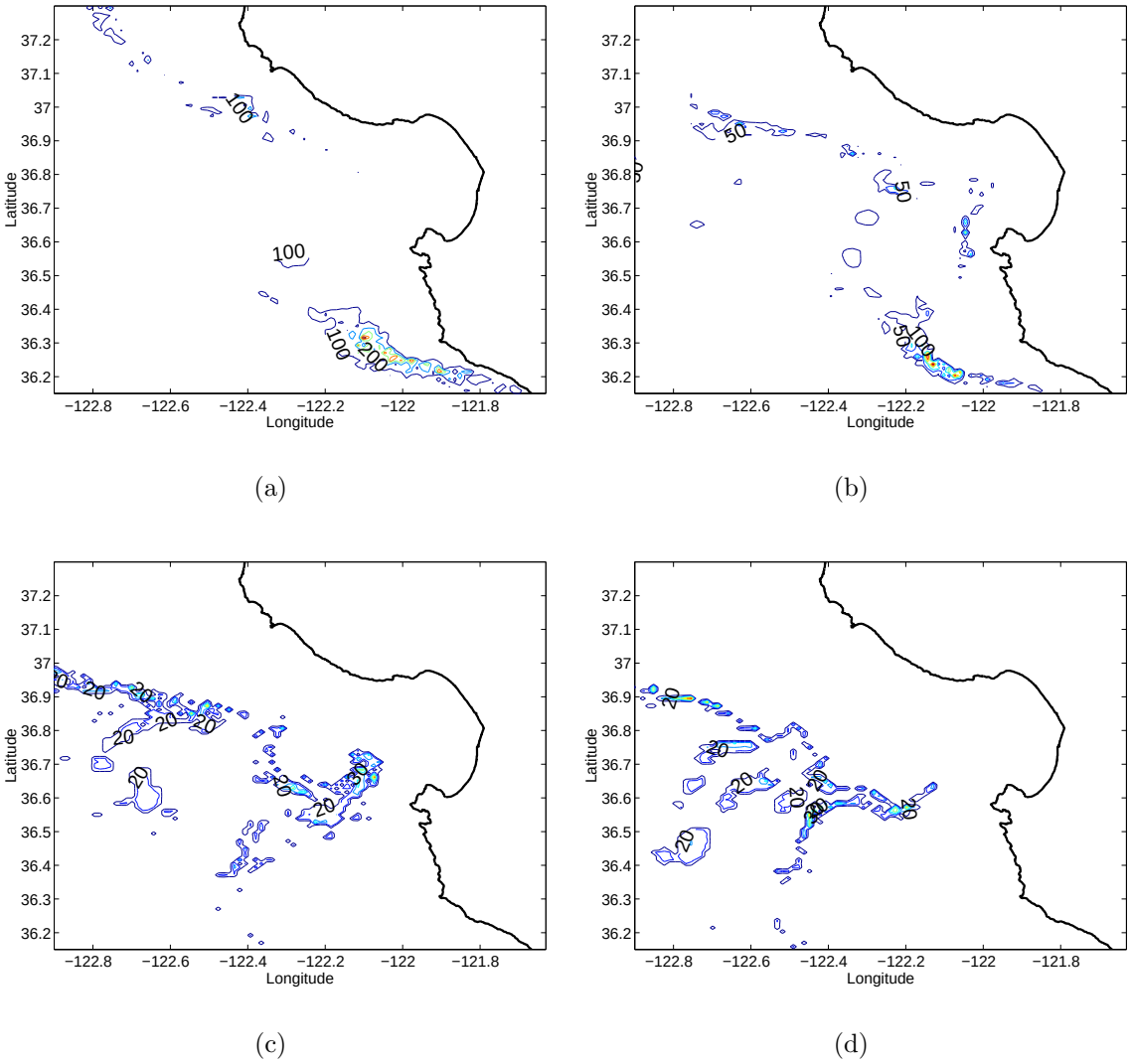

Figure 7.40: The contour of vertical velocity difference ($m/week$) between the hydrostatic and non-hydrostatic models at various depths. (a) 100 m, (b) 700 m, (c) 1500 m, (d) 2000 m, The difference is based on monthly averaged vertical velocity during June (day 150-180).

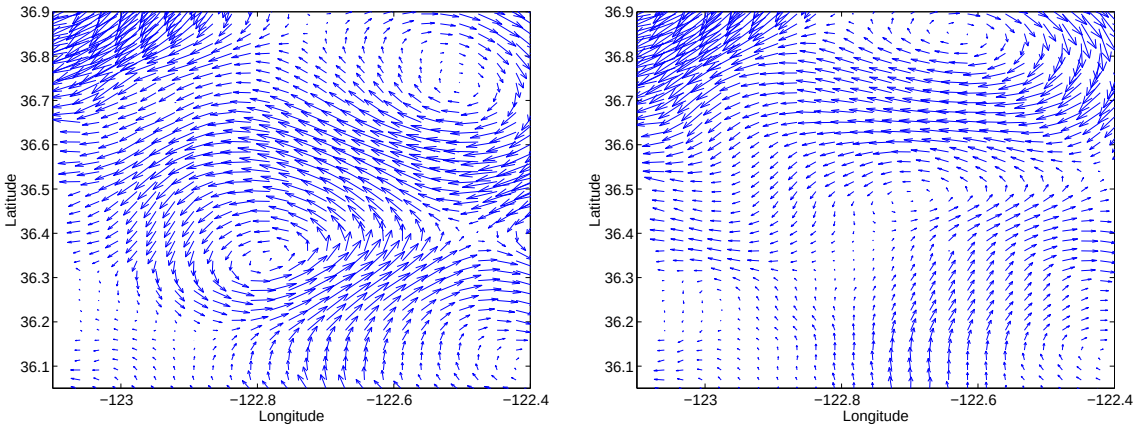

(a) (b)

Figure 7.41: The detailed velocity field in the southwest corner of the domain at depth 10.1 m using the high-resolution MBARM models. The domain includes the intermediate regions (west and south open boundaries) where the depth is smoothed out to match the different depths between the coarse and fine grids (Figure 7.4). The velocity field is monthly averaged during June (day 150-180). (a) hydrostatic and (b) non-hydrostatic.

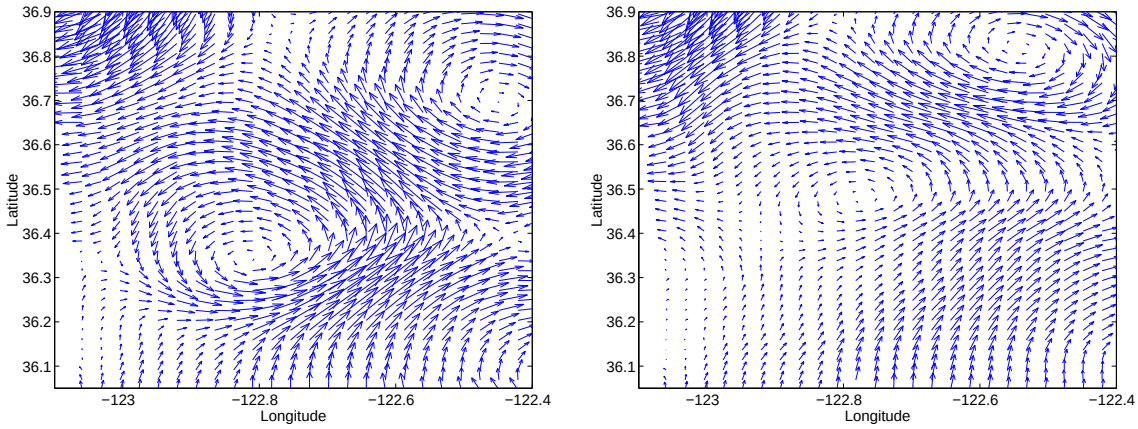

(a) (b)

Figure 7.42: The detailed velocity field in the southwest corner of the domain at depth 50 m using the high-resolution MBARM models. The domain includes the intermediate regions (west and south open boundaries) where the depth is smoothed out to match the different depths between the coarse and fine grids (Figure 7.4). The velocity field is monthly averaged during June (day 150-180). (a) hydrostatic and (b) non-hydrostatic.

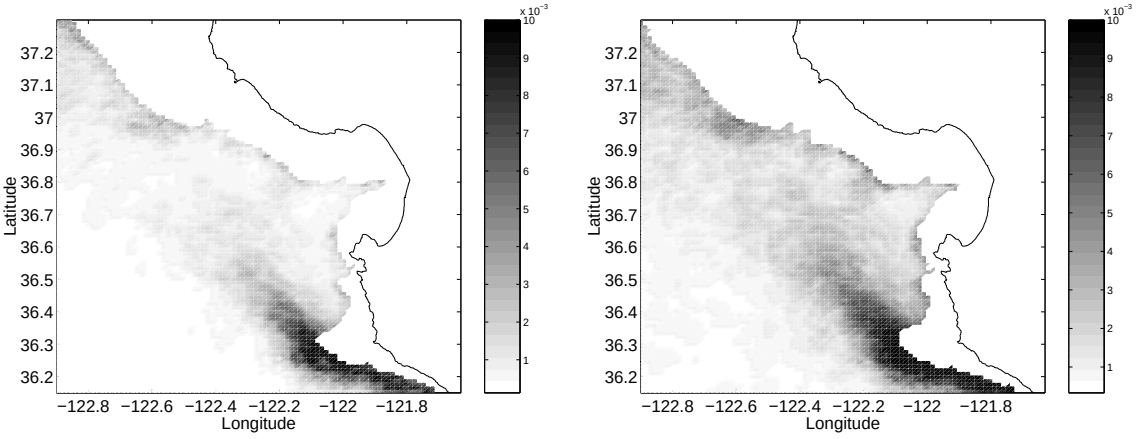

(a) (b)

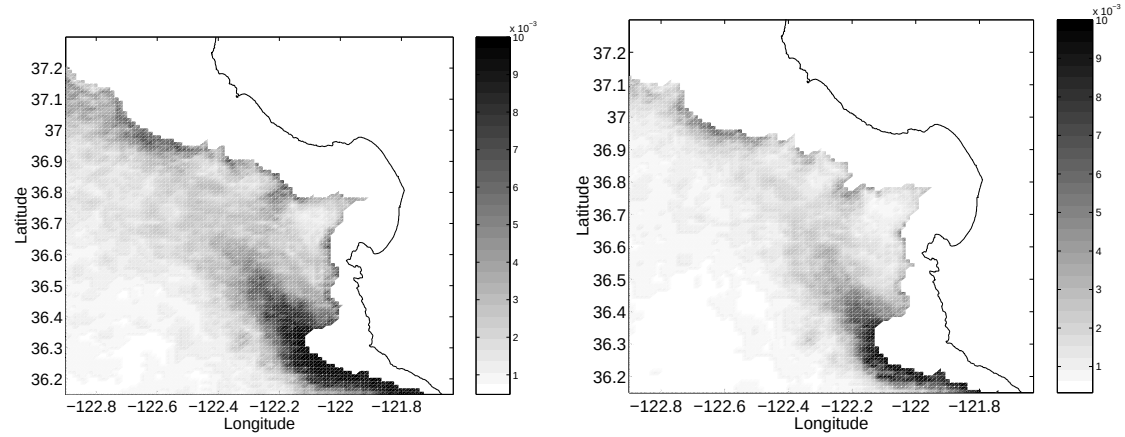

(c) (d)

Figure 7.43: The normalized non-hydrostatic factor at four different depths (a) 170 m, (b) 250 m, (c) 360 m, (d) 500 m. Red color represents the value which is greater than 1×10^{-2}. The maximum value is $O(10)$ locally.

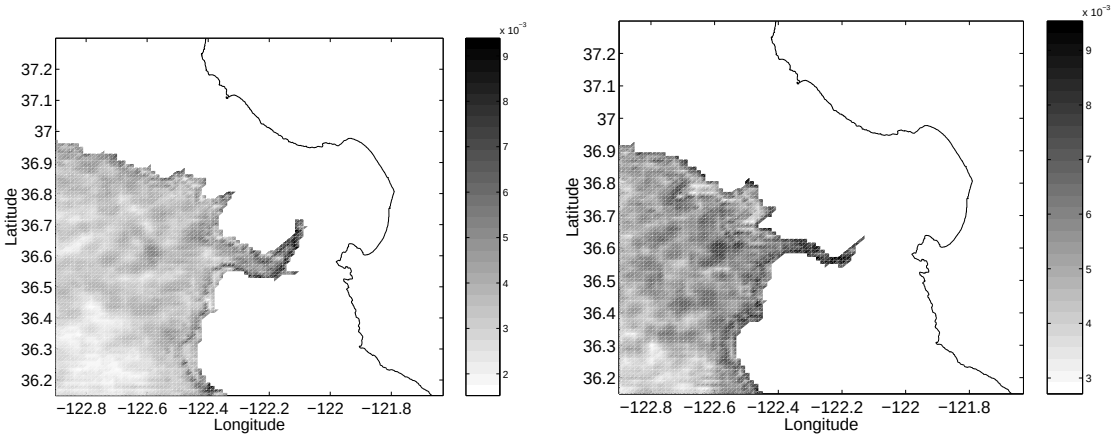

(a) (b)

Figure 7.44: The normalized non-hydrostatic factor at two different depths (a) 1500 m, (b) 1900 m. Red color represents the value which is greater than 1×10^{-2}. The maximum value is $O(10)$ locally.

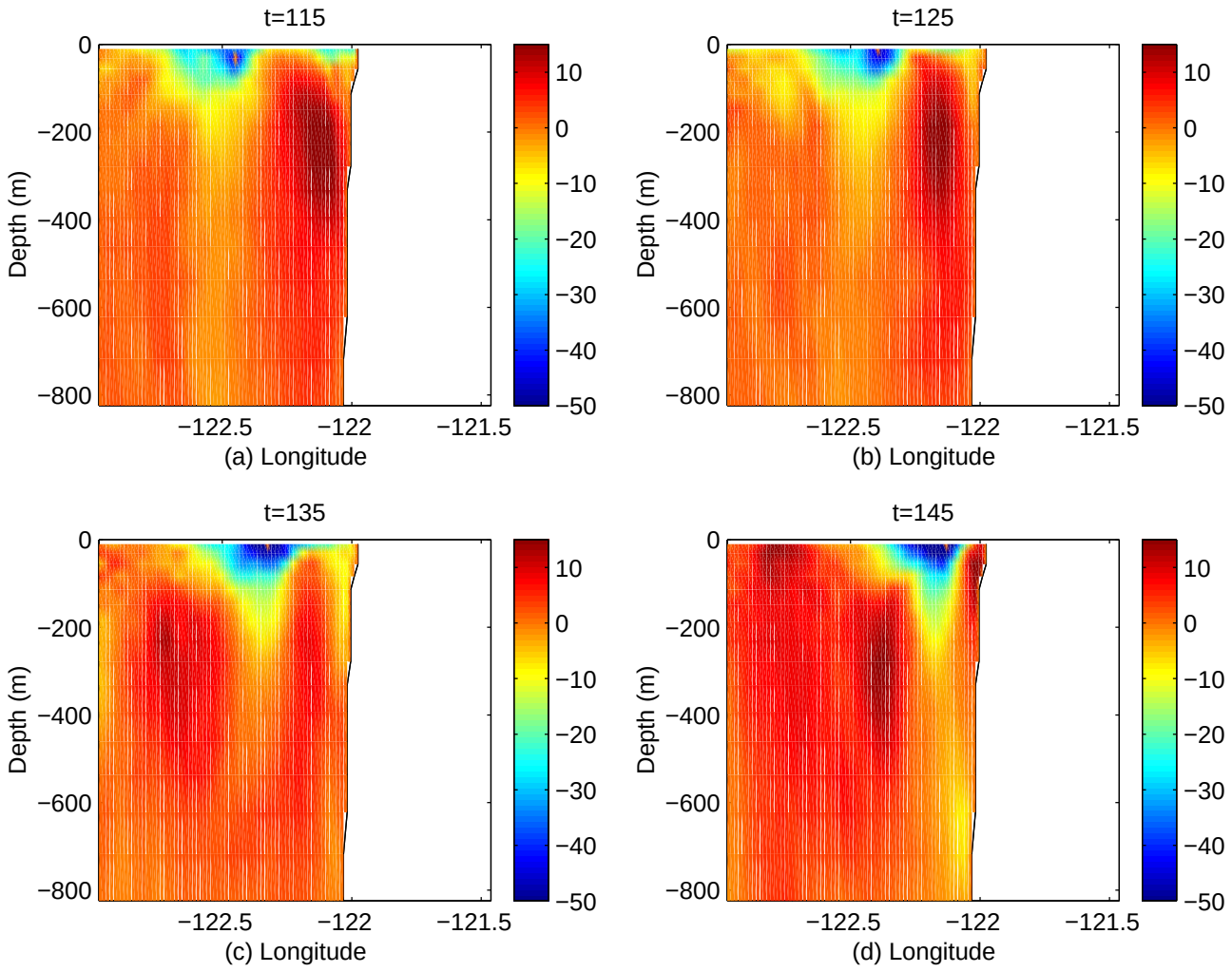

Figure 7.45: Color contours of latitudinal velocity at latitude $36.52°N$ (a) day 115, (b) day 125, (c) day 135, (d) day 145, using the high resolution, non-hydrostatic MBARM model.

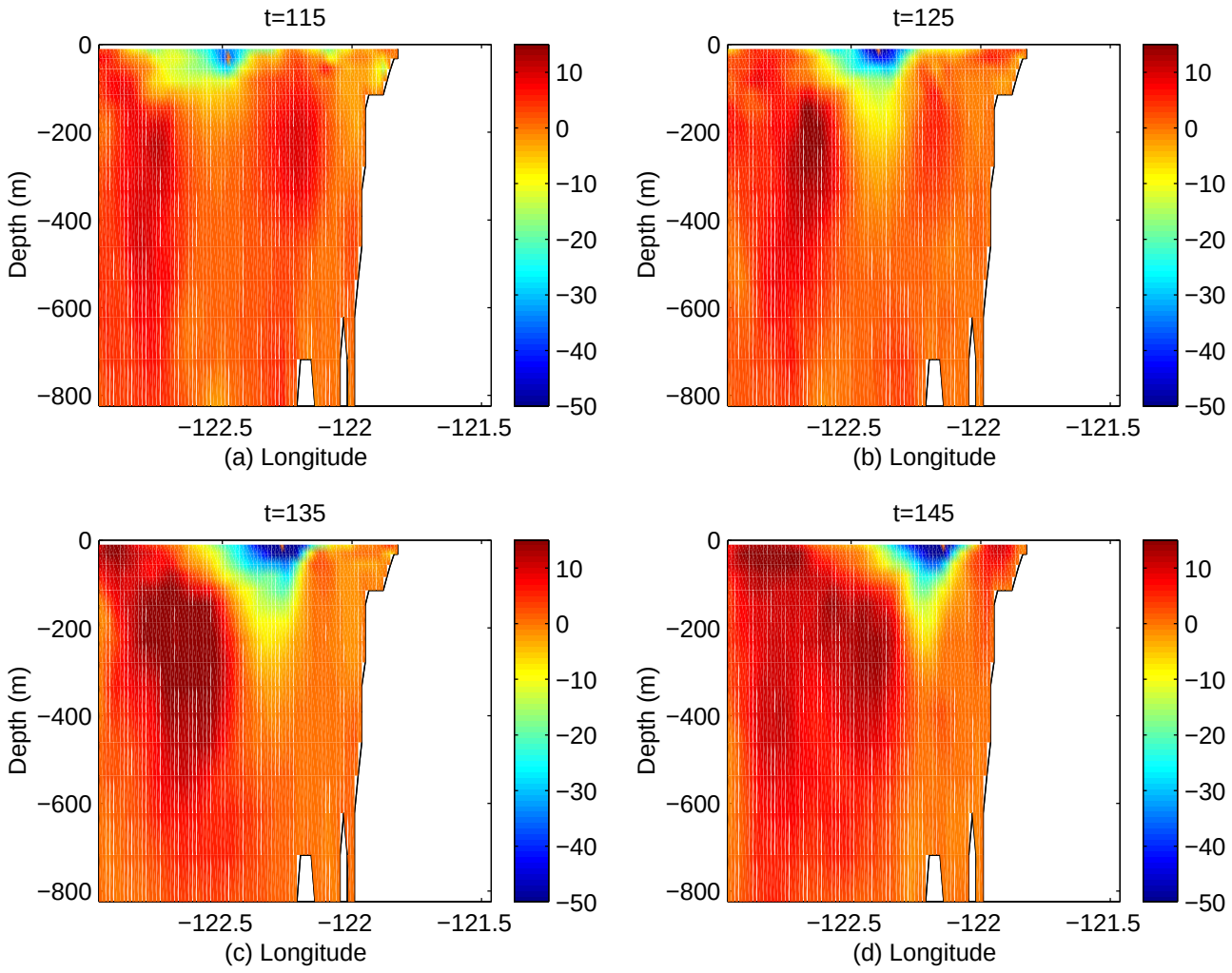

Figure 7.46: Color contours of latitudinal velocity at latitude $36.76°N$ (a) day 115, (b) day 125, (c) day 135, (d) day 145, using the high resolution, non-hydrostatic MBARM model.

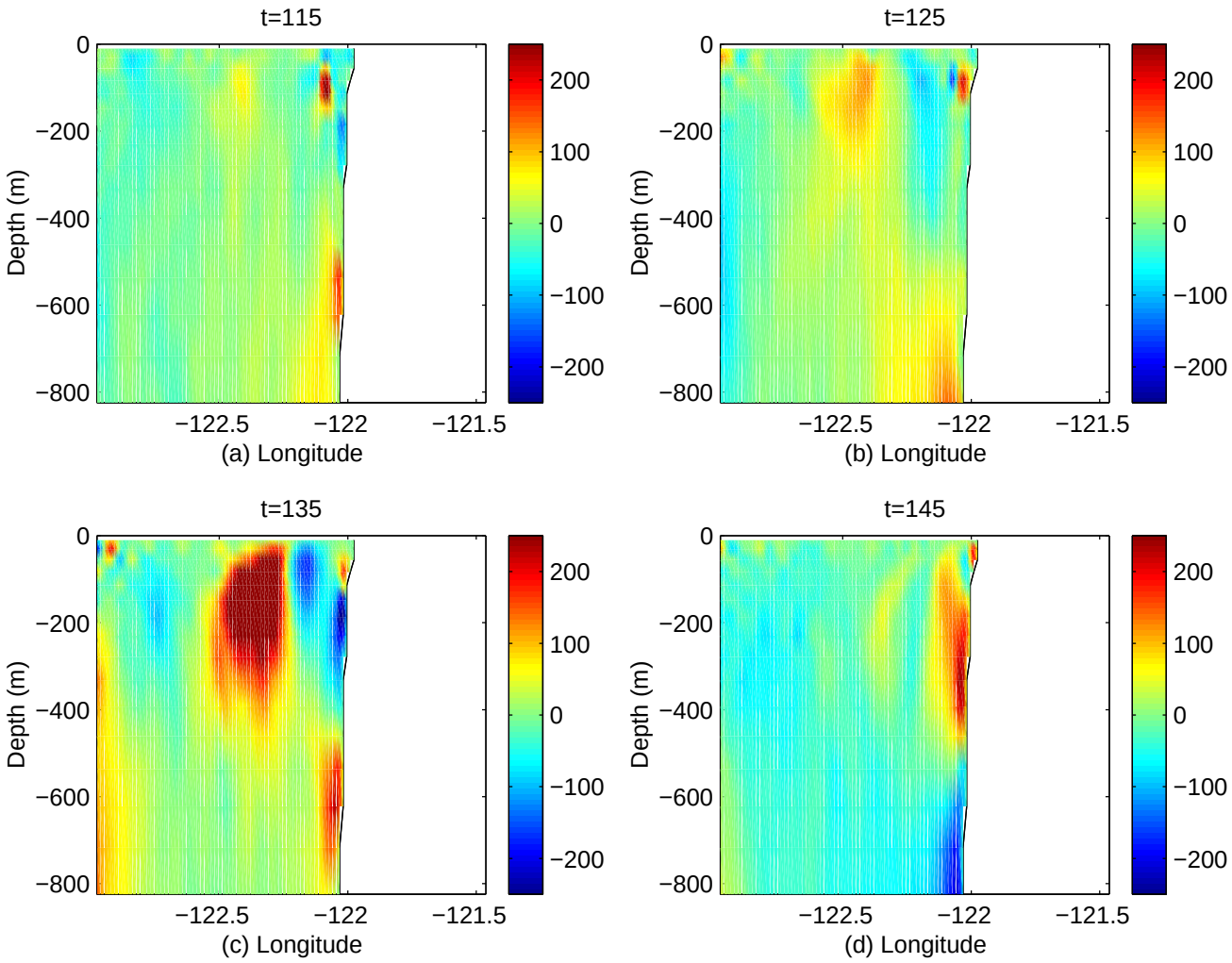

Figure 7.47: Color contours of vertical velocity at latitude $36.52°N$ (a) day 115, (b) day 125, (c) day 135, (d) day 145, using the high resolution, non-hydrostatic MBARM model.

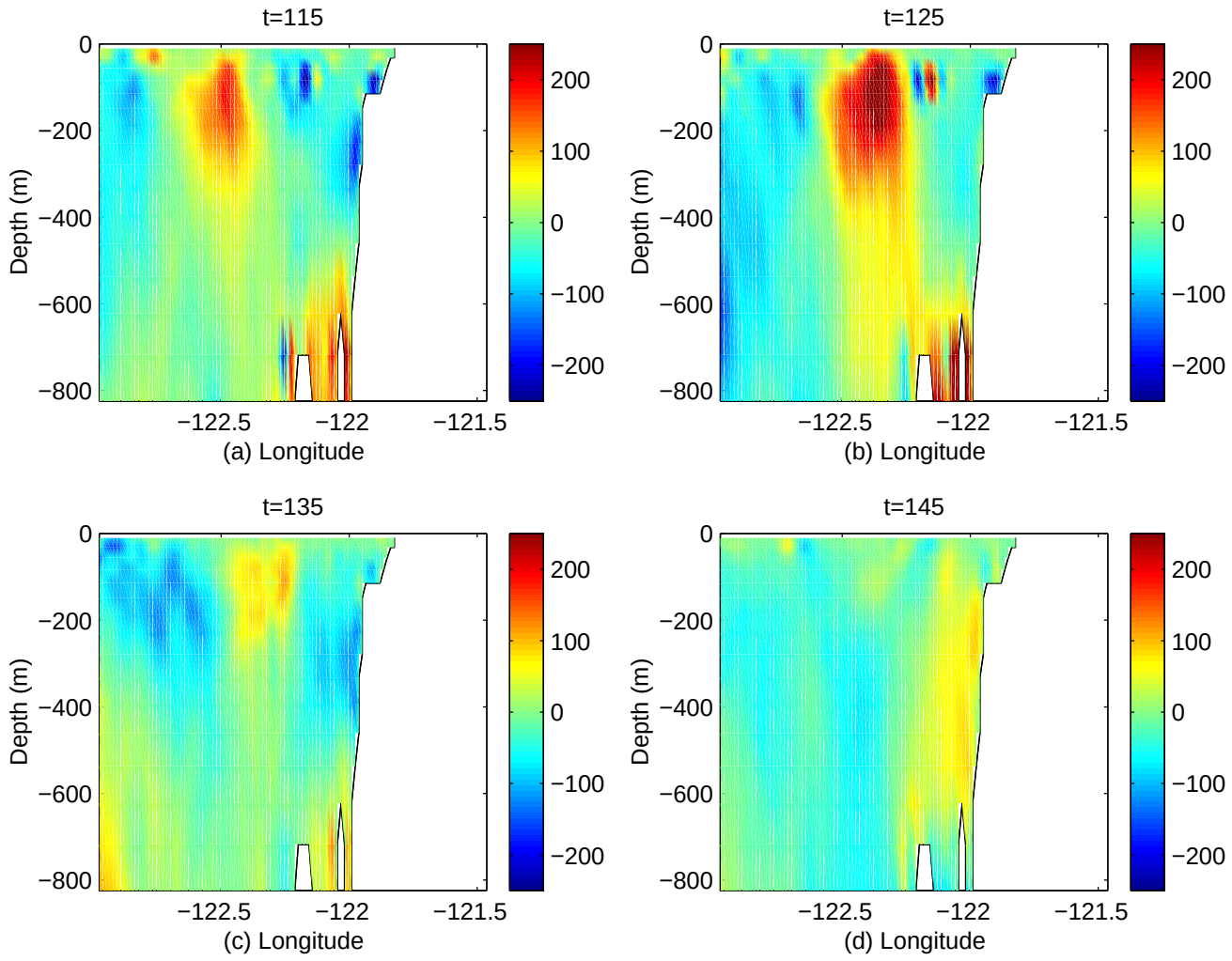

Figure 7.48: Color contours of vertical velocity at latitude 36.76°N (a) day 115, (b) day 125, (c) day 135, (d) day 145, using the high resolution, non-hydrostatic MBARM model.

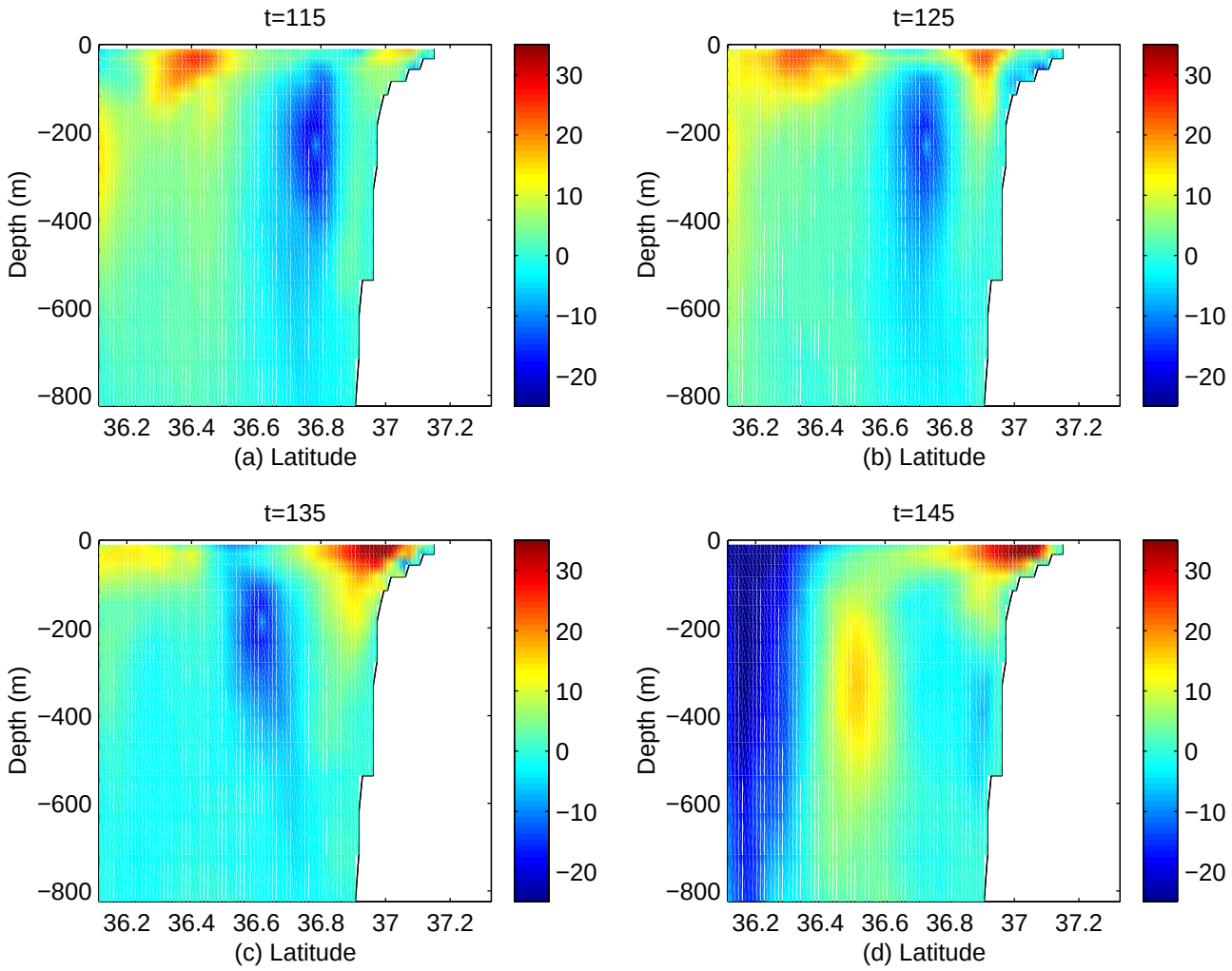

Figure 7.49: Color contours of longitudinal velocity at longitude 122.4°W (a) day 115, (b) day 125, (c) day 135, (d) day 145, using the high resolution, non-hydrostatic MBARM model.

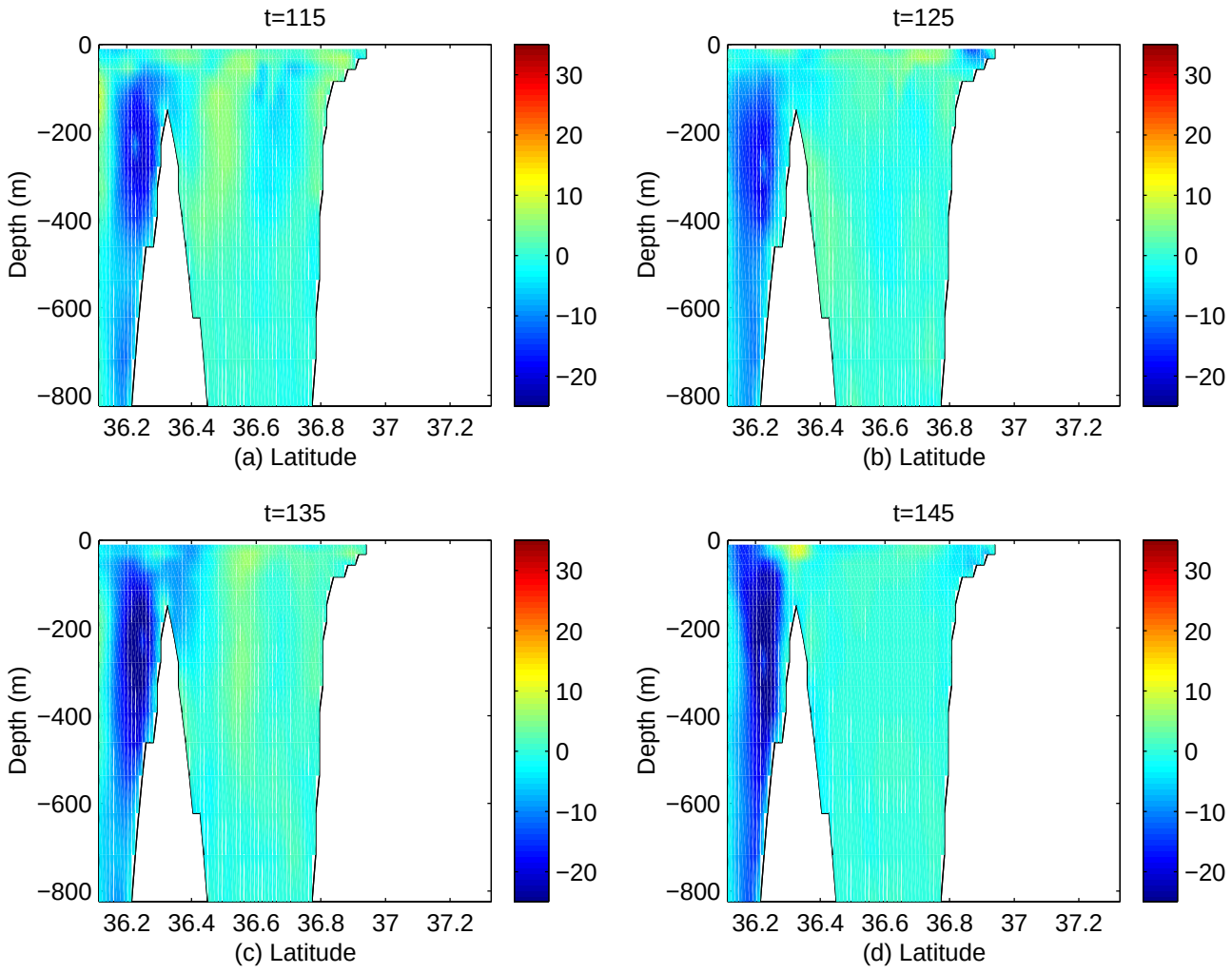

Figure 7.50: Color contours of longitudinal velocity at longitude 122.1°W (a) day 115, (b) day 125, (c) day 135, (d) day 145, using the high resolution, non-hydrostatic MBARM model.

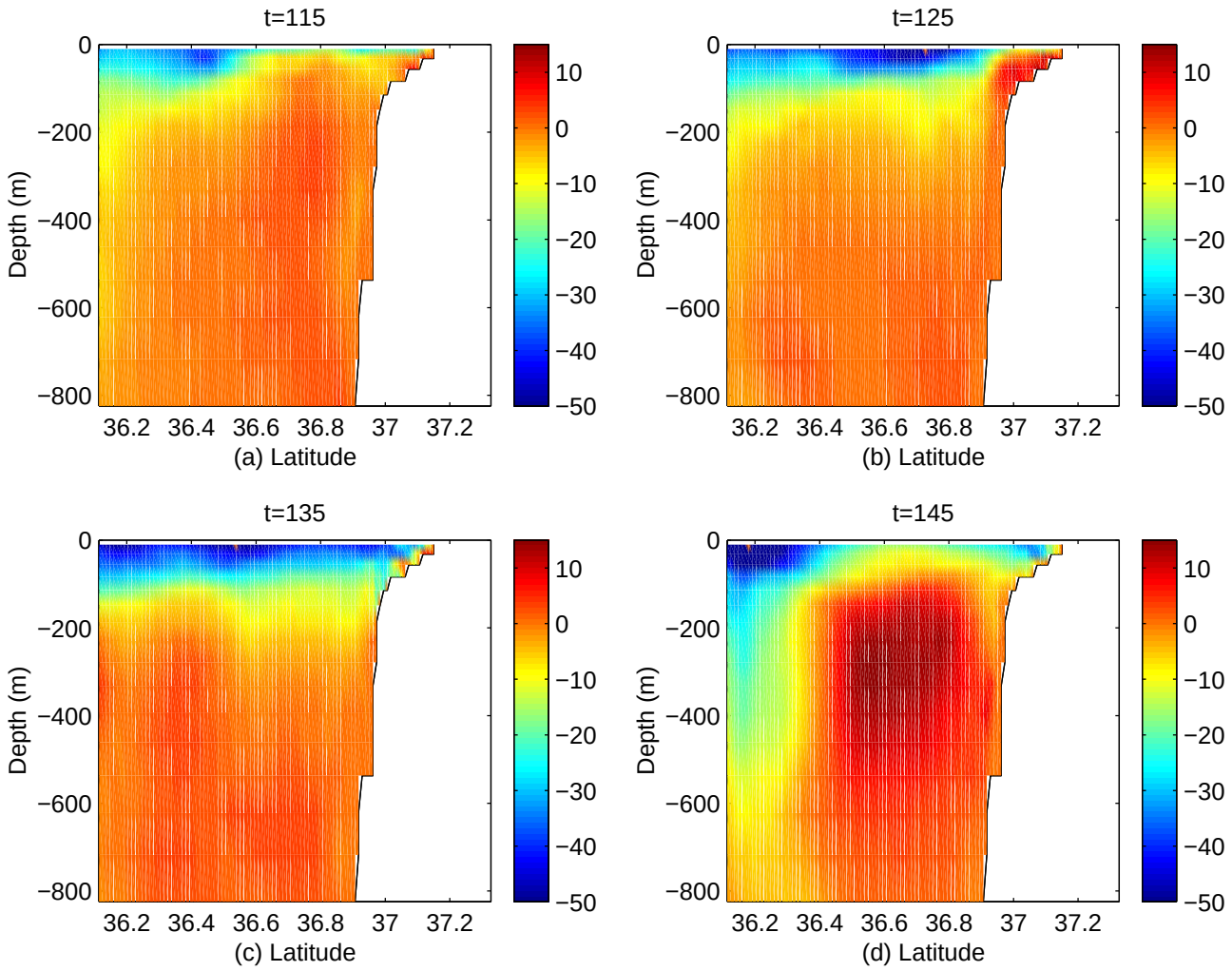

Figure 7.51: Color contours of latitudinal velocity at longitude 122.4°W (a) day 115, (b) day 125, (c) day 135, (d) day 145, using the high resolution, non-hydrostatic MBARM model.

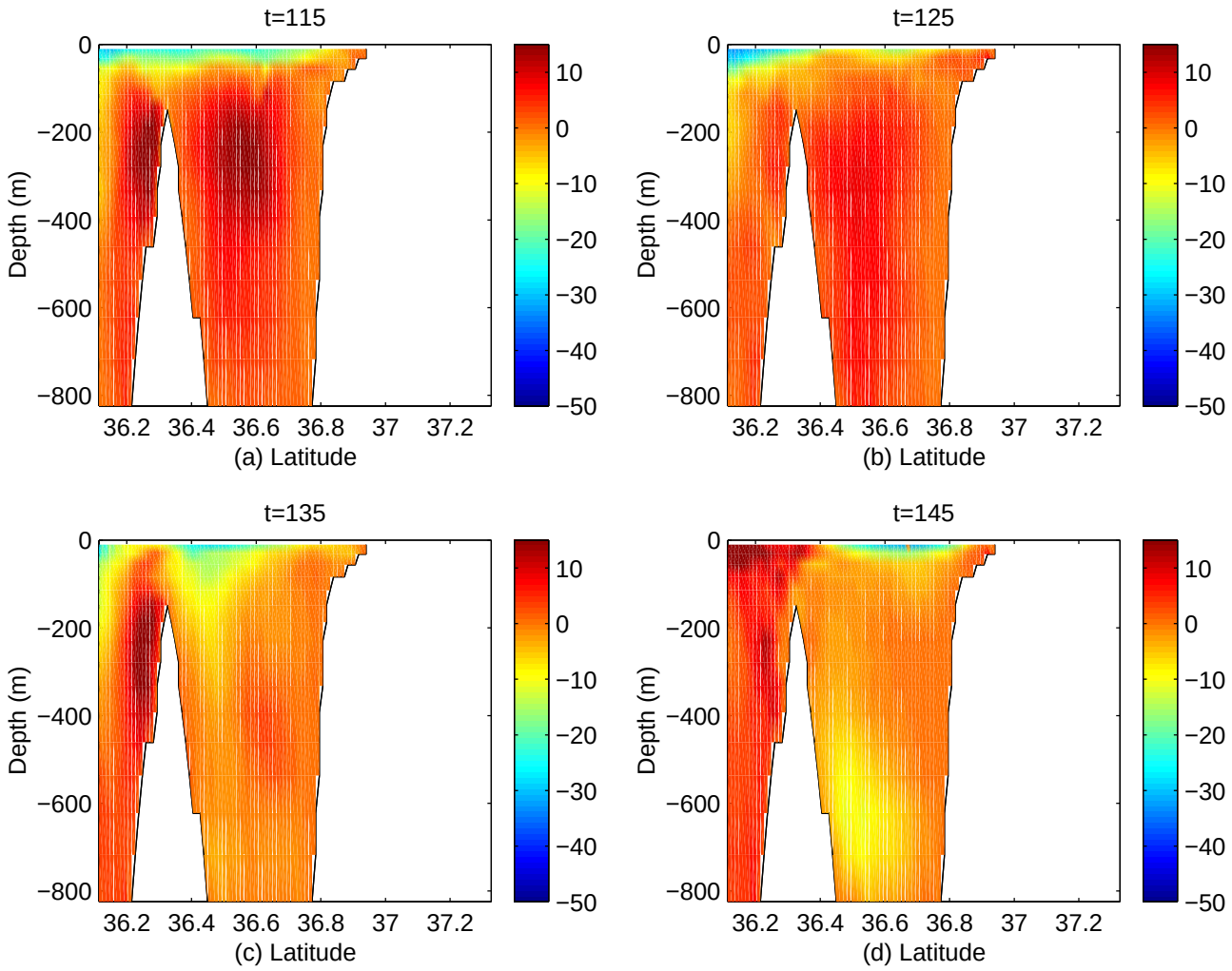

Figure 7.52: Color contours of latitudinal velocity at longitude 122.1°W (a) day 115, (b) day 125, (c) day 135, (d) day 145, using the high resolution, non-hydrostatic MBARM model.

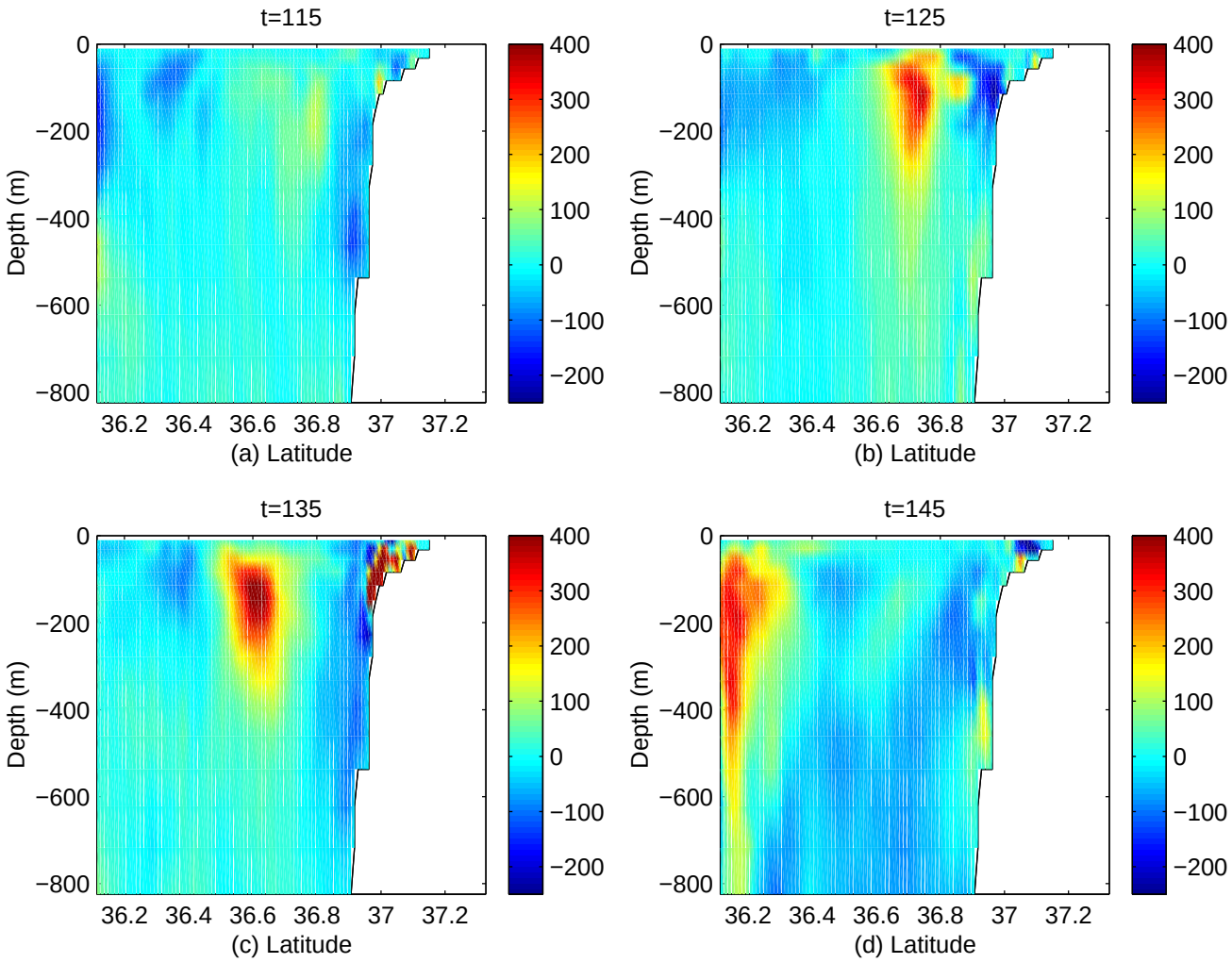

Figure 7.53: Color contours of vertical velocity at longitude 122.4°W (a) day 115, (b) day 125, (c) day 135, (d) day 145, using the high resolution, non-hydrostatic MBARM model.

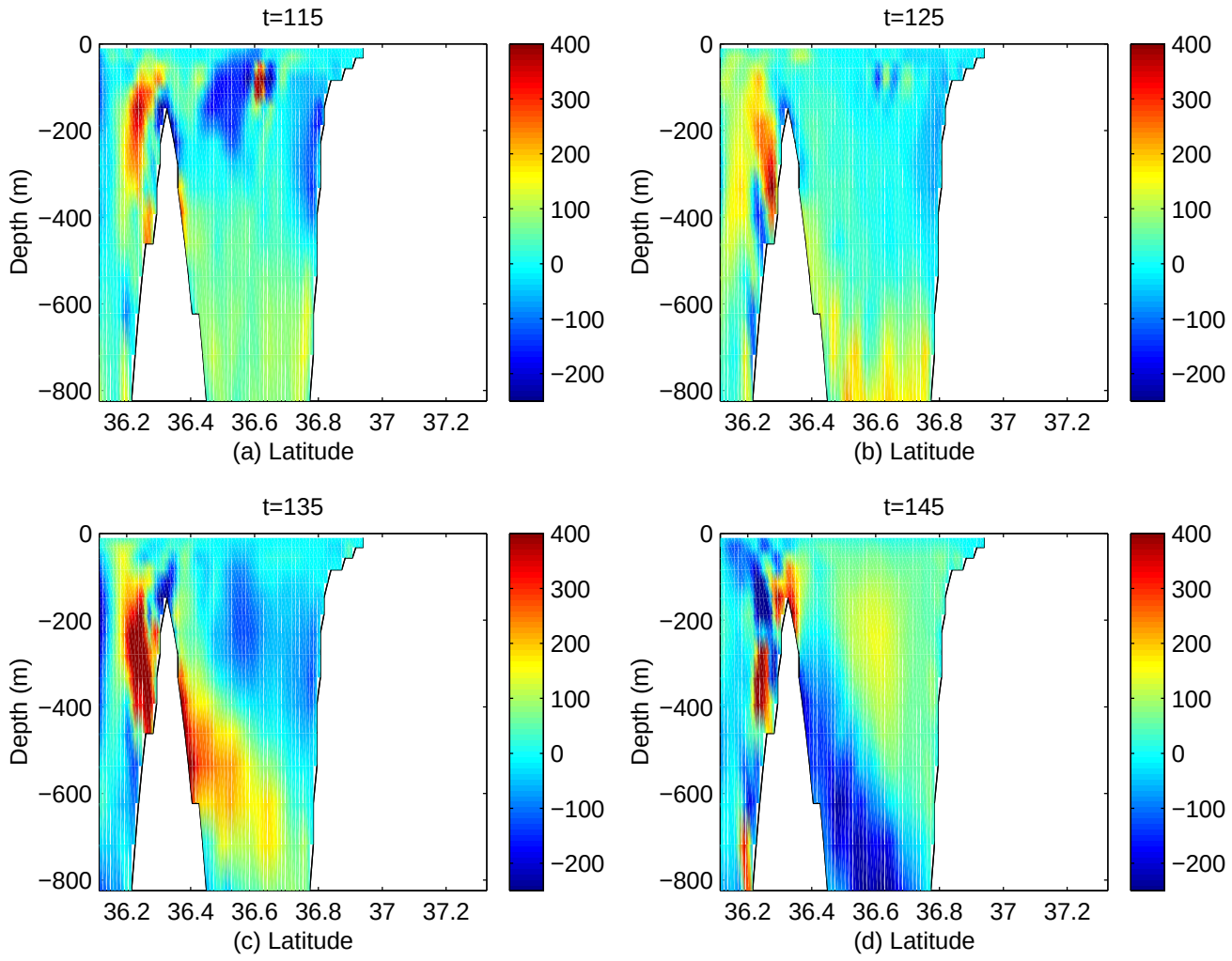

Figure 7.54: Color contours of vertical velocity at longitude 122.1°W (a) day 115, (b) day 125, (c) day 135, (d) day 145, using the high resolution, non-hydrostatic MBARM model.

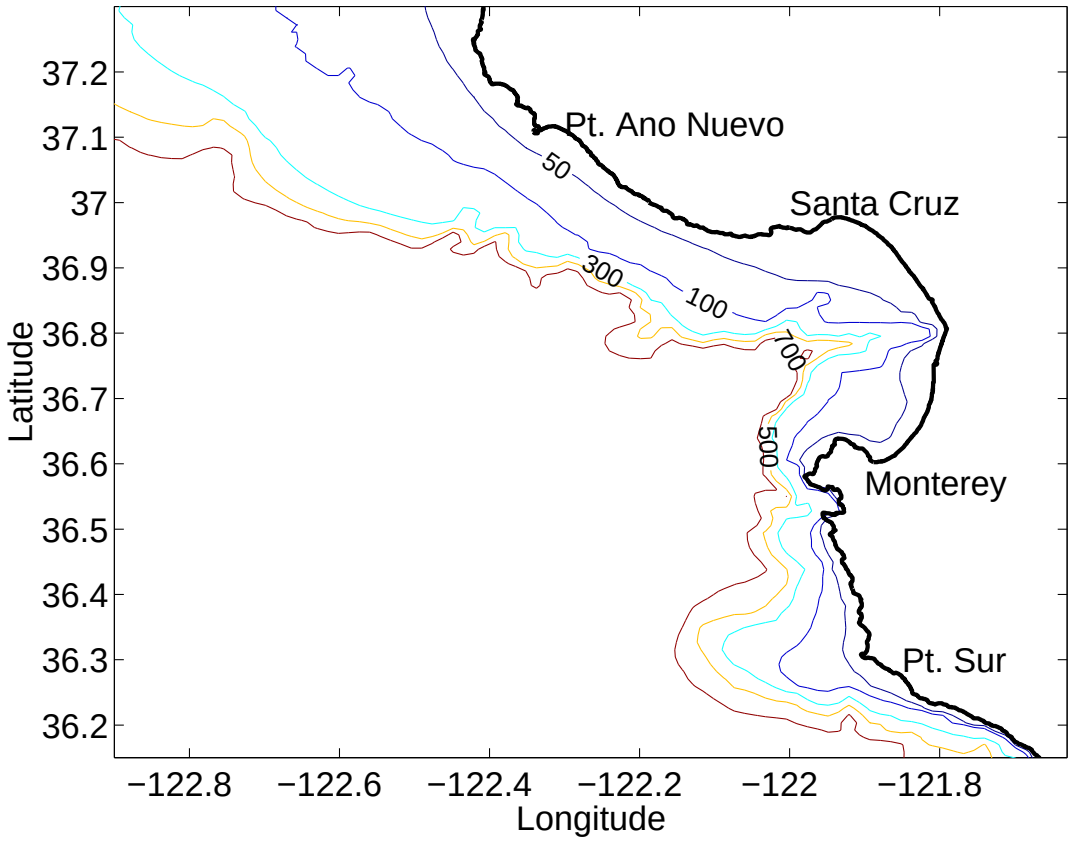

Figure 7.55: The bathymetry of Monterey Bay area without the Monterey Canyon.

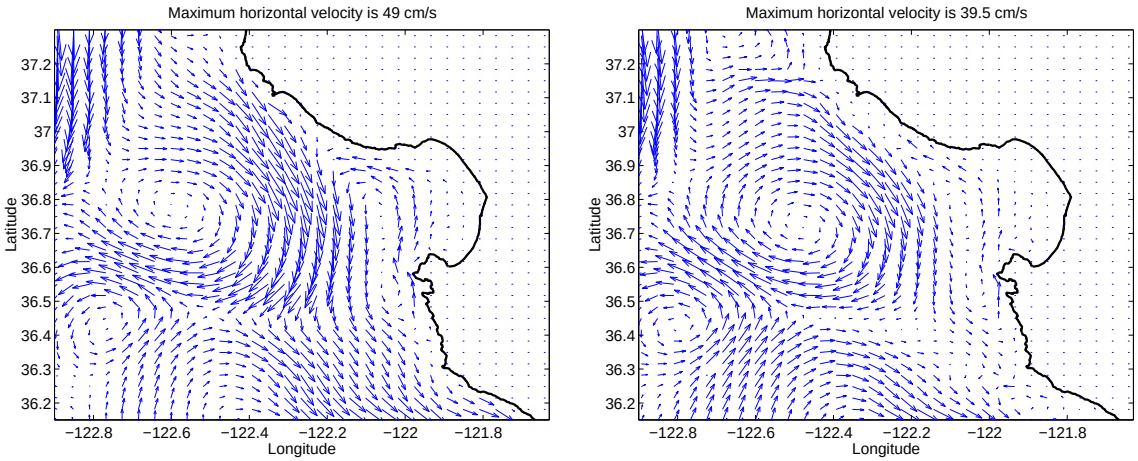

(a) (b)

Figure 7.56: The velocity field at depth (a) 10.1 m and (b) 50 m using the high-resolution MBARM models in the absence of the Monterey Canyon. The velocity field is monthly averaged during June.

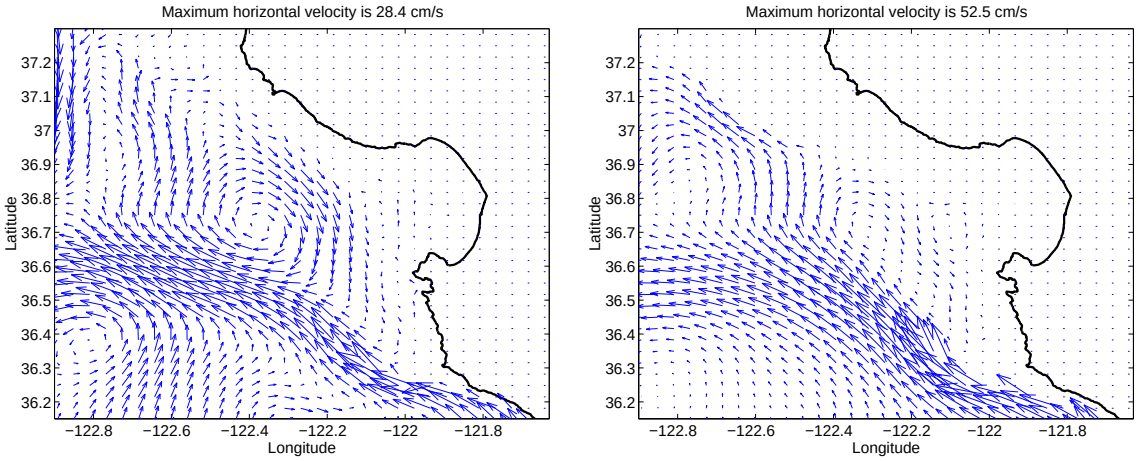

(a) (b)

Figure 7.57: The velocity field at depth (a) 100 m and (b) 300 m using the high-resolution MBARM models in the absence of the Monterey Canyon. The velocity field is monthly averaged during June.

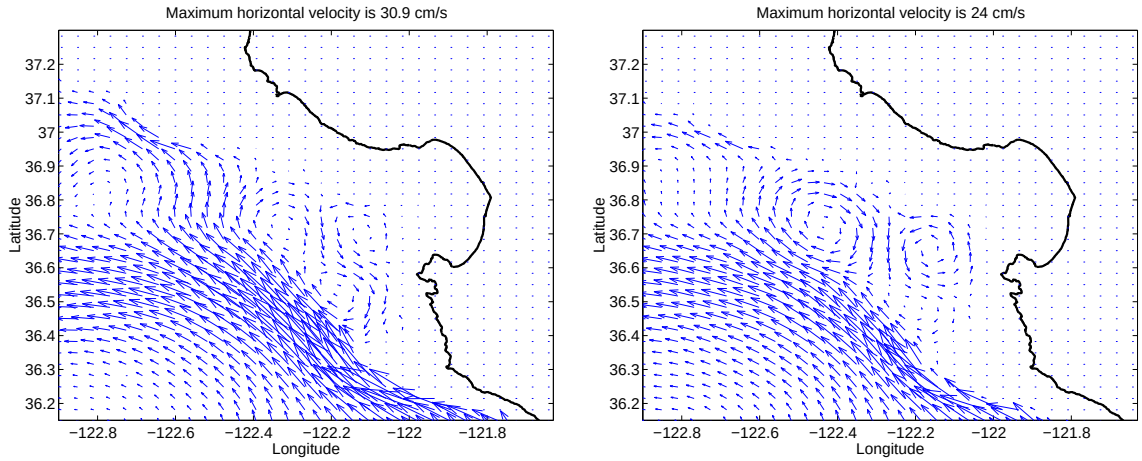

(a) (b)

Figure 7.58: The velocity field at depth (a) 500 m and (b) 700 m using the high-resolution MBARM models in the absence of the Monterey Canyon. The velocity field is monthly averaged during June.

Chapter 8

Conclusions and Recommendations

The objectives of this study were (1) to develop and validate an efficient ghost-cell immersed boundary method (GCIBM) for incompressible flow subject to a variety of boundary conditions, (2) to investigate the effects of coastal perturbations on the eddy evolution and turbulent mixing in a coastal upwelling flow, and (3) to implement the GCIBM in an existing regional ocean model to simulate the coastal circulation in a realistic geometry. Brief conclusions and further recommendations are given in this chapter.

8.1 Conclusions

8.1.1 Ghost-cell immersed boundary method

We formulated a numerical procedure to handle arbitrary geometry on a Cartesian grid. The immersed boundary is represented by piecewise linear segments. A generalized ghost-cell method and polynomial reconstruction schemes were presented. Dirichlet, Neumann and mixed types of boundary conditions may be treated. The image method was used to remove numerical instability. The approach can be used with either non-staggered or staggered grid arrangements. The staggered grid requires slightly more storage but is otherwise no more difficult. The present GCIBM provides flexibility in imposing boundary conditions and is easily implemented. Several

numerical examples are used to demonstrate and validate the current method.

8.1.2 Numerical validation

Two-dimensional uniform flow over a circular cylinder

Laminar flow over a cylinder was used to verify the accuracy of the GCIBM. The simulation results were in good agreement with established experimental and numerical data. A grid resolution study was conducted to verify solution convergence. Both linear and quadratic reconstructions provide overall second-order accuracy although the quadratic one has slightly better convergence.

Three dimensional turbulent flow over a wavy boundary

Large-eddy simulation was used to investigate three-dimensional turbulent flow over a wavy boundary, which was represented by the GCIBM. The accuracy of the current method was then validated by comparing with previous boundary-fitted grid results (Zedler & Street, 2001). The results compare well with the boundary-fitted grid results. The example shows that the GCIBM can be extended to three-dimensional turbulent flow in complex geometry.

Geophysical flow over a three-dimensional bump

In order to verify the realistic geophysical application of the GCIBM, numerical simulations of geophysical flow over a three-dimensional Gaussian bump were performed using the MIT Global Circulation Model (MITGCM). The simulations were compared with the results using stair-step grid, partial-cell and a high resolution study. The comparisons indicated the GCIBM representation was superior to the stair-step grid and had comparable performance to the partial-cell grid.

8.1.3 Effects of coastal geometry and the eddy formation in coastal upwelling

We presented a simulation of coastal upwelling with the aim of understanding the origin and nature of the structures found in the ocean. Cyclones/anti-cyclones and thin filaments observed in satellite infrared images in upwelling regions are rather well reproduced. The instabilities are confirmed to be of mixed baroclinic-barotropic

and modified Rayleigh-Taylor types (Tadepalli, 1997; Cui & Street, 2003). Nonlinear interactions limit the growth of the large scale structures and the latter generate 'fish-hook' structures. The Rayleigh-Taylor and mixed instabilities and fish-hook structures cause sharp increases in mixing. Mixing and stirring are also quantified using a mixedness parameter and a new pdf analysis.

8.1.4 High resolution Monterey Bay area regional model

Finally, we implemented the GCIBM in a high resolution Monterey Bay area regional model (MBARM) to investigate regional circulation. The model was one-way coupled to the California current system model. The model successfully simulated the annual cycle of the CCS and the results compared well with mooring data and satellite images. Non-hydrostatic effects were found to play an important role in the coastal region, $O(1-50)km$ from shore. The results also showed that the general circulation was greatly influenced by Monterey Canyon and the non-hydrostatic effects are largely due to the presence of the deep canyon.

8.2 Recommendations for Future Study

This study has contributed to the development of the generalized ghost-cell immersed boundary method, validating the GCIBM using several well-documented experimental and numerical results, investigating the formation and structure of cyclonic/anticyclonic eddies in coastal upwelling, and assessing the influence of coastal bathymetry and geometry on regional circulation. Some recommendations for future study are given below.

The current GCIBM has been extensively validated for cases with no-slip boundary conditions. It admits other types of boundary conditions. However, we need an accurate way to represent a rough boundary. Cui *et al.* (2003) proposed a force field model to simulate turbulent flow over a rough wavy surface based on the method developed by Verzicco *et al.* (2000). They could not reproduce the mean velocity profile in the near-wall region, and the model requires an empirical drag coefficient. Poor

agreement near a rough wavy wall was found in our investigation of a high Reynolds number ($Re = 5 \times 10^6$) turbulent wavy boundary flow. We implemented the empirical log-law in a Cartesian grid code and compared the mean velocity profile with that in Zedler (2002). The simulation results matched the boundary-fitted grid results well except in the near-wall region. Development of a method of representing a realistic rough boundary is needed.

The components of a successful coastal ocean model and their interactions are illustrated in Figure 8.1. The coastal zone is hardly resolved in regional scale simulation. The GCIBM provides an efficient means of incorporating bathymetry directly. Accurate representation of the bathymetry is required in the coastal region where many currents and eddies are influenced by coastal geometry, e.g. the California undercurrent and the Deep Western Boundary Current of the Gulf Stream. We can generalize the method to include a wall model near the coastal and bottom boundaries and/or to develop a thin shell boundary layer model (Dietrich *et al.*, 1987). Very similar ideas, e.g. turbulent bottom boundary layer model, were proposed in recent years (Song & Chao, 2000; Killworth & Edwards, 1999). The details of the boundary layer need not be resolved if only the average effect is needed.

The current simulation uses a rigid-lid approximation on the sea surface since the low-frequency mode dominates the regional circulation. This constraint can be relaxed by using a free surface to take the effects of waves into account. The hydrostatic version of the current model has been modified to include a free-surface to study an idealized internal tide generation over sloping topography (Lu *et al.*, 2001). The free-surface formulation allows the surface elevation to change in response to divergence and convergence of the depth integrated flow and represents the surface gravity wave explicitly. The updating of free-surface elevation is implicit in time so that the extra computational cost is minimal. This approach can be extended to incorporate the tidal forcing from the open boundary. The effects of waves could be parameterized. In addition, an ultra-high resolution model of Monterey Bay can be used and two-way coupled to the current MBARM.

Another major concern in ocean modeling is the air-sea interface parameterization. The interface involves complicated interactions between the atmosphere and the

ocean. The link between the commonly seen oceanic, cyclonic eddy within Monterey Bay and atmospheric Santa Cruz eddy is still not clear.

In the regional ocean model, the coastal currents develop local jets with large topographically modulated variability. Offshore currents have intrinsic variability from instabilities of the along-shore currents. They are generated as part of the large-scale circulation or emerge from the near-shore regions. In practice, it is not feasible to use a computational domain large enough to resolve all types of currents. The current MBARM uses one-way coupling to allow information from the CCS to enter the coastal region. In order to examine their dynamical interactions, full two-way coupling is needed. Two-way nesting will generate much smoother results and remove artificial fronts when the boundary flow switches between outflow and inflow.

Non-hydrostatic effects have been shown to be important in the coastal region. To better understand the dynamics of the coastal region, which is strongly affected by coastal perturbations and bathymetry, non-hydrostatic effects should be further investigated using non-hydrostatic coastal model with simplified coastal geometry, e.g. an idealized bay and an idealized submarine canyon. The current simulation results identify some important non-hydrostatic effects. However, realistic topography and forcing complicate the analysis and understanding of the physical process. Detailed analysis is required to quantify non-hydrostatic effects on the overall circulation.

Accurate prediction of oceanic circulation using satellite infrared image data and other measurements is very important for hindcasting and real-time forcasting. The current numerical model uses annual forcing from the climatology and generates a realistic annual cycle of the current, temperature, and salinity fields.

Some improvements on the current model can be made in the future. The current DieCAST model uses a leap-frog scheme for the time advance. This method is commonly used in the oceanographic community and is easy to implement. However, the method needs a very small time step in high resolution studies and increases computational cost if the energy-containing modes have long time scales. A leap-frog trapezoidal algorithm could be used to relax the constraint (Rueda, 2001; Rueda *et al.*, 2003). The leap-frog scheme is used in the first iteration and is followed by trapezoidal steps. The trapezoidal steps increase the stability of the code. Another

alternative is to use a fourth-order Runge-Kutta method which provides simplicity and accuracy without a small time-step restriction.

Figure 7.11 (a) shows weak oscillation along the surface temperature front. The oscillation propagates into the computational domain from the southern boundary and is advected in the streamwise direction (boundary current). This could be associated with the one-way nesting at the boundary combined with the high-order numerical scheme, but it seems not degrade the quality of the simulation results. This phenomenon can be removed numerically by adding a sponge layer in the lateral boundary grids adjacent to the coupled coarse grids. Another alternative is to use a new coordinate invariant streamwise upwind formulation (Ferziger & Tseng, 2003). The method adds anisotropic diffusivity/viscosity only in the streamwise direction to eliminate the oscillation and possesses the desirable features of accuracy and stability. This method minimizes the needed diffusivity and is suitable for coastal ocean applications.

Further investigation of turbulent mixing in Monterey Bay is needed to quantify the effects of coastal geometry on the turbulent mixing. The turbulent mixing has been quantified in a laboratory upwelling flow. This task is attractive in the vicinity of the Monterey Bay because of the great diversity and abundance of marine life found there. The interaction of the continental shelf, slope, and open ocean contributes a great deal to the dynamics of coastal upwelling and mixing process in the bay. Particularly, the vertical transport (flux) and turbulence should be carefully quantified in this region due to the significance of the non-hydrostatic effect. The influence of internal waves should not be ignored. The current high-resolution, non-hydrostatic MBARM model provides a unique approach for this study. However, the quantification is not an easy task since the fluxes across lateral open boundary change both kinetic and potential energy budgets inside the simulation domain and the effects have to be considered.

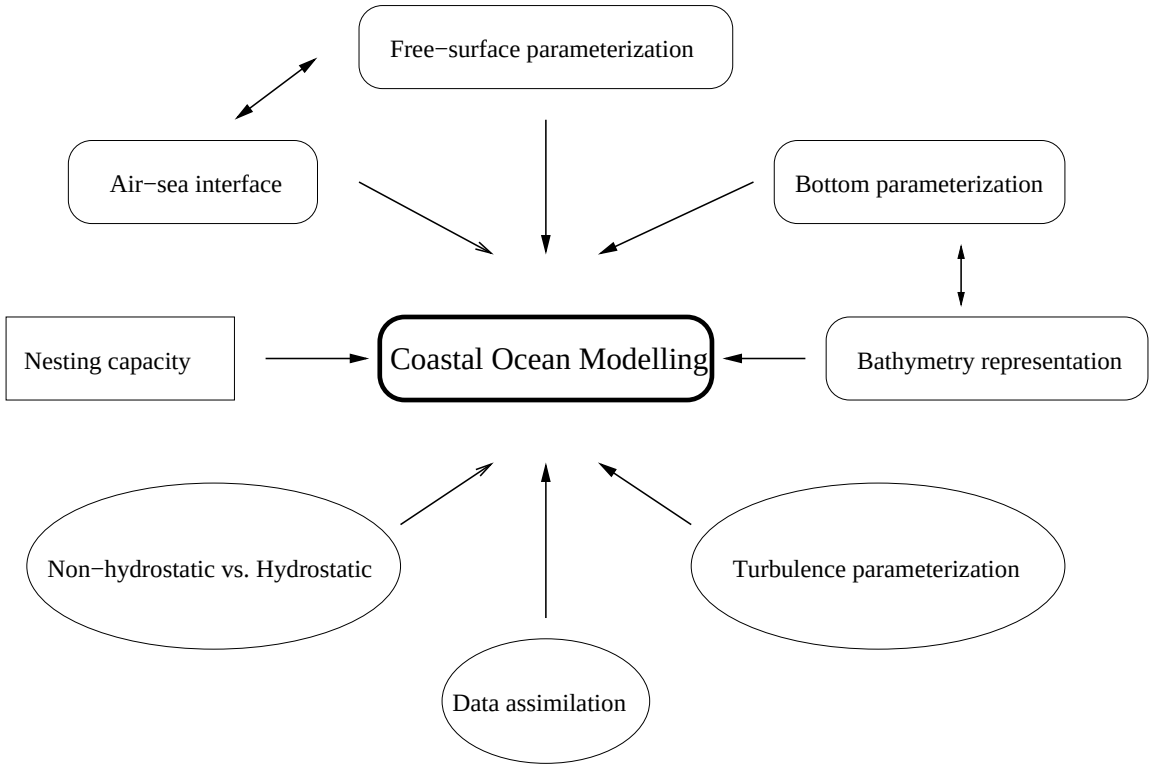

Figure 8.1: Challenging components for a successful coastal ocean model and their interaction.

Appendix A

Filtered Equations for Large Eddy Simulation

In a large-eddy simulation (LES), each flow variable ϕ is decomposed into a large-scale (or resolved) component $\overline{\phi}$ and a subgrid-scale (or unresolved) component ϕ',

$$\phi = \overline{\phi} + \phi' \tag{A.1}$$

A filtered quantity $\overline{\phi}$ is defined as:

$$\overline{\phi} = \int_D \prod_{i=1}^{3} G_i(x_i, x_i')\phi(x_1', x_2', x_3')dx_1'x_2'x_3' \tag{A.2}$$

where G_i is the filter function and D is the entire domain. The governing equations for the LES are space-filtered by applying the above filtering operation to the Equations (2.1)-(2.3) in Chapter 2. The resulting filtered equations are:

$$\frac{\partial \overline{u}_j}{\partial x_j} = 0 \tag{A.3}$$

$$\frac{\partial \overline{u}_i}{\partial t} + \frac{\partial}{\partial x_j}(\overline{u}_i\overline{u}_j + \overline{p}\delta_{ij} - \nu\frac{\partial \overline{u}_i}{\partial x_j}) = -g\overline{\rho}'\delta_{i3} + 2\Omega(-\overline{u}_1\delta_{i2} + \overline{u}_2\delta_{i1}) + \overline{f}_i - \frac{\tau_{ij}}{x_j} \tag{A.4}$$

$$\frac{\partial \overline{s}}{\partial t} + \overline{u}_j\frac{\partial \overline{s}}{\partial x_j} = \frac{\partial}{\partial x_j}(\kappa\frac{\partial \overline{s}}{\partial x_j}) - \frac{\partial \chi_j}{\partial x_j} \tag{A.5}$$

The filtered equations govern the evolution of the large, energy-containing, scales of motions. Two extra terms, which represent the effect of the unresolved scales, appear in the above equation. These two terms are the subgrid-scale (SGS) stress tensor τ_{ij} and subgrid-scale flux vector χ_j. They are defined as

$$\tau_{ij} = \overline{u_i u_j} - \overline{u_i}\ \overline{u_j} \tag{A.6}$$

$$\chi_j = \overline{u_j s} - \overline{u_j}\ \overline{s} \tag{A.7}$$

The large-scale N-S and scalar transport equations are closed by modeling τ_{ij} and χ_j using the filtered quantities.

Appendix B

Bi-CGSTAB Iteration Method with Strongly Implicit Procedure (SIP) Preconditioning

The motivation for Bi-CGSTAB method is to eliminate the need to use A^T in the Bi-CG algorithm and to smooth convergence of the Conjugate Gradient Squared (CGS) method for non-symmetric linear system. CGS is the first of this class of techniques referred to as transpose-free variants of the bi-conjugate gradient method. However, CGS has a quite irregular convergence behavior, in particular when starting the iteration close to the solution. Bi-CGSTAB is an attractive alternative to CGS. Its convergence behavior is much smoother so that it often produces a much more accurate residual, and it converges considerably faster than CGS (van der Vorst, 1992).

When Krylov subspace methods are employed for solving linear systems, the convergence of these iterative methods can be improved by *preconditioning* the linear system $Ax = b$. The preconditioned system $M^{-1}Ax = M^{-1}b$ can be solved faster than the original system if the preconditioner M is an efficient and good approximation to A. The preconditioned Bi-CGSTAB algorithm for solving the linear system $Ax = b$ with preconditioning M is provided in the following.

Compute $r^0 = b - Ax^0$ for some initial guess x^0
Choose arbitrary $\overline{r}^0$ such that $(r^0, \overline{r}^0) \neq 0$ (e.g. $\overline{r}^0 = r^0$)
$\alpha^0, w^0 = 1,$
for $i = 1, 2, ...$
$\rho_{i-1} = (\overline{r}^0, r^{i-1})$
if $i = 1$
$p^i = r^{i-1}$
else
$\beta_{i-1} = (\rho_{i-1}/\rho_{i-2})(\alpha_{i-1}/w_{i-1})$
$p^i = r^{i-1} + \beta_{i-1}(p^{i-1} - w_{i-1}v^{i-1})$
endif
Solve $\overline{p}$ from $M\overline{p} = p^i$
$v^i = A\overline{p}$
$\alpha_i = \rho_{i-1}/(\overline{r}^0, v^i)$
$s = r^{i-1} - \alpha_i v^i$
if $||s||$ small enough then $x^i = x^{i-1} + \alpha_i \overline{p}$ and stop
Solve z from $Mz = s$
$t = Az$
$w_i = (s, t)/(t, t)$
$x^i = x^{i-1} + \alpha_i \overline{p} + w_i z$
if x^i is accurate enough then quit
$r^i = s - w_i t$
end

The ILU preconditioner has been shown to be robust and general (Golub & van Loan, 1996). It uses an approximate LU factorization of A as the preconditioning matrix $M = LU$. A schematic representation of the matrices L and U is shown in Fig. B.1. The procedure needs only backward-solve and forward-solve loops. The elements of the matrices L and U can be calculated only once, prior to the first iteration. SIP is an improved incomplete lower-upper decomposition that is specifically designed for algebraic equations that are discretizations of partial differential equations. The method is not widely used since it does not apply to generic systems of equations (Ferziger & Perić, 2001).

The calculation of the elements of L and U in 3D at location (i, j, k) is summarized in the following equations for SIP preconditioning,

$$
\begin{aligned}
L^B_{(i,j,k)} &= A^B_{(i,j,k)}/[1+\alpha(U^N_{(i,j,k-1)}+U^E_{(i,j,k-1)})] \\
L^W_{(i,j,k)} &= A^W_{(i,j,k)}/[1+\alpha(U^N_{(i,j-1,k)}+U^T_{(i,j-1,k)})] \\
L^S_{(i,j,k)} &= A^S_{(i,j,k)}/[1+\alpha(U^E_{(i-1,j,k)}+U^T_{(i-1,j,k)})] \\
L^P_{(i,j,k)} &= A^P_{(i,j,k)}+\alpha(L^B_{(i,j,k)}U^N_{(i,j,k-1)}+L^W_{(i,j,k)}U^N_{(i,j-1,k)}+ \\
&\qquad L^B_{(i,j,k)}U^E_{(i,j,k-1)}+L^S_{(i,j,k)}U^E_{(i-1,j,k)}+ \\
&\qquad L^W_{(i,j,k)}U^T_{(i,j-1,k)}+L^S_{(i,j,k)}U^T_{(i-1,j,k)})- \\
&\qquad L^B_{(i,j,k)}U^T_{(i,j,k-1)}-L^W_{(i,j,k)}U^E_{(i,j-1,k)}-L^S_{(i,j,k)}U^N_{(i-1,j,k)} \\
U^N_{(i,j,k)} &= (A^N_{(i,j,k)}-L^B_{(i,j,k)}U^N_{(i,j,k-1)}-L^W_{(i,j,k)}U^N_{(i,j-1,k)})/L^P_{i,j,k} \\
U^E_{(i,j,k)} &= (A^E_{(i,j,k)}-L^B_{(i,j,k)}U^E_{(i,j,k-1)}-L^S_{(i,j,k)}U^E_{(i-1,j,k)})/L^P_{i,j,k} \\
U^T_{(i,j,k)} &= (A^T_{(i,j,k)}-L^W_{(i,j,k)}U^T_{(i,j-1,k)}-L^S_{(i,j,k)}U^T_{(i-1,j,k)})/L^P_{i,j,k}
\end{aligned}
\tag{B.1}
$$

The coefficients must be calculated in this sequential order. α is a coefficient between 0 and 1. The optimized α in the current simulation is found to be 0.98. In fact, the iterative scheme is not very sensitive to the value of α when SIP is used as a preconditioner.

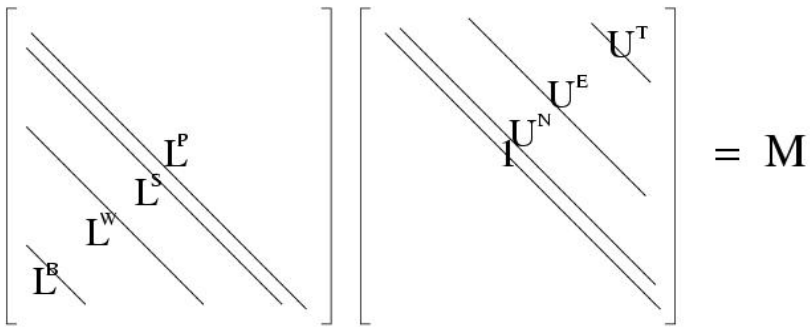

Figure B.1: Schematic of the matrices $LU = M$. L^i and U^i represent the non-zero elements in the matrices.

Appendix C

The Governing Equations and Numerical Details of the DieCAST Ocean Model

We present the details of DieCAST hydrostatic model in this appendix. The governing equations have

Conservation of mass:

$$\nabla \cdot \mathbf{V} = 0 \tag{C.1}$$

Horizontal momentum equations:

$$\frac{\partial u}{\partial t} = -\nabla \cdot u\mathbf{V} + fv - \frac{1}{\rho_0}\frac{\partial p}{\partial x} + \nabla_h \cdot A_h \nabla_h u + \frac{\partial}{\partial z}(A_v \frac{\partial u}{\partial z}) \tag{C.2}$$

$$\frac{\partial v}{\partial t} = -\nabla \cdot v\mathbf{V} - fu - \frac{1}{\rho_0}\frac{\partial p}{\partial y} + \nabla_h \cdot A_h \nabla_h v + \frac{\partial}{\partial z}(A_v \frac{\partial v}{\partial z}) \tag{C.3}$$

Conservation of scalar (salt or potential temperature):

$$\frac{\partial S}{\partial t} = -\nabla \cdot S\mathbf{V} + \nabla_h \cdot K_h \nabla_h S + \frac{\partial}{\partial z}(K_v \frac{\partial S}{\partial z}) \tag{C.4}$$

Hydrostatic equation:

$$\frac{\partial p}{\partial z} = -(\rho - \overline{\rho})g \tag{C.5}$$

Equation of state:

$$\rho = \rho(S, \theta) \tag{C.6}$$

where u and v are the x and y components of velocity vector $\mathbf{V} = (u, v, w)$ respectively; f is the Coriolis parameter; ρ_0 is the mean density; $\overline{\rho}$ is the horizontally averaged density at depth z; p is the pressure; A_h, A_v are the horizontal and vertical eddy viscosity respectively; S is the salinity; K_h, K_v are the horizontal and vertical eddy diffusivity respectively; θ is the potential temperature.

From the staggered grid arrangement shown in Figure C.1, the control volume and time integrated form of equation (C.2) may be written,

$$\begin{aligned}
\frac{\tilde{u}^{n+1}_{i,j,k} - u^{n-1}_{i,j,k}}{\Delta t} = &- \Big(\frac{U^n_{i,j,k}u^n_{i+1/2,j,k} - U^n_{i-1,j,k}u^n_{i-1/2,j,k}}{\Delta x_j} \\
&+ \frac{V^n_{i,j,k}u^n_{i,j+1/2,k} - V^n_{i,j-1,k}u^n_{i,j-1/2,k}}{\Delta y_j} \\
&+ \frac{W^n_{i,j,k+1}u^n_{i,j,k+1/2} - W^n_{i,j,k}u^n_{i,j,k-1/2}}{\Delta z_k}\Big) \\
&+ [2\Omega_e sin(\phi_j) + u^n_{i,j,k}\tan(\frac{\phi_j}{r_e})]v^n_{i,j,k} \\
&- (\frac{\partial \tilde{p}}{\partial x})^n_{i,j,k} + dissipation
\end{aligned} \tag{C.7}$$

where the pressure derivative term is

$$\begin{aligned}
\frac{\partial \tilde{p}}{\partial x}^n_{i,j,k} = &\frac{7}{12}\Big(\frac{\tilde{p}_{i+1,j,k} - \tilde{p}_{i,j,k}}{\Delta x_j} + \frac{\tilde{p}_{i,j,k} - \tilde{p}_{i-1,j,k}}{\Delta x_j}\Big) \\
&- \frac{1}{12}\Big(\frac{\tilde{p}_{i+2,j,k} - \tilde{p}_{i+1,j,k}}{\Delta x_j} + \frac{\tilde{p}_{i-1,j,k} - \tilde{p}_{i-2,j,k}}{\Delta x_j}\Big)
\end{aligned} \tag{C.8}$$

and the dissipation term is the viscous and quadratic bottom drag (bottom layer only) terms. In addition, a wind stress is applied to the top layer. Although standard Earth spherical coordinates are assumed, we do not include the cosine factors here (horizontal grid increments vary with latitude only and vertical grid increments with depth only). The quantity $\tilde{q}$ means the trial value of field q derived from the trial pressure at the rigid-lid. The rigid-lid pressure is hydrostatically related to the slow

mode surface height.

In order to evaluate a cell face average quantity, fourth order accurate interpolation is used (see Appendix D): Then $\overline{q}_{i+1/2,j,k}$ represents the cell face quantity derived from the four nearest control volumes, for example:

$$\overline{q}_{i+1/2,j,k} = \frac{7}{12}(Q_{i,j,k} + Q_{i+1,j,k}) - \frac{1}{12}(Q_{i-1,j,k} + Q_{i+2,j,k}) \tag{C.9}$$

where $\overline{q}_{i+1/2,j,k}$ represents the cell face average quantity derived from its four nearest control volume averages on the right hand side of equation (C.9). After determining the pressure field $\tilde{p}$ from the hydrostatic equation (C.5) using a trial (or most recent) value of rigid-lid pressure, the control volume conservation equations are used to get $\tilde{u}, \tilde{v}, S, T$ at the advanced time level $(n+1)$. All terms except diffusion are evaluated from fields known at leapfrog time level n; diffusion terms are at time level $n-1$.

The numerical procedure for the incompressible correction is summarized in the following:

1. Guess the trial surface pressure $\tilde{p}_s^n$ from the previous time step ($\tilde{p}_s^n = p_s^{n-1}$) and integrate the hydrostatic equation (C.5) to get the intermediate pressure field $\tilde{p}^n$ over the whole domain.

2. Update the trial integral average $\tilde{u}^{n+1}$,$\tilde{v}^{n+1}$ in the control volume using equation (C.7).

3. Interpolate $\tilde{u}^{n+1}, \tilde{u}^{n+1}$ to $\tilde{U}_{i,j,k}^{n+1}, \tilde{V}_{i,j,k}^{n+1}$ at the cell face using 4^{th} order interpolation from equation (C.9).

4. Adjust the rigid-lid pressure such that the divergence of the vertically integrated horizontal velocity matches the specified value (near zero, but small precipitation/evaporation and river sources are included to give non-zero W at the rigid lid which is slightly porous to fresh water). This procedure uses mass conservation and the detailed procedure is listed as follows.

   - Set the final pressure $p^n = \tilde{p}^n + \Delta\tilde{p}$ where $\Delta\tilde{p}$ is due to the change of rigid-lid pressure and thus independent of depth. $\tilde{p}^n$ is derived hydrostatically

from trial rigid-lid pressure in the first step. Then the final velocities can be written as

$$U^{n+1} = \tilde{U}^{n+1} + \Delta\tilde{U} \tag{C.10}$$

$$V^{n+1} = \tilde{V}^{n+1} + \Delta\tilde{V}, \tag{C.11}$$

where $\Delta\tilde{U} = -\Delta t\frac{\partial\Delta\tilde{p}}{\partial x}$ and $\Delta\tilde{V} = -\Delta t\frac{\partial\Delta\tilde{p}}{\partial y}$.

- The final velocity field satisfies mass conservation from equation (C.1) so that the vertically-integrated horizontal velocity can be determined by vertical velocity at the top and bottom:

$$\int_0^D (\frac{\partial U^{n+1}}{\partial x} + \frac{\partial V^{n+1}}{\partial y})dz = W^{n+1}(0) - W^{n+1}(D) = 0 \tag{C.12}$$

- Substitute the final velocity integration in terms of trial velocity and the correction in equations (C.10) and (C.11), thus deriving a 2-D Poisson equation for rigid-lid pressure adjustment. Solve the Poisson equation (C.13) using an efficient EVP elliptic solver (Roache, 1995).

$$\int_0^D (\frac{\partial\tilde{U}^{n+1}}{\partial x} + \frac{\partial\tilde{V}^{n+1}}{\partial y})dz = \int_0^D -(\frac{\partial\Delta\tilde{U}}{\partial x} + \frac{\partial\Delta\tilde{V}}{\partial y})dz \tag{C.13}$$

5. The velocity U^{n+1}, V^{n+1} is corrected from the pressure adjustment $\Delta\tilde{p}$ in the last step.

6. Finally, interpolate cell average changes $\Delta\tilde{u}, \Delta\tilde{v}$ from $\Delta\tilde{U}$,$\Delta\tilde{V}$ using 4^{th} order interpolation, then $u^{n+1} = \tilde{u}^{n+1} + \Delta\tilde{u}$ and $v^{n+1} = \tilde{v}^{n+1} + \Delta\tilde{v}$.

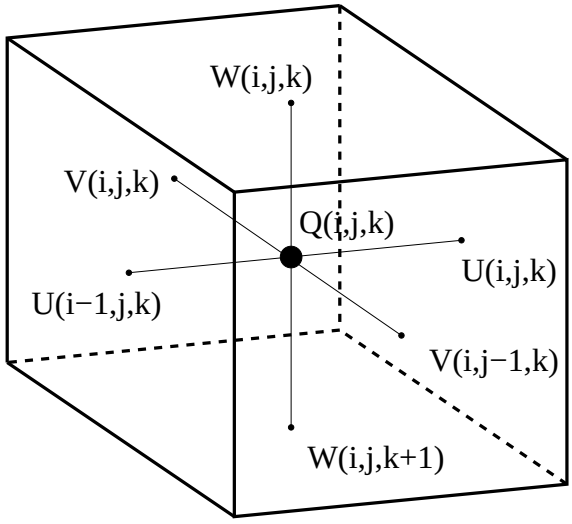

Figure C.1: The staggered and collocated arrangement of grids. $Q(i,j,k)$ is any cell-averaged quantity, u, v, s, t, p or ρ. U, V, W are the face-averaged quantities.

Appendix D

Fourth-Order Interpolation From Nearby Control Volume Averages to a Cell Face

For simplicity, we demonstrate the interpolation scheme in the x-direction only. The same analysis can be applied to the other directions. At a given (y, z), let any variable q (e.g. temperature) be a third-degree polynomial:

$$q(x, y, z) = C_0(y, z) + C_1(y, z)x + C_2(y, z)x^2 + C_3(y, z)x^3 \tag{D.1}$$

We conveniently assign $x_{i+1/2} = 0$, see Figure (D.1) with no loss of generality, so $q(0, y, z) = q(x_{i+1/2}, y, z) = C_0(y, z)$. We can define the quantities q at a time level.

$$q_{i+2}(y,z) = \int_{x_{i+\frac{3}{2}}}^{x_{i+\frac{5}{2}}} q(x,y,z)dx$$
$$= C_0(y,z)x\Big|_{x_{i+\frac{3}{2}}}^{x_{i+\frac{5}{2}}} + \frac{1}{2}C_1(y,z)x^2\Big|_{x_{i+\frac{3}{2}}}^{x_{i+\frac{5}{2}}} + \frac{1}{3}C_2(y,z)x^3\Big|_{x_{i+\frac{3}{2}}}^{x_{i+\frac{5}{2}}} + \frac{1}{4}C_3(y,z)x^4\Big|_{x_{i+\frac{3}{2}}}^{x_{i+\frac{5}{2}}} \tag{D.2}$$

$$q_{i+1}(y,z) = \int_{x_{i+\frac{1}{2}}}^{x_{i+\frac{3}{2}}} q(x,y,z)dx$$
$$= C_0(y,z)x\Big|_{x_{i+\frac{1}{2}}}^{x_{i+\frac{3}{2}}} + \frac{1}{2}C_1(y,z)x^2\Big|_{x_{i+\frac{1}{2}}}^{x_{i+\frac{3}{2}}} + \frac{1}{3}C_2(y,z)x^3\Big|_{x_{i+\frac{1}{2}}}^{x_{i+\frac{3}{2}}} + \frac{1}{4}C_3(y,z)x^4\Big|_{x_{i+\frac{1}{2}}}^{x_{i+\frac{3}{2}}} \tag{D.3}$$

$$q_{i}(y,z) = \int_{x_{i-\frac{1}{2}}}^{x_{i+\frac{1}{2}}} q(x,y,z)dx$$
$$= C_0(y,z)x\Big|_{x_{i-\frac{1}{2}}}^{x_{i+\frac{1}{2}}} + \frac{1}{2}C_1(y,z)x^2\Big|_{x_{i-\frac{1}{2}}}^{x_{i+\frac{1}{2}}} + \frac{1}{3}C_2(y,z)x^3\Big|_{x_{i-\frac{1}{2}}}^{x_{i+\frac{1}{2}}} + \frac{1}{4}C_3(y,z)x^4\Big|_{x_{i-\frac{1}{2}}}^{x_{i+\frac{1}{2}}} \tag{D.4}$$

$$q_{i-1}(y,z) = \int_{x_{i-\frac{3}{2}}}^{x_{i-\frac{1}{2}}} q(x,y,z)dx$$
$$= C_0(y,z)x\Big|_{x_{i-\frac{3}{2}}}^{x_{i-\frac{1}{2}}} + \frac{1}{2}C_1(y,z)x^2\Big|_{x_{i-\frac{3}{2}}}^{x_{i-\frac{1}{2}}} + \frac{1}{3}C_2(y,z)x^3\Big|_{x_{i-\frac{3}{2}}}^{x_{i-\frac{1}{2}}} + \frac{1}{4}C_3(y,z)x^4\Big|_{x_{i-\frac{3}{2}}}^{x_{i-\frac{1}{2}}} \tag{D.5}$$

$$\tag{D.6}$$

Solving the above equations for the interfacial value $C_0(y,z)$, we get

$$C_0(y,z) = q_{i+1/2}(y,z) = \frac{7}{12}(q_i(y,z) + q_{i+1}(y,z)) - \frac{1}{12}(q_{i-1}(y,z) + q_{i+2}(y,z)) \tag{D.7}$$

The coefficients can also be obtained by Taylor series expansion of variable $q(x,y,z)$ along $x-$axis and integrating the cell analytically to get the discretized cell averaged

$$q_i(y,z) = \int_{x_{i-\frac{1}{2}}}^{x_{i+\frac{1}{2}}} q(x,y,z)dx \tag{D.8}$$

which yields

$$\begin{aligned} q_{i+1/2}(y,z) &= q_i(y,z) + q_{i+1}(y,z) + \frac{1}{4}q''(8)(\Delta x)^3 \\ &= q_{i-1}(y,z) + q_{i+2}(y,z) + \frac{1}{4}q''(56)(\Delta x)^3 \end{aligned} \tag{D.9}$$

Then use Richardson extrapolation to obtain the above equation (D.7). Finally, integrate over the control volume face $\sigma(y,z)$ to obtain cell face average,

$$\iint_\sigma q_{i+1/2}(y,z)dydz = \frac{7}{12}\iint_\sigma (q_i(y,z)+q_{i+1}(y,z))dydz - \frac{1}{12}\iint_\sigma (q_{i-1}(y,z)+q_{i+2}(y,z))dydz \tag{D.10}$$

or in the notation of equation (C.9):

$$\overline{q}_{i+1/2,j,k} = \frac{7}{12}(Q_{i,j,k} + Q_{i+1,j,k}) - \frac{1}{12}(Q_{i-1,j,k} + Q_{i+2,j,k}) \tag{D.11}$$

Sanderson and Brassington (1998a) obtained the above face-averaged quantity using a cumulative sum of the cell-averaged quantity. The current derivation is complete and can be extended to non-uniform grids when the expansion ratio is known. The truncation error of various differencing operators is shown in Figure D.2 in the example that a sinusoidal signal is numerically differentiated (Sanderson & Brassington, 1998a). The error is plotted as a function of the ratio of grid spacing Δ to wavelength λ. The power-law scaling of error with the ratio λ/Δ is closely followed for wavelengths greater than 4Δ with C-grid differencing and for wavelengths greater than 6Δ with A-grid (Sanderson & Brassington, 1998a). Further, the scaling applies with reasonable approximation to the smallest wavelengths resolvable on the grid. The error analysis and numerical examples in Sanderson and Brassington (1998a) demonstrate that the fourth-order interpolation used in the DieCAST model is fourth-order accurate on both A-and C-grids.

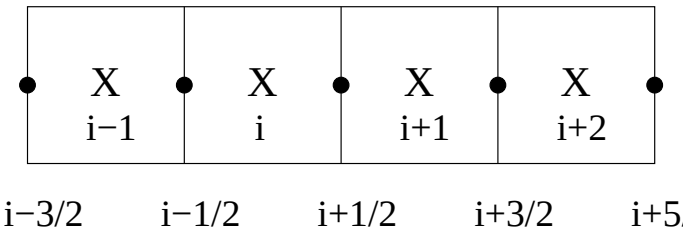

Figure D.1: Schematic of the cells and the index for the fourth-order interpolation.

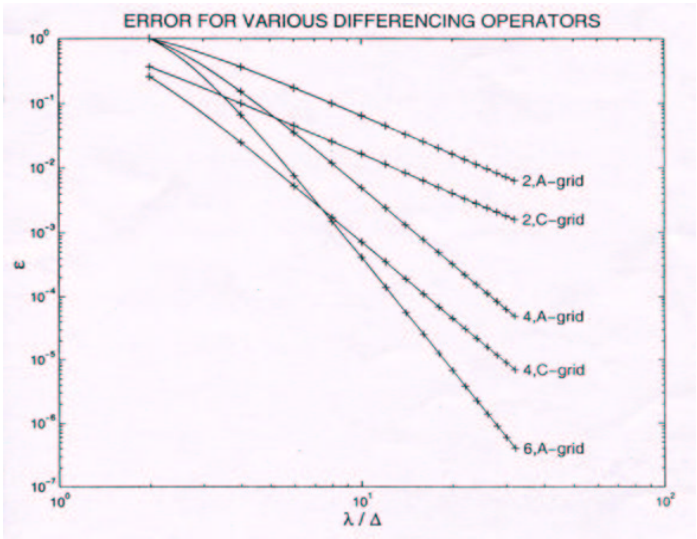

Figure D.2: Error ε for differentiating s sinusoidal function using the A-grid (collocated) and C-grid (staggered) differencing operators. The error is plotted as a function of the ratio of grid spacing Δ to wavelength λ. The label 2,A-grid refers to the second-order operator on a collocated grid. The label 2,C-grid refers to the second-order operator on a staggered grid. Similarly, label 4,A-grid refers to the fourth-order operator on a collocated grid and label 4,C-grid refers to the fourth-order operator on a staggered grid. The sixth-order differencing operator on the A grid is labeled 6,A-grid. [Figure 1 of Sanderson and Brassington (1998a)].

Appendix E

Non-Hydrostatic Modification of the DieCAST Model

Let us consider the two-dimensional set of non-hydrostatic equations. Only one horizontal direction (x) is used to make the interpretation easier. The equations are:
Conservation of mass:

$$\partial u/\partial x + \partial w/\partial z = 0 \tag{E.1}$$

Momentum equations:

$$\partial u/\partial t = -(1/\rho_0)\partial p/\partial x + R_x \tag{E.2}$$

$$\partial w/\partial t = -(1/\rho_0)\partial p/\partial z + R_z - (\rho/\rho_0)g \tag{E.3}$$

where R_x, R_z are the total right-hand side source terms except for the pressure term. The complete procedure for solving the non-hydrostatic equations is as follows,

1. Guess the initial surface pressure $\tilde{P}_{i,1}$ and initial vertical velocity $\tilde{w}_{i,k} = w^n_{i,k}$.

2. Solve for the intermediate pressure field $\tilde{P}_{i,k}$ by integrating equation (E.3) along z. Rewrite equation (E.3) as

$$\partial \tilde{p}/\partial z = \rho_0(R_z - \partial \tilde{w}/\partial t) - g\rho^n \tag{E.4}$$

3. Solve for $\tilde{u}_{i,k}$ from equation (E.2) using $\tilde{P}_{i,k}$.

4. Solve for $\tilde{w}_{i,k}$ from the continuity equation (E.1).

5. The above steps allow vertical velocity w_{i,N_k} at the bottom to be non-zero. Then adjust the surface pressure $P_{i,1}$ such that the divergence of the vertical integration of volume i equals zero, i.e. we get a new guess for surface pressure. This step is the same as the pressure correction step in hydrostatic equations.

6. Use $\tilde{w}_{i,k}$ from the last step and repeat the above procedure until the iteration converges.

The resulting solutions satisfy the non-hydrostatic equations and the continuity equation. The extension of the above procedure to three dimensions is trivial.

References

Adcroft, A., Hill, C., & Marshall, J. 1997. Representation of topography by shaved cells in a height coordinate ocean model. *Monthly Weather Review*, **125**(9), 2293–2315.

Allen, J. S., Newberger, P. A., & Federiuk, J. 1995. Upwelling circulation of the Oregon continental shelf. Part I: Response to ideal forcing. *J. Phys. Oceanogr.*, **25**, 1843–1866.

Allen, S. E., Dinniman, M. S., Klinck, J. M., Gorby, D. D., & Hewett, A. J. 2003. On vertical advection trunctation errors in terrain-following numerical models: Comparison to a laboratory model for upwelling over submarine canyons. *J. Geophys. Res.*, **108**, Art. No. 3003.

Almgren, A. S., Bell, J. B., Colella, P., & Marthaler, T. 1997. A Cartesian grid projection method for the incompressible Euler equations in complex geometries. *SIAM J. Sci. Comput.*, **18**(5), 1289 – 1309.

Baggett, J.S., Jimenez, J., & Kravchenko, A.G. 1997. Resolution requirements in large-eddy simulations of shear flows. *Pages 51–66 of: Annual Research Briefs*. NASA Ames Research Center/Stanfoàrd Univ. Center for Turbulence Research, Stanford, CA.

Barth, J. A. 1989. Stability of a coastal upwelling front 1. Model development and a stability theorem. *J. Geophys. Res.*, **94**, 10844–10856.

Barth, J. A. 1994. Short-wavelength instabilities on coastal jets and fronts. *J. Geophys. Res.*, **99**, 16095–16115.

Batteen, M. L. 1997. Wind-forced modeling studies of currents, meanders, and eddies in the California Current system. *J. Geophys. Res.*, **102**, 985–1010.

Batteen, M. L., & Vance, P. W. 1998. Modeling studies of the effects of wind forcing and thermohaline gradients on the California Current System. *Deep-Sea Res. II*, **45**, 1507–1556.

Beyer, W. H. 1981. *CRC Standard Mathematical Tables*. 26 edn. Boca Raton: CRC Press.

Blumberg, A. F., & Mellor, G. L. 1987. A description of a three-dimensional coastal ocean circulation model. *Pages 1–16 of:* Heaps, N. S. (ed), *Coastal and Estuarine Sciences*, vol. 4. Amer. Geophys. Union Geophysical Monograph Board.

Breaker, L. C., & Broenkow, W. W. 1994. The circulation of Monterey Bay and related processes. *Oceanogr. and Marine Bio.*, **32**, 1–64.

Breaker, L. C., & Mooers, C. N. K. 1986. Oceanic variability off the central California coast. *Progr. Oceanogr.*, **17**, 61–135.

Brink, K. H. 1988. Topographic drag due to barotropic flow over the continental shelf and slope. *J. Phys. Oceanogr.*, **16**, 2150–2158.

Calhoun, D. 2002. A Cartesian grid method for solving the two-dimensional streamfunction-vorticity equations in irregular regions. *J. Comput. Phys.*, **176**(2), 231 – 275.

Calhoun, D., & LeVeque, R. J. 2000. A Cartesian grid finite-volume method for the advection-diffusion equation in irregular geometries. *J. Comput. Phys.*, **157**(1), 143 – 180.

Calhoun, R. J., & Street, R. L. 2001. Turbulent flow over a wavy surface: Neutral case. *J. Geophys. Res.*, **106**, 9277–9293.

Casulli, V., & Stelling, G. S. 1998. Numerical simulation of 3D quasi-hydrostatic, free-surface flow. *J. Hydrau. Eng.*, **124**, 678–686.

Chan, R. K.-C., & Street, R. L. 1970. A computer study of finite-amplitude water waves. *JCP*, **6**, 68–94.

Chao, S. Y., & Shaw, P. T. 2002. Nonhydrostatic aspects of coastal upwelling meanders and filaments off eastern ocean boundaries. *Tellus*, **54(A)**, 63–75.

Collins, C. A., Garfield, N., Rago, T. A., Rischmiller, F. W., & Carter, E. 2000. Mean structure of the inshore countercurrent and California undercurrent off Point Sur, California. *Deep-Sea Res. II*, **47**, 765–782.

Cui, A., & Street, R. L. 2003. Large-eddy simulation of coastal upwelling flow. *Environmental Fluid Mechanics (accepted).*

Cui, J., Patel, V. C., & Lin, C. L. 2003. Prediction of turbulent flow over rough surfaces using a force field in large eddy simulation. *ASME Journal of Fluid Eng.*, **125**(1), 2 – 9.

Daily, C. 1995. *Numerical modeling of upwelling, relaxation, and downwelling in Monterey Bay, California*. M.Phil. thesis, Princeton University.

Dengg, J., Beckmann, A., & Gerdes, R. 1996. The Gulf Stream separation problem. *Pages 253–290 of:* Krauss, W. (ed), *The warmwatersphere of the North Atlantic Ocean*. Berlin: Gebr. Borntraeger.

Dias, A., & Majumdar, S. 2001. *Numerical computation of flow around a circular cylinder*. Tech. rept. PS II Report, BITS Pilani, India.

Dietrich, D. E. 1997. Application of a modified "a" grid ocean model having reduced numerical dispersion to the gulf of Mexico circulation. *Dyn. Atmos. Oceans*, **27**, 201–217.

Dietrich, D. E., & Ko, D. S. 1994. A semi-collocated ocean model-based on the SOMS approach. *Int. J. Numer. Methods Fluids*, **19**, 1103–1113.

Dietrich, D. E., & Lin, C. A. 2002. Effects of hydrostatic approximation and resolution on the simulation of convective adjustment. *Tellus*, **54(A)**, 34–43.

Dietrich, D. E., Marietta, M. G., & Roache, P. J. 1987. An ocean modeling system with turbulent boundary layers and topography: Part 1. Numerical studies of small island wakes in the ocean. *Int. J. Numer. Methods Fluids*, **7**, 833–855.

Fadlun, E. A., Verzicco, R., Orlandi, P., & Mohd-Yusof, J. 2000. Combined immersed-boundary finite-difference methods for three-dimensional complex flow simulations. *J. Comput. Phys.*, **161**, 30–60.

Fedkiw, R. P. 2002. Coupling an Eulerian fluid calculation to a Lagrangian solid calculation with the ghost fluid method. *J. Comput. Phys.*, **175**, 200–224.

Fedkiw, R. P., Aslam, T., Merriman, B., & Osher, S. 1999. A non-oscillatory Eulerian approach to interfaces in multimaterial flows (the ghost fluid method). *J. Comput. Phys.*, **152**, 457–492.

Ferziger, J. H., & Perić, M. 2001. *Computational Methods for Fluid Dynamics*. 3 edn. Berlin Heidelberg: Springer Verlag.

Ferziger, J. H., & Tseng, Y. H. 2003. A coordinate system independent streamwise upwind method for fluid flow computation. *Submitted to Int. J. Numer. Methods Fluids*.

Flament, P., Armi, L., & Washburn, L. 1985. The evolving structure of an upwelling filament. *J. Geophys. Res.*, **90**, 1765–1985.

Forrer, H., & Jeltsch, R. 1998. A higher-order boundary treatment for Cartesian-grid method. *J. Comput. Phys.*, **140**, 259–277.

Franke, R. 1982. Scattered data interpolation: Tests of some methods. *Math. Comput.*, **38**, 181–200.

Garfield, N., Collins, C. A., Paquette, R. G., & Carter, E. 1999. Lagrangian exploration of the California undercurrent. *J. Phys. Oceanogr.*, **29**, 560–583.

Gibou, F., Fedkiw, R. P., Cheng, L. T., & Kang, M. 2002. A second-order-accurate symmetric discretization of the Poisson equation on irregular domains. *J. Comput. Phys.*, **176**, 205–227.

Goldstein, D., Handler, R., & Sirovich, L. 1993. Modeling a no-slip flow boundary with an external force field. *J. Comput. Phys.*, **105**, 354–366.

Golub, G. H., & van Loan, C. F. 1996. *Matrix Computations*. 3 edn. Baltimore: The Johns Hopkins University Press.

Gore, R. 1990. Between Monterey tides. *National Geographic*, **177**, 2–43.

Haney, R. L. 1991. On the pressure gradient force over steep topography in sigma coordinate ocean models. *J. Phys. Oceanogr.*, **21**, 610–619.

Haney, R. L., Hale, R. A., & Dietrich, D. E. 2001. Offshore propagation of eddy kinetic energy in the California Current. *J. Geophys. Res.*, **106**, 11709–11717.

Haworth, D. C., & Jansen, K. 2000. Large-eddy simulation on unstructured deforming meshes: Towards reciprocating IC engines. *Computers and Fluids*, **29**, 493–524.

Hellerman, S., & Rosenstein, M. 1983. Normal monthly wind stress over the world ocean with error estimates. *J. Phys. Oceanogr.*, **13**, 1093–1104.

Henn, D., & Sykes, I. 1999. Large-eddy simulation of flow over wavy surfaces. *J. Fluid Mech.*, **383**, 75–112.

Hickey, B. M. 1997. The response of s steep-sided narrow canyon to strong wind forcing. *J. Phys. Oceanogr.*, **27**, 697–726.

Iaccarino, G., & Verzicco, R. 2003. Immersed boundary technique for turbulent flow simulations. *Applied Mech. Rev.*, **56**, 331–347.

Ikeda, M., Mysak, L. A., & Emery, W. J. 1984. Observation and modeling of satellite-sensed meanders and eddies off Vancouver island. *J. Phys. Oceanogr.*, **14**, 3–21.

Jeong, J., & Hussain, F. 1995. On the identification of a vortex. *J. Fluid Mech.*, **285**, 69–94.

Johansen, H., & Colella, P. 1998. A Cartesian grid embedded boundary method for Poisson's equation on irregular domains. *J. Comput. Phys.*, **147**(1), 60 – 85.

Kelly, K. A., Beardsley, R. C., Limeburner, R., Brink, K. H., Paduan, J. D., & Chereskin, T. K. 1998. Variability of the near-surface eddy kinetic energy in the California Current based on altimetric, drifter, and moored current data. *J. Geophys. Res.*, **103**, 13067–13083.

Killworth, P. D., & Edwards, N. R. 1999. A turbulent bottom boundary layer code for use in numerical ocean models. *J. Phys. Oceanogr.*, **29**, 1221–1238.

Kim, J., & Moin, P. 1985. Application of a fractional-step method to incompressible Navier-Stokes equations. *J. Comput. Phys.*, **59**, 308–323.

Kim, J., Kim, D., & Choi, H. 2001. An immersed-boundary finite-volume method for simulations of flow in complex geometries. *J. Comput. Phys.*, **171**, 132–150.

Kirkpatrick, M. P., Armfield, S. W., & Kent, J. H. 2003. A representation of curved boundaries for the solution of the Navier-Stokes equations on a staggered three-dimensional Cartesian grid. *J. Comput. Phys.*, **184**(1), 1 – 36.

Kosro, P. M. 1987. Structure of the coastal current field off northern Callifornia during the coastal ocean dynamics experiment. *J. Geophys. Res.*, **92**, 1637–1654.

Lai, M.C., & Peskin, C. S. 2000. An immersed boundary method with formal second-order accuracy and reduced numerical viscosity. *J. Comput. Phys.*, **160**, 705–719.

Legg, S., & Adcroft, A. 2003. Internal wave breaking at concave and convex continental slopes. *J. Phys. Oceanogr. (in press).*

Lentz, S. J. 1995. U.S. contributions to the physical oceanography of continental shelves in the early 1990's. *Rev. Geophys.*, **33**, 1225–1236.

Leonard, B. P. 1979. A stable and accurate convective modeling procedure based on quadratic upstream interpolation. *Comp. Methods Appl. Mech. Engr.*, **19**, 58–98.

Lesieur, M., Metais, O., & Garnier, E. 2000. Baroclinic instability and severe storms. *Journal of Turbulence (http://jot.iop.org)*, **1**, 002.

LeVeque, R. J., & Oliger, J. 1983. Numerical-methods based on additive splittings for hyperbolic partial-differential equations. *Math. Comp.*, **40**, 469–497.

Levitus, S. 1982. Climatological atlas of the world oceans. *Page 173 of: NOAA Prof. Pap.* U.S. Govt. Print Off., Washington, D. C.

Lewis, J. K., Shulman, I., & Blumberg, F. 1998. Assimilation of Doppler radar current data into numerical ocean models. *Cont. Shelf Res.*, **18**, 541–559.

Linden, P. F., & Heijst, J. F. Van. 1984. Two-layer spin-up and frontogenesis. *J. Fluid Mech.*, **143**, 69–94.

Liu, X. D., Fedkiw, R. P., & Kang, M. J. 2000. A boundary condition capturing method for Poisson's equation on irregular domains. *J. Comput. Phys.*, **160**(1), 151 – 178.

Lu, Y. Y., Wright, D. G., & Brickman, D. 2001. Internal tide generation over topography: Experiments with a free-surface z-level ocean model. *J. Atmos. Oceanic Technol.*, **18**, 1076–1091.

Luther, M. E., & Bane, J. M. 1985. Mixed instabilities in the Gulf-stream over the continental slope. *J. Phys. Oceanogr.*, **15**, 3–23.

Ly, L. N., & Luong, P. A. 1999. Numerical grid used in a coastal ocean model with breaking wave effects. *J. Comput. Appl. Math*, **103**, 125–137.

Mahadevan, A., Oliger, J., & Street, R. 1996. A nonhydrostatic mesoscale ocean model. Part I: Well-posedness and scaling. *J. Phys. Oceanogr.*, **26**, 1868–1880.

Majumdar, S., Iaccarino, G., & Durbin, P. 2001. RANS solvers with adaptive structured boundary non-conforming grids. *Pages 353–366 of: Annual Research Briefs.* NASA Ames Research Center/Stanford Univ. Center for Turbulence Research, Stanford, CA.

Marchesiello, P., McWilliams, J. C., & Shchepetkin, A. 2003. Equilibrium structure and dynamics of the California current system. *J. Phys. Oceanogr.*, **32**, 753–783.

Marshall, J., Adcroft, A., Hill, C., Perelman, L., & Heisey, C. 1997a. A finite-volume ; incompressible Navier Stokes model for studies of the ocean on parallel computers. *J. Geophys. Res.*, **102**(C3), 5753–5766.

Marshall, J., Hill, C., Perelman, L., & Adcroft, A. 1997b. Hydrostatic ; quasi-hydrostatic ; and nonhydrostatic ocean modeling. *J. Geophys. Res.*, **102**(C3), 5733–5752.

McCorquodale, P., Colella, P., & Johansen, H. 2001. A cartesian grid embedded boundary method for the heat equation on irregular domains. *J. Comput. Phys.*, **173**(2), 620 – 635.

McCreary, J. P., Fukamachi, Y., & Kundu, P. 1991. A numerical investigation of jets and eddies near an eastern ocean boundary. *J. Geophys. Res.*, **96**, 2515–2534.

McKenney, A., Greengard, L., & Mayo, A. 1995. A fast Poisson solver for complex geometries. *J. Comput. Phys.*, **118**(2), 348 – 355.

McWilliams, J. C., Weiss, J. B., & Yavneh, I. 1994. Anisotrophy and coherent structures in planetary turbulence. *Science*, **264**, 410–413.

Mohd-Yusof, J. 1997. Combined immersed boundary/B-Spline methods for simulations of flows in complex geometries. *Pages 317–327 of: Annual Research Briefs*. NASA Ames Research Center/Stanford Univ. Center for Turbulence Research, Stanford, CA.

Monismith, S. 1986. An experimental study of the upwelling response of stratified reservoirs to surface shear stress. *J. Fluid Mech.*, **171**, 407–439.

Narimousa, S., & Maxworthy, T. 1985. Two-layer model of shear-driven coastal upwelling in the presence of bottom topography. *J. Fluid Mech.*, **159**, 503–531.

Narimousa, S., & Maxworthy, T. 1987a. Coastal upwelling on a sloping bottom: the formation of plumes, jets and pinched–off cyclones. *J. of Fluid Mech.*, **176**, 169–190.

Narimousa, S., & Maxworthy, T. 1987b. On the effects of coastline perturbations on coastal currents and fronts. *J. Phys. Oceanogr.*, **17**, 1296–1303.

Narimousa, S., & Maxworthy, T. 1989. Application of a laboratory model to the interpretation of satellite and field observations of coastal upwelling. *Dyn. Atmos. Oceans*, **13**, 1–46.

Narimousa, S., & Maxworthy, T. 1991. Experiments on the structure and dynamics of forced, quasi-two-dimensional turbulence. *J. Fluid Mech.*, **223**, 113–133.

Oliger, J., & Sundstrom, A. 1978. Theoretical and practical aspects of some initial boundary value problems in fluid dynamics. *SIAM J. Appl. Math.*, **35**, 419–446.

Orlanski, I. 1976. A simple boundary condition for unbounded hyperbolic flows. *J. Comput. Phys.*, **21**, 251–269.

Pacanowski, R. C., & Philander, S. G. H. 1981. Parameterization of vertical mixing in numerical models of tropical ocean. *J. Phys. Oceanogr.*, **11**, 1443–1451.

Paduan, J. D., & Rosenfeld, L. K. 1996. Remotely sensed surface currents in Monterey Bay from shore-based HF radar (Coastal Ocean Dynamics Application Radar). *J. Geophys. Res.*, **101**, 20669–20686.

Palma, E. D., & Matano, R. P. 2000. On the implementation of open boundary condition for a general circulation model: The three-dimensional case. *J. Geophys. Res.*, **105**, 8605–8627.

Pember, R. B., Bell, J. B., Colella, P., Crutchfield, W. Y., & Welcome, M. L. 1995. An adaptive Cartesian grid method for unsteady compressible flow in irregular regions. *J. Comput. Phys.*, **120**(2), 278 – 304.

Peskin, C. S. 1972. Flow patterns around heart valves: a numerical method. *J. Comput. Phys.*, **10**, 252–271.

Peskin, C. S. 1977. Numerical analysis of blood flow in the heart. *J. Comput. Phys.*, **25**, 220–252.

Petruncio, E. T. 1996. *Observation and modeling of the internal tide in a submarine canyon.* Ph.D. dissertation, Naval Postgraduate School.

Pierce, S. D., Smith, R. L., Kosro, P. M., Barth, J. A., & Wilson, C. D. 2000. Continuity of the poleward undercurrent along the eastern boundary of the mid-latitude Pacific. *Deep-Sea Res. II*, **47**, 811–829.

Ramp, S. R., Rosenfeld, L. K., Tisch, T. D., & Hicks, M. R. 1997. Moored observations of the current and temperature structure over the continental slop off central California, 1, A basic description of the variability. *J. Geophys. Res.*, **102**, 22877–22902.

Roache, P. J. 1995. *Elliptic marching methods and domain decomposition.* CRC Press.

Roache, P. J. 1998. *Verification and validation in computational science and Engineering.* Hermosa Publishers.

Rosenfeld, L. K., Schwing, F. B., Garfield, N., & Tracy, D. E. 1994. Bifurcated flow from an upwelling center: A cold water source for Monterey Bay. *Cont. Shelf Res.*, **14**, 931–964.

Rosenfeld, L. K., Anderson, T., Hatcher, G., Roughgarden, J., & Shkedy, Y. 1995. Upwelling fronts and barnacle recruitment in central California. *MBARI tech. report*, **95-19**.

Rosenfeld, L. K., Paduan, J. D., Petruncio, E. T., & Gocalves, J. E. 1999. Numerical simulations and observations of the internal tide in a submarine canyon. *Pages 63–71 of: The Proceedings of 11th 'Aha Huliko'a Hawaiian Winter Workshop. Honolulu, HI, January 19-22.*

Roshko, A. 1976. Structure of turbulent shear flows: A new look. *AIAA Journal*, **14**, 1349–1357.

Rueda, F. J. 2001. *A three-dimensional hydrodynamics and transport model for lake environments.* Ph.D. dissertation, Univ. of California, Davis.

Rueda, F. J., Geoffrey, S., & Schladow, S. G. 2003. Dynamics of large polymictic lake. II: numerical simulations. *J. Hydrau. Eng.*, **129**, 92–101.

Saad, Y. 1996. *Iterative methods for sparse linear systems*. Boston: PWS Publishing Company.

Saiki, E. M., & Biringen, S. 1996. Numerical simulation of a cylinder in uniform flow: application of a virtual boundary method. *J. Comput. Phys.*, **123**, 450–465.

Salmon, R. 1998. *Lectures on Geophysical Fluid Dynamics*. New York: Oxford Univ. Press.

Sanderson, B. G. 1998. Order and resolution for computational ocean dynamics. *J. Phys. Oceanogr.*, **28**, 1271–1286.

Sanderson, B. G., & Brassington, G. 1998a. Accuracy in the context of a control-volume model. *Atmos.-Ocean*, **36**, 355–384.

Sanderson, B. G., & Brassington, G. 1998b. Fourth- and fifth order finite difference methods applied to a control volume ocean model. *J. Atmos. Oceanic Technol.*, **19**, 1424–1441.

Scandura, P., Vittori, G., & Blondeaux, P. 2000. Three-dimensional oscillatory flow over steep ripples. *J. Fluid Mech.*, **412**, 355 – 378.

Sheng, J. Y., Wright, D. G., Greatbatch, R. J., & Dietrich, D. E. 1998. CANDIE: A new version of the DieCAST ocean circulation model. *J. Atmos. Oceanic Technol.*, **15**, 1414–1432.

Shulman, I., Wu, C. R., Lewis, J. K., Rosenfeld, J. D. Paduan L. K., Kindle, J. C., Ramp, S. R., & Collins, C. A. 2002. An ocean large-eddy simulation of Langmuir circulations and convection in the surface mixed layer. *Cont. Shelf Res.*, **22**, 1129–1191.

Song, Y. T., & Chao, Y. 2000. An embedded bottom boundary layer formulation for z-coordinate ocean models. *J. Atmos. Oceanic Technol.*, **17**, 546–560.

Staneva, J. V., Dietrich, D.E., Stanev, E.V., & Bowman, M.J. 2001. Rim current and coastal eddy mechanisms in an eddy-resolving Black Sea general circulation model. *J. Marine Systems*, **31**, 137–157.

Stone, H. L. 1968. Iterative solution of implicit approximations of multidimensional partial differential equations. *SIAM J. Num. Anal.*, **5**, 530–558.

Tadepalli, S. 1997. *Numerical simulation and prediction of upwelling flow.* Ph.D. dissertation, Stanford University.

Tisch, T. D., Ramp, S. R., & Collins, C. A. 1992. Observations of the geostrophic current and water mass charcacteristics off Point Sur California, from May 1988 through November 1989. *J. Geophys. Res.*, **97**, 12535–12555.

Townsend, T. L., Hurlburt, H.E., & Hogan, P.J. 2000. Modeled Sverdrup flow in the North Atlantic from 11 different wind stress climatologies. *Dyn. Atmos. Oceans.*, **32**, 373–417.

Tseng, Y. H., & Ferziger, J. H. 2001a. Effects of coastal geometry and the formation of cyclonic/anti-cyclonic eddies on turbulent mixing in upwelling simulation. *J. Turbulence*, **2**, 014.

Tseng, Y. H., & Ferziger, J. H. 2001b. Mixing and available potential energy in stratified flows. *Phys. Fluids*, **13**, 1281–1293.

Udaykumar, H. S., Mittal, R., Rampunggoon, P., & Khanna, A. 2001. A sharp interface Cartesian grid method for simulating flows with complex moving boundaries. *J. Comput. Phys.*, **174**, 345–380.

van der Vorst, H. A. 1992. Bi-CGSTAB: A fast and smoothly converging variant of Bi-CG for the solution of non-symmetric linear systems. *SIAM J. Sci. Stat. Comput.*, **13**, 631–644.

Verzicco, R., Mohd-Yusof, J., Orlandi, P., & Haworth, D. 2000. Large eddy simulation in complex geometry configurations using boundary body forces. *AIAA Journal*, **38**, 427–433.

Wiin-Nielson, A. 1962. On the transformation of kinetic energy between vertical shear flow and the vertical mean flow in the atmosphere. *Monthly Weather Review*, **90**, 311–323.

Winters, Kraig B., Lombard, Peter N., Riley, James J., & D'Asaro, Eric A. 1995. Available potential energy and mixing in density-stratified fluids. *J. Fluid Mech.*, **289**, 115–128.

Wong, F. L., & Eittreim, S. E. 2001. *Continental Shelf GIS for the Monterey Bay National Marine Sanctuary: U.S. Geological Survey Open-File Report 01-179.* Menlo Park, CA: U. S. Geological Survey.

Xu, S. J., Aslam, T., & Stewart, D. S. 1997. High resolution numerical simulation of ideal and non-ideal compressible reacting flows with embedded internal boundaries. *Combustion Theory and Modelling*, **1**(1), 113 – 142.

Ye, T., Mittal, R., Udaykumar, H. S., & Shyy, W. 1999. An accurate Cartesian grid method for viscous incompressible flows with complex immersed boundaries. *J. Comput. Phys.*, **156**, 209–240.

Zang, Y. 1993. *On the development of tools for the simulation of geophysical flows.* Ph.D. dissertation, Stanford University.

Zang, Y., & Street, R. L. 1995. Numerical simulation of coastal upwelling and interfacial instability of a rotating and stratified fluid. *J. Fluid Mech.*, **305**, 47–75.

Zang, Y., Street, R. L., & Koseff, J. R. 1993. A dynamic mixed subgrid-scale model and its application to turbulent recirculating flows. *Phys. Fluids*, **A(5)**, 3186–3196.

Zang, Y., Street, R. L., & Koseff, J. R. 1994. A non-staggered grid, fractional step method for time-dependent incompressible Navier-stokes equations in curvilinear coordinates. *J. Comput. Phys.*, **114**, 18–33.

Zedler, E. A. 2002. *Large eddy simulation of sediment transport in oscillatory flow over wavy terrain.* Ph.D. dissertation, Stanford University.

Zedler, E. A., & Street, R. L. 2001. Large-eddy simulation of sediment transport: Currents over ripples. *J. Hydrau. Eng.*, **127**, 444–452.